

WERNER KRAUS

## Force Control of Cable-Driven Parallel Robots



Universität Stuttgart



Fraunhofer  
IPA

# **STUTTGARTER BEITRÄGE ZUR PRODUKTIONSFORSCHUNG BAND 49**

## **Herausgeber:**

Univ.-Prof. Dr.-Ing. Thomas Bauernhansl

Univ.-Prof. Dr.-Ing. Dr. h.c. mult. Alexander Verl

Univ.-Prof. a. D. Dr.-Ing. Prof. E.h. Dr.-Ing. E.h. Dr. h.c. mult. Engelbert Westkämper

**Werner Kraus**

## **Force Control of Cable-Driven Parallel Robots**

**FRAUNHOFER VERLAG**

**Kontaktadresse:**

Fraunhofer-Institut für Produktionstechnik und Automatisierung IPA, Stuttgart  
Nobelstraße 12, 70569 Stuttgart  
Telefon 0711 9 70-00, Telefax 0711 9 70-13 99  
[info@ipa.fraunhofer.de](mailto:info@ipa.fraunhofer.de), [www.ipa.fraunhofer.de](http://www.ipa.fraunhofer.de)

**STUTTGARTER BEITRÄGE ZUR PRODUKTIONSFORSCHUNG****Herausgeber:**

Univ.-Prof. Dr.-Ing. Thomas Bauernhansl  
Univ.-Prof. Dr.-Ing. Dr. h.c. mult. Alexander Verl  
Univ.-Prof. a. D. Dr.-Ing. Prof. E.h. Dr.-Ing. E.h. Dr. h.c. mult. Engelbert Westkämper

Fraunhofer-Institut für Produktionstechnik und Automatisierung IPA, Stuttgart  
Institut für Industrielle Fertigung und Fabrikbetrieb (IFF) der Universität Stuttgart  
Institut für Steuerungstechnik der Werkzeugmaschinen und Fertigungseinrichtungen (ISW)  
der Universität Stuttgart

Titelbild: © Rainer Bez, Fraunhofer IPA

**Bibliografische Information der Deutschen Nationalbibliothek**

Die Deutsche Nationalbibliothek verzeichnet diese Publikation in der Deutschen Nationalbibliografie;  
detaillierte bibliografische Daten sind im Internet über [www.dnb.de](http://www.dnb.de) abrufbar.

ISSN: 2195-2892

ISBN (Print): 978-3-8396-0979-8

**D 93**

Zugl.: Stuttgart, Univ., Diss., 2015

Druck: Mediendienstleistungen des Fraunhofer-Informationszentrum Raum und Bau IRB, Stuttgart  
Für den Druck des Buches wurde chlor- und säurefreies Papier verwendet.

© by **FRAUNHOFER VERLAG**, 2016

Fraunhofer-Informationszentrum Raum und Bau IRB  
Postfach 80 04 69, 70504 Stuttgart  
Nobelstraße 12, 70569 Stuttgart  
Telefon 0711 9 70-25 00  
Telefax 0711 9 70-25 08  
E-Mail [verlag@fraunhofer.de](mailto:verlag@fraunhofer.de)  
URL <http://verlag.fraunhofer.de>

Alle Rechte vorbehalten

Dieses Werk ist einschließlich aller seiner Teile urheberrechtlich geschützt. Jede Verwertung, die über die engen Grenzen des Urheberrechtsgesetzes hinausgeht, ist ohne schriftliche Zustimmung des Verlages unzulässig und strafbar. Dies gilt insbesondere für Vervielfältigungen, Übersetzungen, Mikroverfilmungen sowie die Speicherung in elektronischen Systemen.

Die Wiedergabe von Warenbezeichnungen und Handelsnamen in diesem Buch berechtigt nicht zu der Annahme, dass solche Bezeichnungen im Sinne der Warenzeichen- und Markenschutz-Gesetzgebung als frei zu betrachten wären und deshalb von jedermann benutzt werden dürfen. Soweit in diesem Werk direkt oder indirekt auf Gesetze, Vorschriften oder Richtlinien (z.B. DIN, VDI) Bezug genommen oder aus ihnen zitiert worden ist, kann der Verlag keine Gewähr für Richtigkeit, Vollständigkeit oder Aktualität übernehmen.

## GELEITWORT DER HERAUSGEBER

Produktionswissenschaftliche Forschungsfragen entstehen in der Regel im Anwendungszusammenhang, die Produktionsforschung ist also weitgehend erfahrungsbasiert. Der wissenschaftliche Anspruch der „Stuttgarter Beiträge zur Produktionsforschung“ liegt unter anderem darin, Dissertation für Dissertation ein übergreifendes ganzheitliches Theoriegebäude der Produktion zu erstellen.

Die Herausgeber dieser Dissertations-Reihe leiten gemeinsam das Fraunhofer-Institut für Produktionstechnik und Automatisierung IPA und jeweils ein Institut der Fakultät für Konstruktions-, Produktions- und Fahrzeugtechnik an der Universität Stuttgart.

Die von ihnen betreuten Dissertationen sind der marktorientierten Nachhaltigkeit verpflichtet, ihr Ansatz ist systemisch und interdisziplinär. Die Autoren bearbeiten anspruchsvolle Forschungsfragen im Spannungsfeld zwischen theoretischen Grundlagen und industrieller Anwendung.

Die „Stuttgarter Beiträge zur Produktionsforschung“ ersetzt die Reihen „IPA-IAO Forschung und Praxis“ (Hrsg. H.J. Warnecke / H.-J. Bullinger / E. Westkämper / D. Spath) bzw. ISW Forschung und Praxis (Hrsg. G. Stute / G. Pritschow / A. Verl). In den vergangenen Jahrzehnten sind darin über 800 Dissertationen erschienen.

Der Strukturwandel in den Industrien unseres Landes muss auch in der Forschung in einen globalen Zusammenhang gestellt werden. Der reine Fokus auf Erkenntnisgewinn ist zu eindimensional. Die „Stuttgarter Beiträge zur Produktionsforschung“ zielen also darauf ab, mittelfristig Lösungen für den Markt anzubieten. Daher konzentrieren sich die Stuttgarter produktionstechnischen Institute auf das Thema ganzheitliche Produktion in den Kernindustrien Deutschlands. Die leitende Forschungsfrage der Arbeiten ist: Wie können wir nachhaltig mit einem hohen Wertschöpfungsanteil in Deutschland für einen globalen Markt produzieren?

Wir wünschen den Autoren, dass ihre „Stuttgarter Beiträge zur Produktionsforschung“ in der breiten Fachwelt als substanzell wahrgenommen werden und so die Produktionsforschung weltweit voranbringen.

Alexander Verl

Thomas Bauernhansl

Engelbert Westkämper



# Force Control of Cable-Driven Parallel Robots

Von der Fakultät Konstruktions-, Produktions- und Fahrzeugtechnik  
der Universität Stuttgart  
zur Erlangung der Würde eines Doktor-Ingenieurs (Dr.-Ing.)  
genehmigte Abhandlung

Vorgelegt von  
Werner Kraus  
aus Villingen-Schwenningen

Hauptberichter: Junior-Prof. Dr.-Ing. Andreas Pott  
Mitberichter: Univ.-Prof. Dr.-Ing. Prof. E.h. Peter Eberhard  
Tag der mündlichen Prüfung: 23. September 2015

Institut für Steuerungstechnik der Werkzeugmaschinen und Fertigungseinrichtungen  
(ISW)

der Universität Stuttgart

2015

---

# Foreword of the Author

This thesis results from my work as research fellow at the Fraunhofer Institute for Manufacturing Engineering and Automation IPA in Stuttgart, Germany, partially funded by the Fraunhofer internal program "ATLAS, Automatisierte Montage von Großanlagen mit krantchnischen Seilrobotern". My very special thanks go to Junior-Prof. Dr.-Ing. Andreas Pott for supporting my scientific work, his role as team leader and supervisor and his great endorsement at any stage of this PhD thesis project. I am sincerely thankful to Prof. Dr.-Ing. Prof. E.h. Peter Eberhard for accepting the responsibility of co-reviewing my thesis.

My gratitude goes to my colleagues within the department of robot and assistive systems. I want to thank Dipl.-Ing. Martin Hägele, M.Sc. as head of the department for his mental support, challenging tasks and trust. Especially, I am grateful to my colleagues also working on cable robotics Valentin Schmidt, M.Eng., Dipl.-Ing. Philipp Miermeister and Dipl.-Ing. Philipp Tempel for a good working atmosphere, inspiring discussion and support. I want to thank Patrick Stelzer, M.Sc. for discussions on control theory. I am obliged to Dr.-Ing. Alexander Spiller for the intensive discussions about force control and energy efficiency of robot systems as well as for his collegial advice.

I also wish to express my gratitude to the members of Robotics Research Institute (RRI) in Korea under the leading of Prof. Jong-Oh Park and Prof. Seong Young Ko for the research stays in Korea. Special thanks go to Dr. Dragoljub Surdilovic with his wide experience in the field of admittance control and kinematics.

I thank Fabian Büsis, Sebastian Schmidinger, Clemens Honold, Julian Koller, Puneeth Rajendra, Tobias Simon, Bernhard Sieber, Simon Stoll, Daniel Ehmann, Maximilian Schön-herr, Wei Yang Ho, Alexander Mangold, Michael Keßler, Patric Skalecki, Marco Schröter, Max Daiber-Huppert, Moritz Arns and Lea Berberich for their student work that accompanied this project.

I am also very grateful to Luzia Schuhmacher, M.A. for proof-reading all the papers and the thesis with great dedication and conscientiousness.

Especially, I would like to thank my parents and sister for their ongoing support and family cohesion.

---

# Kurzinhalt

In dieser Dissertation wird eine relativ neue Klasse von Robotern untersucht, die Seile zur Kraftübertragung einsetzt. Da Seile nur Zugkräfte übertragen, stellen die sogenannten parallelen Seilroboter hohe Anforderung an ihre Regelung. Die in dieser Arbeit zu Grunde gelegten Seilroboter besitzen mehr Seile als Bewegungsfreiheitsgrade der Plattform und zählen damit zur Klasse der redundanten Roboter. Die Redundanz erlaubt es, die Seile gegeneinander zu verspannen. In dieser Arbeit wird zunächst ein Ansatz zur Regelung der Plattformposition und eine synchrone Regelung der Seilkräfte vorgeschlagen. Hierzu werden auf Basis der elastischen Seile dynamische Modelle entwickelt und auch die Vorwärtskinematik erweitert. Mit dem vorgeschlagenen Verfahren zur Berechnung der Seilkräfte lässt sich die interne Verspannung der Seile stufenlos einstellen. Die Untersuchungen zeigen, dass sich durch die Änderung der Vorspannung die Eigenfrequenzen der Plattform um 15-30% verschieben lassen. Durch die Wahl einer geringen Seilverspannung lässt sich der Energieverbrauch bei bleibender Leistung des Roboters um bis zu 20% senken.

Zur Verifikation des Regelungskonzeptes wird die Positionsgenauigkeit des Roboters experimentell untersucht. Als Referenz dient die Steuerung des Roboters auf Basis eines geometrischen Modells, welches keine geschlossenen Regelkreise für die Plattformposition und die Seilkräfte besitzt. Im Zentrum des Arbeitsraumes konnte mit beiden Ansätzen eine vergleichbare Genauigkeit mit Nutzlast von 80 kg von etwa 70 mm und  $2.5^\circ$  erreicht werden. Auch am Arbeitsraumrand kann mit dem vorgeschlagenen Verfahren eine vergleichbare Genauigkeit erreicht werden, da die Seile unter Spannung gehalten werden.

Für Bearbeitungsprozesse wie z.B. Schleifen wird die bekannte hybride Positions- und Kraftregelung auf Seilroboter übertragen. Mit dem Regelungsansatz kann die Roboterplattform in einer gewünschten Richtung eine Kontaktkraft aufbringen, währenddessen die Plattform in den verbleibenden Richtungen positionsgesteuert verfahren werden kann. Zur Mensch-Roboter-Kooperation wird eine Admittanzregelung vorgeschlagen. Die Plattform simuliert dabei ein Feder-Masse-Dämpfer-System, mit Hilfe dessen ein virtueller Arbeitsraum realisiert wird. Die Evaluierung zeigt, dass eine Bandbreite bis 13 Hz dargestellt werden kann.

---

# Short Summary

In this thesis, a relatively new class of robots which use cables instead of rigid links is investigated. As cable can transmit only pull forces, cable robots make high demands on the control. The cable robots investigated in this thesis have more cables than degrees-of-freedom of the platform and, thus, belong to the class of redundant robots. The redundancy allows to tense the cables against each other. A control approach for synchronous control of the platform position and the cable forces is proposed. For this purpose, system identifications for dynamic models of the robot are carried out and the forward kinematics is expanded to deal with non-linear cable stiffness. The proposed approach for calculation of the desired cable forces allows for step-less adjustment of the internal tensions. The investigations show that with change of the internal tension the eigenfrequencies of the robot can be influenced by 15-30%. By choice of a minimal tension level, the energy consumption of the robot can be decreased by up to 20% while the performance of the robot remains on the same level.

For the proposed control scheme, extensive investigations of the positional accuracy are carried out. As reference approach, the control assuming a rigid robot model without closed-loop control of the operational space position and cable forces is used. The two approaches delivered comparable results in the workspace centre. The position accuracy with a payload of 80 kg amounted to roughly 70 mm and 2.5°. Using the proposed controller at the workspace border, almost the same accuracy could be reached as well, as the cables are kept under tension.

For machining processes like grinding, the well-known hybrid position and force control approach is incorporated on a cable robot. With the control approach, the robot can apply a contact force in a programmable direction, while the platform can be position-controlled in the lasting directions. For the human robot cooperation, an admittance controller is proposed. The platform simulates a virtual spring-mass-damper system which enables for the implementation of a virtual workspace. With the demonstrator, a bandwidth of 13 Hz is reached.

---

# Table of Contents

<b>List of Figures</b>	viii
<b>List of Tables</b>	xii
<b>List of Formula Items</b>	xiii
<b>List of Abbreviations</b>	xiv
<b>1 Introduction</b>	1
1.1 Motivation . . . . .	1
1.2 Literature Overview . . . . .	3
1.3 Problem Statement . . . . .	8
1.4 Objective and Content of this Work . . . . .	9
1.5 Remarks on the Notation . . . . .	11
<b>2 Fundamentals</b>	12
2.1 Robot Model . . . . .	12
2.1.1 Kinematic and Static Model . . . . .	12
2.1.2 Stiffness Model . . . . .	15
2.1.3 Robot Dynamics with Elastic Cables . . . . .	19
2.1.4 Forward Kinematics . . . . .	21
2.2 Workspace and Cable Force Algorithms . . . . .	22
2.2.1 Workspace Definitions and Analysis . . . . .	22
2.2.2 Cable Force Algorithms . . . . .	23
2.3 Demonstrators . . . . .	27
2.3.1 Robot Hardware Design . . . . .	29
2.3.2 Control Architecture . . . . .	30
2.3.3 Measuring Equipment . . . . .	35
<b>3 Controller for Redundant Cable Robots with Elastic Cables</b>	37
3.1 Derivation of the General Control Approach . . . . .	37
3.1.1 General Model of a Feedback Control Loop . . . . .	38
3.1.2 Cable Force Control . . . . .	39
3.1.3 Stability Analysis of Cable Force Control . . . . .	40

3.1.4	Synchronous Control of Position and Cable Forces . . . . .	41
3.1.5	Proposed Control Architecture for Redundant Cable Robot . . . . .	43
3.2	Forward Kinematics with non-linear Cable Stiffness . . . . .	45
3.3	Modelling and System Identification . . . . .	47
3.3.1	Dynamics of the Actuator Unit . . . . .	47
3.3.2	Platform's Dynamics . . . . .	48
3.4	Controller Synthesis and Stability Analysis . . . . .	51
3.4.1	Controller Synthesis for Operational Space Position Control . . . . .	52
3.4.2	Controller Synthesis for Joint Space Cable Force Control . . . . .	53
3.5	Controller Implementation . . . . .	54
3.5.1	Operational Space Position Control . . . . .	54
3.5.2	Cable Force Control . . . . .	55
3.6	Cable Force Algorithm . . . . .	56
3.6.1	Wrench Set-Point Generation . . . . .	56
3.6.2	Cable Force Set-Point Generation . . . . .	58
3.7	Cable Force Measurement . . . . .	64
3.7.1	Measurement Principles . . . . .	64
3.7.2	Friction Model for the Pulleys . . . . .	65
3.7.3	Implementation . . . . .	71
3.7.4	Verification of the Friction Model: Wrench Hysteresis . . . . .	72
<b>4</b>	<b>Experimental and Model-Based Investigation of Robot Properties</b>	<b>73</b>
4.1	Load Identification and Compensation . . . . .	74
4.1.1	Offline Load Identification . . . . .	74
4.1.2	Online Load Identification and Compensation . . . . .	79
4.1.3	Experimental Evaluation . . . . .	80
4.2	Position Accuracy . . . . .	83
4.2.1	Comparison of linear and non-linear Cable Model . . . . .	83
4.2.2	Static Investigation . . . . .	86
4.2.3	Experimental Workspace Analysis . . . . .	87
4.2.4	Dynamic Investigation . . . . .	94
4.3	Eigenfrequencies of the Platform . . . . .	96
4.4	Energy Consumption . . . . .	99
4.4.1	Energy Consumption Model of the Actuator Unit . . . . .	99
4.4.2	Identification and Verification of the Energy Consumption Model . .	103
4.4.3	Analysis of Energy Efficiency . . . . .	103
4.5	Summary of this Chapter . . . . .	108

<b>5 Operational Space Force Controller</b>	<b>111</b>
5.1 Hybrid Position and Force Control . . . . .	111
5.1.1 Approach . . . . .	112
5.1.2 Controller Design and Implementation . . . . .	114
5.1.3 Experimental Evaluation of Contact Establishment and Following Behaviour . . . . .	117
5.2 Haptic Interaction with Admittance Control . . . . .	121
5.2.1 Virtual System Behaviour for Haptic Interaction . . . . .	121
5.2.2 Controller Design and Implementation . . . . .	125
5.2.3 Experimental Investigation of the Performance . . . . .	126
5.2.4 Elimination of Oscillations due to Pulley Friction . . . . .	129
<b>6 Conclusions and Outlook</b>	<b>130</b>
6.1 Conclusions . . . . .	130
6.2 Outlook . . . . .	132
<b>References</b>	<b>133</b>

---

# List of Figures

1.1	Skycam system for the transmission of sport events . . . . .	2
1.2	Examples for serial (a) and parallel topologies (b) and (c) . . . . .	3
1.3	Research targets of this thesis and core elements of a cable robot . . . . .	4
1.4	Cable robot prototypes for research . . . . .	6
2.1	Schematic representation of the general kinematic parameters . . . . .	13
2.2	Model for the pulley kinematics . . . . .	14
2.3	Spring characteristic of a 6.0 mm Dyneema® cable . . . . .	17
2.4	Non-linearity of cable stiffness . . . . .	17
2.5	Workspace hull of the IPAnema3 robot . . . . .	23
2.6	Convergence of the closed-form method . . . . .	25
2.7	Comparison of the workspace computed with different methods . . . . .	26
2.8	Cable-driven parallel robot IPAnema3 . . . . .	28
2.9	Cable-driven parallel robot IPAnema3 Mini . . . . .	31
2.10	Overview over different control architectures . . . . .	32
2.11	Structure of a typical industrial CNC . . . . .	33
3.1	General model of a feedback control loop . . . . .	38
3.2	Control structures with open-loop position control in operational space . . . . .	39
3.3	Approaches for synchronous position and force control . . . . .	42
3.4	Proposed control architecture . . . . .	44
3.5	Proposed implementation of the forward kinematics . . . . .	45
3.6	Experimental system identification of the actuator . . . . .	47
3.7	Bode diagram of the servo drive . . . . .	49
3.8	Course of the winch movement during a sinus sweep . . . . .	49
3.9	Bode diagram of the minimal and maximal dynamic of the platform . . . . .	51
3.10	Nyquist diagram of the open-loop transfer function $G_{OSPC,0,z}(s)$ . . . . .	53
3.11	Nyquist diagram for the open-loop transfer function $G_{CFC,0}(s)$ . . . . .	54
3.12	Control structure of the joint space cable force controller . . . . .	55
3.13	Determination of the feed-forward term for the platform dynamics . . . . .	58
3.14	Comparison of the resulting cable forces along a trajectory . . . . .	62
3.15	Principles for cable force measurement . . . . .	65

---

3.16	Pulley unit of the IPAnema 3 Mini robot for cable force measurement $F_s$	66
3.17	Determination of the relevant cable forces of a series of pulleys	67
3.18	Structure of the pulley friction compensation	71
3.19	Reduction of the wrench hysteresis using the pulley friction compensation	72
4.1	Platform of the IPAnema 3 robot with additional loads	75
4.2	Circle trajectory for identifying the mass parameters	76
4.3	First harmonics of the forces in $x$ - and $y$ -axis	77
4.4	First harmonics of the torques around the $x$ - and $y$ -axis	78
4.5	Structure of the load identification and compensation	80
4.6	Dynamic response of the platform	82
4.7	Displacement of the platform under different loads	82
4.8	Progression of the pose using the linear cable model	84
4.9	Progression of the pose using the non-linear cable model	85
4.10	Settlement of the cable while reaching a new tension level	85
4.11	Investigated points (blue boxes) within one quarter of the robot's workspace	86
4.12	Position accuracy with inverse kinematics	87
4.13	Position accuracy with force control and minimum cable forces	88
4.14	Position accuracy with force control and medium cable forces	88
4.15	Investigated points at the workspace border	89
4.16	Position accuracy and cable forces on a straight line with $m_p = 25 \text{ kg}$	90
4.17	Position accuracy and cable forces on a straight line with $m_p = 105 \text{ kg}$	90
4.18	Position accuracy at the workspace border using IK with $m_p = 105 \text{ kg}$	92
4.19	Position accuracy at the workspace border using QP with $m_p = 105 \text{ kg}$	93
4.20	Validity of the cable forces at the position relative to the workspace border	93
4.21	Progression of velocity and acceleration along a trajectory (IPAnema 3)	94
4.22	Absolute position error on a trajectory using IK and force control	95
4.23	Experimental and calculated wrench in $x$ -axis (IPAnema 3 Mini)	95
4.24	Progression of the cable forces along a trajectory (IPAnema 3 Mini)	96
4.25	Investigated points for the identification of the eigenfrequencies	97
4.26	Eigenfrequency of the platform in $z$ -axis for different tension levels	98
4.27	Minimal and maximal eigenvalues of the operational space stiffness matrix	99
4.28	Minimal and maximal eigenvalues of the geometric and cable stiffness	100
4.29	Subsystems of the energy consumption model	100
4.30	Verification of the energy consumption model	104
4.31	Distribution of the losses on the subsystems	105
4.32	Efficiency map of the IPAnema 3 winch including planetary gear box	106
4.33	Effect of the tension level on the power consumption of the robot	107
4.34	Cable robot IPAnema 3 and industrial robot	108

4.35 Comparison of the power consumption between industrial and cable robot . . . . .	109
5.1 Principle set-up at the mobile platform for hybrid position and force control	112
5.2 Hybrid position and force control proposed . . . . .	113
5.3 Proposed implementation of the hybrid position and force control . . . . .	114
5.4 State machine with transition conditions for the contact establishment . . . . .	116
5.5 Progression of the force during contact control . . . . .	117
5.6 Investigated areas for contact establishment . . . . .	118
5.7 Test set-up for the evaluation of the following behaviour . . . . .	119
5.8 Course of the contact force normal to the surface on the oil barrel . . . . .	120
5.9 Course of the cable forces during the force control along the oil barrel . . . . .	120
5.10 Model of a 1D spring-mass-damper system with external force $F(t)$ . . . . .	122
5.11 Zones of the virtual workspace and workspace hull of the cable robot . . . . .	123
5.12 Simulation of the virtual workspace . . . . .	124
5.13 Structure of the implementation with admittance and cable force controller .	126
5.14 Bode diagram of the transfer function of the IPAnema3 Mini drive $G_a(s)$ . . .	127
5.15 Experiment: measured user-applied force $w_x$ and resulting position $r_{d,x}$ . . . . .	128
5.16 Reduction of the oscillation of the admittance control . . . . .	129

---

# List of Tables

2.1	Cable robot IPAnema 3: parameters and main components . . . . .	29
2.2	Cable robot IPAnema 3 Mini: parameters and main components . . . . .	30
2.3	Geometrical parameters of the IPAnema 3 robot . . . . .	30
2.4	Geometrical parameters of the IPAnema 3 Mini robot . . . . .	31
3.1	Identified parameters and control parameters for OSPC and CFC . . . . .	51
3.2	Comparison of the different cable force algorithms along a trajectory . . . . .	61
3.3	Mean cable forces within the workspace for different payloads . . . . .	62
3.4	Final parametrization for all eight cables of the IPAnema 3 Mini . . . . .	70
3.5	Improvement of the wrench hysteresis . . . . .	71
4.1	Comparision of the theoretically derived amplitudes with the experiment . .	76
4.2	Load parameters: comparison of nominal and estimated values . . . . .	78
4.3	Investigated points within the workspace with $m_p=25\text{ kg}$ and $m_p=105\text{ kg}$ . .	86
4.4	Investigated points at the workspace border . . . . .	89
4.5	Investigated points for the identification of the eigenfrequencies (IPAnema 3) .	97
4.6	Identified parameters for the energy consumption model . . . . .	104
4.7	Summary of the absolute position accuracies evaluated in different scenarios	110
5.1	Control parameters of hybrid position and force control . . . . .	116
5.2	Resulting overshoot and settling time while contact establishment . . . . .	118
5.3	Verification of the dynamic parameters of the simulated system . . . . .	127

# List of Formula Items

variable	description	cross-reference
$\mathbf{a}_i$	position vector to the last pulley before the platform	fig. 2.1, p. 13
$\mathbf{A}^T$	structure matrix	eq. (2.10), p. 15
$\alpha$	motor angles	sec. 2.3.2, p. 30
$\mathbf{b}_i$	position vector of the cable's platform anchor point described in $\mathcal{K}_p$	fig. 2.1, p. 13
$\beta$	wrapping angle of a cable along a pulley	eq. (2.6), p. 14
$\mathbf{c}_i$	position vector to the point where the cable leaves the pulley towards the platform	fig. 2.2b, p. 14
$\mathbf{c}_{m_p}$	vector to the centre of gravity of $m_p$	ec. 2.1.3, p. 21
$\mathbf{D}$	damping matrix	sec. 3.3.2, p. 50
$\mathbf{f}$	actual cable forces	eq. (2.10), p. 15
$f_{\min}, f_{\max}$	minimum and maximum feasible cable force	sec. 2.2.1, p. 22
$f_{\text{ref}}$	reference cable force used to calculate a cable force distribution	sec. 2.2, p. 22
$\mathbf{F}_d$	desired operational space force	eq. (5.2) , p. 115
$\mathbf{H}$	a basis of the kernel of $\mathbf{A}^T$	eq. (2.41), p. 24
$\mathbf{J}_w$	rotational inertia of the joints w.r.t. drive angle $\alpha$	eq. (2.28 ), p. 20
$\mathbf{k}_{\text{spec}}$	specific spring constant	eq. (2.16), p. 16
$\mathbf{K}_c$	cable stiffness of the robot in operational space	eq. (2.22), p. 18
$\mathbf{K}_g$	geometrical stiffness of the robot in operational space	eq. (2.22), p. 18
$\mathbf{K}_l$	cable stiffness matrix in joint space	sec. 2.1.2, p. 15
$\mathbf{K}_x$	operational space stiffness matrix	eq. (2.22), p. 18
$l_0$	free cable length between the drum and the last pulley	sec. 2.1.2, p. 15
$\mathbf{l}_i$	cable vector pointing from the platform to the last pulley at the frame	eq. (2.1), p. 12
$l_t$	free total cable length between the drum and the platform	eq. (2.22), p. 18
$\lambda$	eigenvalue of a matrix	sec. 4.3, p. 96
$\boldsymbol{\lambda}_H$	multiplier for $\mathbf{H}$	eq. (2.41), p. 24

variable	description	cross-reference
$m$	number of cables	sec. 1.2, p. 3
$m_p$	platform mass including payload	sec. 2.1.3, p. 21
$\mathbf{M}$	inertia matrix	eq. (2.27), p. 20
$n$	number of degrees-of-freedom (DOF)	sec. 1.2, p. 3
$\omega$	eigenfrequency of a dynamic system	eq. (4.8), p. 96
$\mathbf{P}$	power	sec. 4.4, p. 102
$\varphi$	Kardan angles describing the rotation matrix $\mathbf{R}$	sec. 2.1, p. 12
$\mathbf{q}$	generalized position of the winches (joint space)	eq. (2.2), p. 13
$r$	degree-of-redundancy	sec. 1.2, p. 3
$r_p$	radius of a pulley	sec. 2.1, p. 13
$r_w$	generalized gear ratio including ratio of the gear box and drum radius of the winch	sec. 2.3.2, p. 30
$\mathbf{r}$	position vector of the platform coordinate system $\mathcal{K}_p$ w.r.t. the world frame $\mathcal{K}_0$	fig. 2.1, p. 13
$\mathbf{R}$	rotation matrix of platform coordinate system $\mathcal{K}_p$ w.r.t. the world frame $\mathcal{K}_0$	sec. 2.1, p. 12
$\mathbf{R}_A$	orientation of the installation position of the pulley $\mathcal{K}_A$ w.r.t. $\mathcal{K}_0$	sec. 2.1.1, p. 13
$\mathbf{R}_t$	orientation of the task frame $\mathcal{K}_t$ w.r.t. $\mathcal{K}_0$	sec. 5.1.1, p. 112
$\tau$	torque	eq. (2.32), p. 20
$\theta$	cable length reflected by the motor angles	sec. 2.3.2, p. 30
$\mathbf{u}_i$	unit vector describing the direction of the cable starting from the platform	sec. 2.1, p. 12
$\mathbf{w}$	wrench (external forces and torques) acting at the platform	eq. (2.10), p. 15
$\mathbf{x}$	generalized actual operational space position of the platform w.r.t. the world frame $\mathcal{K}_0$	sec. 2.1, p. 12

---

# List of Abbreviations

---

abbreviation	definition	cross-reference
AC	alternating current	p. 36
ACF	advanced closed-form method	p. 26
AD	analogue-to-digital	p. 33
CF	closed-form method	p. 24
CFC	cable force control	p. 39
CFE	closed-form method energy-efficient	p. 24
CNC	computerized numerical control	p. 32
DC	direct current	p. 101
DOF	degrees-of-freedom	p. 1
DFT	discrete Fourier transformation	p. 76
GUI	graphical user interface	p. 34
HLI	high level interface	p. 34
HPFC	hybrid position and force control	p. 43
I/O	input/output	p. 33
IK	inverse kinematics	p. 14
IPM	improved puncture method	p. 27
JS	joint space	p. 21
NC	numerical control	p. 35
OS	operational space	p. 21
OSPC	operational space position control	p. 41
PI	proportional-integral	p. 52
PID	proportional-integral-derivative	p. 5
PLC	programmable logic controller	p. 34
PM	puncture method	p. 25
PT <sub>1</sub>	low-pass filter of 1 <sup>st</sup> order	p. 48
QP	quadratic programming	p. 27
ST	structured text	p. 34
WFW	wrench feasible workspace	p. 22

---

---

# 1 Introduction

## 1.1 Motivation

Cable-driven systems can be found in hundreds of applications like cranes, cable railways, elevators and stage technique. The mechanical principles of cables, winches and pulleys are well understood. With the availability of control PCs with high computational power, the synchronized control of a set of cables became possible. A cable-driven system which is well known in public is the Skycam shown in Fig. 1.1, which uses four cables to move a TV camera over the playing area (Cone 1985). The Skycam is one example of a cable-driven parallel robot, in the following referred to as cable robot. It bears impressively the advantages of a cable robot which are huge workspace, low moved mass and the parallel structure so that the actuator units can be installed fixed, e.g. in the building.

Robot kinematics can be classified regarding their topology as shown in Fig. 1.2. The most common form is the serial robot, which is familiar with the human arm and can be found, e.g. in industrial robots (Fig. 1.2a). The characteristic is that the joints are stacked serially one after each other. In parallel robots however, the actuators are fixed to the machine frame and connected with legs to the mobile platform. Typical parallel robots are the Stewart Gough platform using actuated prismatic joints as depicted in Fig. 1.2b or the delta kinematic using actuated revolute joints shown in Fig. 1.2c. In cable robots, the rigid links are replaced by cables as visualized in Fig. 1.3. As they have the same topology, they share some common properties and theoretical foundations with parallel robots.

The core elements of a cable robot with  $m=8$  cables and  $n=6$  degrees-of-freedom (DOF) are depicted in Fig. 1.3. The winches with servo drives are attached to the machine frame, which is called base for classical parallel robot. The mobile platform is manipulated through eight cables in six DOF.

The workspace, available payload, dynamics and position accuracy are important design parameters when developing a robot for an application. Using elastic cables for the force transmissions new questions arise about the control and the performance of such a robot. The workspace of a cable robot depends on the feasibility of the cable forces and thus, the workspace depends strongly on the payload.

Cable robots are known to be energy efficient due to the low moved mass. Both for economic and ecological reasons, the energy consumption of robots received more and more



Figure 1.1: Skycam system for the transmission of sport events (special thanks to Stephen Wharton, CTO SkyCam LLC)

attention in the past. In this thesis, the influence of the tension level on the energy consumption is investigated. Another important comparison criterion is the position accuracy of the robot. Cable robots exhibit good stiffness at the platform, which depends mainly on the cable stiffness. This is evident in large cable robots, where a decrease in stiffness is observed due to the additional cable length. In industrial manipulation or material handling operations, the payload changes and is often not predictable. This leads to errors in the accuracy due to cable elasticity.

Processes like grinding and polishing demand an accurately controlled contact force to give reliable results. One application example is the surface grinding in the air plane maintenance. Force control also allows compensating for deviations in a work piece geometry by keeping the tool constantly in contact with the surface.

In the last decade, human robot cooperation became more important, where human worker share the workspace with a robot. One key technology is compliance control, so the robot can be safely controlled. Cable robots are also interesting for the use in human robot cooperation, as due to the low moved mass, small drives are sufficient what makes the robot system inherently safe. Additionally, the high dynamics of cable robots allow for a high bandwidth of platform dynamics which makes them interesting as haptic device with a large workspace.

Within this thesis, controllers to enhance the performance of cable robots are developed. Based on experiments and models, workspace, position accuracy and energy efficiency are studied. In the following, an overview on the state of the art in cable robots and focusing on the research targets is given.

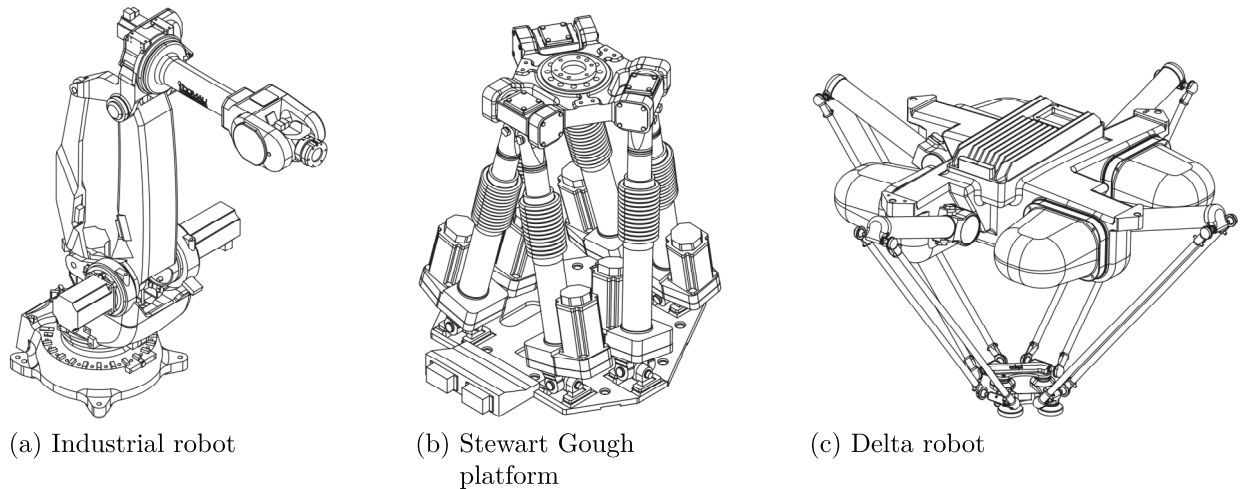


Figure 1.2: Examples for serial (a) and parallel topologies (b) and (c)

## 1.2 Literature Overview

In the last decades, cable robots attracted several research groups worldwide. Already in the early nineties, the National Institute of Standards and Technology (NIST in USA) developed the Robocrane family with cable robot demonstrators for industrial applications like painting, welding or manipulation (Albus, Bostelman et al. 1992). Further application examples for cable robots in general are e.g. the large-scale assembly of solar power plant (Pott, Meyer et al. 2010), cleaning of façades (Voss, Wijk et al. 2012), (Izard, Gouttefarde et al. 2012), inspection of large structures, e.g. high storage bays (Kraus, Schmidt et al. 2012). Starting with the thesis of Verhoeven (2004), research on workspace analysis, design and motion control of cable robots is conducted at University of Duisburg-Essen (UDE). In the earlier days, it was done on the Segesta (Bruckmann 2010), nowadays on a larger robot used as high storage retrieval system (Lalo 2013), which is depicted in Fig. 1.4b. Apart from industrial applications, cable robots are developed for a locomotion interface (Otis, Mokhtari et al. 2008) and rehabilitation, e.g. the STRING-MAN system (Surdilovic, Jinyu Zhang et al. 2007).

For cable robots, it is usual to categorize the number of rotational and translational DOF by motion patterns according to Verhoeven (2004). A fully movable robot has six DOF and is denoted by  $3R3T$ , where  $R$  stands for Rotation and  $T$  for Translation. Another typical robot configuration is the  $1R2T$  robot, which corresponds to a planar robot and has usually four cables.

The relation between the number of cables  $m$  and DOF  $n$  is characterized by the degree-of-redundancy  $r$  defined as  $r = m - n$ . For a cable-driven parallel robot, redundancy means more specifically force redundancy. The force redundancy leads to another categorization, which was mainly defined by Ming and Higuchi (1994) and Verhoeven (2004).

## Research targets

Position and force control of redundant cable robots

Control of elastic joints with position-controlled drives

External force control for contact control and haptic interaction

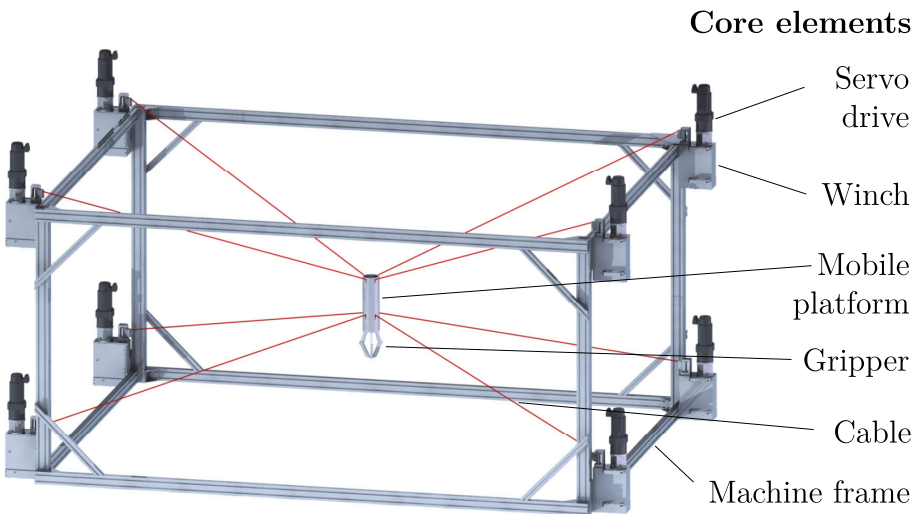


Figure 1.3: Research targets of this thesis and core elements of a cable robot

Three categories are distinguished regarding the relation between number of cables and the DOF. If  $m \leq n$ , not all  $n$  DOF can be controlled: such incompletely restrained positioning mechanisms (IRPM) are not force redundant. Workspace analysis and control have to be performed under the consideration of the kinematic constraints and the force equilibrium (e.g. geometrico-static analysis (Carricato and Merlet 2010)). Also the case  $m = n$  is considered as incompletely restrained, as external forces are needed to guarantee positive cable forces. If  $m = n + 1$ , the robot belongs to the class of completely restrained positioning mechanisms (CRPM). With the force redundancy of degree one, the cables can be tensed against each other and positive cable forces can be reached. If  $m > n + 1$ , the robot belongs to the class of redundantly restrained positioning mechanisms (RRPM). The collective term of CRPM and RRPM is referred to as fully constrained robot which lies in the focus of this thesis.

The dynamic control of classical parallel kinematic machines are discussed by Paccot, Andreff et al. (2009) and Wang, Wu et al. (2009). Experimental studies of control concepts for a parallel manipulator with flexible links are presented in (Burkhardt, Seifried et al. 2014). Computed torque control approaches for cable robots are proposed by Liu, Zhang et al. (2009). Control approaches with simulation are shown by Meunier, Boulet et al. (2009) and Laroche, Chellal et al. (2012) and an extensive work on the control of a cable-driven locomotion interface can be found in (Otis, Nguyen Dang et al. 2009).

The control problem of a cable robot can be solved either in joint or operational space. With joint space position control, promising results are already reached in the past. For example, the Falcon robot accelerated with 40 g (Kawamura, Kino et al. 2000) using small DC drives and the IPAnema 1 cable robot reached with state of the art industrial servo drive dynamics of 10 m/s and 100 m/s<sup>2</sup> (Pott, Mütherich et al. 2012). To enhance the dynamics

of cable robots, model-based control approaches by the mean of the inverse dynamics and feed-forward torques were pursued in (Shiqing, Franitza et al. 2004).

A control scheme, which applies internal cable force controller and position control in operational space for a spatial cable robot of type CRPM was proposed in (Fang 2005). For this robot with only one degree-of-redundancy, the real-time algorithms for force distribution and forward kinematics were analysed and implemented. A computed torque controller based on a proportional-integral-derivative (PID) control law formulated either in operational or joint space was proposed in ((Lamaury, Gouttefarde et al. 2013), (Lamaury and Gouttefarde 2013b)) referred to as dual-space controller. The controller is adapted from high speed delta kinematics. The demonstrator named CoGiRo is shown in Fig.1.4a. The robot with  $r=2$ ,  $n=6$  is in crane configuration, which means that the platform is always below the anchor points of the cables at the machine frame. The kinematic is assumed as rigid and the cable forces are not controlled. The cable force sensors are only for performing measurements. Another computed torque controller for a spatial robot with  $r=2$  is proposed in (Reichert, Müller et al. 2014) based on an impedance control law with disturbance observer. Beside the position tracking of the platform in operational space, the cable forces are controlled to a feasible level. This controller is applied on the Segesta demonstrator. Both the dual-space and impedance controller were implemented on the IPAnema 3 Mini in a preliminary version in (Skalecki 2014). In the evaluation, the computed-torque controller did not reach the reference which was based on the position-controlled approach proposed in this thesis.

One key problem in the control of redundant cable robots is the distribution of the external forces and torques acting on the platform to the cables. This problem is denoted as cable force distribution problem and is underdetermined for redundant cable robots. Many publications address the determination of feasible force distributions for cable robots, e.g. in (Taghirad and Bedoustanti 2011), (Borgstrom, Jordan et al. 2009). For the use in control purposes, the algorithms must deliver continuous solutions for the cable forces and fulfil the real-time constraint (Lamaury and Gouttefarde 2013a), (Pott 2014a), (Yu, Lee et al. 2010). A detailed survey about the different methods to compute force distributions can be found in (Pott 2014a). The comparison reveals that there exist several methods which are real-time capable, find all solutions within the workspace and deliver continuous solutions along a trajectory. No method of these allows for arbitrary adjustment of the tension level. The relevant cable force algorithms are reviewed in detail in section 2.2.

The basic problem of cable force distribution can also be found in other areas of technique: calculating the contact forces in multi-finger grasping is quite familiar, as the contact has also an unilateral force transmission and is underdetermined (Liu, Xu et al. 2004). The problem of sharing load on parallel structures can also be found in parallel arranged pinions in gear boxes (Yu, Eberhard et al. 2013). The calculation of joint velocities for a serial



(a) The CoGiRo project cable-driven parallel robot prototype built by CNRS-LIRMM and Tecnalia (special thanks to Marc Gouttefarde, Ph.D., LIRMM, France)

(b) Cable-Based robot for Logistic Applications and Research (CABLAR) (special thanks to Christopher Reichert, University of Duisburg-Essen, Germany)

Figure 1.4: Cable robot prototypes for research

redundant robot shares the same problem class due to the redundancy. For this kind of robots in (Gravagne and Walker 2000), it is shown that infinity-norm optimization tends to deliver non-continuous solutions.

Position accuracy is an important property of a robot in general and, thus, the influences on accuracy are also topic of research. One approach is the identification of the external loads applied to the mobile platform and the compensation of position errors due to the elasticity of the kinematic. Approaches for load identification can be found for industrial robots , e.g. in (Verdonck 2004) and for classical parallel robots in (Schulte and Gerland 2004). Maximum likelihood estimation and weighted least-squares estimators are used to estimate the ten characteristic parameters of the load which are the mass, vector to the centre of gravity and the components of the inertia tensor. A real-time stiffness compensation for machining with an industrial robot was presented by Zengxi and Hui (2009) and for a parallel mechanism by Klimchik, Pashkevich et al. (2012). The stiffness of a cable robot based on a linear model for the cables has been well-analysed in the past, e.g. by Verhoeven (2004) and is reviewed in section 2.1.2.

The modelling of cable-driven systems can be found in several areas of robotics: for example in humanoid robots, the upper limb is often cable actuated and the load cell is placed in the body. These systems are realized using pulleys or bowden cables. Discrete elements with friction losses are applied for a cable-conduit system used for surgical robots in (Agrawal, Peine et al. 2010). Viscous and dry friction coefficients are applied in the computed torque control approach for a cable robot by Lamaury, Gouttefarde et al. (2013). The modelling of friction during the transition between static and kinetic needs special consideration due to the presliding state (Dupont, Hayward et al. 2002). The Coulomb model is stateless and cannot model friction in standstill. Well-known models for dynamic

friction are the Dahl and LuGre model (Dahl 1968), (Canudas de Wit, Olsson et al. 1995). For example, the Dahl model was applied for the modelling of the reel friction by Otis, Nguyen Dang et al. (2009).

The electrical and mechanical losses of a robot lead to the question of its energy efficiency and methods to analysis and improve the energy consumption is subject of research. The task execution of pick-and-place manipulator for optimization of energy efficiency was investigated by Pellicciari, Giovanni et al. (2011). The effect of closing the brakes during dwell times and the use of point-to-point movement instead of linear movement for industrial robots in automotive industry was investigated by Meike and Ribickis (2011). An energy consumption model for an industrial robot was developed by Müller, Spiller et al. (2011). In (Lee, Jeong et al. 2013), the energy consumption using redundantly actuated mechanisms could be reduced compared to a non-redundant kinematic. The experiments showed worse energy efficiency than simulation as joint friction was not modelled. In (Li and Bone 2011), it was shown that parallel manipulators are more energy efficient than serial robots. The investigation also showed that the energy efficiency depends on the geometrical robot design. For cable robots, a method for energy efficient trajectories considering the ohmic losses ( $I^2R$ ) of the drives is proposed by Borgstrom, Borgstrom et al. (2008). In (Reichert, Unterberg et al. 2015), the energy consumption of a cable robot is improved by the installation of passive elements and an energy-optimal trajectory planning.

For the control of contact forces between a robot and the environment, additional devices can be mounted on the robot platform like air controlled cylinders or stiffness actuators (Osypiuk and Kröger 2011). The drawback of these devices is that they add additional weight to the platform and the direction of the force is typically fixed with respect to the mobile platform frame. Furthermore, these systems need a power and signal supply on the mobile platform. This motivated the research on force control for robots. The idea to control the contact force between the environment and robot platform in one direction, while the other directions are position-controlled, is called hybrid position and force control and was already developed in the eighties (Raibert and Craig 1981). The hybrid control law was implemented on parallel manipulators, e.g. by Madani and Moallem (2011) and Deng, Lee et al. (2010). For a serial robot, the concept of an additional null-space control loop for decoupling the motion from the contact force is described in (Park 2006).

In connection with the hybrid position and force control, the contact establishment is challenging. The major concern regarding stability are the transient system properties when the platform comes in contact with the environment. The contact problem was investigated for both serial (Albu-Schaeffer, Ott et al. 2003), (Raibert and Craig 1981) and parallel robots with stiff legs (Tang, Yao et al. 2011). In (Assuncao and Schumacher 2003) this problem was solved by a state machine based approach using acceleration and brake controllers for bringing the robot into contact. An alternative approach for eliminating the

switching strategy was presented in (Almeida, Lopes et al. 1999) using an adaptive gain of an impedance controller.

Cable-driven systems were also developed for the haptic interaction with humans. Already in 1993, Kawamura and Ito (1993) proposed a cable-driven system with impedance control as master device for tele-operation . Several string-based force displays were developed as haptic devices for virtual reality applications (Sato 2002). In (Billette and Gosselin 2009), a cable-driven haptic interface with an impact generating winch for the simulation of rigid impacts is proposed. A planar haptic device with four cables with a focus on the manipulability is investigated in (Gallina, Rosati et al. 2001) and (Gallina and Rosati 2002). The concept of a spatial cable-driven haptic interface is proposed by Williams II (1998). Exhaustive work in the simulation of a virtual reality with a cable-driven locomotion interface including a hybrid control scheme was presented by Otis, Mokhtari et al. (2008). An admittance control for a cable robot with four cables and force measurement with an external sensor attached to the platform was proposed by Fortin-Côté, Cardou et al. (2014).

The review of the state of the art shows that several cable robots were built as laboratory test set-ups and a lot of research in the theory and practice was carried out. The control approaches make mostly use of the torque interface to the drives. No work is reported which incorporates position-controlled drives like industrial servo drives controlling a redundant robot with force control. At this point, this thesis starts to investigate the control of cable robots using position-controlled drives.

### 1.3 Problem Statement

This thesis focuses on the problems arising from controlling a parallel robot with force-redundancy, elastic joints and position-controlled drives. The main control problem of this thesis can be formulated in general as follows: the robot platform has to be controlled to the desired position and the cable forces have to be kept within a feasible limit. Using position-controlled drives, one has to solve this problem for the corresponding drive positions. This falls into three basic problems.

The redundancy of the robot makes the main problem of this thesis not uniquely solvable because infinite many combinations of drive positions which result in different (feasible) cable forces exist to stabilize the platform in a desired position. To the best author's knowledge, no approach is reported in literature, which simultaneously allows to adjust the tension level of the cable step-less from minimal to maximal cable forces for higher degree-of-redundancy than one. Simultaneously, the effects of the tension level on the robot stiffness and energy consumption needs further investigation. There is a lack of quantitative investigation of the influence of the tension level on the robot properties.

The second basic problem arises from the use of elastic cables and position-controlled drives. The cable elasticity determines the transfer behaviour between the winches and the robot platform. To keep the cables under tension, position set-points for the drives have to be found. The control approaches have to control both the position and the cable forces of the robot. In this context, the cable force measurement has to be considered as well. For controlling the platform position in closed-loop, the forward kinematics, which incorporates the cable stiffness, has to be solved to estimate the platform position. Thus, to solve the main problem, the stiffness of the cable has to be modelled and incorporated in the control approaches. As the model-based control is subject to uncertainties in the parameters, experimental verification has to be carried out using external measurement devices for position accuracy.

In the main problem formulation, it is assumed that the platform position is the desired variable. The third basic problem expands these assumptions by the introduction of external force controllers. Hereby, the problem lies in the control of forces between the robot platform and the environment, while the cable forces have to remain within the feasible limits. For the hybrid position and force control, solutions for adopting the known approaches regarding the contact establishment and contact force control on the cable robot are not reported in literature and have to be investigated. For the haptic interaction with the cable robot, the performance which can be reached using industrial servo drives and indirect measurement of the user force by means of the cable force sensors is worth to investigate.

## 1.4 Objective and Content of this Work

The objective of this thesis is the development of a control architecture which incorporates the solutions of the main problems. For this purpose, the relation between the cable forces and the platform position are analysed in detail. To reach the thesis's objective, dynamic models of the actuator and platform are established and parametrized using system identification. Algorithms which are real-time capable and compatible with the target system have to be developed for forward kinematics, cable force set-point determination and force controller. For the implementation and experimental evaluation, the cable robot IPAnema 3 and IPAnema 3 Mini both with eight cables and six DOF are used. The experimental evaluation focuses on the position accuracy within the workspace and at the border, dynamic behaviour of the platform, energy efficiency and performance of the external force controller. This thesis is structured as follows:

In chapter 2, the basic foundations for the model of a cable robot are described. These include the kinematic and static relations and stiffness model of the robot in joint and operational space. On this basis, the model is expanded by the robot dynamics and elastic cables. Subsequently, existing forward kinematics approaches are reviewed. Next, the

workspace definitions are reviewed and existing approaches for the calculation of cable force distributions are presented. In the last section of this chapter, the cable robot demonstrator with the hardware design, control architecture and measurement equipment are presented. Also the reference approach for controlling the cable robot using only a geometrical model of the robot is described.

Based on the state of the art, the control architecture is derived in chapter 3. For this purpose, several known control approaches are discussed. On this basis, the approach for synchronous position and cable force control is derived. The results are incorporated in the proposed control architecture, which considers all controllers developed within this thesis. Subsequently, the subsystems of the control approach are described in detail. At first, the forward kinematics incorporating non-linear cable stiffness is presented, which is needed to estimate the platform position. Next, the modelling and system identification are done to establish dynamic models of the control plant. On this basis, the controller synthesis is performed and stability of the controller is analysed. Subsequently, the implementation is described. For the calculation of the desired force distribution, the cable force algorithm using a quadratic programming algorithm is described. In the last section, the winch-integrated cable force measurement is discussed. Hereby, the focus lies on the modelling and compensation of the pulley friction occurring between the force sensor and the robot platform.

After the basic control approach is implemented on the robot, an experimental and model-based evaluation is presented in chapter 4. At first, the load identification and compensation is described which makes use of the cable force measurement for the compensation of the position errors induced by additional loads on the platform. Next, the focus lies on the experimental evaluation of the position accuracy of the proposed control approach. A comparison between the linear and non-linear cable models regarding the position accuracy of the platform is presented. Afterwards, the investigation of position accuracy is performed for discrete positions which lie within the robot workspace. Subsequently, the investigation is carried out at the workspace border including the analysis of the cable forces. After the static investigation, the behaviour of the robot under maximum dynamic load is studied. Next, the change of the robot stiffness is analysed according to the eigenfrequencies of the platform for different tension levels. The chapter concludes with the study about the energy consumption and a comparison with an industrial serial robot.

Chapter 5 focuses on investigation of the external force controller. At first, the hybrid position and force control is presented which allows for applying forces on the environment. In the second part of this chapter, an admittance controller is proposed for haptic interaction with the cable robot. For the demonstration of the controller, a virtual workspace is implemented.

The conclusion of the work and outlook on further research are given in chapter 6.

## 1.5 Remarks on the Notation

All relevant symbols which are used throughout this thesis are summarized on page xiii. The conventions used for notations are explained in the following. Scalar values are written in normal font  $a$ , vector and matrices are printed bold like  $\mathbf{a}$ . Hereby, matrices are denoted with upper case letters, while vectors are in lower case. The Euclidean norm of a vector  $\mathbf{a}$  is denoted as  $\|\mathbf{a}\|$ . Transposed variables  $\mathbf{a}^T$  are marked with  $T$ . Reference frames are denoted in calligraphic letters as  $\mathcal{K}_i$ .

The actual value of a variable is always denoted without index like  $f$  and the desired value is labelled with the subscript  $d$ , as example  $\mathbf{f}_d$ . The difference between the desired and actual value is the measured error and denoted by  $e_f$ , where the subscript stands for the referred variable.

The controller synthesis is carried in the complex frequency domain using the Laplace transformation. Transfer functions formulated in the frequency domain are denoted as  $G(s)$ , where  $s$  is the complex Laplace variable. For example, the Laplace transformation of a signal  $f(t)$  is represented as  $\mathcal{L}\{f(t)\}$ .

---

## 2 Fundamentals

In this chapter, the basic foundations for this thesis are given. At first, the robot model including the kinematic transformation, stiffness model of the cables and equation of motions are described. Subsequently, the focus lies on the robot's workspace and the determination of cable force distributions. In the last section, the cable robot demonstrators with their hardware design and control architecture are presented.

### 2.1 Robot Model

The robot model is the base for the development of the controllers. The kinematic structure of the robot is related to parallel robots and described by the geometry of the base and the platform. Beside kinematic relations, the force and torque equilibrium has also to be considered for dealing with the need of positive cable forces. For modelling both the static and dynamic behaviour of the robot, the joint stiffness represented by the cable stiffness has to be modelled.

#### 2.1.1 Kinematic and Static Model

For beginning, the kinematic and static model which is based on (Verhoeven 2004) is briefly reviewed. The geometry of the robot is described by its proximal anchor points on the robot base  $A_i$  and the distal anchor points on the platform  $B_i$ , which are defined by the vectors  $\mathbf{a}_i$  and  $\mathbf{b}_i$ , respectively. The index  $i$  denotes the cable number and  $m$  is the absolute number of cables. By applying a vector loop, as shown in Fig. 2.1, the cable vector  $\mathbf{l}_i$  follows as

$$\mathbf{l}_i = \mathbf{a}_i - \mathbf{r} - \mathbf{R} \mathbf{b}_i , \quad (2.1)$$

where  $\mathbf{r}$  and  $\mathbf{R}$  describe the position and orientation of the platform fixed frame  $\mathcal{K}_p$  w.r.t. the world coordinate frame  $\mathcal{K}_0$ . For convenience, the position and orientation is collectively referred as the generalized coordinates  $\mathbf{x} = [r_x, r_y, r_z, \varphi_x, \varphi_y, \varphi_z]^T$ , which is also denoted as pose. Using Kardan angles for the parametrization of the orientation,  $\mathbf{R} = \mathbf{R}_x(\varphi_x)\mathbf{R}_y(\varphi_y)\mathbf{R}_z(\varphi_z)$  holds. The inverse kinematics solution  $\mathbf{q}$  for the cable robot is

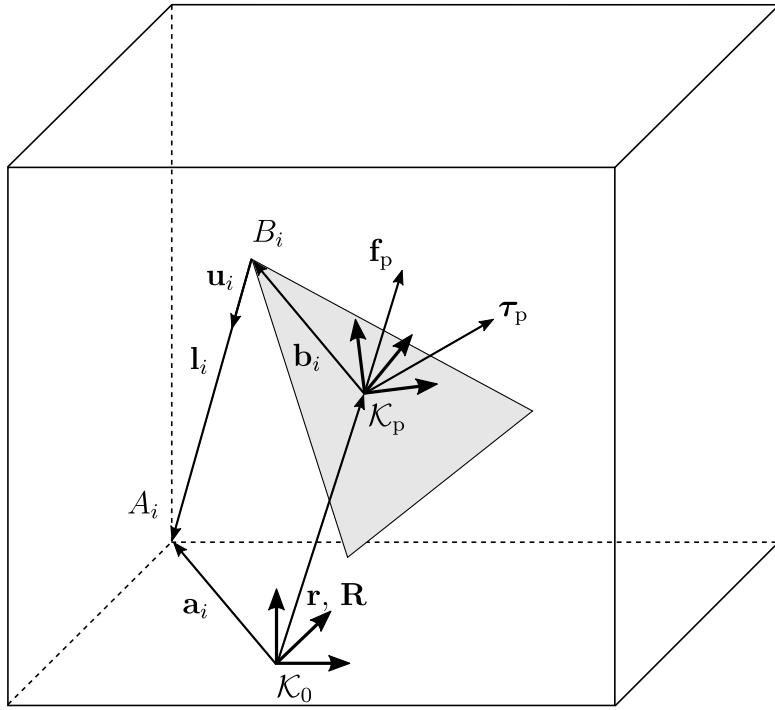


Figure 2.1: Schematic representation of the general kinematic parameters

simply the length of the cable vector  $\mathbf{l}_i$  and reads as

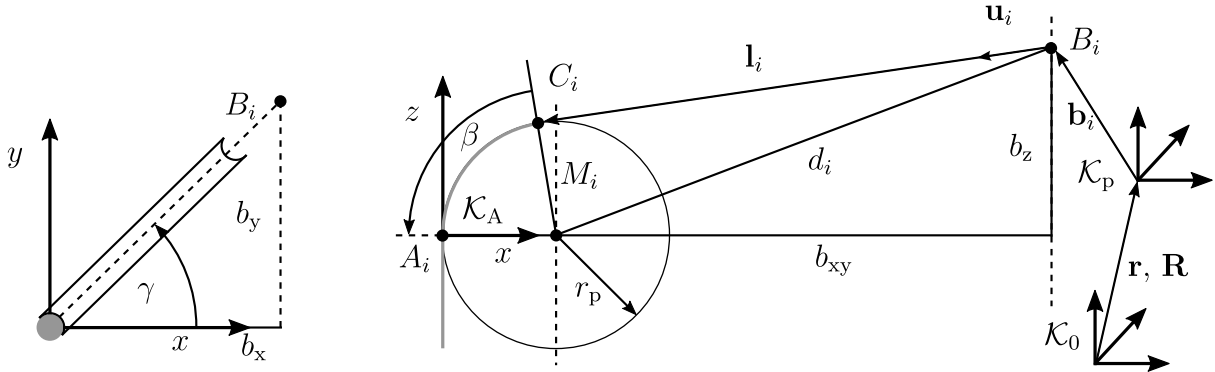
$$q_i = \|\mathbf{l}_i\| , \quad (2.2)$$

whereas the forward kinematics is much more complex and is described in its own section 2.1.4.

In a typical robot design, swivelling pulleys are used to guide the cable at the point  $A_i$  towards the platform. Thus, the starting point of the cable described by the position vector  $\mathbf{a}_i$  is no longer a constant but depends on the current pose of the robot. Consequently, (2.1) has to be expanded by the effect of the pulleys. The modelling of the pulley kinematics was presented in (Pott 2012) and is visualized in Fig. 2.2. The main equations are given in the following. For the geometrical description of the pulley kinematics, the frame  $\mathcal{K}_A$  is introduced, whose origin  $A_i$  and its orientation w.r.t.  $\mathcal{K}_0$  is described by the vector  $\mathbf{a}_i$  and the rotation matrix  $\mathbf{R}_A$ , respectively. The rotation matrix is parametrized with the Kardan angles  $\varphi_A$ :

$$\mathbf{R}_A = \mathbf{R}_x(\varphi_{A,x})\mathbf{R}_y(\varphi_{A,y})\mathbf{R}_z(\varphi_{A,z}) \quad (2.3)$$

The orientation is defined in such a way that the  $z$ -axis coincides with the first revolute joint of the pulley mechanism and the rotation angle  $\gamma$  is zero for the initial position of the pulley.



(a) Pulley rotated by  $\gamma$  out of the  $xz$ -plane    (b) Determination of the point  $C_i$  where the cable leaves the pulley

Figure 2.2: Model for the pulley kinematics

Let vector  $\mathbf{b}$  describe the points  $B_i$  with reference to the frame  $\mathcal{K}_A$ . With  $b_{xy} = \sqrt{b_x^2 + b_y^2}$ , the distance  $d_i$  between the points  $M_i$  and  $B_i$  is given by

$$d_i = \sqrt{(b_{xy} - r_p)^2 + b_z^2} , \quad (2.4)$$

where  $r_p$  stands for the pulley radius. The free cable length between the platform and the pulley  $l_f$  is given by the Pythagorean theorem and reads

$$l_f = \sqrt{d_i^2 - r_p^2} . \quad (2.5)$$

The wrapping angle of the cable around the pulley  $\beta$  is evaluated by

$$\beta = \arccos\left(\frac{l_f}{d_i}\right) + \arccos\left(\frac{b_z}{d_i}\right) , \quad (2.6)$$

which allows to solve the inverse kinematics (IK) by

$$q_i = l_f + \beta r_p , \quad (2.7)$$

which is the counterpart to (2.2).

Further calculations are needed for the determination of the cable vector  $\mathbf{l}_i$  in dependence of the pulley. The rotation around the first revolute joint  $\gamma$  can be determined by the four quadrant arcus tangens  $\gamma = \arctan 2(b_y, b_x)$  as illustrated in Fig. 2.2a. Applying the angles  $\beta$  and  $\gamma$ , the position vector  $\mathbf{c}_i$  pointing to the point  $C_i$  described in the reference frame  $\mathcal{K}_0$  can be determined by

$$\mathbf{c}_i = \mathbf{a}_i + \mathbf{R}_A \left( \mathbf{R}_z(\gamma) ((\mathbf{I} - \mathbf{R}_y(\beta)) [r_p, 0, 0]^T) \right) . \quad (2.8)$$

Analogue to (2.1), the cable vector now becomes

$$\mathbf{l}_i = \mathbf{c}_i(\mathbf{r}, \mathbf{R}) - \mathbf{r} - \mathbf{R} \mathbf{b}_i . \quad (2.9)$$

In this thesis, the cables are assumed to be straight and not sagging. Thus, the unit vector of the cables, which reads  $\mathbf{u}_i = \frac{\mathbf{l}_i}{\|\mathbf{l}_i\|}$ , gives the direction of the cable forces. The force and torque equilibrium at the mobile platform is described by the structure equation which reads as

$$\underbrace{\begin{bmatrix} \mathbf{u}_1 & \cdots & \mathbf{u}_m \\ \mathbf{b}_1 \times \mathbf{u}_1 & \cdots & \mathbf{b}_m \times \mathbf{u}_m \end{bmatrix}}_{\mathbf{A}^T(\mathbf{r}, \mathbf{R})} \underbrace{\begin{bmatrix} f_1 \\ \vdots \\ f_m \end{bmatrix}}_{\mathbf{f}} = - \underbrace{\begin{bmatrix} \mathbf{f}_p \\ \boldsymbol{\tau}_p \\ \mathbf{w} \end{bmatrix}}_{\mathbf{w}} , \quad (2.10)$$

where  $\mathbf{A}^T$  is the structure matrix and  $\mathbf{f}$  is the cable force vector, also called cable force distribution, containing the  $m$  scalar cable forces. The wrench  $\mathbf{w}$  consists of external forces  $\mathbf{f}_p$  and torques  $\boldsymbol{\tau}_p$  acting at the platform. The wrench includes e.g. acceleration forces and contact forces with the environment. The structure matrix  $\mathbf{A}^T$  corresponds to the negative Jacobian matrix  $\mathbf{J}$  of the robot.

From (2.10) follows that the actual wrench  $\mathbf{w}$  acting at the platform can be determined according to

$$\mathbf{w} = -\mathbf{A}^T \mathbf{f} , \quad (2.11)$$

for a measured cable force distribution  $\mathbf{f}$ . Beside the projection of forces from the joint to operational space, the structure matrix also describes the velocity and acceleration mapping from operational to joint space. For a given operational space velocity  $\dot{\mathbf{x}}$ , the cable velocity  $\dot{\mathbf{q}}$  is determined by

$$\dot{\mathbf{q}} = -\mathbf{A} \dot{\mathbf{x}} , \quad (2.12)$$

and the cable acceleration  $\ddot{\mathbf{q}}$  by

$$\ddot{\mathbf{q}} = -\mathbf{A} \ddot{\mathbf{x}} - \dot{\mathbf{A}} \dot{\mathbf{x}} . \quad (2.13)$$

The time derivative of the structure matrix given by  $\dot{\mathbf{A}}$  can be computed analytically by deriving the cable unit vector  $\mathbf{u}_i$  and the cross product  $\mathbf{b}_i \times \mathbf{u}_i$  separately.

The introduction of the basic equation for describing the robot kinematics and statics is hereby completed. In the following, the stiffness model is derived.

## 2.1.2 Stiffness Model

The cable stiffness plays a key role in the control of cable robots, as it influences both the stiffness of robot's platform as well as the available bandwidth for high dynamic movements.

Compared to the cables, the machine frame and the platform can be assumed as rigid and their compliance is, thus, neglected. The effective cable stiffness depends on the free cable length and changes with the position of the platform by winding the cable on the drum. The free total cable length  $\mathbf{l}_t$  is calculated by

$$\mathbf{l}_t = \mathbf{q} + \mathbf{l}_0 \quad , \quad (2.14)$$

with the inverse kinematics solution  $\mathbf{q}$  which describes the free cable length between the last pulley and the platform, and a constant cable length  $\mathbf{l}_0$  accounting for the additional free cable length between the drum and last pulley. For convenient calculation of the cable stiffness under changing cable length, the material dependant stiffness is parametrized as specific stiffness  $k_{\text{spec}}$ . With this parametrization, the cable stiffness  $\mathbf{C}$  is derived by

$$C_i = \frac{k_{\text{spec}}}{l_{t,i}} \quad , \quad (2.15)$$

which is represented in matrix form as  $\mathbf{K}_t = \text{diag}(C_1, \dots, C_m)$ . In the literature, e.g. in (Verhoeven 2004), the cables are commonly assumed as linear springs and, thus, the specific stiffness is a constant  $k_0$ . The synthetic fibre cables used throughout this thesis reveal a progressive spring characteristic including hysteresis effects as discussed in detail by Miermeister, Kraus et al. (2014). For illustration, the spring characteristic of the Dyneema® cable used in the IPAnema 3 robot with a diameter of 6.0 mm and a breaking load of 43,000 N is shown exemplary in Fig. 2.3. The elongation is determined based on the drive encoder and the cable force is measured by the cable force sensor. In the rated operation, the maximum cable force amounts to 3,000 N. For a cable length of 19.5 m, this corresponds to a maximum elongation of 75 mm, or 0.385% in relative terms.

Taking into account the non-linear cable stiffness, the specific stiffness depends on the actual cable force. It is now modelled as a polynomial of second degree which reads

$$k_{\text{spec}} = k_0 + k_1 f + k_2 f^2 \quad \text{for } f > 0 \quad , \quad (2.16)$$

and is visualized in Fig. 2.4a and Fig. 2.4b for a Dyneema® cable with diameters of 1.5 mm and 6.0 mm, respectively. The spring function  $f = C \Delta q$  for the non-linear specific stiffness described by (2.16) follows to

$$f = \frac{k_0 + k_1 f + k_2 f^2}{l_t} \Delta q \quad , \quad (2.17)$$

which is visualized in Fig. 2.3, denoted as polynomial model. The hysteresis effect is not taken into account in this thesis. Thus, the polynomial spring function lies in the middle of the upward and downward path of the hysteresis curve.

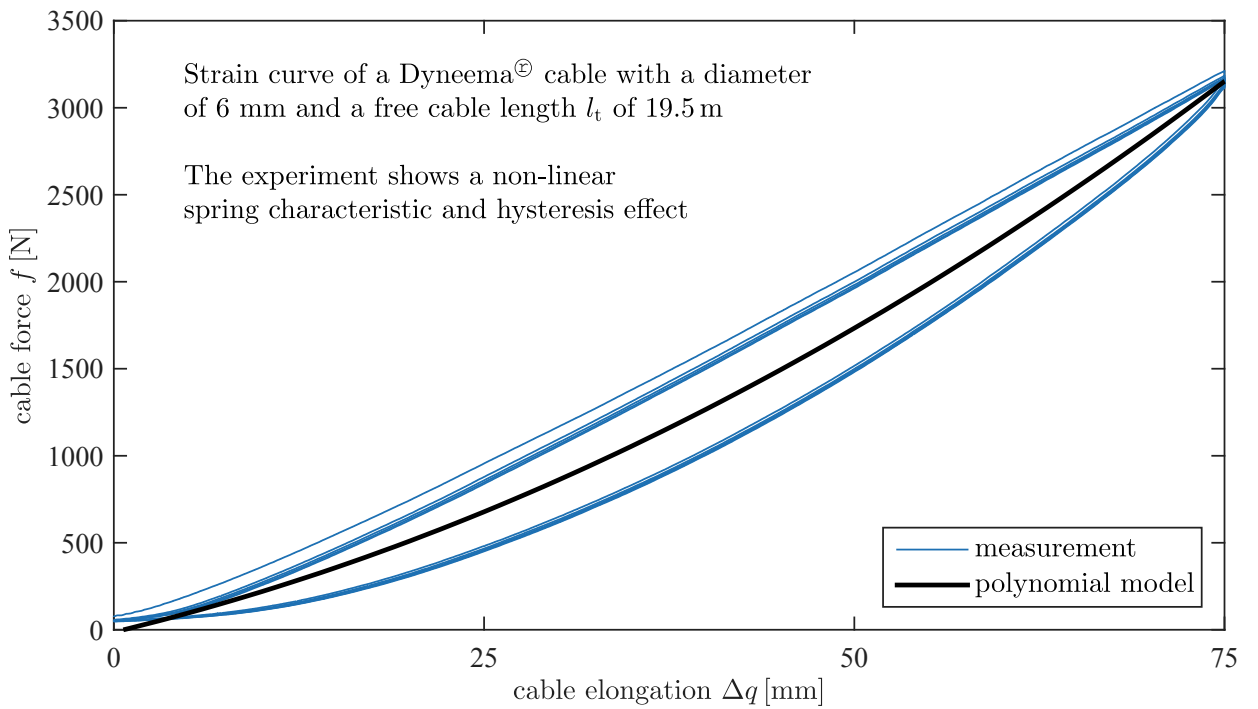


Figure 2.3: Spring characteristic of a 6.0 mm Dyneema<sup>®</sup> cable with a length of  $l_t=19.5$  m

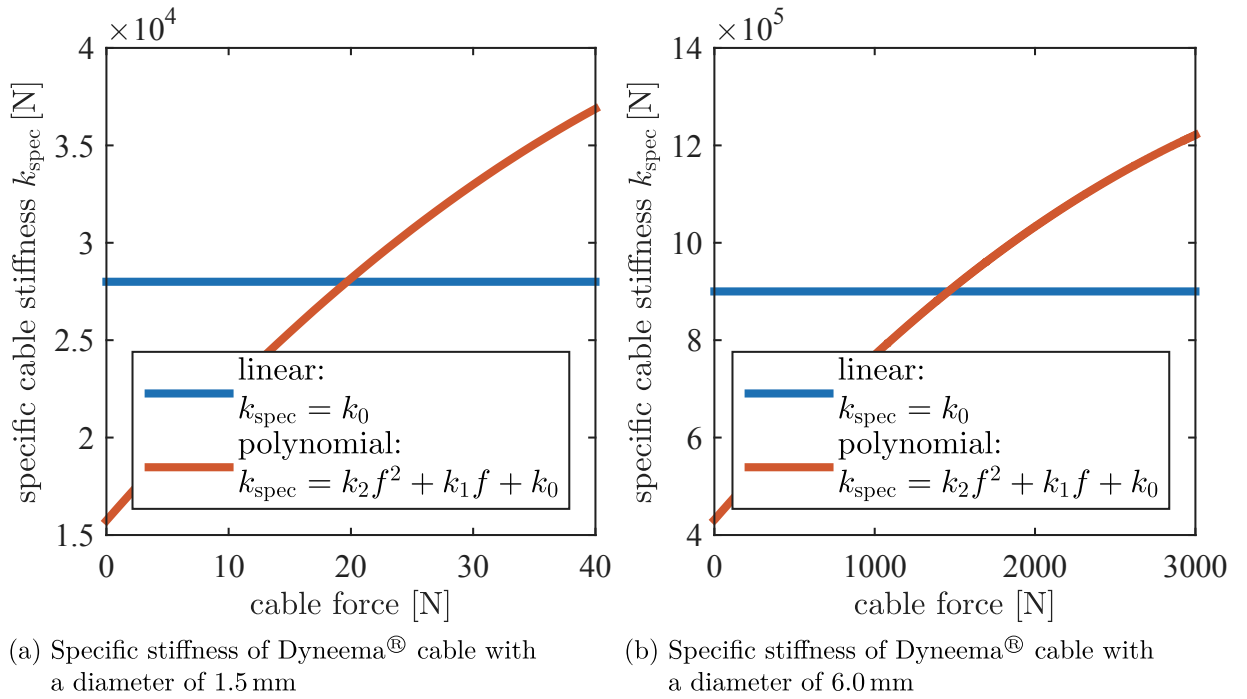


Figure 2.4: Non-linearity of cable stiffness

In the following, we derive the foundations for the stiffness matrix in operational space  $\mathbf{K}_x$ , which describes the linearised relation

$$d\mathbf{w} = \mathbf{K}_x d\mathbf{x} \quad , \quad (2.18)$$

between an infinitesimal wrench  $d\mathbf{w}$  and deflection  $d\mathbf{x}$  of the platform. The following derivation assumes linear spring behaviour and can be found in (Verhoeven 2004), (Yu, Lee et al. 2010) and (Behzadipour and Khajepour 2006). For the analytic expression for  $\mathbf{K}_x$ , the structure equation (2.10) has to be differentiated with respect to  $\mathbf{x}$ , what yields

$$d\mathbf{w} = -\frac{\partial \mathbf{A}^T}{\partial \mathbf{x}} \mathbf{f} d\mathbf{x} - \mathbf{A}^T d\mathbf{f} \quad (2.19)$$

where  $\frac{\partial \mathbf{A}^T}{\partial \mathbf{x}}$  is the derivation of the structure matrix w.r.t. the generalized coordinates. The relation between the incremental cable forces  $d\mathbf{f}$  and the incremental change in cable length  $d\mathbf{q}$  for a linear spring model can be expressed by

$$d\mathbf{f} = \mathbf{K}_l d\mathbf{q} \quad . \quad (2.20)$$

Incremental changes in the platform pose  $d\mathbf{x}$  are transformed to the operational space with

$$d\mathbf{q} = -\mathbf{A} d\mathbf{x} \quad . \quad (2.21)$$

Applying (2.21), (2.20) and (2.19), (2.18) becomes

$$\mathbf{K}_x d\mathbf{x} = -\underbrace{\frac{\partial \mathbf{A}^T}{\partial \mathbf{x}} \mathbf{f}}_{\mathbf{K}_g} d\mathbf{x} + \underbrace{\mathbf{A}^T \mathbf{K}_l \mathbf{A}}_{\mathbf{K}_c} d\mathbf{x} \quad . \quad (2.22)$$

Above equation shows that the stiffness is based on two separate effects. The geometrical stiffness  $\mathbf{K}_g$  results from the change of the structure matrix when deflecting the platform. Beside geometrical parameters, the height of this part depends on the cable forces. The second term of (2.22),  $\mathbf{K}_c$ , results from the cable stiffness. Only when the cables have a non-linear characteristic, this term depends also on the cable forces.

The cable stiffness contributes for the main part of the robot stiffness. In special cable robot configurations, the geometrical stiffness becomes important. The stiffness of a planar robot moving out of its plane depends only on the geometrical stiffness, as in the first instance, the cable is not elongated (Schmidt, Kraus et al. 2014).

From the review of the stiffness model follows that the elasticity plays an important role for cable robots and is incorporated in the robot model in the following.

### 2.1.3 Robot Dynamics with Elastic Cables

The dynamic robot behaviour is of interest for the controller synthesis. Using elastic cables as a transmission element influences the static and dynamic robot behaviour. The modelling and control of elastic joint robots was initially proposed by Spong (1987) for serial robots and is for example applied to the controller development of the DLR-Light-Weight-Arms in (Albu-Schaeffer, Ott et al. 2003). Taking into account the joint elasticity, each joint has no longer one but two degrees-of-freedom and is modelled by the link position  $q_i$  and the motor position  $\theta_i$ . In serial kinematics with elastic joints,  $\theta_i$  corresponds to the encoder value on the motor side scaled by the constant gear ratio, while  $q_i$  describes the position on the output side of the gear box. Applying this principle to the constellation of parallel cable robots, this means that  $q_i$  describes the distance between the platform point  $\mathbf{b}_i$  and the winch point  $\mathbf{a}_i$  derived from the inverse kinematics, while  $\theta_i$  reflects the cable length derived from the motor encoder scaled by the gear ratio. Under application of this model, the cable forces can be determined straight forward using the joint space stiffness matrix by

$$\mathbf{f} = \mathbf{K}_1(\mathbf{q} - \boldsymbol{\theta}) , \quad (2.23)$$

and in the following, the cable elongation is denoted as  $\Delta\mathbf{q}$  and defined as

$$\Delta\mathbf{q} = \mathbf{q} - \boldsymbol{\theta} . \quad (2.24)$$

The motor angle  $\alpha$ , which is measured by the motor encoder, is obtained from the generalized motor variable  $\theta$  formulated in cable length by

$$\alpha = \frac{\theta}{r_w} , \quad (2.25)$$

where the generalized transmission ratio  $r_w$  includes the gear ratio and the effective winch radius. The determination of the transmission ratio is not trivial because the effective circumference of the drum depends on the cable diameter and the pre-tension of the cable. Under high cable forces, the cable is wound up tighter around the drum and, thus, the effective drum radius decreases. This effect is called ovalisation and is discussed by Schmidt, Mall et al. (2015). The influence of the actual force on the transmission ratio disturbs the accuracy of the cable length measurement by means of the motor encoder. As this effect cannot be modelled at the moment, the cable ovalisation is one source of position inaccuracies of the robot.

The equation of motion of the robot platform including the elastic behaviour of the cables can be derived with the Lagrange equation based on the potential and kinetic energy of the system. The following derivation is extracted from the paper (Khosravi and Taghirad

2014). The potential energy  $V$  of the platform and the cables acting as spring reads

$$V = V_0 + \frac{1}{2}(\mathbf{q} - \boldsymbol{\theta})^T \mathbf{K}_l (\mathbf{q} - \boldsymbol{\theta}) , \quad (2.26)$$

where  $V_0$  is the potential energy of the platform. The kinetic energy  $T$  of the robot is

$$T = \frac{1}{2}\dot{\mathbf{x}}^T \mathbf{M}(\mathbf{x})\dot{\mathbf{x}} + \frac{r_w^2}{2}\dot{\mathbf{q}}^T \mathbf{J}_w \dot{\mathbf{q}} , \quad (2.27)$$

where  $\mathbf{J}_w$  contains the rotational inertia of the joints w.r.t. the motor axis formulated in motor angles  $\alpha$ . The Lagrangian yields

$$L = T - V = \frac{1}{2}\dot{\mathbf{x}}^T \mathbf{M}(\mathbf{x})\dot{\mathbf{x}} + \frac{1}{2}\dot{\mathbf{q}}^T \mathbf{J}_w \dot{\mathbf{q}} - \frac{1}{2}(\mathbf{q} - \boldsymbol{\theta})^T \mathbf{K}_l (\mathbf{q} - \boldsymbol{\theta}) - V_0 . \quad (2.28)$$

With the Lagrange equation of second kind

$$\frac{d}{dt} \left( \frac{\partial L}{\partial \dot{\mathbf{x}}} \right) = \frac{\partial L}{\partial \mathbf{x}} , \quad (2.29)$$

the equation of motion in operational space becomes

$$\mathbf{M}(\mathbf{x}) \ddot{\mathbf{x}} + \mathbf{N}(\mathbf{x}, \dot{\mathbf{x}}) = \mathbf{A}^T(\mathbf{x}) \mathbf{K}_l (\mathbf{q} - \boldsymbol{\theta}) , \quad (2.30)$$

with

$$\mathbf{N}(\mathbf{x}, \dot{\mathbf{x}}) = \mathbf{C}(\mathbf{x}, \dot{\mathbf{x}})\dot{\mathbf{x}} + \mathbf{G}(\mathbf{x}) , \quad (2.31)$$

where  $\mathbf{C}(\mathbf{x}, \dot{\mathbf{x}})$  includes the Coriolis and centrifugal terms and  $\mathbf{G}(\mathbf{x})$  contains the gravity terms. The equation of motion of one joint holds

$$\boldsymbol{\tau} = \mathbf{J}_w \ddot{\boldsymbol{\alpha}} + r_w \mathbf{K}_l (\mathbf{q} - \boldsymbol{\theta}) , \quad (2.32)$$

where  $\boldsymbol{\tau}$  denotes the torque of the drives.

Based on the equation of motion (2.30) and the assumption that the cable forces have to balance the wrench  $\mathbf{w} = \mathbf{K}_l (\mathbf{q} - \boldsymbol{\theta})$ , the platform inverse dynamics can be formulated. The dynamic wrench on the platform  $\mathbf{w}_{dyn}$  for a given translational and rotational acceleration  $\ddot{\mathbf{r}}$  and  $\ddot{\boldsymbol{\varphi}}$ , respectively, and rotational velocity  $\dot{\boldsymbol{\varphi}}$  can be described as follows

$$\mathbf{w}_{dyn} = \begin{bmatrix} \mathbf{f}_{dyn} \\ \boldsymbol{\tau}_{dyn} \end{bmatrix} = \begin{bmatrix} m_p \mathbf{I} & -m_p [\mathbf{c}_{mp}] \\ m_p [\mathbf{c}_{mp}] & \mathbf{J}_c - m_p [\mathbf{c}_{mp}] [\mathbf{c}_{mp}] \end{bmatrix} \begin{bmatrix} \ddot{\mathbf{r}} \\ \ddot{\boldsymbol{\varphi}} \end{bmatrix} + \begin{bmatrix} m_p \dot{\boldsymbol{\varphi}} \times (\dot{\boldsymbol{\varphi}} \times \mathbf{c}_{mp}) \\ \dot{\boldsymbol{\varphi}} \times (\mathbf{J}_c - m_p [\mathbf{c}_{mp}] [\mathbf{c}_{mp}]) \dot{\boldsymbol{\varphi}} \end{bmatrix} , \quad (2.33)$$

where  $m_p$  is the mass of the platform,  $\mathbf{J}_c$  is the inertia tensor w.r.t. the platform's centre of mass  $\mathbf{c}_{mp}$  and  $[\mathbf{c}_{mp}]$  denotes the skew-symmetric matrix, for which with an arbitrary vector

$\mathbf{a}$  holds  $[\mathbf{c}_{\mathbf{m}_p}]\mathbf{a} = \mathbf{c}_{\mathbf{m}_p} \times \mathbf{a}$ . The representation corresponds to the Newton-Euler equations of a rigid body. Next, the forward kinematics is described which incorporates the cable stiffness.

### 2.1.4 Forward Kinematics

The forward kinematics aims to estimate the pose of the platform  $\mathbf{x}$  from the actual cable lengths  $\boldsymbol{\theta}$  represented by the motor encoders. For a redundant cable robot, the forward kinematics problem is overdetermined, as the number of equations (number of cables) exceeds the number of unknowns (DOF). One possible solution is to transfer the forward kinematics problem into an optimization problem as proposed by Pott (2010). The objective function is formulated in joint space (JS) and considers the error in cable length. The  $m$ -dimensional objective function  $\Psi_{JS}(\boldsymbol{\theta}, \mathbf{x})$  represents the difference between the cable length obtained from the encoder  $\boldsymbol{\theta}$  and the cable length derived from the inverse kinematics solution  $\mathbf{q}_{IK}(\mathbf{x})$  for the actual pose estimation  $\mathbf{x}$  and is obtained by

$$\Psi_{JS}(\boldsymbol{\theta}, \mathbf{x}) = IK\{\mathbf{x}\} - \boldsymbol{\theta} . \quad (2.34)$$

Here, the errors of each cable are equally rated, which implies that the cables are assumed as springs with equal stiffness. The optimization problem can be stated as

$$\phi_{JS}(\boldsymbol{\theta}) = \min_{\mathbf{x}} \sum_{i=1}^m \Psi_{JS,i}^2(\boldsymbol{\theta}, \mathbf{x}) , \quad (2.35)$$

which is solved by a Levenberg-Marquardt algorithm. This approach was already successfully implemented for the use as tracking error recognition in operational space and for the estimation of the platform position for starting the kinematic transformation. The extension of this algorithm taking into account the pulley kinematics was presented by Schmidt and Pott (2012).

A formulation of the forward kinematics in operational space (OS) was proposed by Miermeister, Kraus et al. (2012). Based on the actual pose estimation, the cable elongation and subsequently the cable forces are obtained by

$$\hat{\mathbf{f}} = \mathbf{K}_1 \Delta \mathbf{q} = (IK\{\mathbf{x}\}_i - \theta_i) \frac{k_{\text{spec}}}{l_t} \quad \text{for } i = 1, \dots, m , \quad (2.36)$$

with the stiffness model of the cables. Then, the  $n$ -dimensional objective function  $\Psi_{OS}$  incorporates the structure equation (2.10) and reads

$$\Psi_{OS}(\boldsymbol{\theta}, \mathbf{x}) = \mathbf{W}(\mathbf{A}^T \hat{\mathbf{f}} - \mathbf{w}_0) , \quad (2.37)$$

where  $\mathbf{w}_0$  is the static wrench resulting from the weight of the platform and  $\mathbf{W}$  is a weighting matrix to balance the sensitivity between the translational and rotational DOF. The weighting matrix can be interpreted as leverage to transform the rotations to translations. The optimization problem is formulated as

$$\phi_{\text{OS}}(\boldsymbol{\theta}) = \min_{\mathbf{x}} \sum_{i=1}^n \Psi_{\text{OS},i}^2(\boldsymbol{\theta}, \mathbf{x}) \quad , \quad (2.38)$$

and aims to find the pose with the minimum quadratic error in the wrench.

The basic robot model is hereby introduced and in the next section the focus lies on the cable forces which define also the robot's workspace.

## 2.2 Workspace and Cable Force Algorithms

The workspace of a cable robot is mainly limited by the unilateral force transmission of the cables. In the following, the workspace definitions are given, the problem of calculating cable force distributions is elaborated and existing solution approaches are presented.

### 2.2.1 Workspace Definitions and Analysis

For the workspace analysis of a robot, different criteria can be considered. As cables can only transmit pull forces, the most important criterion for a cable robot is related to the cable forces.

The wrench-closure workspace is defined as a set of poses where a positive solution for the structure equation (2.10) can be found (Duan and Duan 2014). The wrench-feasible workspace (WFW) is limited to the poses, where the cable forces lie between a minimum force  $\mathbf{f}_{\min}$  and a maximum force  $\mathbf{f}_{\max}$  and, thus,

$$0 \leq \mathbf{f}_{\min} \leq \mathbf{f} \leq \mathbf{f}_{\max} \quad (2.39)$$

holds (Bosscher, Riechel et al. 2006). The lower limit is chosen to pre-tense the cable to avoid cable sagging. The upper limit is chosen to avoid static cable break, dynamic cable break due to bending and the operation limit of the servo drives. A detailed analysis of the limitations of the lower and upper cable limits can be found in (Pott 2014b).

For the workspace analysis, different algorithms can be used to check if a feasible solution of the structure equation exists. The most important algorithms are presented in the following. An iterative algorithm using an alternating projection on the solution space and on the cable force limits using the Dykstra algorithm was reported in (Hassan and Khajepour 2011). This algorithm finds a solution if one exists.

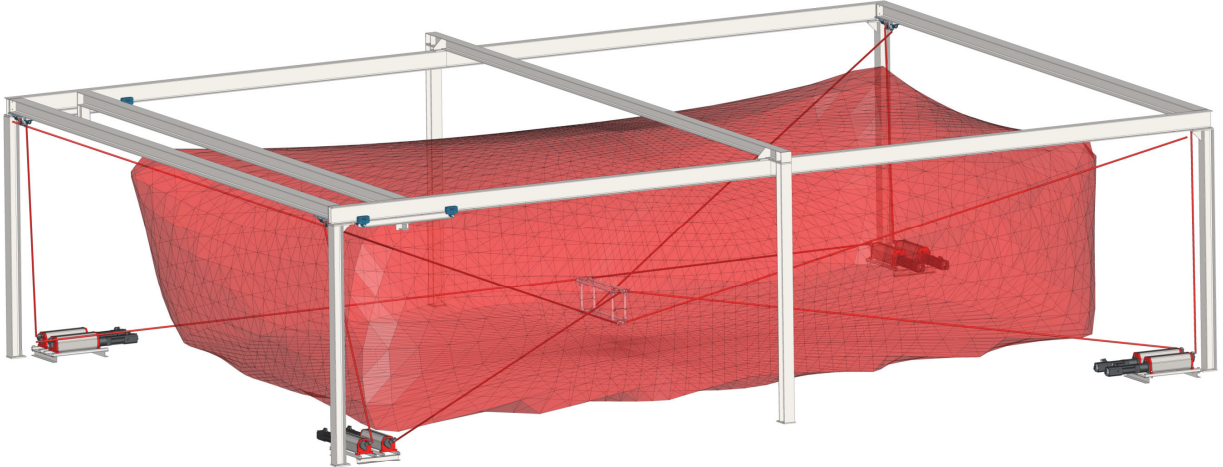


Figure 2.5: Workspace hull representing the wrench feasible workspace of the IPAnema 3 robot with  $m_p=30\text{ kg}$ ,  $f_{\min}=100\text{ N}$  and  $f_{\max}=3000\text{ N}$

The wrench-set approach presented in (Bouchard, Moore et al. 2010) delivers only a binary statement if a pose belongs to the workspace or not without solving the structure equation explicitly. Beside a given wrench, intervals of wrenches parametrized by an ellipsoid can be investigated. Acceleration requirement can, thus, be represented as a wrench ellipsoid. This leads to a realistic workspace estimation including the dynamic forces.

For the representation of workspaces, the triangulation method proposed in (Pott 2008) is applied. It describes the hull of the robot's workspace. As an example, the WFW workspace for the cable robot IPAnema 3 is visualized in Fig. 2.5. For the depicted workspace, a constant orientation of the platform is assumed and the dynamic forces are neglected. All positions within this volume are reachable with limited cable forces.

For the workspace analysis, it is sufficient to know whether a feasible force distribution exists or not. For the cable force control, the force distribution has to be evaluated explicitly.

### 2.2.2 Cable Force Algorithms

For the control of a redundant cable robot, a special focus lies on the calculation of the cable forces. Due to the redundancy, infinite many solutions for the cable forces exist which balance the external load acting at the platform. The cable force algorithm aims to find a cable force distribution  $\mathbf{f}$  which fulfills the linear equation system

$$\mathbf{A}^T \mathbf{f} = -\mathbf{w} \quad \text{subject to} \quad \mathbf{f}_{\min} \leq \mathbf{f} \leq \mathbf{f}_{\max}, \quad (2.40)$$

for a given wrench  $\mathbf{w}$ . If the cable force distribution fulfills the constraints, it is denoted as feasible and the pose belongs to the WFW. For a redundant cable robot, this problem is not straightforward to solve, as the linear equation system is under-determined and inhomogeneous on the one hand, and on the other hand the solution space is bounded by

the cable force limits. The general solution of this problem reads

$$\mathbf{f} = \underbrace{-\mathbf{A}^{+T} \mathbf{w}}_{\mathbf{f}_{\text{ext}}} + \underbrace{\mathbf{H} \boldsymbol{\lambda}_H}_{\mathbf{f}_{\text{int}}} , \quad (2.41)$$

where  $\mathbf{A}^{+T}$  is the Moore-Penrose matrix inverse of the structure matrix,  $\mathbf{H}$  describes a basis of the kernel of  $\mathbf{A}^T$  and  $\boldsymbol{\lambda}_H$  is a  $r$ -dimensional vector scaling  $\mathbf{H}$ . From the presentation of (2.41) follows that the cable force distribution consists of two parts: the external part  $\mathbf{f}_{\text{ext}}$  lies in the image-space of the structure matrix and solves the inhomogeneous part of the structure equation which is represented by the wrench  $\mathbf{w}$ . The internal tensions  $\mathbf{f}_{\text{int}}$  however lie in the null-space of the structure matrix and do not appear in the image-space (Verhoeven 2004). Thus, the internal tensions can be used to tense the cables against each other without generating external forces and is important to achieve positive cable forces. To find all feasible solutions is a non-trivial problem, as the null-space spans a  $r$ -dimensional hyperspace and different solution approaches exist.

In the following, five cable force algorithms which are candidates for the use as set-point algorithms for cable force control are introduced, namely closed-form (Pott, Bruckmann et al. 2009), advanced closed-form (Pott 2014a), puncture method (Müller, Reichert et al. 2014), closed-form energy efficient (Kraus, Spiller et al. 2013) and quadratic programming (Bruckmann 2010). All algorithms can be used for redundant robots and are basically not limited to a specific degree-of-redundancy  $r$ . The tension level reached by these algorithms is highlighted, as it influences e.g. the energy consumption and dynamic behaviour of the robot.

The closed-form solution (CF) is one method to find a solution for the structure equation (Pott, Bruckmann et al. 2009). A reference force  $\mathbf{f}_{\text{ref}} = (\mathbf{f}_{\min} + \mathbf{f}_{\max})/2$  is introduced which lies in the middle of the minimum and maximum cable force. A 2-norm optimization regarding  $\mathbf{f}_{\text{ref}}$  is performed and this optimization problem is solved explicitly by

$$\mathbf{f}_{\text{CF}} = \mathbf{f}_{\text{ref}} - \mathbf{A}^{+T}(\mathbf{w} + \mathbf{A}^T \mathbf{f}_{\text{ref}}) . \quad (2.42)$$

In general, the result is not energy optimal, as the cable force may be higher than the minimum cable force which is sufficient for stability of the robot. To bring the cable forces to a lower level, the approach was further developed to the closed-form energy efficient (CFE) in (Kraus, Spiller et al. 2013). The basic idea is to decrease the reference force  $\mathbf{f}_{\text{ref}}$  until at least one cable reaches the minimum cable force. Reformulating (2.42) delivers

$$\mathbf{f}_{\text{CF}} = -\mathbf{A}^{+T} \mathbf{w} + (\mathbf{I} - \mathbf{A}^{+T} \mathbf{A}^T) \mathbf{f}_{\text{ref}} , \quad (2.43)$$

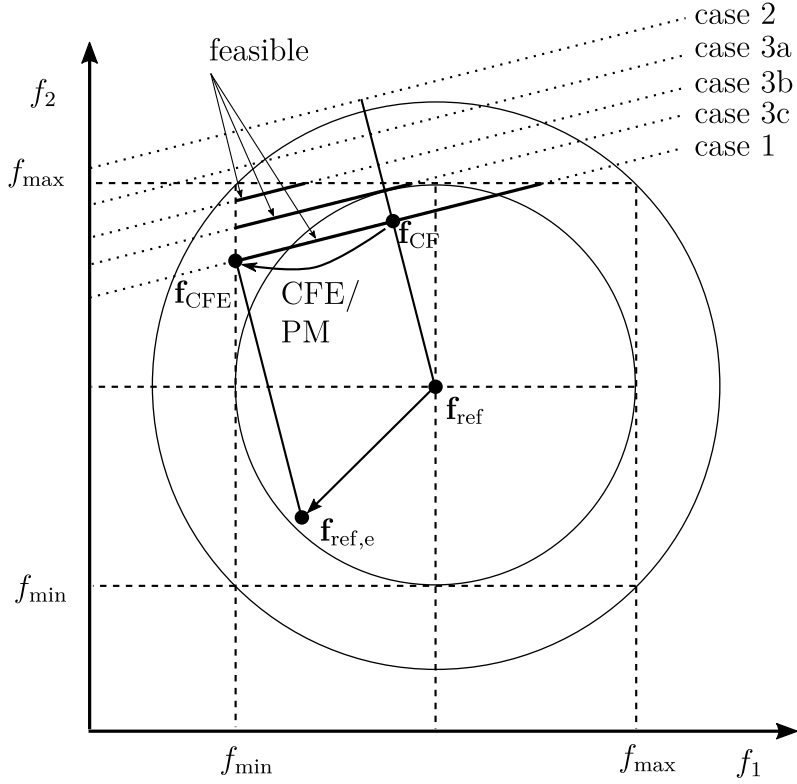


Figure 2.6: Convergence of the closed-form method and reduction of the cable forces with the closed-form energy efficient and puncture method (the figure builds up on (Pott, Bruckmann et al. 2009))

and shows the following linear relation between the reference force and the resulting cable force distribution:

$$\frac{d\mathbf{f}_{CF}}{d\mathbf{f}_{ref}} = (\mathbf{I} - \mathbf{A}^{+T} \mathbf{A}^T) \quad (2.44)$$

The potential to decrease the cable forces is described by the distance from the minimum cable force  $\Delta\mathbf{f} = \mathbf{f} - \mathbf{f}_{min}$ . Based on this consideration, a new reference force  $\mathbf{f}_{ref,e}$  is searched for which at least one cable has the minimum force. The new cable force distribution is then evaluated by

$$\mathbf{f}_{CFE} = -\mathbf{A}^{+T} \mathbf{w} + (\mathbf{I} - \mathbf{A}^{+T} \mathbf{A}^T) \mathbf{f}_{ref,e} \quad . \quad (2.45)$$

The puncture method (PM) presented in (Müller, Reichert et al. 2014) is also an approach to reduce the tension level. It establishes a straight line between the cable force distribution evaluated with CF method, (2.42), and the cable forces needed to exert the desired wrench  $\mathbf{f}_{ext} = -\mathbf{A}^{+T} \mathbf{w}$ . The puncture through the minimum limit of the cable forces is used as new solution for the cable force distribution. Applied to the CF algorithm, it delivers the same result as the CFE.

For illustration, the structure of the optimization problem is visualized for two cables in Fig. 2.6. For the visualized cases, the external force is varied which leads to different values for  $\mathbf{f}_{ext}$ . They stand exemplary for different cases of solutions. The CF algorithm will

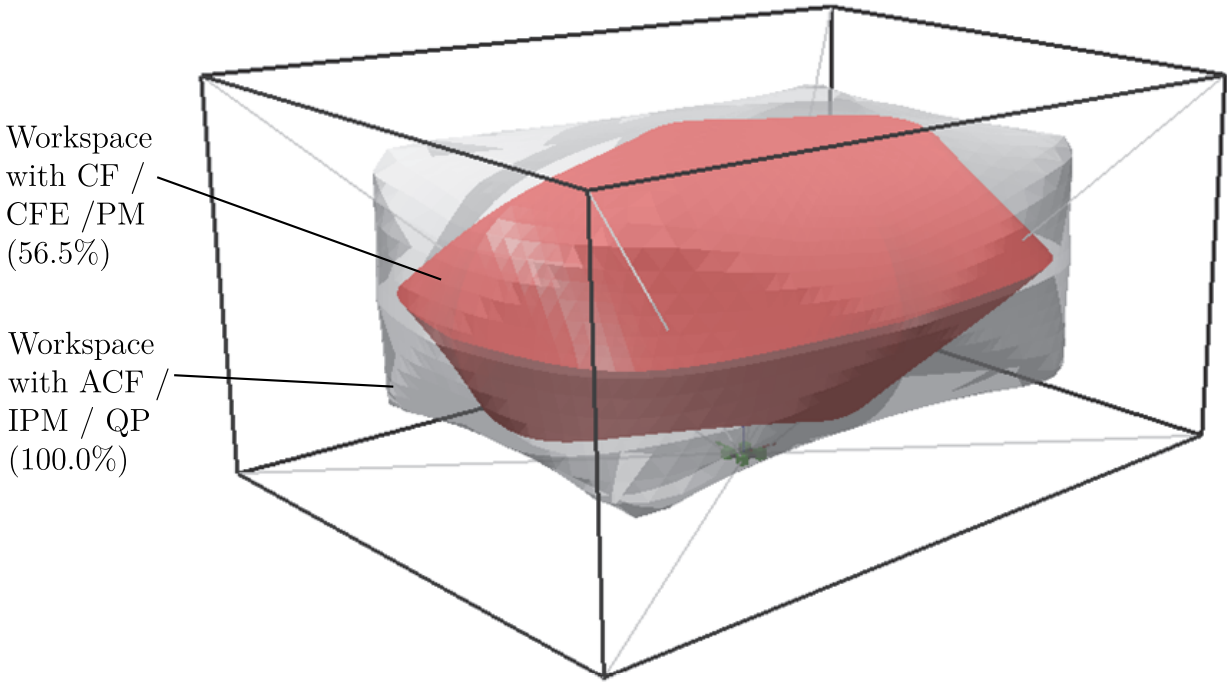


Figure 2.7: Comparison of the workspace computed with different methods: the methods based on the closed-form algorithm do not find all solutions and hence their workspace is smaller

deliver the solution with the shortest distance to the centre of the rectangle, defined by  $\mathbf{f}_{\text{ref.}}$ . In case 1, the solution of the CF algorithm  $\mathbf{f}_{\text{CF}}$  lies inside the rectangle and is, therefore, feasible. Using the CFE or PM algorithms, the solution is shifted along the straight line in the null-space of  $\mathbf{A}^T$  till cable 1 has the minimum cable force which is marked as  $\mathbf{f}_{\text{CFE}}$ .

In some cases, the CF algorithm does not find a feasible solution although such solutions exist. This is due to the 2-norm optimization and can be explained by case 3. In case 3c a feasible solution is found and in case 3a no feasible solution exists. In case 3b the CF method gives an infeasible solution although a feasible exists in the null-space. This results in a smaller workspace as shown in Fig. 2.7. To find also the lasting solutions, the CF algorithm has to be expanded.

An improved version of the CF algorithm, which finds all solutions, was presented in (Pott 2014a) named advanced closed-form (ACF). It consists of the evaluation of the closed-form solution and an order reduction of the linear equation system in case, the cable force limits are violated. The largest violation of the cable limits is detected and the cable force is set to the corresponding limit value. Next, this cable is excluded from the structure matrix and the exerted force and torque of this cable is added to the wrench. This procedure is repeated until a feasible solution is reached or the structure matrix is quadratic and no further reduction is possible. The computational effort is strictly bounded. In the worst case,  $r$  iterations have to be performed.

The adoption of the puncture method on ACF was proposed in (Müller, Reichert et al. 2014) as improved puncture method (IPM). For the result of ACF, the puncture is determined and the force distribution is shifted as described above.

We also applied the CFE method on ACF by adapting  $f_{\text{ref}}$  in every iteration step. With this algorithm, it was not possible to generate continuous solutions and, thus, the idea has not been further pursued.

The force distribution can also be derived by optimization algorithms. In (Bruckmann 2010), the solution with quadratic programming (QP) algorithm is described. It solves

$$\min g(\mathbf{f}) = \frac{1}{2} \mathbf{f}^T \mathbf{Q} \mathbf{f} \quad (2.46)$$

$$\text{with } \mathbf{f}_{\text{min}} \leq \mathbf{f} \leq \mathbf{f}_{\text{max}} \text{ and } \mathbf{A}^T \mathbf{f} = -\mathbf{w} , \quad (2.47)$$

and, thus, the cable force distribution is minimal regarding the Euclidean norm with reference to the zero force. Typically, all cable forces are equally balanced and, therefore, the matrix  $\mathbf{Q}$  is chosen as identity matrix. As the QP algorithm is based on an iterative solver, computational run-time may prohibit the use on real-time controllers (Bruckmann 2010).

It can be concluded that several methods to solve the structure equation exist, which will deliver different tension levels: the CF and ACF will deliver medium tension level, and the CFE, PM and QP algorithms will yield minimal cable forces. No method exists which allows to adjust the tension level arbitrarily.

The review of the theoretical foundations is now complete, and in the following, the cable robot demonstrators including their current control architecture are described.

## 2.3 Demonstrators

For the experimental investigation, two cable robot demonstrators are used in this thesis. The IPAnema 3 is a relatively large robot installation designed for handling applications which is depicted in Fig. 2.8a and whose parameters and main components are given in Table 2.1. The IPAnema 3 Mini is significantly smaller and is used for the evaluation of the haptic interaction. The robot is shown in Fig. 2.9 and Table 2.2 represents the main components and technical data. For the later modelling of the robot, some aspects of the hardware design are explained. Furthermore, the current control architecture and the interfaces for the implementation of the controller are described. The existing control approach using the inverse kinematics is explained as reference for the experimental evaluation. Finally, the measuring equipment used for the experimental evaluation of the position accuracy and robot's energy consumption are presented.



(a) Main structure of the robot installation



(b) Winch design with integrated cable force measurement

Figure 2.8: Cable-driven parallel robot IPAnema 3

Table 2.1: Cable robot IPAnema 3: parameters and main components

parameter	value	unit
Number of cables $n$	8	-
Degrees-of-freedom $m$	$6, 3R3T$	-
Size of the robot frame	$17.0 \times 12.0 \times 4.5$	m
Rated cable force	3,000	N
Max. cable velocity	1.7	m/s
Drive	Bosch Rexroth MSK071E-0300-NN-M1-UG1-NNNN	-
Drive power	5.0	kW
Gear Box	Bosch Rexroth GTE160-NN2-012B-NN16	-
Gear ratio	12:1	-
Drum diameter	0.1	m
Cable type	LIROS D-Pro 01505-0600	-
Cable diameter	6.0	mm
Specific cable stiffness	900,000	N
Cable force sensor	Tecsis F2301	-
Cable force measurement range	0 - 4,000	N

### 2.3.1 Robot Hardware Design

The mechanical key elements of a cable robot are the winches. The winches of the IPAnema robots are designed for single layer winding which is supported by grooves in the drum as can be seen in Fig. 2.8b. In the IPAnema 3 winch, a pulley connected to a spooling traverse is used to ensure the correct cable winding. A leverage arm connects the pulley with a one-dimensional force sensor for cable force measurement. In the current design, the lever arm amplifies the cable forces by factor 1.25. Thus, the rated force of 5.0 kN of the sensor corresponds to a maximum cable force of 4.0 kN. In combination with the current drives, the rated cable force amounts to 3.0 kN and the maximum cable velocity to 1.7 m/s. The winches of the IPAnema 3 are installed on the floor as depicted in Fig. 2.8a. The lower cables start directly from the outer pulley at the winch housing. For the upper cables, a cable deflection unit consisting of two swivelling pulleys is installed in each upper edge of the steel frame. The platform of the IPAnema 3 was initially designed for the handling of solar panels. Nowadays, it acts as a test platform for control algorithms.

The complete hardware of the IPAnema 3 Mini is installed in an aluminium frame as depicted in Fig. 2.9a. The winches are installed in the lower part of the aluminium frame as shown in Fig. 2.9c. The spooling traverse is replaced by a longer free cable between the drum and the pulley. In combination with the grooved drum, this ensures safe winding. The drives of the IPAnema 3 Mini are directly coupled with the drum which allows for a maximum velocity of 2.0 m/s and a rated cable force of 40 N. The platform of the IPAnema 3 Mini shown in Fig. 2.9b is designed as handle used for haptic interaction between the robot

Table 2.2: Cable robot IPAnema 3 Mini: parameters and main components

parameter	value	unit
Number of cables $n$	8	-
Degrees-of-freedom $m$	$6, \beta R3T$	-
Size of the robot frame	$1.1 \times 0.8 \times 1.0$	m
Rated cable force	40	N
Max. cable velocity	2.0	m/s
Drive	Beckhoff AM3121-0201-0001	-
Drive power	0.2	kW
Gear Box	gear less	-
Gear ratio	1:1	-
Drum diameter	0.02	m
Cable type	LIROS D-Pro 01505-0150	-
Cable diameter	1.5	mm
Specific cable stiffness	28,500	N
Cable force sensor	Futek LRM200	-
Cable force measurement range	0 - 111	N

and humans. The cable force measurement is conducted within the aluminium frame and the depicted additional force sensor is only installed during the identification of the pulley friction.

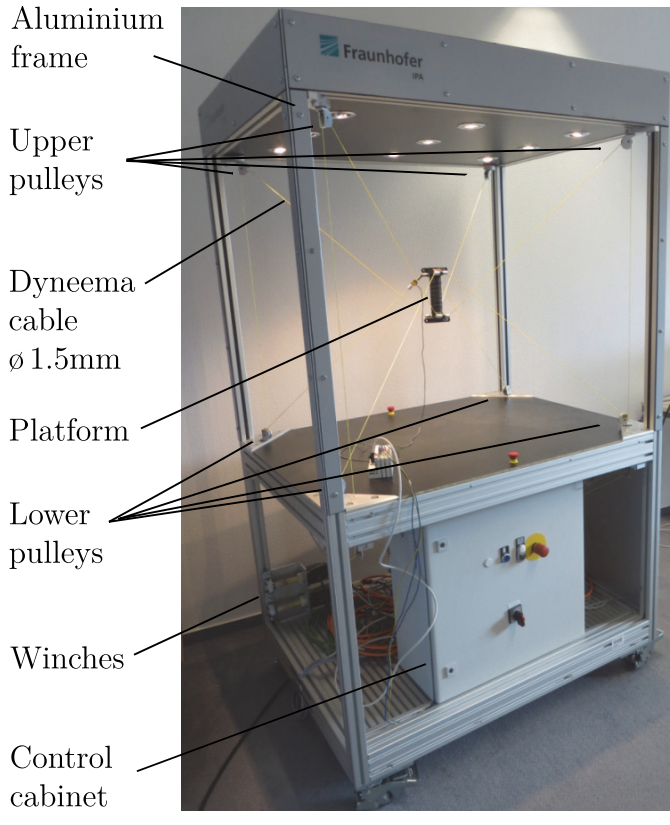
As reference, the geometrical values describing the robot kinematics are given in Table 2.3 and 2.4 for both robots. Next, the control architecture is elaborated.

### 2.3.2 Control Architecture

Control architectures can be classified according the location of the control task into centralized and decentralized control. For classification of different control approaches, three

Table 2.3: Geometrical parameters of the IPAnema 3 robot

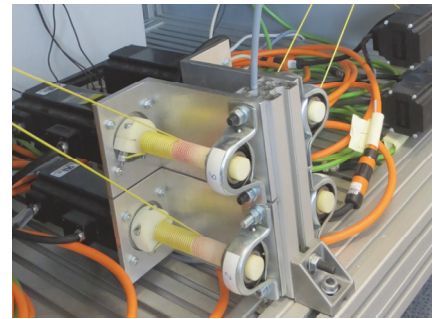
cable $i$	base vector $\mathbf{a}_i$ [m]	platform vector $\mathbf{b}_i$ [m]	pulley orientation $\varphi_A$ [°]	$r_p$ [mm]	$l_0$ [m]
1	$[8.185, 5.693, 3.203]^T$	$[0.061, 0.649, -0.262]^T$	$[90, 0, -90]^T$	52.0	4.6
2	$[8.224, -5.492, 3.236]^T$	$[0.061, -0.651, -0.262]^T$	$[90, 0, 90]^T$	52.0	4.6
3	$[-8.491, -5.322, 3.250]^T$	$[-0.070, -0.652, -0.261]^T$	$[90, 0, 90]^T$	52.0	4.3
4	$[-8.545, 5.464, 3.221]^T$	$[-0.070, 0.648, -0.261]^T$	$[90, 0, -90]^T$	52.0	4.5
5	$[7.208, 6.464, -0.590]^T$	$[0.095, 0.749, 0.261]^T$	$[90, 0, -90]^T$	35.0	0.3
6	$[7.869, -5.558, -0.549]^T$	$[0.095, -0.746, 0.261]^T$	$[-90, 180, 0]^T$	35.0	0.3
7	$[-8.271, -5.546, -0.528]^T$	$[-0.086, -0.746, 0.262]^T$	$[90, 0, 90]^T$	35.0	0.3
8	$[-8.192, 5.648, -0.583]^T$	$[-0.086, 0.749, 0.262]^T$	$[-90, 0, 180]^T$	35.0	0.3



(a) Main structure of the robot



(b) Platform with additional force sensor



(c) Winch design

Figure 2.9: Cable-driven parallel robot IPAnema 3 Mini

Table 2.4: Geometrical parameters of the IPAnema 3 Mini robot

cable <i>i</i>	base vector $\mathbf{a}_i$ [m]	platform vector $\mathbf{b}_i$ [m]	pulley orientation $\varphi_A$ [°]	$r_p$ [mm]	$l_0$ [m]
1	$[0.500, -0.378, 0.447]^T$	$[0.022, -0.040, -0.083]^T$	$[0, 0, 0]^T$	10.5	1.8
2	$[-0.500, -0.378, 0.447]^T$	$[-0.022, -0.040, -0.083]^T$	$[0, 0, 0]^T$	10.5	1.8
3	$[-0.500, 0.378, 0.447]^T$	$[-0.022, 0.040, -0.083]^T$	$[0, 0, 0]^T$	10.5	2.0
4	$[0.500, 0.378, 0.447]^T$	$[0.022, 0.040, -0.083]^T$	$[0, 0, 0]^T$	10.5	2.0
5	$[0.531, -0.344, -0.447]^T$	$[0.022, -0.040, 0.083]^T$	$[0, 0, 0]^T$	10.5	0.8
6	$[-0.531, -0.344, -0.447]^T$	$[-0.022, -0.040, 0.083]^T$	$[0, 0, 0]^T$	10.5	0.8
7	$[-0.531, 0.344, -0.447]^T$	$[-0.022, 0.040, 0.083]^T$	$[0, 0, 0]^T$	10.5	1.0
8	$[0.531, 0.344, -0.447]^T$	$[0.022, 0.040, 0.083]^T$	$[0, 0, 0]^T$	10.5	1.0

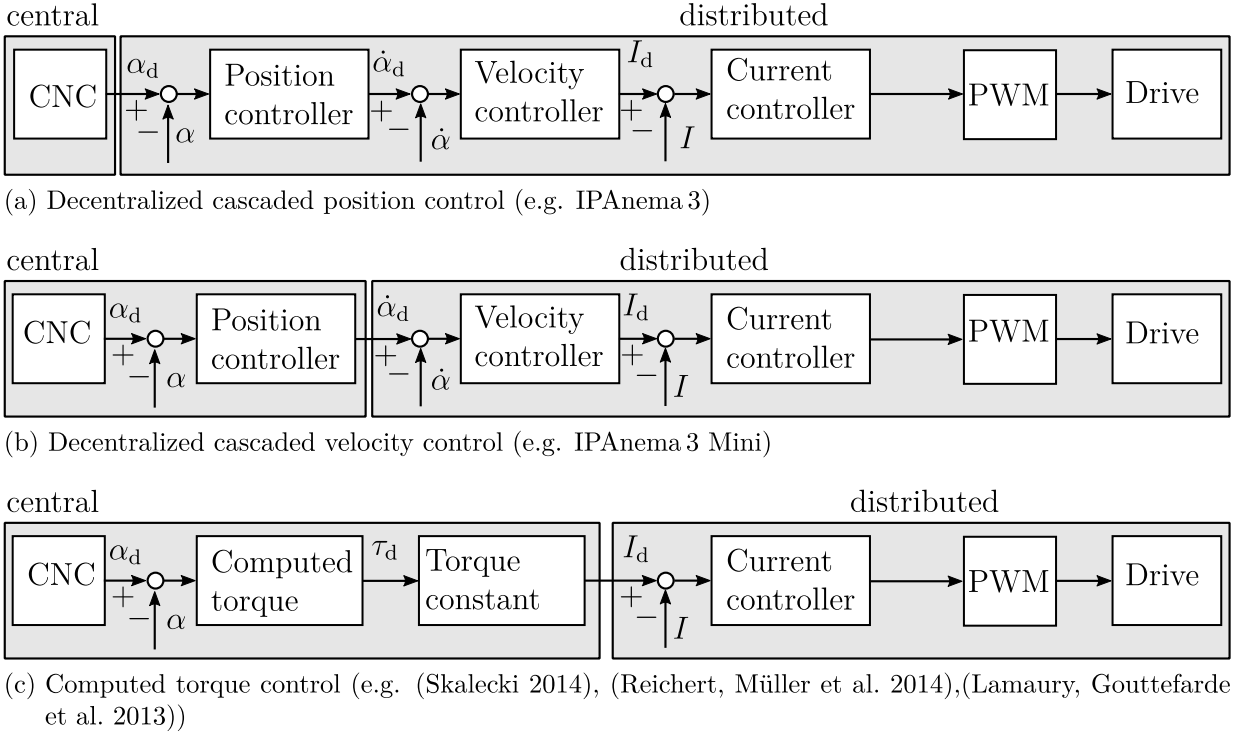


Figure 2.10: Overview over different control architectures and division between the central and distributed controller

structures are presented in the following and visualized in Fig. 2.10. Hereby, the central controller of the robot is realized by a computerized numerical control (CNC).

A control architecture using position-controlled drives is depicted in Fig. 2.10a. The decentralized controller has a cascaded structure with position, velocity and current control loops. Lastly, the pulse width modulation (PWM) controls the power electronics of the servo amplifier which results in the desired current  $I_d$ . The drives in the IPAnema 3 rely on such a control scheme. The cascaded position controller is encapsulated in the servo amplifier and is used without modifications within this thesis.

In some more basic configurations of servo amplifiers, the position control loop is not implemented on the servo amplifier due to the limited performance of the distributed controller. In this case, the position control is executed in the centralized controller as depicted in Fig. 2.10b. The control of the IPAnema 3 Mini has such a structure. As the centralized position control is already foreseen in the centralized controller, the interfaces are the same as on the IPAnema 3.

For computed-torque control, the decentralized position and velocity control are neglected and only the current control is executed in the servo amplifier as shown in Fig. 2.10c. This control approach can often be found in the control of high dynamic and coupled systems as it allows for model-based control e.g. using the inverse dynamics. Based on a system model, the desired torque  $\tau_d$  is calculated centralized for each drive and transformed to a desired current  $I_d$ .

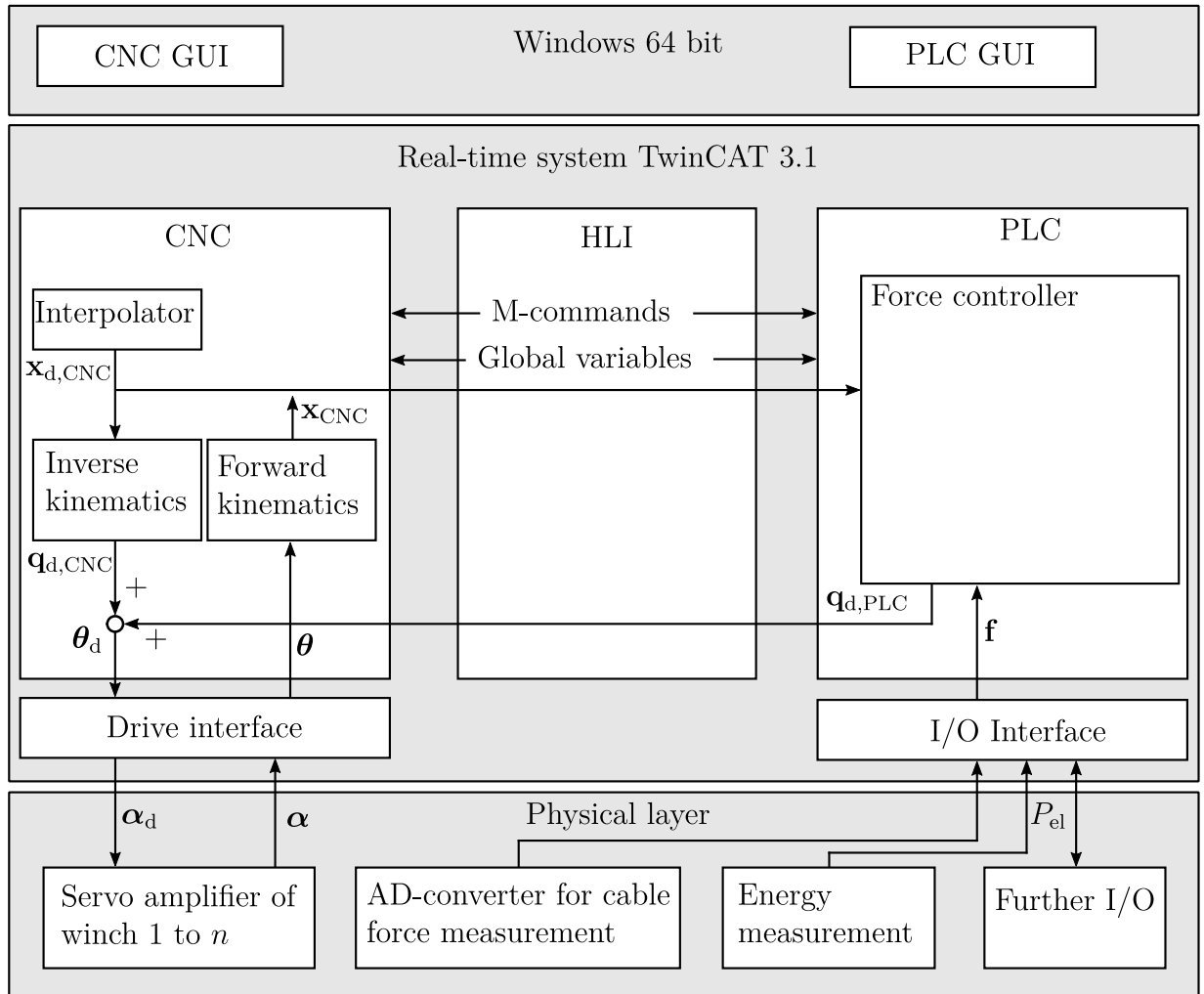


Figure 2.11: Structure of a typical industrial CNC

In the following, the central controller, which is designed for the control of position-controlled drives, is described.

The cable robot control is realized utilising the state of the art industrial real-time controller Beckhoff TwinCAT 3.1, whose structure is shown in Fig. 2.11. In the following, a short summary of the main parts of the controller is given, which is needed to understand the interfaces and restrictions of the target system. The control architecture can be divided into three main layers: non real-time tasks in Windows 64 bit, the real-time tasks of TwinCAT and the physical layer with the decentralized controllers which are connected via the field bus to the control PC. Both robots use EtherCAT as field bus. Beside the servo amplifier, the analogue-to-digital (AD) converter for cable force measurement, energy measurement and further input-output (I/O) devices are connected. The cycle time of the field bus, the interpolation within the CNC and the PLC are equal and amounts in the current configuration to 1 ms. The real-time controller itself is divided in a CNC which is basically developed for the control of tooling machines and a programmable logic controller

(PLC) which allows for user-specific implementations. The communication between the two parts is realized by a shared memory called High Level Interface (HLI). Both, CNC and PLC have an asynchronous communication interface to the non-real-time tasks which enables e.g. for graphical user interface (GUI).

In automatic operation, the CNC interprets paths programmed in standardized G-Code. A geometric path planning is carried out, which transforms the path programmed e.g. by the edge points to a connected path. By the application of jerk-limited acceleration profiles which are defined by the maximum velocity, acceleration and ramp time, the trajectory planning is carried out. Next, the interpolator transforms the trajectory to a time-discrete series of positions, which yields  $\mathbf{x}_d$ . The programming of a parallel kinematics is typically done solely in operational space, as the platform cannot be controlled in a stable way by the control of only one joint. With the inverse kinematics transformation, the desired position is transformed from operational space to joint space and results in the desired cable length  $\mathbf{q}_{d,IK}$ . On this layer, the CNC provides an interface named external commanding, which allows to add additional position set-points from the PLC denoted by  $\mathbf{q}_{d,PLC}$ . The resulting set-point  $\boldsymbol{\theta}_d$  is then transformed to rotation angles of the drives  $\boldsymbol{\alpha}_d$  by the drive interface. The position set-point is the input of the decentralized cascaded position controller of the servo drive. Based on the drive encoder value  $\boldsymbol{\alpha}$ , the actual cable length  $\boldsymbol{\theta}$  is derived and fed back to the CNC. For this value, the forward kinematics is solved and gives the actual position  $\mathbf{x}_{CNC}$ . Within the CNC, the actual position is used for the detection of excessive position lag and as starting point after enabling the kinematic transformation. For convenience, the absolute encoders of the drives are set to zero cable length when the platform is in its home position and the cables are under tension. It is typical for a CNC that the control in operational space is conducted in open-loop. For this, the dynamic parameters of the trajectory generator are adjusted to the available dynamics of the drives. Using the inverse kinematics, which is based on the geometrical model of the robot, high dynamics can be reached.

The control of the cable robot with the inverse kinematics is the starting point of this thesis and is used as reference for the proposed controller during the experimental evaluation. The control is based on the rigid geometrical model including the pulley kinematics, while the cable elasticity is neglected. The cables are initially tensed in the home position ( $\mathbf{x} = \mathbf{0}$ ) to a cable force distribution lying in the middle between the minimum and maximum feasible force. During operation, the cables forces are not controlled and result from the actual elongation which arises from the equilibrium position of the platform.

The closed-loop operational space position control and cable force control which are necessary for redundant cable robots are not an integral part in the CNC but can be implemented in the PLC as follows. The PLC can be programmed in classical manner by structured text (ST). With advanced tools, the ST can also be generated directly from the

simulation environment, e.g. by using the PLC-Coder of Matlab Simulink®. TwinCAT provides also a direct coupling with Simulink®. For more complex algorithms which make use of external libraries, C++ programming is supported.

The industrial controller implies some restrictions regarding the interfaces. The inverse kinematics is an inherent part of the CNC and it processes only the desired position  $\mathbf{x}_{d,CNC}$  from the interpolator and no additional offset can be added from outside. Thus, for the developed operational space controller, the inverse kinematics is implemented a second time in the PLC. Furthermore, an extended version of the forward kinematics is implemented in the PLC due to the lack of the access of the cable forces in the CNC. This implementation detail is not taken into account in the further progress of this thesis and it is assumed that only one implementation of the forward and inverse kinematics exists.

Numerical control (NC) programs written in G-Code are used for task programming. The G-Code includes manifold commands for motion sequences like straight lines, circle paths, smoothing of edges. For the interaction between a NC program and the PLC, machine commands and global variables are available. The machine commands can be beneficially applied for the generation of automated test procedures by combining motion sequences with triggering external measurement devices or setting parameter values of implemented controllers. With the HLI, internal states of the CNC like the actual position set-point and feedback value in both operational and joint space can be accessed. With exception of the drive, all interaction with further I/O like AD-converter of the cable force sensors is realized in the PLC. In the next section, measuring equipment which is partly coupled with the PLC for synchronous measurements is described.

### 2.3.3 Measuring Equipment

For system identification and verification of the control approaches, internal variables of the control loops are accessed and additional measuring equipment is applied.

The platform position of the cable robot can only be estimated by the forward kinematics which is subject to model uncertainties. For reliable statements about the position accuracy, the platform position and orientation has to be measured with an external measurement device. In this thesis, an absolute position measurement device of type Leica laser tracker AT901-MR is applied. The laser tracker is able to measure the position of a reflector within a sphere with a diameter of 18 m and a precision of 25  $\mu\text{m}$  (Leica Geosystems AG 2008). With this method, one single point can be measured with high accuracy. For the complete evaluation of the position accuracy, this information is not sufficient, as it gives no insight about the orientation. Thus, for the static investigation of the position accuracy, three reflectors are attached on the platform. After the platform has reached the target position, the absolute position of all three reflectors is subsequently measured. With a coordinate transformation, the position and orientation information can be obtained from these points.

The measurement results are given in the coordinate frame of the laser tracker which is sufficient for the evaluation of the relative position accuracy. For the absolute position accuracy, the pose has to be transformed into the world frame of the robot  $\mathcal{K}_0$ . For this purpose, the transformation matrix to the world frame is established for the actual set-up location of the laser tracker. For position measurement of the moving robot, only the position of one point on the platform can be measured.

For the identification of the energy consumption model, internal states of the servo drive like actual motor currents, voltages and intermediate circuit power are required. For the data acquisition, a limited number of signals can be added to the communication protocol between the drives and the CNC. In this way, synchronized measurements can be carried out including signals from the CNC and the decentralized position controller. For the measurement of the energy consumption of the complete robot, a three phase current and voltage measurement is connected to the alternating current (AC) input of the control cabinet. The energy measurement is also connected to the field bus.

---

# 3 Controller for Redundant Cable Robots with Elastic Cables

In this chapter, the development of the control approach for redundant cable robots with elastic cables is presented. A stability analysis delivers that a cable force control in joint space is not sufficient in all cases for stable operation of the robot. Thus, the control approach is further developed and an approach incorporating a cable force control with an operational space position control is proposed. For decoupling of the two controllers, the null-space projection is introduced and applied on the control scheme. This leads to the proposed control architecture of this thesis. For the operational space control, a further developed forward kinematics approach considering the non-linear cable stiffness and the pulley kinematics is presented. For the controller synthesis, the transfer functions of the plant have to be known. In section 3.3, identification experiments are carried out to find the transfer functions of the actuator unit and the platform dynamics. The models are formulated in the frequency domain and represent linear, time-invariant systems apart from the transfer delay. For the parametrization and stability analysis, the dynamic models for the actuator, cables, platform and sensor in the feedback loop are derived. Next, the controller synthesis and stability analysis is carried out based on the open-loop transfer function using Nyquist diagrams, which visualize the stability margins. After the principal control approach is established and stability is ensured, the implementation is presented. Here, the focus lies on the calculation of the cable force distribution. The main contribution is the extension of the quadratic programming algorithm for step-less adjustment of the tension level. This chapter closes with the analysis of cable force measurement. For winch-integrated force measurement, the pulley friction between the force sensor and the mobile platform influences the measurement accuracy. To compensate for the pulley friction, a model is derived and implemented.

## 3.1 Derivation of the General Control Approach

The result of this section is the general control approach, which is detailed in the further course of this chapter. The control approach has to incorporate the three basic problems of this thesis. The focus lies on the question, how to find a desired motor position to reach

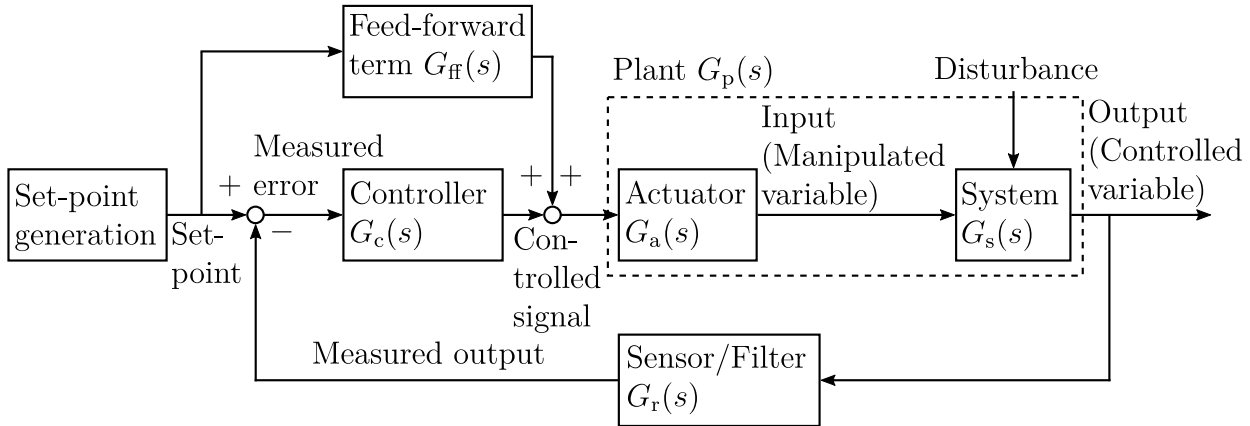


Figure 3.1: General model of a feedback control loop consisting of a set-point generation, a controller  $G_c(s)$ , the plant  $G_p(s)$ , which can be divided in the actuator and the controlled system, and sensor and filter in the feedback loop  $G_r(s)$

the desired platform position in operational space and to keep the cable forces within the feasible force limits. Starting with the model of a general feedback control loop, the control approach is developed step-by-step. For this purpose, the control with the inverse kinematics (section 2.3.2), the inverse kinematics with a parallel cable force controller (Kraus, Schmidt et al. 2014), dual-space controller (Lamaury, Gouttefarde et al. 2013), (Lamaury and Gouttefarde 2013b) and internal tension controller (Fang 2005) are analysed and discussed.

### 3.1.1 General Model of a Feedback Control Loop

For the derivation of the controller for redundant cable robots, the general model of a closed-loop controller with a feed-forward term is taken as basis as depicted in Fig. 3.1 (Lunze 2010). The system, which has to be controlled is the plant  $G_p(s)$ . The plant can be further divided into the actuator  $G_a(s)$  and the system  $G_s(s)$ , e.g. the mechanical set-up of the robot itself. The set-point generator delivers the actual desired signal, also called set-point value or reference signal. In the illustrated model, the controlled signal is derived from a feed-forward term  $G_{ff}(s)$  and a closed-loop controller  $G_c(s)$ . The system  $G_s(s)$  is influenced by the manipulated variable and disturbances. The controlled variable is the output of the system, which can be measured by a sensor or a filter with the transfer function  $G_r(s)$ . The difference between the set-point signal and the measured output yields the measured error, which is the input of the feedback controller. In the following, the control using the inverse kinematics and an improved approach incorporating a cable force control are reviewed.

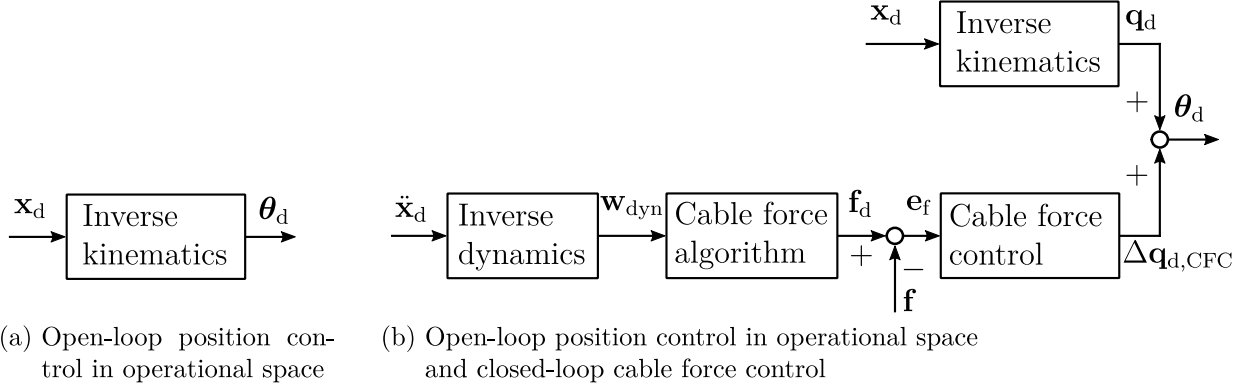


Figure 3.2: Control structures with open-loop position control in operational space

### 3.1.2 Cable Force Control

Basis of this thesis is the control of the cable robot using the inverse kinematics as presented in section 2.3.2. This approach is visualized in Fig. 3.2a for a desired position  $\mathbf{x}_d$ , for which the inverse kinematics gives the desired cable length  $\theta_d$ . In combination with position-controlled drives this approach is easy to implement and is well-known from tooling machines. The cable forces can only be controlled in limited manner by the initial pre-tension of the cables in the home position. The extension of the existing approach towards the control of the cable forces is to add a cable force control (CFC) in parallel to the CNC which outputs a change in cable length  $\Delta \mathbf{q}_{d,CFC}$  for influencing the cable forces as shown in Fig. 3.2b. For this purpose, the desired wrench is derived from the platform inverse dynamic (2.33) using the nominal values of the platform mass  $m_p$ , vector to the centre of gravity  $\mathbf{c}_{m_p}$  and inertia tensor of the platform  $\mathbf{J}_c$  and

$$\mathbf{w}_d = \mathbf{w}_{dyn} \quad (3.1)$$

holds. For the desired wrench, the cable force algorithm delivers a feasible cable force distribution  $\mathbf{f}_d$ . With the actual cable forces  $\mathbf{f}$  the errors in cable forces  $\mathbf{e}_f$  are defined as

$$\mathbf{e}_f = \mathbf{f}_d - \mathbf{f} \quad , \quad (3.2)$$

which is the input of the cable force controller. In a redundant robot, the number of cables is higher than the DOF and, thus, the cable force controller will not reach static accuracy (no steady-state error). The lasting control errors can be projected with the structure matrix into the operational space and result in an error wrench  $\mathbf{e}_w$  which is calculated by

$$\mathbf{e}_w = -\mathbf{A}^T(\mathbf{f}_d - \mathbf{f}) \quad (3.3)$$

and can be interpreted as free force and torque acting on the platform. This wrench may accelerate the platform and lead to instabilities. Experimental results on a former version of the IPAnema robot showed a comparatively better position accuracy with cable force control compared to the solely inverse kinematics (Kraus, Schmidt et al. 2014). The question about the stability and the consequences of force control needs further analytical investigation, which is presented in the following.

### 3.1.3 Stability Analysis of Cable Force Control

The cable force control aims to set the cables under a desired force by elongating the cables by  $\Delta\mathbf{q}_{d,CFC}$ . This has an important influence on the robot's stiffness. As shown in section 2.1.2, the operational space stiffness matrix is set up from the cable stiffness  $\mathbf{K}_c$  and geometrical stiffness  $\mathbf{K}_g$ . In a realistic spatial robot configuration, the contribution of the geometric stiffness is significantly lower than the cable stiffness. The part  $\mathbf{K}_c$  depends on the spring behaviour of the cables: applying an external load, the elongated cable length changes and, subsequently, the forces adapt and create a rejection force. The closed-loop servo controller can be regarded as stiff and, thus, the drive will keep the desired position  $\theta_d$  under external load. Therefore, in a closed-loop position-controlled robot in joint space, the cable stiffness is dominant for the compliance of the robot.

If the robot is cable-force-controlled and an external load is applied on the platform, the force controller interprets the change in cable force as control error  $e_f$  and will control the cable forces to the initial set-point  $f_d$ . Assuming an ideal force control, the cable stiffness is cancelled out by the cable force control. Only the geometrical stiffness remains, as it depends on the change of the structure matrix under a position deviation. Thus, the platform stiffness of a force-controlled robot has to be expected significantly lower than position-controlled by the inverse kinematics.

The stiffness is also a measure for the robustness of the robot. Physically interpreted, stiffness means that the platform can resist external loads acting from arbitrary directions, e.g. in form of disturbances by a displacement of the platform which leads to rejection forces. The platform stability assumes positive definiteness of the operational space stiffness matrix. A matrix is positive definite, when all its eigenvalues are positive. The part depending on the cable stiffness  $\mathbf{K}_c$  is in general positive definite when all cables are under tension and the robot is in a non-singular configuration. The geometrical stiffness matrix is not in general positive definite. Investigating the IPAnema 3 robot showed that the positive definiteness of  $\mathbf{K}_g$  depends not only on the robot geometry but also on the robot pose and the actual cable force distribution. This will be described in section 4.3. As the cable stiffness vanishes under force control, the geometrical stiffness determines the stabilizability of the robot.

In the implementation of the force controller, one can limit the influence of the cable force controller on the position accuracy by the introduction of saturations. The saturation

limits are originally motivated to avoid excessive position changes due to cable force control. Cables, which are in saturation, will also contribute to the operational space stiffness with their cable stiffness and, thus, the influence of  $\mathbf{K}_c$  can partly be regained.

The operational space stiffness matrix describes also the effect of control errors  $\mathbf{e}_w$  according to (3.3) on the platform position. Assuming a positive definite stiffness matrix  $\mathbf{K}_x$ , the position deviation  $\Delta\mathbf{x}$  can be approximated by

$$\Delta\mathbf{x} = \mathbf{K}_x^{-1}\mathbf{e}_w . \quad (3.4)$$

It follows, that the position accuracy depends not only on the geometrical model parameters but also on the parameters coincident with the force control loop, namely the cable stiffness, platform mass parameters and accuracy of cable force sensors. Disturbances in these parameters will lead to control errors according to (3.3) and will last in position errors. If, for example, the mass  $m_p$  is modelled too low, the platform will drop and the actual structure matrix changes, till the measured wrench equals almost the theoretical one. Therefore, the static equilibrium would be shifted, which leads to a position inaccuracy.

In some robot applications, the decreased stiffness is acceptable: e.g for the haptic interaction with the robot, the cable force control is applied on the robot. Robots used for inspection processes, force control may be applicable, as the platform load does not change and, thus, the model uncertainties are limited.

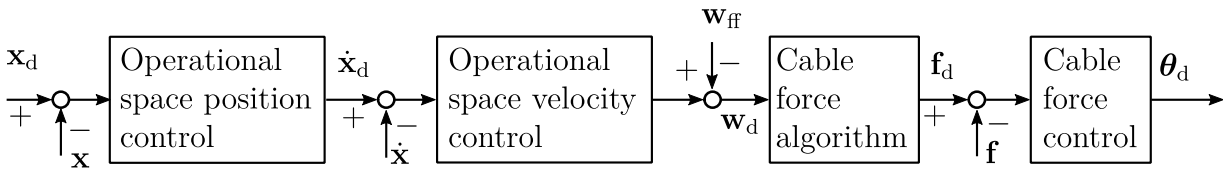
It can be concluded that the robot stiffness will decrease under cable force control. Due to the lower stiffness, the robot becomes more sensitive for model error, e.g. also in terms of additional loads on the platform. Force control can be stable but has to be checked for the specific robot configuration and cable force distribution. To solve this problem in general, the control approach has to be extended and operational space position has to be considered.

### 3.1.4 Synchronous Control of Position and Cable Forces

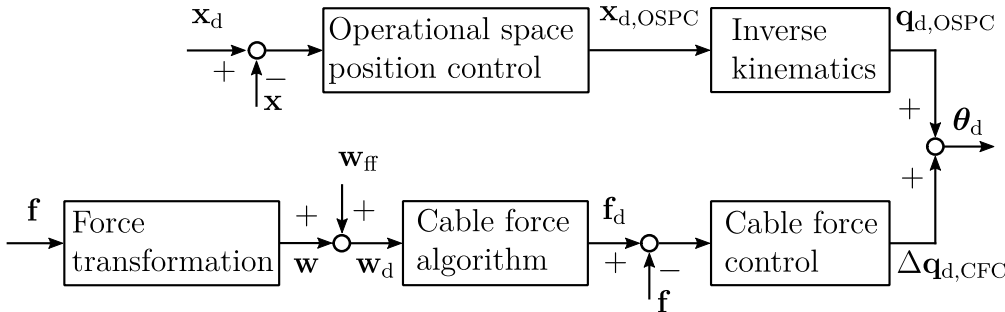
The stability analysis of the cable force control showed that it is not sufficient for stable operation of a cable robot in all cases. For the further development, also the platform position has to be considered which leads to an operational space position control (OSPC). The input of the OSPC is the position error  $\mathbf{e}_x$  which is established by

$$\mathbf{e}_x = \mathbf{x}_d - \mathbf{x} , \quad (3.5)$$

where the desired position  $\mathbf{x}_d$  is derived from the CNC and the actual position  $\mathbf{x}$  has to be estimated by the forward kinematics. For the synchronous control of operational space position and cable forces, the number of manipulated and controlled variables gives



(a) Cascaded structure



(b) Parallel structure using null-space cable force control

Figure 3.3: Approaches for synchronous operational space position control and cable force control

a valuable insight. The cable force control has  $m$  manipulated ( $\Delta\mathbf{q}_{d,CFC}$ ) and  $m$  controlled variables ( $\mathbf{f}$ ). Controlling additionally the platform position, the number of manipulated variables remains, while the number of controlled variables rises by  $n$ . In first instance, the control problem is underdetermined and has to be reformulated under consideration of the force redundancy.

The cable force distribution can be divided into the force which generate a wrench  $\mathbf{f}_{ext}$  and the internal force  $\mathbf{f}_{int}$  according to (2.41). With the wrench, the accelerations are applied to the platform, which results to a velocity and subsequently the position of the platform. However, the internal tensions remain in the null-space and do not influence the platform position in the ideal case. The controlled variables are, thus, the position vector  $\mathbf{x}$  and multiplier  $\boldsymbol{\lambda}_H$ . In the cable force algorithms investigated in this thesis, the basis of the kernel is not calculated explicitly and, thus, the scale factor  $\boldsymbol{\lambda}_H$  follows implicitly from the solution of the cable force distribution. For the realization of the null-space control, two approaches are known from the state of the art.

The first approach uses a cascaded structure which outputs a desired wrench and is proposed in the dual-space controller (Lamaury, Gouttefarde et al. 2013), (Lamaury and Gouttefarde 2013b). The desired wrench is distributed with the cable force algorithm on the drives, which gives the desired torques. Although the dual-space controller does not control cable forces and uses torque-controlled drives, one can transform the control scheme on the present problem. The structure corresponds to a cascaded controller, where the cable force controller is subordinated to the position controller as depicted in Fig. 3.3a. Thus, the OSPC forms the outer cascade and delivers a velocity set-point  $\dot{\mathbf{x}}_d$  to the inner

velocity controller. The obtained acceleration is, next, transformed to a desired wrench  $\mathbf{w}_d$  incorporating a feed-forward term  $\mathbf{w}_{ff}$  by the inverse dynamics for which a feasible cable force distribution is evaluated.

The second approach is based on the concept of the internal tension controller proposed by Fang (2005). Using the null-space projection for the actual cable force distribution  $\mathbf{f}$ , the actual internal tensions can be calculated explicitly by

$$\mathbf{f}_{int} = \mathbf{H}\boldsymbol{\lambda}_H = \mathbf{f} - \mathbf{A}^{+T}\mathbf{A}^T\mathbf{f} . \quad (3.6)$$

This property can be incorporated in the cable force algorithm by using the actual wrench  $\mathbf{w}$  derived from (2.11). The resulting cable force distribution will reflect the actual wrench and only manipulates the internal tensions, e.g. for reaching minimal cable forces. This allows for decoupling the cable force control from the image-space and, thus, from the operational space position control. The control scheme was designed for torque-controlled drives but can also be adopted on position-controlled drives. The resulting parallel structure of the decoupled controllers is shown in Fig. 3.3b: the OSPC controls the platform position, while the CFC acts in the null-space to control the cable forces.

In this thesis, the second approach is pursued because it is based on the initial cable force controller. This allows to switch between the two control approaches for the later implementation of the operational space force controller. In the following, the general control architecture is presented.

### 3.1.5 Proposed Control Architecture for Redundant Cable Robot

The core elements of the control approach are the operational space position control and the cable force control. On this basis, the general control approach can be derived as visualized in Fig. 3.4. For the sake of completeness, operational space control algorithms, which are explained in the following chapters 4 and 5, are already incorporated in the control scheme: the load compensation delivers the position offset  $\mathbf{x}_{d,LC}$  for compensating the cable elasticity under changing payload and is presented in section 4.1. The hybrid position and force control (HPFC) establishes a defined contact force to the environment with the desired position  $\mathbf{x}_{d,HPFC}$ , which will be described in section 5.1. The admittance control presented in section 5.2 allows for the simulation of a desired system dynamic and outputs a desired position  $\mathbf{x}_{d,Adm}$ . The outputs of the operational space control algorithms are summarized to the desired position  $\mathbf{x}_d$  in operational space, which is transformed by the inverse kinematics to the joint space and gives the desired cable length  $\mathbf{q}_{dJ}$ . The cable force sensors deliver the actual cable force  $\mathbf{f}_w$  measured in the winch-integrated cable force sensors, which is corrected by the pulley friction compensation (section 3.7) and yields  $\mathbf{f}$ . To obtain the actual wrench  $\mathbf{w}$ , the actual cable forces are projected to the operational space

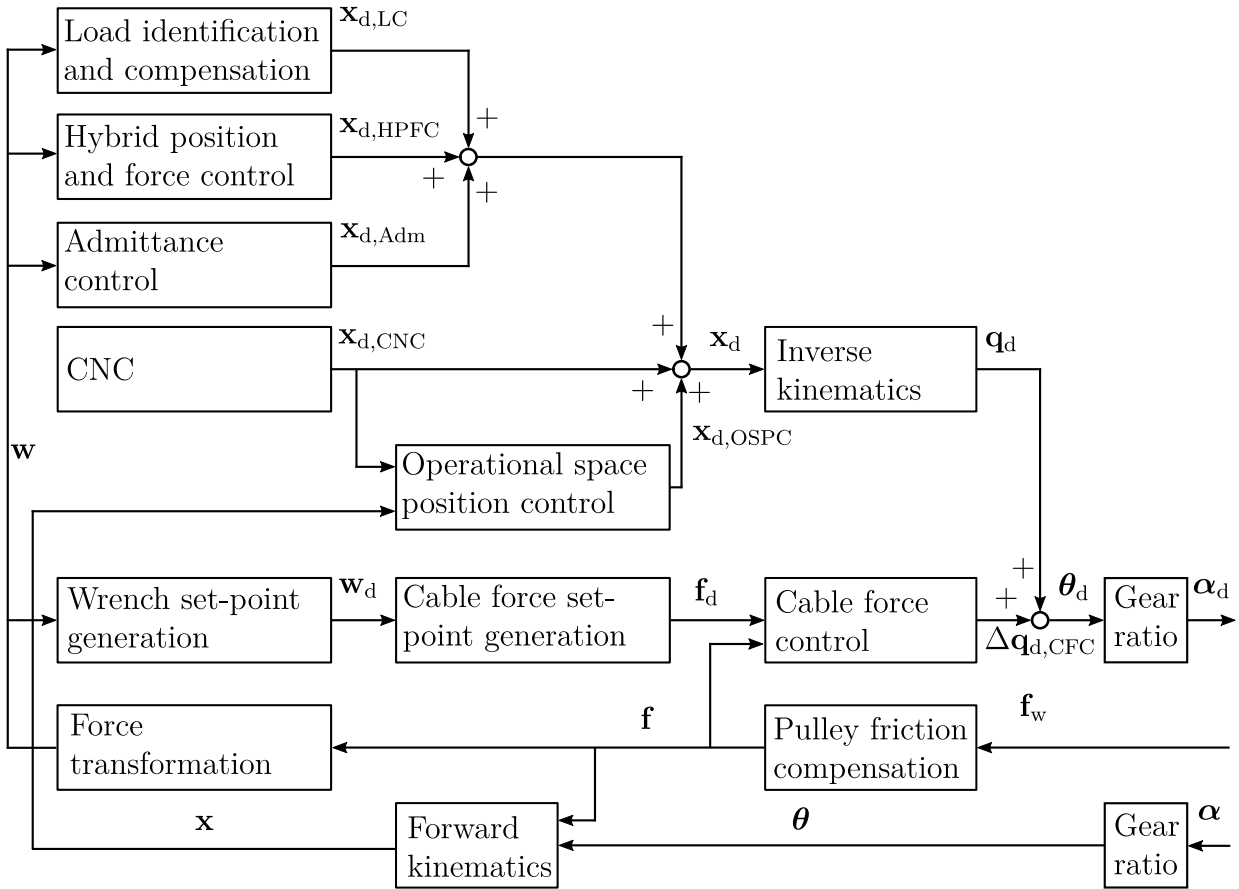


Figure 3.4: Control approach incorporating joint space cable force control, operational space position control and operational space force controller

by the force transformation using the structure matrix. The actual wrench is incorporated in the operational space controller and the wrench set-point generation.

From the drive encoder, the actual cable length  $\theta$  is obtained, for which under consideration of the actual cable forces the forward kinematics estimates the actual position of the platform  $\mathbf{x}$ . The operational space position control outputs a change in the operational space position  $\mathbf{x}_{d,OSPC}$ . In the wrench set-point generation module, based on the actual wrench and the inverse dynamics, the wrench for the cable force distribution  $\mathbf{w}_d$  is prepared. Next, the cable force distribution  $\mathbf{f}_d$  is calculated by solving the structure equation for the desired position  $\mathbf{x}_d$  and desired wrench  $\mathbf{w}_d$ . The cable forces are controlled within the cable force controller, which gives the desired change of cable lengths  $\Delta \mathbf{q}_{d,CFC}$ . With the gear ratio, the desired cable length  $\theta_d$  is transformed to the motor angles  $\alpha_d$ , which is then further processed in the distributed position controllers.

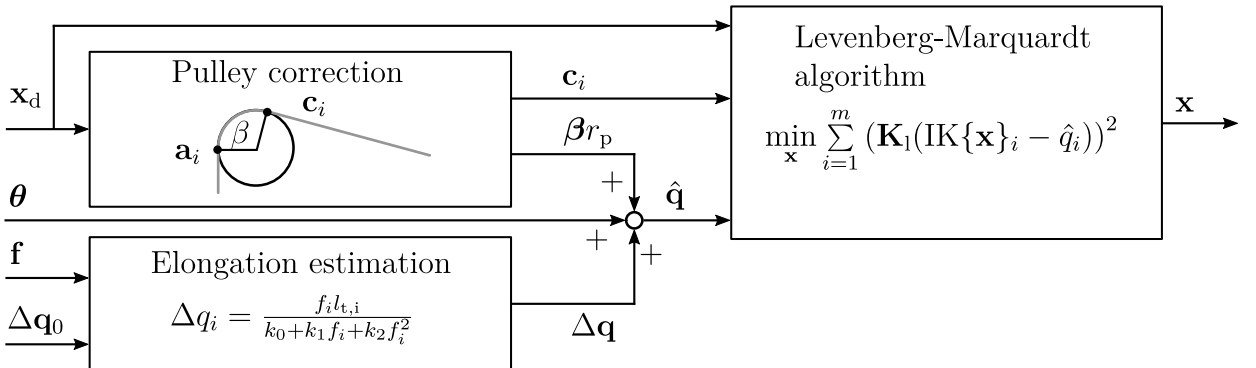


Figure 3.5: Proposed implementation of the forward kinematics taking into account pulley kinematics and elongation estimation with non-linear cable stiffness

## 3.2 Forward Kinematics with non-linear Cable Stiffness

For operational space position control, the actual position of the platform is derived based on the joint space variables. Thus, the position accuracy, which can be reached with operational space position control, depends on the model applied for the forward kinematics. Incorporating the forward kinematics in a force controlled robot increases the requirements for the algorithm: due to the cable force controller, the solution space of the inverse kinematics is left and the inverse kinematics can not be easily inverted. As the resulting pose is used to establish the control error, continuity of the forward kinematics solution is necessary. As reviewed in section 2.1.4, the actual implementations do not consider the actual cable force which gives an information about the actual cable elongation. At this point, the forward kinematics is further developed.

In the following, the implementation of the forward kinematics which takes into account the non-linear cable stiffness and a simplification of the pulley kinematics for saving computational runtime is described and visualized in Fig. 3.5.

In each iteration of the Levenberg-Marquardt algorithm, the inverse kinematics is solved for the actual guess of the platform pose and based on the actual cable length received from the encoder, the cable elongation  $\Delta\mathbf{q} = \text{IK}\{\mathbf{x}\} - \boldsymbol{\theta}$  is derived. Thus, a positive value for  $\Delta\mathbf{q}$  stands for a cable under tension. For the incorporation of the stiffness model, the objective function can now be either formulated in cable forces or cable lengths. For the formulation with forces, the elongation  $\Delta\mathbf{q}$  has to be transformed to a cable force. For this, one has to solve the polynomial equation of second order (2.17) for  $\mathbf{f}$ . This equation has to be evaluated in every iteration step of the Levenberg-Marquardt algorithm and is also considered in the Jacobian matrix of the objective function. Thus, the computational runtime is quite high.

The formulation in cable length is more convenient, as the estimated elongation is determined initially for the measured cable force. Based on the cable length derived from the encoder  $\theta$ , the untensioned length  $\hat{\mathbf{q}}$  is estimated by  $\hat{\mathbf{q}} = \theta + \Delta\mathbf{q} - \Delta\mathbf{q}_0$ . The initial elongation  $\Delta\mathbf{q}_0$  is determined at the startup of the controller for the cable force and the actual elongation  $\Delta\mathbf{q}$  is obtained from the stiffness model (2.17) for the actual cable force  $\mathbf{f}$  and reads

$$\Delta q_i = \frac{f_i l_{t,i}}{k_0 + k_1 f_i + k_2 f_i^2} \quad \text{for } i = 1, \dots, m , \quad (3.7)$$

which has to be evaluated only once in the initialization of the forward kinematics implementation.

For representing the different cable stiffness, the objective function (2.34) is expanded by weighting the cable length error with the actual cable stiffness matrix  $\mathbf{K}_l$  according to (2.15) using the non-linear cable model and reads

$$\Psi_{JS,NL}(\hat{\mathbf{q}}, \mathbf{x}) = \mathbf{K}_l(\text{IK}\{\mathbf{x}\} - \hat{\mathbf{q}}) , \quad (3.8)$$

where  $\text{IK}\{\mathbf{x}\}$  is the solution of the inverse kinematics for the actual estimated pose in each iteration step. The optimization problem follows to

$$\phi_{JS,NL}(\hat{\mathbf{q}}) = \min_{\mathbf{x}} \sum_{i=1}^m \Psi_{JS,NL,i}^2(\hat{\mathbf{q}}, \mathbf{x}) . \quad (3.9)$$

Due to the iterative solution of the optimization problem, computational runtime may be an issue. Therefore, the objective function should be formulated as simple as possible. Using the objective function which is based on the inverse kinematics taking into account the pulley kinematics, the computational runtime rises by approximately 30% compared to the model assuming a constant anchor point of the cable  $\mathbf{a}_i$ . This is also reflected by the source code of the objective function and the analytical Jacobian matrix, which has three time more lines of codes than the proposed solution.

For improving the computational runtime of the forward kinematics incorporating the effects of swivelling pulley, the following simplification is proposed. As starting value of the optimization algorithm for forward kinematics the desired platform position  $\mathbf{x}_d$  is used. Assuming that the control error  $\mathbf{e}_x$  is small, it follows that the wrapping angle  $\beta$  and the point  $C_i$ , where the cable leaves the pulley, will only marginally change during the Levenberg-Marquardt optimization and can be assumed as constant. Thus, the vector  $\mathbf{c}_i$ , which denotes the point where the cable leaves the pulley, can be initially computed. Using  $\mathbf{c}_i$  instead  $\mathbf{a}_i$  and subtracting the cable length wound around the pulley  $\beta r_p$  from the actual cable length, the forward kinematics for the standard model can be solved. With this simplification, the inverse kinematics with the influence of the pulleys has to be evaluated only once instead in each iteration step of the Levenberg-Marquardt algorithm. Thus, the

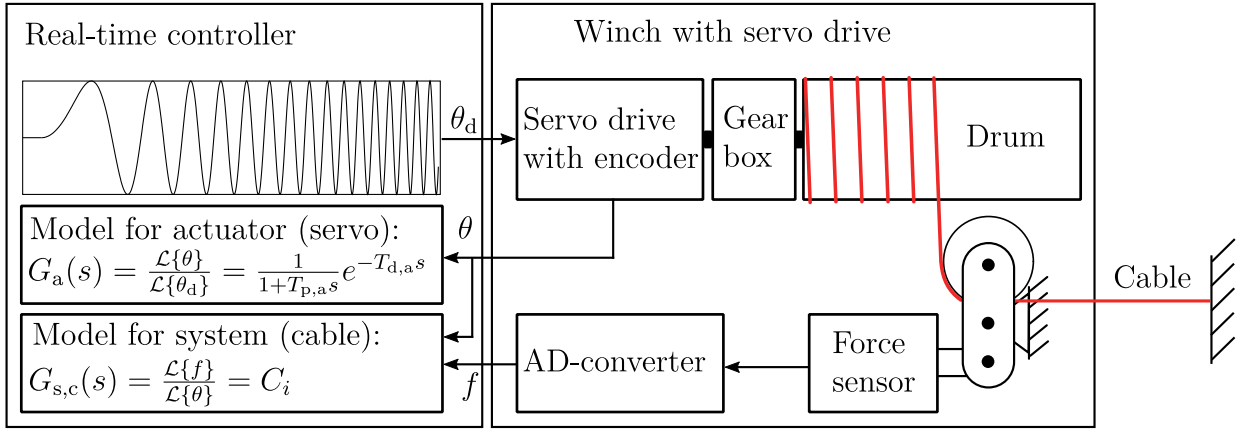


Figure 3.6: Experimental system identification of the transfer function of the actuator  $G_a(s)$  and one cable  $G_{s,c}(s)$  using a sinus sweep applied on a winch, where the cable end is fixed to the steel frame

computational runtime of the simple model neglecting the pulleys can be regained. Next, the models for the control plant are identified.

### 3.3 Modelling and System Identification

For the controller synthesis, the dynamics of the control plant described in form of transfer functions is of interest. For the CFC, models for the actuator and the cables are identified. The platform's dynamics is investigated for the synthesis of the OSPC. The identification is described exemplary for the IPAnema 3 robot.

#### 3.3.1 Dynamics of the Actuator Unit

In the first step, the dynamic behaviour of one winch including decentralized position controller, drive, cable and force measurement is investigated. This allows for identifying the parameters of a transfer function for the actuator  $G_a(s)$  and the system  $G_{s,c}(s)$ .

For system identification, the cable of a single winch is connected to a fixed point at the steel frame. The structure of the identified system is shown in Fig. 3.6. A sinusoidal oscillation with rising frequency from 0.5 to 17.0 Hz for the cable length  $\theta_d$  is generated in the PLC and commanded via the fieldbus to the servo amplifier. Using the cascaded position controller, the drive follows the desired trajectory. The relation between the desired position and the actual cable length  $\theta$  obtained from the motor encoder allows for the identification of the actuator's dynamics, which is represented by the transfer function  $G_a(s)$ .

The following behaviour of the drive during the sinus sweep with an amplitude of 5.0 mm is presented in Fig. 3.8. The diagram reveals a good tracking behaviour of the drive even up to a frequency of 17 Hz. The maximum error occurs at about 8 Hz, where the actual

amplitude is 1.14% below the set-point amplitude. This corresponds to a damping of -0.1 dB. As the amplitude rises again with higher frequency, this is a hint for a dynamic system with at least two poles. Actually, the poles lie outside the investigated frequencies and it is not possible to extrapolate the poles of the dynamic system in a reliable manner. A low-pass filter behaviour of the servo drive seems to be an adequate estimation, which leads to a damping at frequencies higher than applied in this experiment. Thus, the dynamic behaviour of the drive is modelled as a low-pass filter of 1<sup>st</sup> order ( $PT_1$ ) including a transfer delay  $T_{d,a}$ , which reads

$$G_a(s) = \frac{1}{1 + T_{1,a}s} e^{-T_{d,a}s} , \quad (3.10)$$

where the transfer delay arises from the time needed for communication between the PLC and the drives. The parameter identification of the transfer function is done with the Matlab System Identification Toolbox. The resulting parameters are listed in Table 3.1.

The Bode diagram for the actuator is shown in Fig. 3.7. The phase curve is plotted for the complete system  $G_a(s)$  and is, furthermore, divided into the system dynamics

$$G_{a,1}(s) = \frac{1}{1 + T_{1,a}s} , \quad (3.11)$$

and the influence of the transfer delay

$$G_{a,2}(s) = e^{-T_{d,a}s} . \quad (3.12)$$

The phase curve reveals a decay due to the dead time of 6.3 ms. The contribution of the remaining system dynamics is relatively small.

The transfer function of the system corresponds to the cable dynamics. Cable vibrations are not considered in this thesis. A further analysis showed that there is no time delay between the actual cable length  $\theta$  and the cable force  $f$ . This means that the signal travel time from the motor encoder to the PLC equals the time of the force signal including the AD-conversion. Thus, a static model incorporating the cable stiffness  $C_i$  as gain factor is applied and the simplified transfer function of the cable reads

$$G_{s,c}(s) = C_i . \quad (3.13)$$

Hereby, the identification of the actuator's dynamics is complete and next, the platform's dynamics is studied.

### 3.3.2 Platform's Dynamics

From the equation of motion (2.30) follows that the platform's dynamics is pose-dependent and influenced by the actual platform mass. For the dynamic model of the platform, the

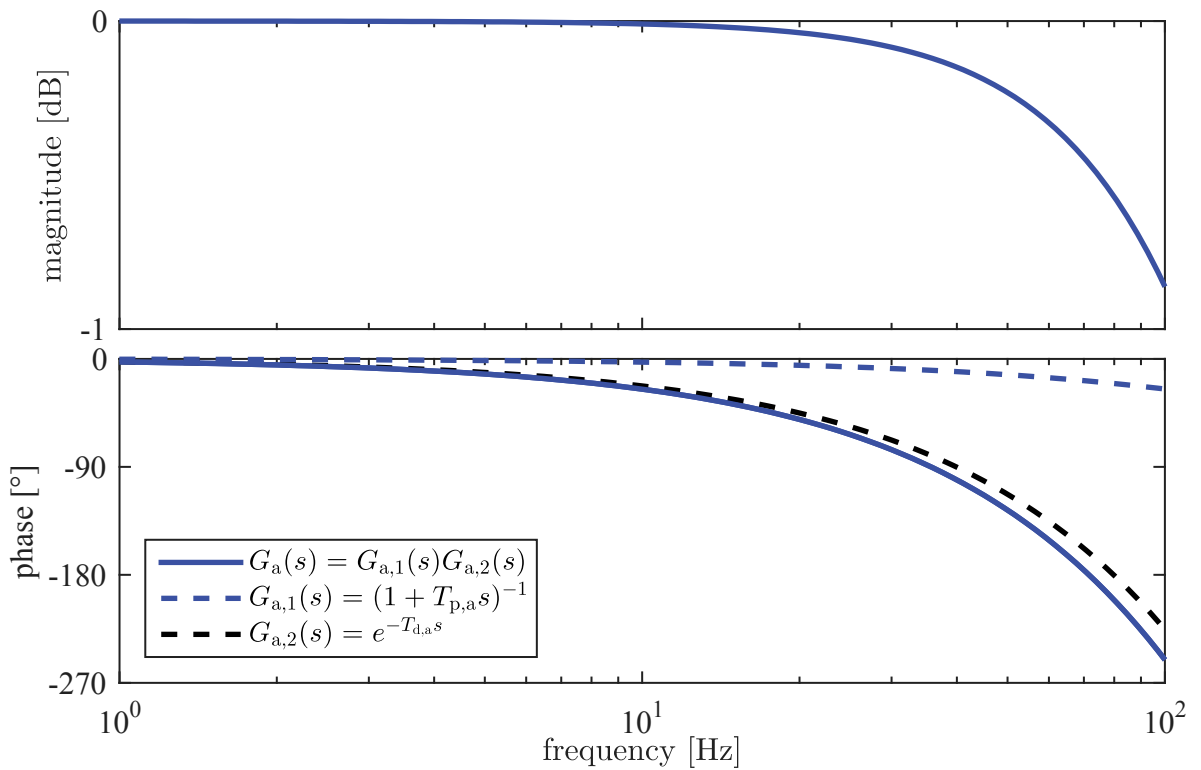


Figure 3.7: Bode diagram of the servo drive with transfer function  $G_a(s)$  including the communication between PLC and the drive

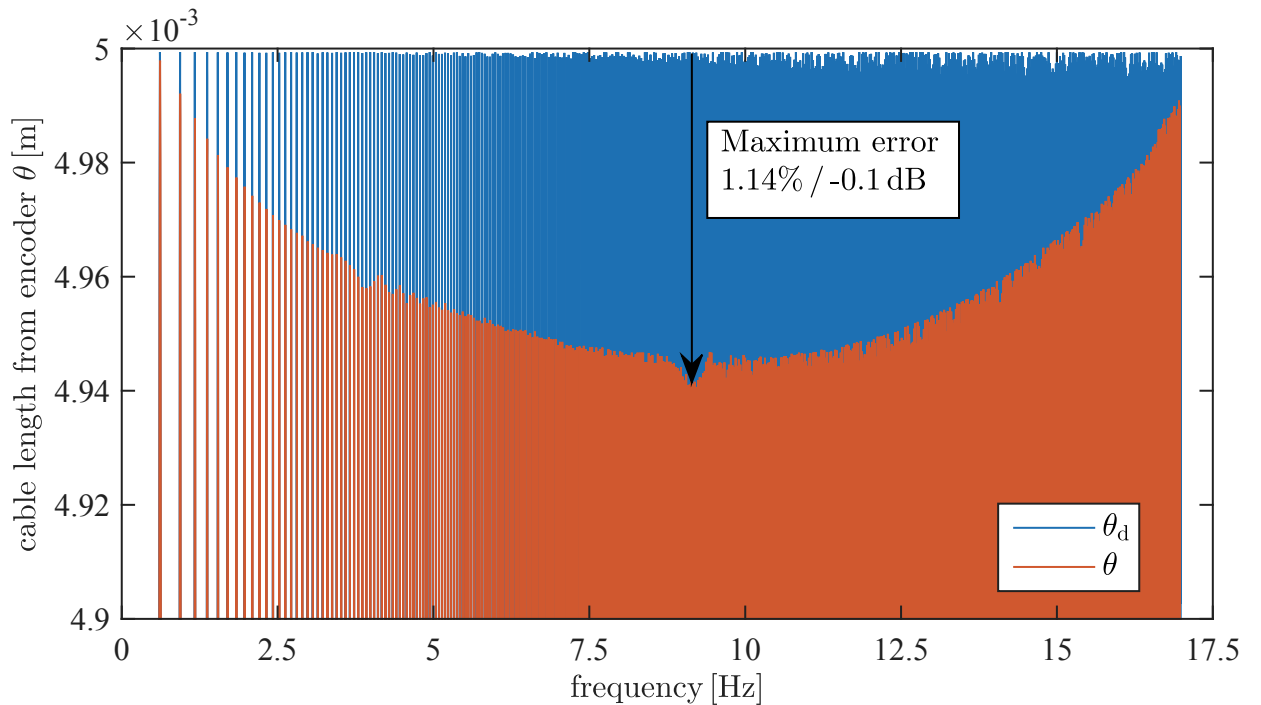


Figure 3.8: Course of the winch movement  $\theta$  during a sinus sweep with an amplitude of 5 mm: the drive reveals a good set-point tracking

equation of motion is transformed to the frequency domain. For simplification, only the diagonal elements of the stiffness matrix  $\mathbf{K}_x$  are considered and the non-diagonal elements are neglected. Furthermore, it is assumed that the centre of gravity lies in the origin of the platform and, thus,  $\mathbf{c}_{m_p} = 0$  holds. With this assumption, the robot platform can be considered as six decoupled spring-mass-damper systems and, therefore, the platform dynamics can be formulated independently for every DOF. The analysis of the servo drive showed a good following behaviour of the drive and, therefore, it is an appropriate approximation that  $\theta = \theta_d$  holds. The desired motor position itself relies on the inverse kinematics solution. The right term of the equation of motion (2.30) reads  $\mathbf{A}^T(\mathbf{x})\mathbf{K}_l(\mathbf{q} - \boldsymbol{\theta})$ , where  $\mathbf{q} = \text{IK}\{\mathbf{x}\}$  and  $\boldsymbol{\theta} = \boldsymbol{\theta}_d = \text{IK}\{\mathbf{x}_d\}$  hold, as no cable force control is applied. Thus, the equation of motion is established w.r.t. the actual and desired platform position. This leads to the simplified equation of motion with the actual platform position in one axis  $x_j$  and the desired platform position  $x_{d,j}$  for  $j \in \{x, y, z, \varphi_x, \varphi_y, \varphi_z\}$  and reads as

$$m_j \ddot{x}_j + d_j \dot{x}_j + c_j x_j = c_j x_{d,j} \quad , \quad (3.14)$$

where  $m_j$ ,  $d_j$  and  $c_j$  are the  $j^{\text{th}}$  diagonal elements of the generalized mass matrix  $\mathbf{M}$ , damping matrix  $\mathbf{D}$  and stiffness matrix  $\mathbf{K}_x$ , respectively. The Laplace transformation of this differential equation gives the transfer function of the platform  $G_{s,p,j}(s)$  and reads

$$G_{s,p,j}(s) = \frac{\mathcal{L}\{x_j(t)\}}{\mathcal{L}\{x_{d,j}(t)\}} = \frac{c_j}{m_j s^2 + d_j s + c_j} \quad . \quad (3.15)$$

For illustration of the dynamic behaviour of the platform, a numerical example for the IPAnema3 in  $z$ -axis (vertical direction) is conducted. The platform is located in the centre of the workspace at the position  $\mathbf{r} = [0.0 \ 0.0 \ 0.5]^T \text{m}$ . The platform mass  $m_p$  amounts to 25 kg and to 105 kg with an additional payload. Assuming a completely linear stiffness behaviour, the stiffness in the three translational DOF amounts to  $c_{j=\{x,y,z\}} = \{159,290, 317,918, 28,500\} \text{ N/m}$ . Measuring the amplitudes of the platform during an identification experiment with the laser tracker delivered that the damping  $d_j$  can be estimated by 83.3 Ns/m. The Bode plots for this example are presented in Fig. 3.9. As can be seen in the Bode plots, the dynamics differs strongly between the DOF due to the inhomogeneous stiffness. Simultaneously, the platform mass has a strong influence on the dynamics in all DOF. For the determination of the control parameters, the lowest dynamic is taken as basis.

With the established models, next, the controller synthesis and stability analysis can be carried out.

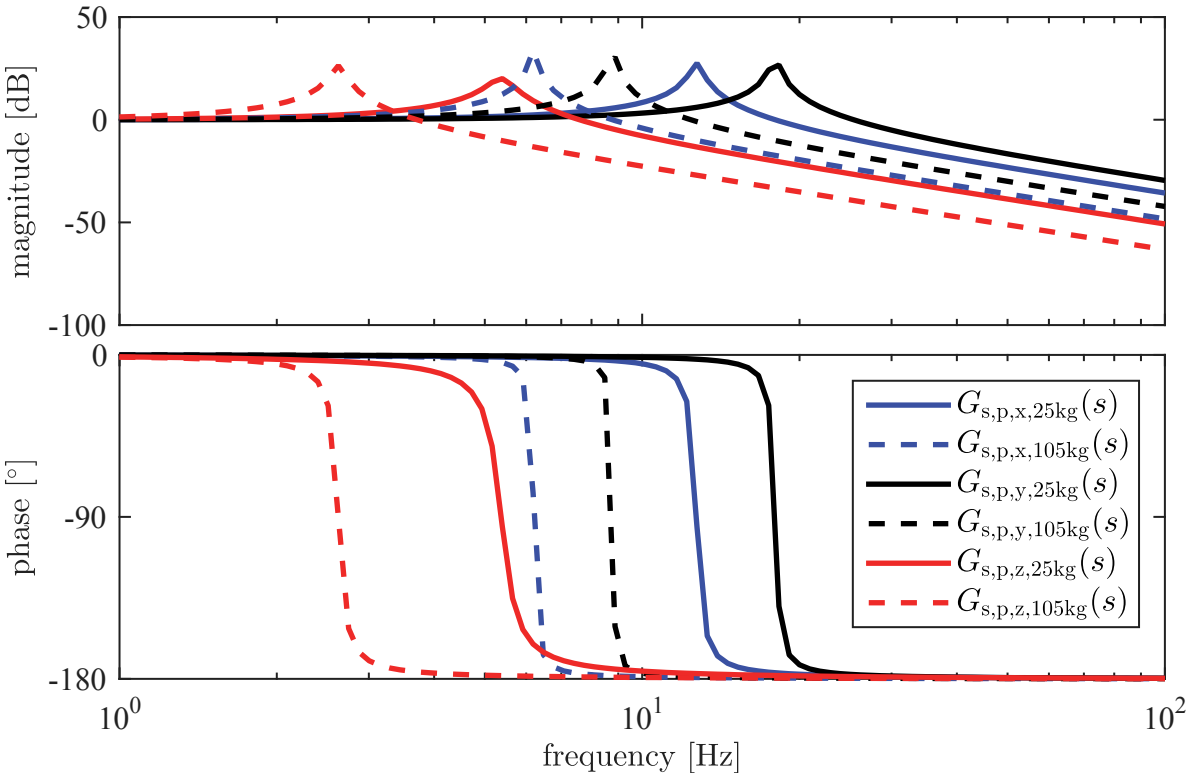


Figure 3.9: Bode diagram of the minimal and maximal dynamic of the platform for the three translational DOF derived from the numerical example

### 3.4 Controller Synthesis and Stability Analysis

With the transfer function derived from the system identification, next, the controller synthesis and stability analysis is carried out. The stability analysis is conducted for the open-loop transfer function according to the Nyquist diagrams. On that base, the stability reserves of the controller is discussed.

Table 3.1: Identified parameters and control parameters for OSPC and CFC

parameter	definition	value	unit
$K_{p,CFC}$	proportional gain	0.85	-
$T_{i,CFC}$	integrator reset time	0.1	s
$K_{p,OSPC,z}$	proportional gain in $z$ -axis	0.07	-
$T_{i,OSPC,z}$	integrator reset time in $z$ -axis	0.18	s
$T_{1,a}$	PT <sub>1</sub> time constant of the actuator	0.000745	s
$T_{d,a}$	dead time of the actuator	0.0215	s
$T_{1,r}$	PT <sub>1</sub> time constant of the cable force filter	0.08	s

### 3.4.1 Controller Synthesis for Operational Space Position Control

Based on the forward kinematics, the operational space position control is developed. The control error  $\mathbf{e}_x$  is established by (3.5). The control plant of the OSPC includes the actuator's and the platform's dynamics. Using the position interface of the drives, the control plant with the input signal  $\mathbf{x}_{d,\text{OSPC}}$  has no integral behaviour itself. Thus, the controller needs integral action to reach static accuracy in the control loop. Therefore, a proportional-integral (PI) controller for both cable force and operational space position control is applied. The transfer function of the PI-controller reads

$$G_{c,\text{OSPC}}(s) = \frac{\mathcal{L}\{x_{d,\text{OSPC}}(t)\}}{\mathcal{L}\{e_x(t)\}} = K_{p,\text{OSPC}} \left( 1 + \frac{1}{T_{i,\text{OSPC}} s} \right) , \quad (3.16)$$

where  $K_{p,\text{OSPC}}$  is the gain and  $T_{i,\text{OSPC}}$  the integrator reset time. For stability analysis, the open-loop transfer function  $G_{\text{OSPC},0}(s)$  of the operational space position control is analysed, which reads

$$G_{\text{OSPC},0}(s) = G_{c,\text{OSPC}}(s) G_a(s) G_{s,p}(s) . \quad (3.17)$$

The dead time in the transfer function  $G_a(s)$  described in (3.10) leads to a transcendental transfer function, which cannot be handled by control design algorithms. Therefore, the transfer delay  $T_{d,a}$  is transformed to an all-pass filter with a Padé approximation

$$e^{-T_{d,a}s} \approx \tilde{G}_{a,2}(s) = \frac{1 - \frac{T_{d,a}s}{2} + \frac{(T_{d,a}s)^2}{12}}{1 + \frac{T_{d,a}s}{2} + \frac{(T_{d,a}s)^2}{12}} \quad (3.18)$$

of second order and the transfer function  $\tilde{G}_a(s) \approx G_{a,1}(s) \tilde{G}_{a,2}(s)$  is established.

The system identification confirms that the platform dynamics is position-dependent and changes with the payload. In special configurations, this may lead to a different behaviour or even to instabilities of the control loop, what can be analysed by the stability margins. For this reason, the controller has to be parametrized conservatively. Exemplary for a configuration with low and high dynamic, the Nyquist diagram of the open-loop transfer function  $G_{\text{OSPC},0,z}(s)$  is presented in Fig. 3.10 for  $m_p=25\text{ kg}$  and  $105\text{ kg}$  in the direction of the  $z$ -axis. Without load, the phase reserves are relatively high with a phase margin higher than  $90^\circ$  and gain margin higher than  $10\text{ dB}$ . For the given numerical example, under application of the payload, the phase margin amounts only to  $17.7^\circ$ , which may lead to instabilities.

The evaluation shows that the control loops are stable in both cases but, obviously, with the additional payload the stability reserves are smaller. This finding is also of practical interest when tuning the control value experimentally. The tuning of the controller has to be done in the configuration with the lowest platform's dynamics, which is characterized by the combination of low stiffness and high payload. As the platform's dynamics differs

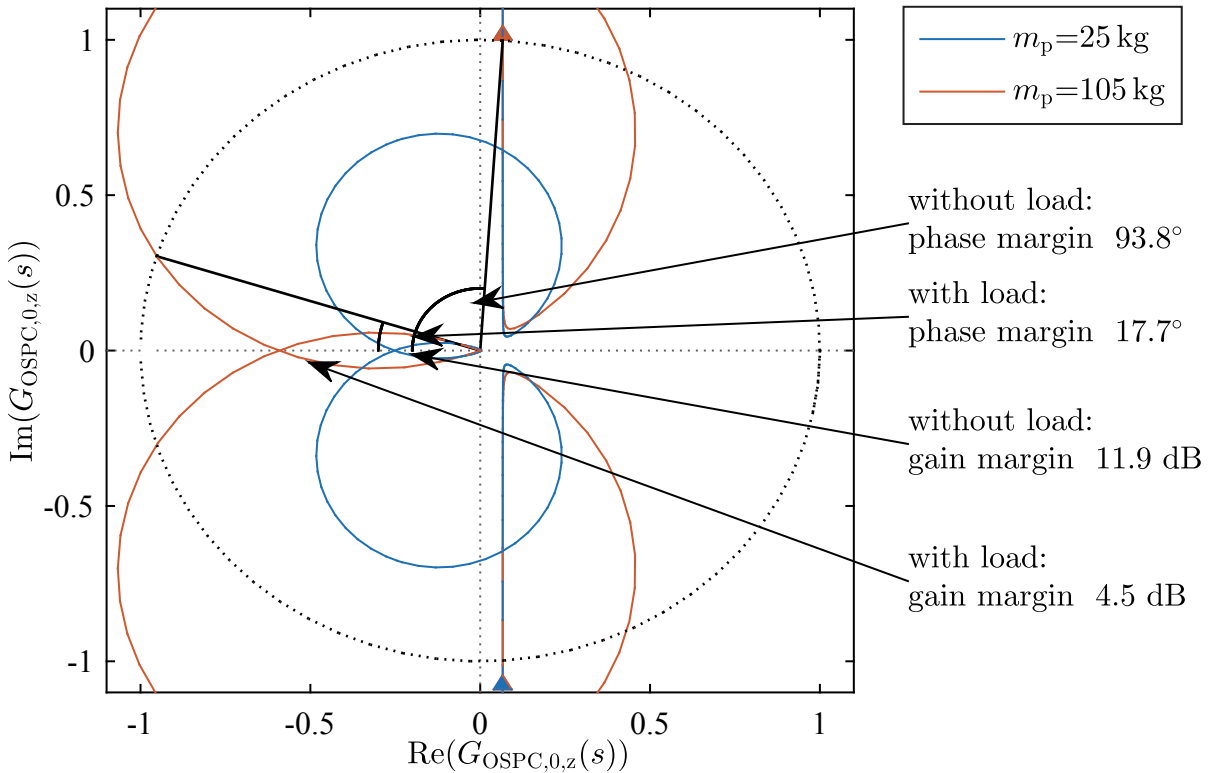


Figure 3.10: Nyquist diagram of the open-loop transfer function  $G_{\text{OSPC},0,z}(s)$  for different payloads

strongly for the DOF, individual control parameters for each DOF are reasonable. In the next section, the controller synthesis of the cable force controller is described.

### 3.4.2 Controller Synthesis for Joint Space Cable Force Control

The control plant of the cable force controller includes the dynamics of the winch, cables and filter for the cable force measurement. Parallel to the OSPC, the plant has no integral action and, thus, a PI controller  $G_{c,CFC}(s)$  is applied. The transfer function of the controller reads

$$G_{c,CFC}(s) = \frac{\mathcal{L}\{\Delta q_{d,CFC}(t)\}}{\mathcal{L}\{e_f(t)\}} = K_{p,CFC} \left( 1 + \frac{1}{T_{i,CFC}s} \right) , \quad (3.19)$$

with the gain  $K_{p,CFC}$  and integrator reset time  $T_{i,CFC}$ . In the feedback loop  $G_{r,c}(s)$ , a PT<sub>1</sub>-filter

$$G_{r,c}(s) = \frac{1}{1 + T_{1,c}s} \quad (3.20)$$

with time constant  $T_{1,c}$  is introduced to reduce the influence of sensor noise.

The stability of the controller can now be evaluated with the open-loop transfer function  $G_{CFC,0}(s)$

$$G_{CFC,0}(s) = G_{c,CFC}(s)G_a(s)G_{s,c}(s)G_{r,c}(s) , \quad (3.21)$$

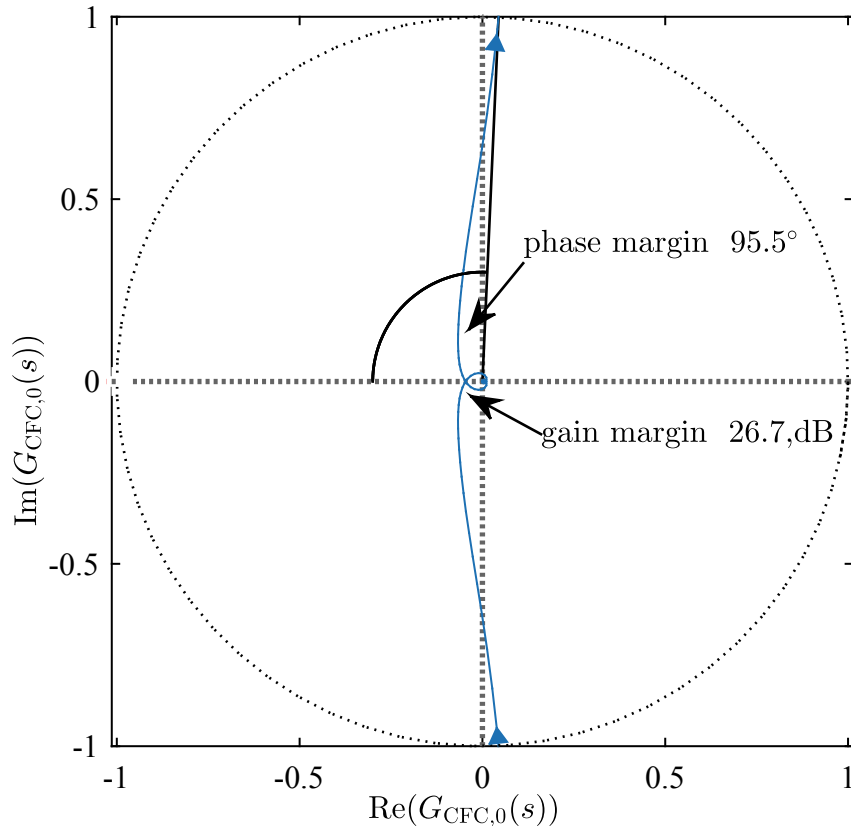


Figure 3.11: Nyquist diagram for the open-loop transfer function  $G_{\text{CFC},0}(s)$

which is visualized as Nyquist diagram with the stability margins in Fig. 3.11. The controller is parametrized regarding a high stability with conservative gain and phase margins of 26.7 dB and  $95.5^\circ$ , respectively. The conservative parametrization is necessary, on the one hand, to avoid oscillations due to the possible interactions of the individual controllers and, on the other hand, to deal with the neglected progressive spring characteristic of the cables.

With the completion of the controller synthesis, the controllers can be incorporated in the control architecture. For the realization of the controllers, several subsystems have to be developed. In the following, the implementations of the OSPC and CFC including the set-point generation are presented.

## 3.5 Controller Implementation

### 3.5.1 Operational Space Position Control

The implementation of the operational space position control is straightforward. The position set-point is derived from the CNC and for the derivation of the actual position the forward kinematics is used. For each DOF, an individual PI controller is implemented according to (3.16). To avoid excessive control signals, the controller output is limited by a

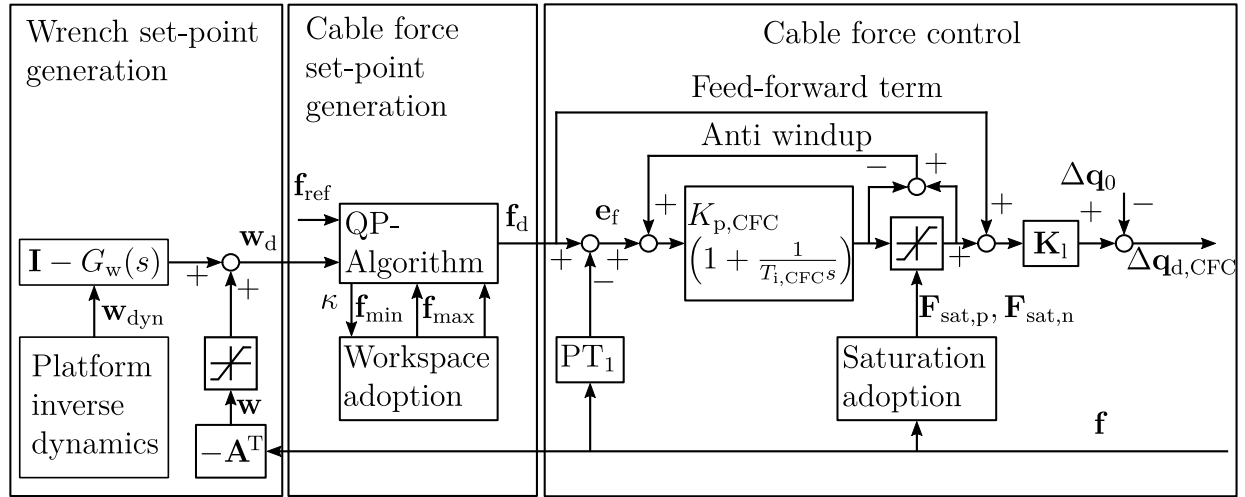


Figure 3.12: Control structure of the joint space cable force controller with set-point generation for wrench  $\mathbf{w}_d$  and cable forces  $\mathbf{f}_d$

saturation. An anti-windup is implemented to restrict the integral part of the controller. The controller output is transformed to joint space using the inverse kinematics.

In the following, the implementation of the joint space cable force control is described, which is significantly more extensive and includes the algorithms for the evaluation of the cable force distribution.

### 3.5.2 Cable Force Control

The cable force controller consists of the set-point generation for the desired wrench  $\mathbf{w}_d$  and, subsequently, for the desired cable force distribution  $\mathbf{f}_d$ . In the following, the closed-loop cable force controller itself is described as depicted in Fig. 3.12.

For joint space cable force control, a model-based feed-forward control and a PI control with anti-windup for each cable is applied. The gains of the controller are adapted with the actual cable stiffness matrix  $\mathbf{K}_l$  to account for the changing cable length. Hereby, the linear cable model is applied and the non-linearities are considered as model inaccuracies. The idea of the feed-forward term is to tension the cable according to the stiffness model neglecting the feedback value. This allows for fast adoption to changing set-point values and improves the system response and stability. The feed-forward control term  $\mathbf{f}_{ff}$  is determined by

$$\mathbf{f}_{ff} = \mathbf{f}_d \quad (3.22)$$

and is directly added to the controller output  $\mathbf{f}_{c,out}$ .

To limit the influence of the cable force controller on the desired cable length to reasonable values, the maximum output is limited by negative and positive saturation limits  $\mathbf{F}_{sat,n}$  and  $\mathbf{F}_{sat,p}$ , respectively. When the controller is in saturation, further integration of the error

within the PI controller is prohibited by an anti-windup. During saturation, the cable forces may exceed the predefined cable force limits due to model inaccuracies. To avoid exceeding cable forces, the saturation limit is increased, when the force of a cable is near the force limit. At low cable forces, the cable probably sags. This can lead to winding errors on the drum, decreased operational space stiffness and uncontrollable own movements of the platform. As the effective stiffness of a sagging cable is significantly smaller than that of a tensed cable, the output of the cable force controller has to be higher. Cable forces exceeding the maximum cable force can lead to damages of the mechanics and should, therefore, be avoided. Thus, also for high cable forces the saturation limits are increased.

In the initial configuration of the robot, the cables are already under tension to stabilize the platform. The pre-tension can be interpreted as an initial offset in cable length  $\Delta\mathbf{q}_0$ . This pre-tension has to be taken into account in the feed-forward formulation and is, thus, subtracted at the output of the controller. The controller output  $\mathbf{f}_{c,out}$ , which consists of the PI controller with saturation and the feed-forward term, is transformed with the stiffness estimation (2.15) of the cables by

$$\Delta\mathbf{q}_{d,CFC} = \mathbf{K}_l^{-1}(l_t)\mathbf{f}_{c,out} - \Delta\mathbf{q}_0 \quad (3.23)$$

into the change in cable length  $\Delta\mathbf{q}_{d,CFC}$ .

The implementation of the closed-loop controllers is hereby finished and in the next section, the generation of the desired cable force distribution is described.

## 3.6 Cable Force Algorithm

The cable force algorithm aims to calculate a cable force distribution which is used as set-point in the cable force control. Consequently, the algorithm has to be real-time capable and must deliver a continuous solution for the cable forces. Within the cable force algorithm, one has the opportunity to adjust the internal tension of the cables. For this purpose, the extension of the quadratic programming is proposed and a comparison to existing approaches is carried out. For the derivation of the desired cable force distribution, at first, the desired wrench is established and next, the cable forces are calculated.

### 3.6.1 Wrench Set-Point Generation

Using the null-space control, a special focus lies on the determination of the wrench. The decoupling of the cable force control from the image-space can be realized by using the measured wrench for the calculation of the cable force set-point. Actually, the measured wrench is disturbed for several reasons: the structure matrix  $\tilde{\mathbf{A}}^T$  contains uncertainties, as on the one hand, the geometrical parameters  $\mathbf{a}_i$  and  $\mathbf{b}_i$  can only be determined with a limited

accuracy and, on the other hand, the position of the platform contains errors. Furthermore, errors in the cable force measurement  $\tilde{\mathbf{f}}$  disturb the wrench. Under consideration of these disturbances, (2.11) can be reformulated as

$$\mathbf{w}_{\text{nom}} + \mathbf{w}_{\text{dist}} = \tilde{\mathbf{w}} = -\tilde{\mathbf{A}}^T \tilde{\mathbf{f}} , \quad (3.24)$$

where the disturbances are summarized in  $\mathbf{w}_{\text{dist}}$ . The nominal wrench  $\mathbf{w}_{\text{nom}}$  is derived by the inverse dynamics of the platform (2.33) based on the nominal mass  $m_p$  and centre of gravity  $\mathbf{c}_{m_p}$  of the platform. The workspace analysis for a cable robot is typically carried out for a set of wrenches based on the nominal platform parameters for defined accelerations including gravity. Contrary to the workspace analysis, the cable force distribution has to be evaluated for a wrench including disturbances, thus, the desired wrench reads  $\mathbf{w}_d = \mathbf{w}_{\text{nom}} + \mathbf{w}_{\text{dist}}$ . As these errors are included in the cable force set-point generation, the cable force controller does not create external forces. Taking into account these disturbances for the cable force distribution will influence the available workspace. To limit the influence of the disturbed wrench on the cable force distribution, saturations can be applied on the measured wrench with the consequence that the decoupling from the image-space is partly cancelled. This problem will be further discussed in connection with the cable force algorithms in section 3.6.2. Next, the influence of the dynamics is analysed.

In the measured wrench signal  $\mathbf{w}$ , the inertia forces of the platform appear as visualized in Fig. 3.13. Compared to the wrench evaluated with the platform inverse dynamics  $\mathbf{w}_{\text{dyn}}$  with the desired acceleration  $\ddot{\mathbf{x}}_d$ , differences appear. The measured signal reflects some oscillations and a time delay of 10 ms becomes visible. Basically, this means that the cable force controller will try to reproduce the acceleration forces after they are measured by the cable force sensors. In this way, the cable force control adds acceleration forces to the robot, while the acceleration is already undergoing. This may lead to overshoots of the platform after acceleration, as the cable force controller is behind the desired movement.

To solve this problem, the expected acceleration forces derived from the inverse dynamics are combined with the measured forces. The transfer behaviour between the two signals is mainly characterized by a transfer delay  $T_{d,w}$  and the transfer function reads

$$G_w(s) = \frac{\mathcal{L}\{w_j(t)\}}{\mathcal{L}\{w_{d,i}(t)\}} = e^{-T_{d,w}s} . \quad (3.25)$$

For controller dealing with plants with transfer delay, the Smith predictor is a well-known approach. The basic idea is that the transfer function of the system is evaluated for the actual controller output and, in this way, the system behaviour is anticipated (Smith 1959).

The Smith predictor is now adopted on the determination of the desired wrench. The nominal wrench is added under consideration of the system dynamic  $G_w(s)$ . The desired

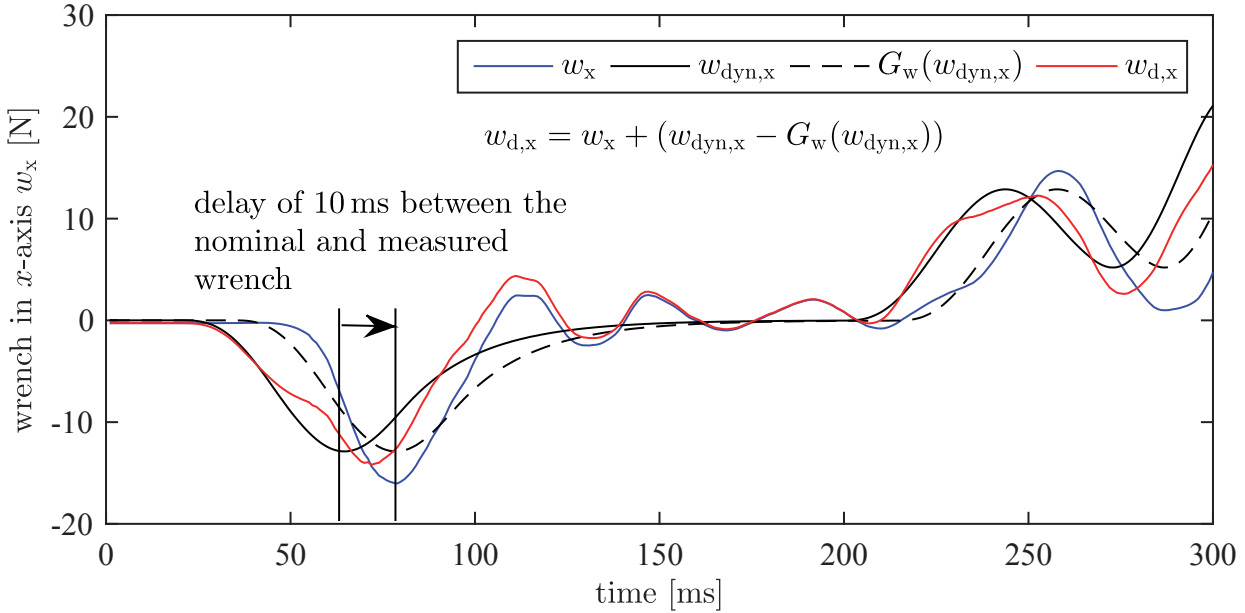


Figure 3.13: Determination of the feed-forward term for the platform dynamics based on the measured and nominal wrench  $\mathbf{w}$  and  $\mathbf{w}_{dyn}$ , respectively

wrench  $\mathbf{w}_d$  is evaluated by

$$\mathbf{w}_d = \mathbf{w} + (\mathbf{I} - G_w(s)) \mathbf{w}_{dyn} \quad , \quad (3.26)$$

which can be also interpreted as a feed-forward term and is visualized in Fig. 3.13. With this approach, the desired wrench anticipates the inertia forces and, thus, the aforementioned lag error can be compensated. In the next step, a feasible cable force distribution is evaluated for the desired wrench.

### 3.6.2 Cable Force Set-Point Generation

The cable force set-point generation aims to deliver a desired cable force distribution  $\mathbf{f}_d$ , which generates the desired wrench  $\mathbf{w}_d$  and fulfils the force limits of the cables. At first, an extension of the well-known quadratic programming (QP) approach which allows for a step-less choice of the tension level is presented. Next, the QP approach is compared to the advanced closed-form and improved puncture method. Finally, the behaviour of the cable force algorithm at transient leaving of the workspace is discussed.

#### Quadratic Programming

The review of the existing cable force algorithms in section 2.2 showed that no algorithm is able to adjust the tension level step-less. Step-less adjustment of the tension levels is desirable to smoothly switch between different tension level to reduce the energy consumption

or to receive high stiffness of the platform. For this, the QP approach is further developed. In the current formulation of the objective function (2.46), the QP algorithm delivers a feasible cable force distribution with the minimal 2-norm error relative to zero. To adjust the tension level, the objective function is now expanded by the reference force  $\mathbf{f}_{\text{ref}}$  and reads

$$\min g(\mathbf{f}) = \frac{1}{2}(\mathbf{f} - \mathbf{f}_{\text{ref}})^T \mathbf{Q}(\mathbf{f} - \mathbf{f}_{\text{ref}}) \quad (3.27)$$

$$\text{with } \mathbf{f}_{\min} \leq \mathbf{f} \leq \mathbf{f}_{\max} \text{ and } \mathbf{A}^T \mathbf{f} = -\mathbf{w} , \quad (3.28)$$

where  $\mathbf{Q}$  is an identity matrix. With the introduction of the reference force, the tension level can be adjusted step-less within the feasible force limits. Both, the force limits and the reference force are represented as  $m$ -dimensional vectors and one can choose individual parameters for each cable. Individual values for the minimal cable force can be applied for incorporating the minimum force, which is needed to avoid excessive cable sagging for the actual pose (Pott 2014b). In robots with different drives, the individual feasible cable force of each winch can be considered in the force distribution problem. With the reference force vector, one can adjust the load sharing between the drives. Reasonable values for the reference force are given by the force limit and, thus,  $f_{\min} \leq f_{\text{ref}} \leq f_{\max}$  holds. In this thesis, equal values for all drives are applied for the force limits and the reference force.

To deal with the concerns about computational runtime, a high efficient implementation of the QP algorithm is used. In (Mattingley and Boyd 2012), an automatic code generation for QP solving complex problems is proposed. The authors claim that the implementation is at least 20 times faster compared to a state of the art implementation. To receive a real-time capable implementation of (3.27), the automatic code generation is applied. Comparing the implementation generated by the automatic code generation with a freely available optimization toolbox (Currie and Wilson 2012) delivered that it is ten times faster solving the cable force distribution for a reference trajectory with  $r=2$ . In Matlab, the mean computational time for one cable force distribution amounted to 0.5 ms, what is half the cycle time of the real-time controller.

For  $m=8$  cables, the QP algorithm is implemented on the real-time controller. With a controller cycle time of 1 ms, the algorithm converges reliable and can, thus, be assumed to be real-time capable. The QP algorithm can basically be applied on a robot with arbitrary degrees-of-redundancy. According to Bruckmann (2010), the computational runtime will rise with  $r$  and, thus, the algorithm may no longer be real-time capable. To receive an estimation of the computational runtime at higher degree-of-redundancy, the QP algorithm is applied on a robot with 12 cables and 6 DOF. A trajectory consisting of 15,000 discrete points was evaluated in simulation for a robot design with 8 and 12 cables. The computational runtime for solving the QP problem for all discrete points amounted in the mean to

2.2 s and 3.0 s for the robot with 8 and 12 cables, respectively. Applying the algorithm for workspace analysis delivers that the computational runtime for the robot with 12 cables is approximately 40% higher than with eight cables. This short study showed that the computational runtime of the QP algorithm rises only by roughly 40% with  $r=6$  compared to  $r=2$ . Thus, it can be expected that the QP algorithm will be also real-time capable for high redundant robots.

### Comparison of Cable Force Algorithms

In the following, the QP algorithm is compared to the algorithms presented in section 2.2 regarding their usability as set-point generator for cable force control. The comparison criteria are the resulting workspace size, smoothness of the solution along a trajectory and resulting tension level.

In the realizable workspace size, the differences between the different algorithms appear as visualized in Fig. 2.7. The set  $\mathcal{W}_{\text{CF}}$  represents the poses for which a feasible cable force distribution can be derived with the CF algorithm and  $\mathcal{W}_{\text{ACF}}$  stands for the advanced closed-form. For the IPAnema cable robot with  $r=2$ , the workspace derived with the closed-form solution amounts only 57.5% of the possible workspace which can be found with advanced closed-form, improved puncture method or QP.

As an infinite number of solutions exists for the cable forces of a redundant robot, the progression of the cable forces along a trajectory can have jumps. Indeed, the solution will fulfil the structure equation but it will lead to large control effort for cable force control or even instabilities. Therefore, the different cable force algorithms are compared regarding the smoothness along a trajectory. According to Verhoeven (2004), cable forces derived by a  $p$ -norm optimization result in a continuous solution along a continuous trajectory, whereas an infinity optimization tends to generate solutions which jump. The CF algorithm uses a 2-norm optimization and, therefore, continuous solutions are expected. The QP and ACF are also based on a 2-norm optimization but, additionally, take the cable force limits into account to find all solutions. To make the smoothness of the different algorithms measurable and comparable, the change rate of the cable force distribution  $\dot{\xi} = \frac{d}{dt}\xi(t)$  along a trajectory is analysed. As characteristic value, the mean absolute change rate  $\xi_M = |\mathbb{E}\dot{\xi}|$  and the root mean square (RMS)  $\xi_{\text{RMS}} = \sqrt{\mathbb{E}\dot{\xi}^T\dot{\xi}}$  are investigated. To reach scalar values, the evaluation is averaged over all eight cables. A jump in the cable force distribution along a trajectory results in a peak in  $\dot{\xi}$ . As the RMS focuses on peaks, it is the more important value. Different characteristics between the workspaces gained with CF and ACF are expected and, thus, the sets  $\mathcal{W}_{\text{CF}}$  and  $\mathcal{W}_{\text{ACF}} \setminus \mathcal{W}_{\text{CF}}$  are evaluated separately.

The evaluation is conducted applying a trajectory which connects all points of the workspace grid of the IPAnema 3 robot underneath each other. The results presented in Table 3.2 show that the QP algorithm has the lowest change rate  $\xi_M$  along the trajectory

Table 3.2: Comparison of the different cable force algorithms along a trajectory which covers the complete workspace regarding tension level and smoothness. The investigated approaches are closed-form (CF), advanced closed-form (ACF), puncture method (PM), improved puncture method (IPM), closed-form energy efficient (CFE) and quadratic programming (QP)

method	workspace set	$\mathcal{O} \mathbf{f}$ [N]	$\xi_M$ [N/ms]	$\xi_{RMS}$ [N/ms]
ACF/CF	$\mathcal{W}_{CF}$	1314.4	0.739	0.537
IPM/PM/CFE	$\mathcal{W}_{CF}$	358.0	0.784	0.299
QP <sub>min</sub>	$\mathcal{W}_{CF}$	320.4	0.477	0.211
QP <sub>med</sub>	$\mathcal{W}_{CF}$	1314.4	0.739	0.537
QP <sub>max</sub>	$\mathcal{W}_{CF}$	1977.6	1.355	0.824
ACF	$\mathcal{W}_{ACF}$	1279.3	0.997	0.588
IPM	$\mathcal{W}_{ACF}$	434.5	1.160	0.396
QP <sub>min</sub>	$\mathcal{W}_{ACF}$	378.8	0.996	0.342
QP <sub>med</sub>	$\mathcal{W}_{ACF}$	1279.3	0.998	0.589
QP <sub>max</sub>	$\mathcal{W}_{ACF}$	1900.8	1.308	0.794
ACF	$\mathcal{W}_{ACF} \setminus \mathcal{W}_{CF}$	1017.8	2.597	1.107
IPM	$\mathcal{W}_{ACF} \setminus \mathcal{W}_{CF}$	1005.0	2.944	1.185
QP <sub>min</sub>	$\mathcal{W}_{ACF} \setminus \mathcal{W}_{CF}$	813.7	2.802	1.330
QP <sub>med</sub>	$\mathcal{W}_{ACF} \setminus \mathcal{W}_{CF}$	1017.9	2.600	1.109
QP <sub>max</sub>	$\mathcal{W}_{ACF} \setminus \mathcal{W}_{CF}$	1329.1	2.456	0.779

and, thereby, the highest smoothness. The comparison also shows that the smoothness  $\xi_{RMS}$  outside the set  $\mathcal{W}_{CF}$  is only half as high. This is clear, due to the fact that the outer part of the workspace  $\mathcal{W}_{ACF} \setminus \mathcal{W}_{CF}$  is exploited using the rank reduction method. In the complete workspace, represented by the set  $\mathcal{W}_{ACF}$ , the QP with minimal forces delivers the cable forces with the highest smoothness. Using the QP algorithm with medium reference force ( $f_{ref} = \frac{1}{2}(f_{min} + f_{max})$ ) delivers almost the same tension level and smoothness as the ACF. One can conclude that in spite of the different solution approaches of QP and ACF they obtain the same result. Thus, the ACF and QP<sub>med</sub> can be equally applied and no differences in the robot behaviour has to be expected.

For illustration of the influence of the reference force  $f_{ref}$  on the tension level, the cable forces are evaluated for a trajectory with the QP and ACF algorithm. The resulting cable forces are visualized in Fig. 3.14. One can see that using the QP algorithm with  $f_{ref} = f_{min}$  (or  $f_{ref} = f_{max}$ ), at least one cable has the minimum (or maximum) force and the average force amounts to 244.0 N (or 2217.9 N). The ACF results in a medium tension level with an average cable force of 1401.6 N. The results show that the internal tension can be strongly influenced with the choice of the reference force.

To investigate the effectiveness of cable force minimization within the workspace, the mean cable force within a grid of discrete points covering the complete workspace is studied. The mean cables forces and the relative difference to the medium tension level calculated

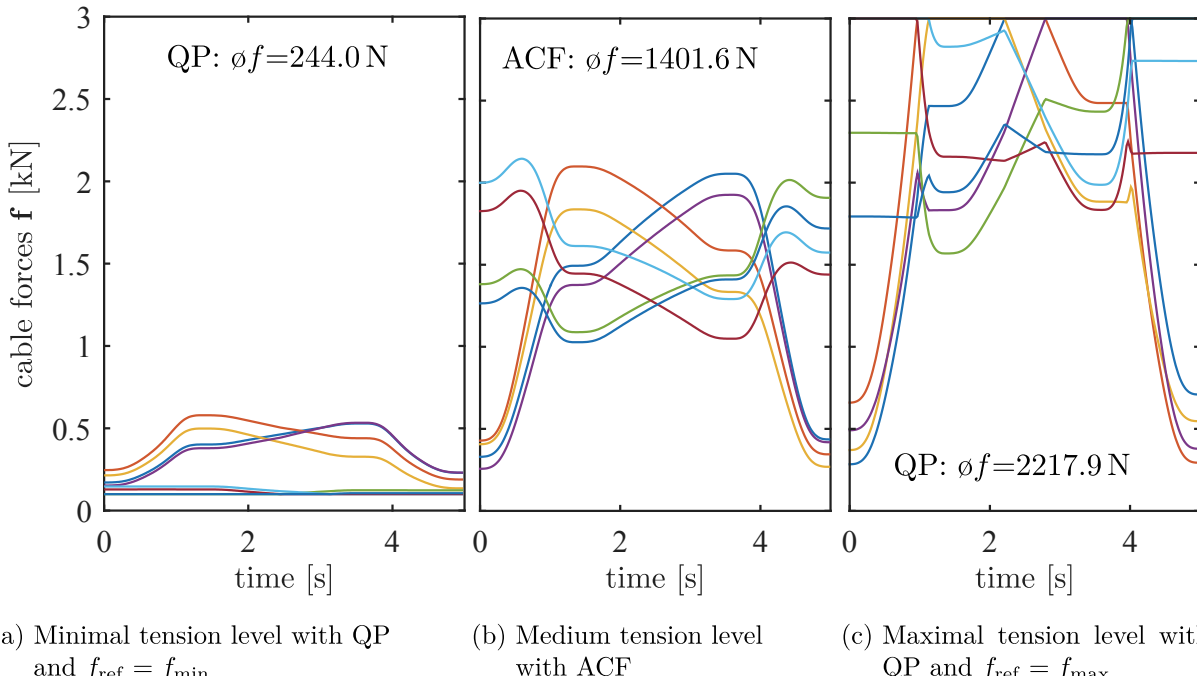


Figure 3.14: Comparison of the resulting cable forces along a trajectory for a cable robot with eight cables,  $m_p = 30 \text{ kg}$ ,  $f_{\min} = 100 \text{ N}$  and  $f_{\max} = 3000 \text{ N}$

Table 3.3: Mean cable forces within the workspace for different payloads

payload $m_p [\text{kg}]$	QP with $f_{\text{ref}} = f_{\min}$		ACF		QP with $f_{\text{ref}} = f_{\max}$	
	force $\bar{\otimes} \mathbf{f}$ [N]	$\Delta$ to ACF [%]	force $\bar{\otimes} \mathbf{f}$ [N]	force $\bar{\otimes} \mathbf{f}$ [N]	$\Delta$ to ACF [%]	
30	487.8	-56.1	1112.1	1536.8	38.2	
50	519.6	-53.8	1125.0	1555.0	38.2	
100	661.1	-43.1	1161.0	1564.9	34.8	
150	754.3	-37.2	1200.1	1574.6	31.2	

with ACF for a set of payloads are presented in Table 3.3. One can see that especially for low payloads the tension level can be decreased strongly by around the half. At higher payloads, the influence of the inhomogeneous part  $\mathbf{f}_{\text{ext}}$  of the force distribution rises, which limits the possible displacement of the tension level within the limited cable forces.

It can be concluded that ACF, IPM and QP cover the complete workspace but the QP algorithm combines the step-less selection of the tension level with the best smoothness. For a medium tension level, which can be desirable for higher stiffness, the ACF and QP can be used with lower smoothness. In this thesis, the QP and ACF algorithms are used as set-point generator covering the complete workspace of a cable robot. In the following, the behaviour of the cable force algorithms, when no feasible solution can be found, is discussed.

## Behaviour at the Workspace Border

As described in section 2.2.1, the workspace of a cable robot can principally be calculated for a given set of wrenches acting on the platform. In the actual controller, the force distribution algorithm has to deal with a wrench which includes model errors and is, therefore, partly unknown as discussed in section 3.6.1. To limit this effect, saturations for the wrench are proposed as a possible solution. Nonetheless, the shape of the workspace is non-trivial and changes with the current payload. Workspace monitoring is foreseen in the current control architecture in form of workspace borders for translational movements, e.g. based on user-defined convex line-strips. Programming the robot without offline simulation of the path may lead to leave the workspace during operation. For this reasons, the cable force controller has to deal with temporary leaving of the workspace. The behaviour of the cable force algorithms, when no feasible solution can be found, differs strongly. The CF algorithm delivers a continuous solution, as the exceeding of the cable limits does not influence the algorithm. Evaluating the ACF algorithm when leaving the workspace leads to very high forces in some cables which cannot be used for control. Using the QP algorithm, the number of iterations strongly increases, and the delivered cable force distribution does not necessarily solve the structure equation.

The nominal value for the maximum cable force is determined according to the torque, which the drive can deliver continuously without overheating. Under consideration of the thermal capacity of the drive, for short time, a multiple of the rated torque can be generated. For example, the maximum torque of the IPAnema 3 drives amounts to the triple of the continuous torque (Bosch Rexroth AG 2010). This property is used in practice, e.g. for acceleration ramps, where additional torque is needed to overcome the inertia of the system.

Under consideration of the overload capacity, the maximum cable force can be temporarily increased to enlarge the workspace. To a limited extent, a feasible force distribution can be found again. Using the QP algorithm, the number of iterations  $\kappa$  is observed, as a high value signals that no solution can be found. When a violation of the cable force limits is detected, the maximum cable force is smoothly increased.

For closed-loop cable force control and the estimation of the cable elongation used in the forward kinematics, the actual cable force is incorporated in the control scheme. The realization of the cable force measurement in the winches arises new questions regarding the influence of pulley friction between the force sensor and the platform, which will be discussed in the next section.

## 3.7 Cable Force Measurement

For cable force control in each cable of the robot, a force measurement is necessary. The force sensors can be integrated either directly at the platform or within the winch. In this section, different measurement principles and calibration procedures are presented. Using winch-integrated cable force sensors, pulley friction disturbs the measurement. For the compensation of this disturbance, a friction model incorporating microscopic and macroscopic friction is proposed.

### 3.7.1 Measurement Principles

For the control, the cable forces acting at the platform are of interest. Thus, it is straightforward to integrate the cable force sensors directly at the attachment point of the cables at the platform as visualized in Fig. 3.15a. On the one hand, as the cable forces are measured directly at the point of interest, the external disturbances on the force measurement are reduced to a minimum. On the other hand, the cable force sensors and their AD-converters are part of the moving platform and there has to be an electric connection to the control PC over the field bus. This may lead to an additional source of damage.

To avoid the cable force sensors on the platform, the sensors can be integrated as measurement units using pulleys (Fig. 3.15b) or integrated in the winch (Fig. 3.15c). The advantages are that the force sensor is covered and protected and the electric wiring can be fixed inside the robot frame. This simplifies the assembly of the platform, as the cable is just connected with a bolt. In a typical robot design, multiple pulleys are used to guide the cable. The pulleys lying between the force sensor and the platform disturb the force measurement. Pulling in the cable will lead to higher measured cable forces, as additionally the friction of the pulleys has to be overcome and vice versa.

For the IPAnema 3 robot, the force sensor is integrated in the winch as can be seen in Fig. 2.8b. All winches have another pulley outside the housing to guide the cable to the platform. As all winches are mounted on the floor, an additional pulley unit using two pulleys per cable is used for the upper cables as shown in Fig. 2.8a. In the IPAnema 3 Mini, for cable force measurement additional pulleys are installed as depicted in Fig. 3.16.

The force sensors applied in the cable robot consist of strain gauges and an integrated amplifier which delivers an analogue signal of voltage or current. In the AD-converter, the analogue signal is digitized with a typical resolution of 16 bit. As the force sensor is incorporated in the closed-loop cable force control, the measurement dynamic influences the reachable control performance and stability. As discussed in (Kraus, Schmidt et al. 2014), the conversion time of the AD-converter is important, as it acts as transfer delay within the control loop. In the former robot, the conversion amounted to multiples of the

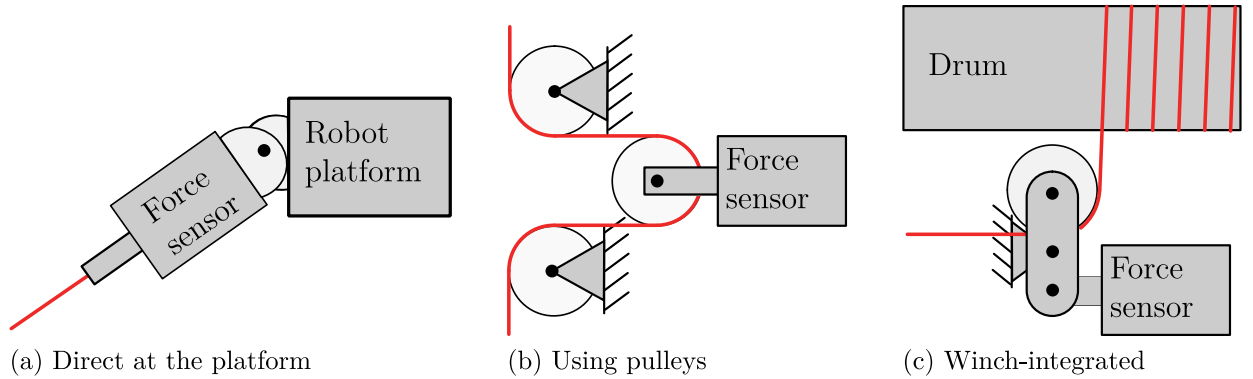


Figure 3.15: Principles for cable force measurement

field bus cycle time of 1 ms and had an significant influence. The current AD-converters have a conversion time of  $100 \mu\text{s}$  and, thus, the resulting transfer delay can be neglected.

For the relation between the actual force  $f$  and the measurement signal  $\gamma$ , one can assume a linear model. Thus, the characteristic of each force sensor is modelled as straight line

$$f = \gamma_1(\gamma - \gamma_0) , \quad (3.29)$$

with slope  $\gamma_1$  and offset value  $\gamma_0$ . For the identification of the parameters, known weights are used. With a least square approach, the best fitting values are identified. Due to manufacturing tolerances, each force sensor has its own characteristic as discussed in (Kraus, Schmidt et al. 2013) and, thus, the calibration procedure has to be conducted for each force sensor. For calibration, the winch-integrated force sensors remain installed and the known weights are attached to the cable while the winch lifts the load. With this procedure, mechanical ratios which arise, e.g. by the leverage arm shown in Fig. 2.8b, are also included in the calibration parameters. During this procedure the pulley friction disturbs the calibration. To compensate the pulley friction the force sensor is calibrated based on a slow movement of the cable in both directions to average over the pulley friction. To compensate for the pulley friction during operation of the robot, a friction model for a series of pulleys is described in the following. The initial idea was published in (Kraus, Kessler et al. 2015).

### 3.7.2 Friction Model for the Pulleys

A Coulomb friction model provides already a good estimation of the friction forces during a constant movement. In a force-controlled cable robot, the cable movement becomes dynamic, which means that the direction of movement often changes. The friction leads to a hysteresis effect which is not included in the Coulomb friction model and needs more sophisticated models. To account for this hysteresis effect, the Dahl model seems to be

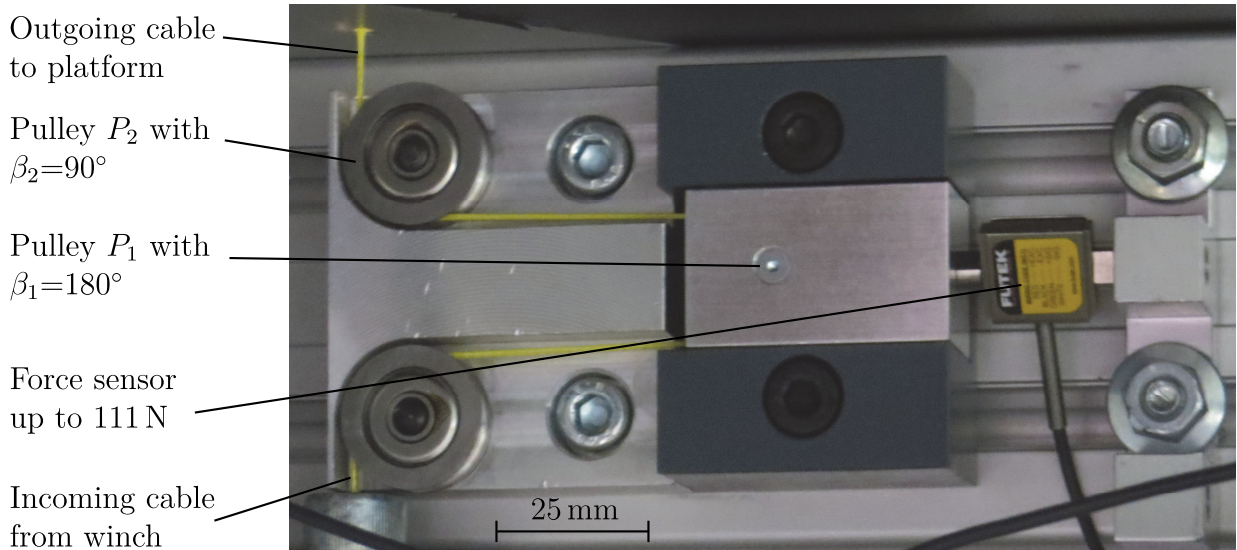


Figure 3.16: Pulley unit of the IPAnema 3 Mini robot for cable force measurement  $F_s$

sufficient compared to the more complicated LuGre model, as stick slip effects are not expected.

The aim of the friction model is to calculate the cable force  $\mathbf{f}$  at the platform based on the measurement signal of the force sensor  $\mathbf{F}_s$  which is integrated in the winch. In the first step, the pulley friction model is derived.

### Coulomb and Viscose Friction Model of a Series of Pulleys

In the following, the basic equations for the determination of the friction forces for a series of pulleys are derived as depicted in Fig. 3.17. It is assumed that the pulleys are always moved by friction due to tension in the cable. Thus, the friction is caused mainly by the pulley's bearing.

The force equilibrium for a cable guided around a pulley under the consideration of a friction force  $F_{R,j}$  and the cable velocity with reference to the motor encoder  $\dot{\theta}$  can be determined by

$$F_j = F_{j-1} + \text{sgn}(\dot{\theta})F_{R,j} \quad , \quad (3.30)$$

where  $F_j$  and  $F_{j-1}$  are the cable forces before and after the pulley, respectively. The friction force of one pulley  $F_{R,j}$  is modelled with the Coulomb friction coefficient  $\mu_i$  and a viscose friction parameter  $F_{pv}$  by

$$F_{R,j} = \mu_i F_{N,j} + F_{pv}\dot{\theta} \quad , \quad (3.31)$$

where  $F_{N,j}$  is the normal force acting on the bearing. Thus, for the friction estimation, the force acting on the pulley is relevant. The normal force  $F_{N,j}$  is the sum of incoming and

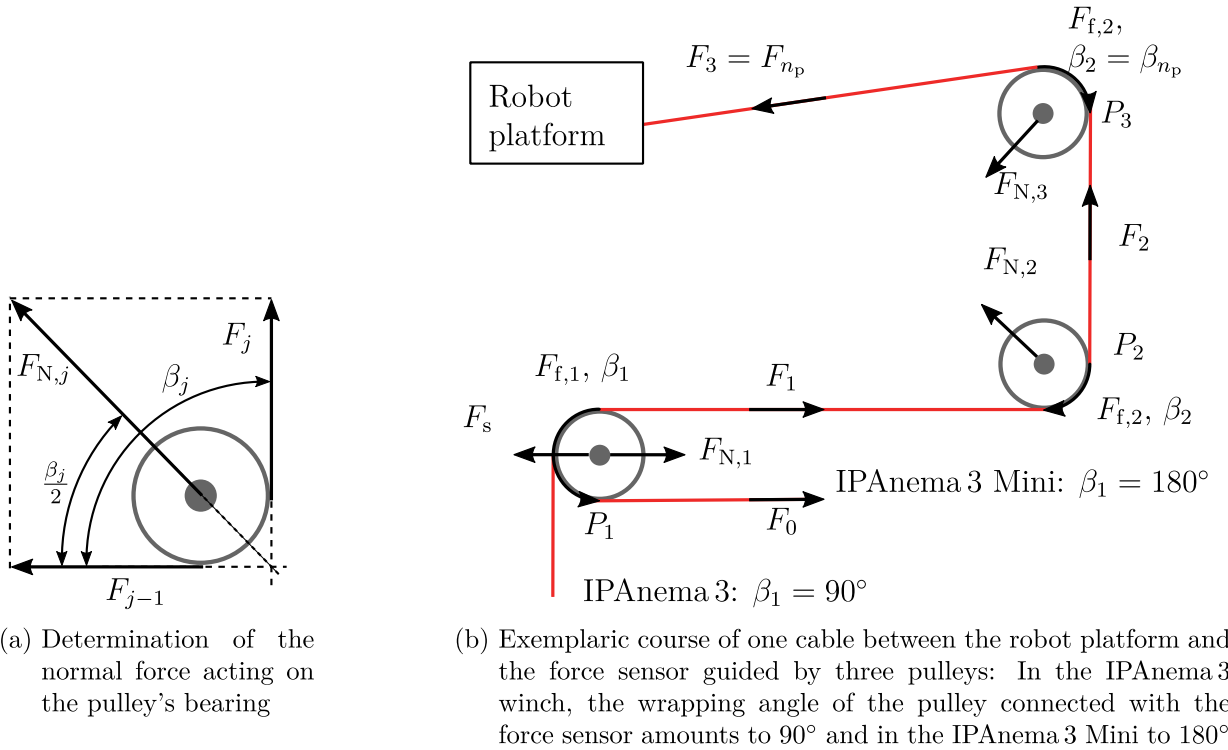


Figure 3.17: Determination of the relevant cable forces of a series of pulleys

outgoing cable forces acting under the actual wrapping angle  $\beta_j$  and is determined by

$$F_{N,j} = \sqrt{F_{j-1}^2 - 2F_{j-1}F_j \cos(\beta_j) + F_j^2} . \quad (3.32)$$

The assumption that the normal force vector is the bisection of the wrapping angle allows for the approximation

$$F_{N,j} \approx \frac{F_{j-1} + F_j}{2} \sqrt{2(1 - \cos(\beta_j))} , \quad (3.33)$$

which is visualized in Fig. 3.17a. Inserting (3.33) in (3.31) and subsequently in (3.30) results in

$$F_j = F_{j-1} + \text{sgn}(\dot{\theta})\mu_j \frac{F_{j-1} + F_j}{2} \sqrt{2(1 - \cos(\beta_j))} + F_{pv}\dot{\theta} \quad (3.34)$$

and solving for the cable force after pulley  $F_j$  yields

$$F_j = \frac{F_{j-1} (2 + \text{sgn}(\dot{\theta})\mu_j \sqrt{2(1 - \cos(\beta_j))}) + 2F_{pv}\dot{\theta}}{2 - \text{sgn}(\dot{\theta})\mu_j \sqrt{2(1 - \cos(\beta_j))}} . \quad (3.35)$$

Since the force sensor is connected to the first pulley  $P_1$ , it needs special consideration. The force equilibrium for the first pulley along the direction of the force sensor vector  $F_s$  reads

$$-F_0 \cos(\beta_j) + F_1 = F_s . \quad (3.36)$$

In the IPAnema3 winch, the wrapping angle around the first pulley is not precisely a right angle because the cable course from the pulley towards the drum is slightly sloping due to the drum pitch. This effect can be neglected in the friction model, as the exact relation between the cable force and the sensor signal is incorporated in the force sensor calibration. Thus,  $\beta_1 = 90^\circ$  holds, which leads to the trivial solution:

$$F_1(\beta_1 = 90^\circ) = F_s . \quad (3.37)$$

In the IPAnema3 Mini design,  $\beta_1 = 180^\circ$  holds and according to (3.36)  $F_0 = F_s - F_1$  follows. Inserting this into (3.35) for  $j=1$  yields

$$F_1 = (F_s - F_1) \frac{1 + \mu_1 \operatorname{sgn}(\dot{\theta})}{1 - \mu_1 \operatorname{sgn}(\dot{\theta})} . \quad (3.38)$$

Resolved for  $F_1$ , the cable force in the first segment returns

$$F_1(\beta_1 = 180^\circ) = F_s \frac{1 + \mu_1 \operatorname{sgn}(\dot{\theta})}{2} . \quad (3.39)$$

Neglecting friction, (3.37) and (3.38) can be summarized by

$$f_w = F_1 = \frac{1}{2} F_s (1 + \sin(\beta_1)) , \quad (3.40)$$

where  $f_w$  is the cable force measured by the winch-integrated cable force sensors and is disturbed by the pulley friction.

To get the cable force acting at the platform, which corresponds to the cable force in the last segment  $F_{n_p}$ , one has to evaluate (3.35) for every pulley starting from  $F_1$ . The wrapping angle  $\beta_{n_p}$  of the last pulley before the platform depends on the actual pose of the platform and is calculated by the inverse kinematics (2.6). The wrapping angles around all other pulleys are defined during mechanical installation of the robot and are constant during operation.

The macroscopic friction  $F_f$  of one cable follows to

$$F_f = F_{n_p} - F_1 , \quad (3.41)$$

and is now extended by the Dahl model to deal with both microscopic and macroscopic cable movements.

## Dahl Model

The Dahl model builds on the friction force derived from the Coulomb and viscose friction and models a hysteresis behaviour. The general form of the Dahl model is a first order

differential equation

$$\frac{df}{d\theta} = \sigma \left( 1 - \frac{f}{f_c} \operatorname{sgn}(\dot{\theta}) \right)^\alpha , \quad (3.42)$$

where  $\alpha$  describes the shape of the hysteresis area. Like in other literature,  $\alpha$  is set to one (Otis, Nguyen Dang et al. 2009), (Mahvash and Okamura 2006), (Canudas de Wit, Olsson et al. 1995). The basic idea of the Dahl model is to store the friction force acting at a direction change and to apply a smooth transition between the stored and actual calculated friction described by a stiffness value. An implementable solution of the Dahl model reads

$$F_D = F_f \operatorname{sgn}(\dot{\theta}) + \left( F_0 + F_f(\operatorname{sgn}(\dot{\theta})) \right) e^{-\frac{\sigma}{F_f} |\theta - \theta_0|} , \quad (3.43)$$

where  $\sigma$  is a design parameter describing the stiffness value of the transition between microscopic and macroscopic movement. When the direction of movement changes, the actual friction force and the cable length are stored according to  $\theta_0 = \theta$  and  $F_0 = F_D$ , respectively (Mahvash and Okamura 2006).

With the cable force measured in the winch  $f_w$  derived from (3.40) and the friction force  $F_D$  delivered from the Dahl model (3.43), the final estimation of the cable force acting at the platform can now be established by

$$f = f_w + F_D = \frac{1}{2} F_s (1 + \sin(\beta_1)) + F_D . \quad (3.44)$$

The friction model is now complete and in the following the parameter identification for the IPAnema 3 Mini is described.

## Identification Experiment

For the identification of the pulley friction, an additional force sensor is attached directly at the platform, as shown in Fig. 2.9b. In this way, the cable force acting at the platform  $F_{n_p}$  is measured directly, which can be assumed as ideal, because there is no friction. The cable force derived from the additional sensor is denoted as  $\bar{F}_{n_p}$  in the following to distinguish it from the model-based value  $F_{n_p}$ . The reference trajectory is chosen to investigate both microscopic and macroscopic movements of the robot:

- Stop-and-go movement in the same direction with amplitudes from 0.25 to 10 mm, velocity of 0.083 m/s and a pause of 0.5 s. This experiment is conducted in both positive and negative directions.
- Alternating movement with amplitudes from 0.25 to 10 mm, velocity of 0.083 m/s and a break of 0.5 s.
- Alternating movement with an amplitude of 100 mm and rising velocity of 0.167 m/s up to 1.0 m/s.

Table 3.4: Final parametrization for all eight cables of the IPAnema3 Mini based on the reference trajectory and comparison of the model errors. The index  $i$  refers to the cable number

$i$	$\mu$ [ ]	$\sigma$ [N/mm]	$F_{\text{pv}}$ [Ns/m]	$\bar{F}_{n_p} - f_w$ [N]	$\bar{F}_{n_p} - f_w - F_D$ [N]	$\bar{F}_{n_p}$ [N]
1	0.016	1.000	1.70	0.46	0.16	8.11
2	0.011	1.003	3.50	0.43	0.21	5.33
3	0.014	0.999	1.55	0.84	0.14	6.54
4	0.017	0.602	1.38	0.49	0.14	8.22
5	0.024	1.000	1.75	0.55	0.18	5.10
6	0.023	0.999	2.08	0.43	0.16	5.83
7	0.024	1.001	1.18	0.44	0.10	3.98
8	0.025	0.998	1.29	0.65	0.24	8.11
mean	0.019	0.950	1.80	0.54	0.17	6.40

- Rectangular trajectory with a velocity of 0.167 m/s and 0.5 m/s which covers the complete workspace.

The experiments are conducted with operational space position and cable force control. Especially when the platform reaches a rest pose, microscopic cable movement is typical due to the control signals of OSPC and CFC. These transient oscillations lead to frequent changes of direction which cause the hysteresis effect of the pulley friction.

### Final parametrization for all cables

For the identification, the reference trajectory is repeated for each cable and the reference sensor is changed from one cable to another. A Levenberg-Marquardt optimization is used for parameter identification for each cable. In the IPAnema3 Mini, all pulleys are of same type. Thus, the friction coefficient is assumed to be the same. For each cable, the friction model is described with three friction parameters. To deal with calibration differences between the two force sensors, a constant offset  $\epsilon$  is introduced for the optimization but neglected in the later implementation. For a time series of measurement data derived from the reference trajectory and the parameter set  $p = \{\mu, \sigma, F_{\text{pv}}, \epsilon\}$ , the optimization problem for one cable can be stated as

$$\min_p \sum (\Psi_{\text{PF}}(F_s, \dot{\theta}_i, \theta_i, \beta_{n_p}) + \epsilon - \bar{F}_{n_p})^2 \quad , \quad (3.45)$$

where  $\Psi_{\text{PF}}$  encapsulates the friction model. The resulting parameters for the friction model derived by the optimization function can be seen in Table 3.4. The overview over the identified parameters for all eight cables reveals quite a high variance of the real parameters. The Coulomb friction ranges between 0.011 and 0.025 and the viscose friction between 1.18 and 3.5 Ns/m. The parameter  $\sigma$  is always around 1 N/mm with exception of cable 4. The

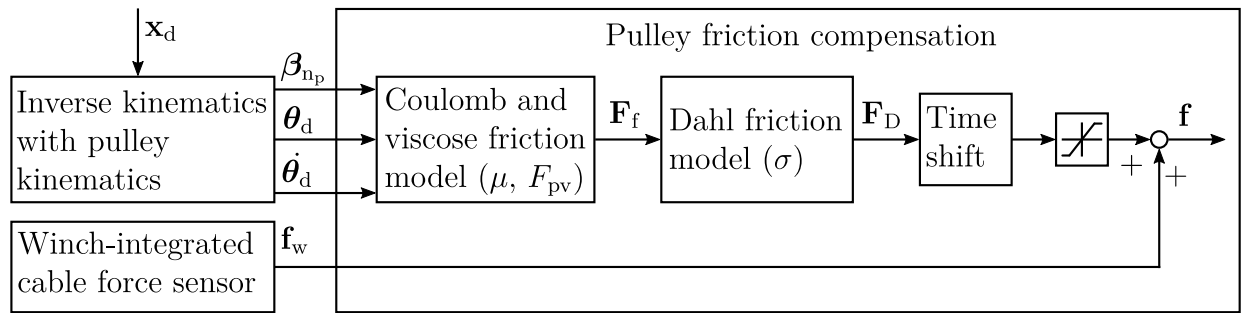


Figure 3.18: Structure of the pulley friction compensation

Table 3.5: Improvement of the wrench hysteresis with and without pulley friction compensation for the IPAnema 3 Mini around the home position ( $\mathbf{x} = [0 \ 0 \ 0 \ 0 \ 0 \ 0]^T$ )

Operational space axis	Hysteresis width [N, Nm] without comp.	Hysteresis width [N, Nm] with comp.	Lasting hysteresis [%]
$x$ translation	7.376	0.979	13.3
$y$ translation	4.183	0.463	11.1
$z$ translation	7.619	0.817	10.7
$x$ rotation	0.519	0.165	31.8
$y$ rotation	0.528	0.154	29.2
$z$ rotation	0.111	0.020	18.1

outlier of cable 4 indicates some mechanical differences in assembly of the corresponding pulleys. The influence of the pulley friction before,  $\bar{F}_{n_p} - f_w$ , and after the compensation  $\bar{F}_{n_p} - f_w - F_D$  is also given in Table 3.4. In average, the results show a reduction of the error by approximately two thirds. This means that one third of the force difference between the two force signals  $f_w$  and  $\bar{F}_{n_p}$  is not included in the model. The mean cable force amounts to 6.40 N, while the friction force created by the pulleys is 0.54 N. Without compensation, the pulley friction disturbs the force measurement by 8.4%, which is a significant value.

### 3.7.3 Implementation

An overview of the implementation of the friction model is shown in Fig. 3.18. The input parameters are the signals of the eight cable force sensors  $F_s$ , the desired position  $\theta_d$  and velocities  $\dot{\theta}_d$  of the winches and the pose-depending wrapping angle  $\beta_{np}$  of the last pulley calculated in the inverse kinematics module. As the desired velocity is used, the model is always ahead of the real friction. Thus, the output of the Dahl model is time-shifted to correlate the modelled friction with the real effect. A time shift of 50 ms has the best correlation. The pulley friction compensation outputs the corrected force signal  $f$ .

The accuracy of the wrench measurement depends obviously on the reliability of the cable force measurement. Using winch-integrated cable force sensors, one can observe an hysteresis effect: the measured wrench depends on the actual direction of movement. To

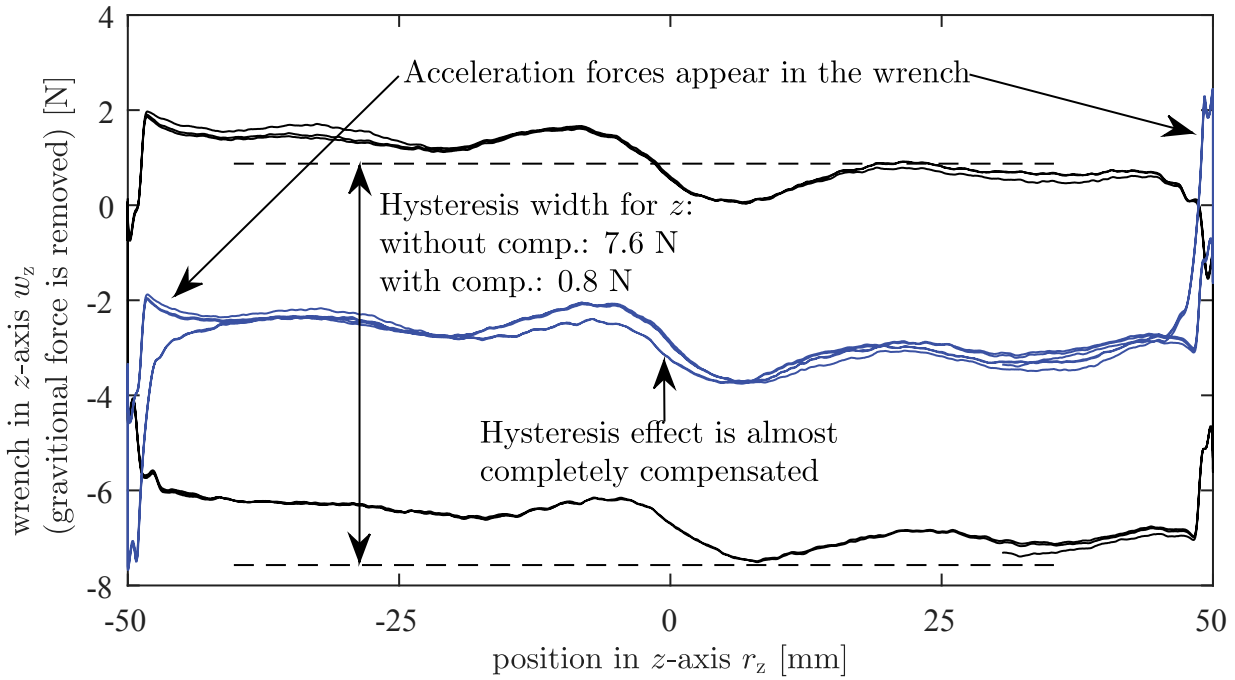


Figure 3.19: Reduction of the wrench hysteresis using the pulley friction compensation, exemplary in vertical axis

investigate the influence of pulley friction on the wrench measurement, the IPAnema 3 Mini robot was programmed to cyclically cross the home position which lies in the centre of the workspace in all six DOF.

### 3.7.4 Verification of the Friction Model: Wrench Hysteresis

The measurement results are summarized in Table 3.5 and show the influence of the pulley friction on the measured wrench. The hysteresis ranges in the same dimension as the gravitational force of the unload platform which is 4 N. Especially for translational movements, the friction compensation is able to compensate for a significant part of the hysteresis. The compensation around the rotational DOF is comparatively lower. Probably this is due to the limited orientation workspace. Exemplary, the hysteresis curve for the investigation of the  $z$ -axis of the robot is shown in Fig. 3.19. The width of the hysteresis curve amounts to 7.6 N. Using the friction compensation, the hysteresis can almost completely be compensated to a width of only 0.8 N.

With the friction model, the effect of the pulley friction on the cable force measurement is reduced by around 70% on the IPAnema 3 Mini. The same model is also applied to the IPAnema 3 robot. Due to the higher cable forces, also the friction amounts to higher values. The improvement ranges in the same area as of the IPAnema 3 Mini.

---

# 4 Experimental and Model-Based Investigation of Robot Properties

This chapter is dedicated to the investigation of several properties of cable robots, which are associated with the control of cable forces. An important performance criterion of a robot is its position accuracy. It denotes how precise a robot can position its platform within the workspace. In a cable robot, a special focus lies on the accuracy which can be reached under additional payload due to the cable elasticity. For the dimensioning of a robot for a specific task, the workspace has to cover all positions, which the robot has to reach. Compared to an industrial robot, the workspace of a cable robot depends on its actual payload and the question arises how the cables behave at the workspace border. The development of the controller showed that it allows for choosing different tension levels. The influence of the tension level on the reachable position accuracy, the dynamic behaviour of the platform, the stiffness and the energy consumption are of interest for the design and operation of cable robots. Starting with the position accuracy, these properties are investigated in the following.

The position accuracy describes with which position error the platform reaches a position. Hereby, a distinction is made between relative and absolute accuracy. The relative accuracy describes the variation of the platform position relative to the mean value established by several repetitions. The absolute accuracy describes the error w.r.t. the world coordinate frame  $\mathcal{K}_0$ . The position error refers to the origin of the platform frame  $\mathcal{K}_p$  and is calculated by  $\Delta r = \|\mathbf{r}_d - \mathbf{r}\|$ . The orientation error is also based on the Euclidean norm for the Kardan angles and reads as  $\Delta\varphi = \|\boldsymbol{\varphi}_d - \boldsymbol{\varphi}\|$ .

For a reliable evaluation of the position accuracy, external measurement devices have to be used. For this reason, the laser tracker described in section 2.3.3 is applied. The measurement system is calibrated to the world frame which allows for the investigation of both absolute and relative position accuracy. Each experiment is carried out at least three times to establish the standard deviation. The mean measurement value can be interpreted as absolute position and the standard deviation gives insight in the relative accuracy.

The first part of the following chapter focuses on the improvement of the relative position accuracy in combination with the inverse kinematics. Robots for handling applications have to deal with changing payloads which leads to position deviations of the platform due to

finite stiffness of the robot. At first, the identification of the actual payload using the cable force sensors is studied. This is carried out using a circle path and arbitrary trajectories. Based on the load identification, it is shown how to augment the inverse kinematics by a compensation of the estimated platform position errors due to the additional load.

Next, the experimental investigation of the proposed control scheme for operational space position and cable forces is presented. The controller development showed that it is non-trivial to control the platform position while keeping the cable forces on the desired level. Model-based approaches are applied especially for estimating the platform position with the forward kinematics. The focus lies on the position accuracy of the robot for different positions, tension levels and payloads to investigate the model accuracy. In order to make a meaningful comparison of the results possible, the experiments are also conducted using the inverse kinematics. The investigations are carried out in standstill and under movement.

Beside a static deflection of the platform under additional payloads, an influence on the dynamic behaviour of the platform is also expected. The eigenfrequency of the platform is a characteristic point of the robot's dynamics and is also influenced by the stiffness of the platform. It is evaluated, in which range the stiffness of the robot and subsequently the dynamics can be influenced by the choice of the tension level.

Finally, the energy consumption of the robot is investigated. For this purpose, a simulation model for the mechanical and electrical losses arising in the pulleys, winches, servo drives and power electric is established. This model allows for conclusions about the energy efficiency of the robot. This investigation is completed with a comparison of the energy consumption between a cable robot and a serial industrial robot.

## 4.1 Load Identification and Compensation

With the load identification, the actual mass of the platform including the payload  $m_p$  and the vector to the centre of gravity  $\mathbf{c}_{m_p}$  w.r.t.  $\mathcal{K}_p$  is estimated during handling operations. This estimation is based on the cable force measurement and knowledge of the actual acting accelerations on the platform. Within the experiments, only translational movements are investigated. Analysing angular accelerations for determining the inertia tensor is difficult, as the orientation workspace of a cable robot is relative small. Before the load identification is implemented on the robot, the investigation is done offline using recorded measured data.

### 4.1.1 Offline Load Identification

For the offline identification, a circular path in the horizontal plane with a given constant velocity is chosen which results in a constant acceleration acting on the platform. To analyse the influence of changing loads, additional weights are fixed on the platform, as illustrated

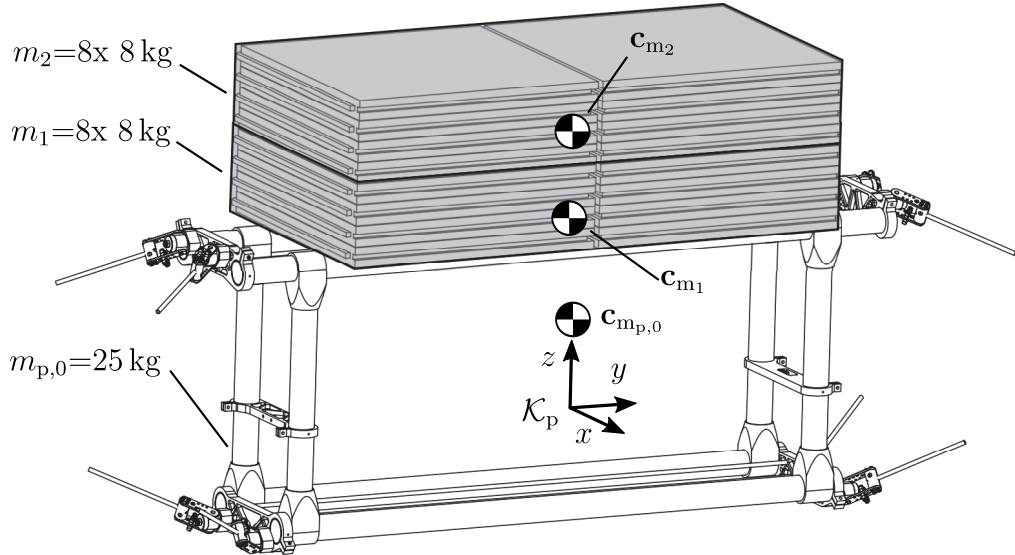


Figure 4.1: Platform of the iPanema 3 robot with additional loads and corresponding centres of gravity

in Fig. 4.1. For the load identification, the empty platform is described by the mass  $m_{p,0}$  with centre of gravity  $\mathbf{c}_{m_{p,0}}$  and the additional weights are summarized as  $m_1$  and  $m_2$  with their centres of gravity  $\mathbf{c}_{m_1}$  and  $\mathbf{c}_{m_2}$ , respectively. The resulting centre of gravity  $\mathbf{c}_{m_p}$  can be derived by the weighted average

$$\mathbf{c}_{m_p} = \frac{m_{p,0}\mathbf{c}_{m_{p,0}} + m_1\mathbf{c}_{m_1} + m_2\mathbf{c}_{m_2}}{m_{p,0} + m_1 + m_2} \quad (4.1)$$

depending on the mass  $m_j$  and the position of the centre of gravity  $\mathbf{c}_{m_j}$  of each load for  $j \in \{p, 1, 2\}$ . This consideration can be expanded to arbitrarily many loads.

The circular trajectory with the midpoint  $\mathbf{r}_{c,0}$  is parametrized in polar coordinates with radius  $r_c$  and angle  $\vartheta_c$  as shown in Fig. 4.2. With the angular velocity  $\dot{\vartheta}_c$ , the translational acceleration  $\ddot{\mathbf{x}}$  results to

$$\ddot{\mathbf{x}} = -r_c \dot{\vartheta}_c^2 \begin{bmatrix} \cos(\vartheta_c) \\ \sin(\vartheta_c) \\ 0 \end{bmatrix}, \quad (4.2)$$

where  $\dot{\vartheta}_c = \text{const}$ . The resulting dynamic wrench according to (2.33) reads

$$\mathbf{w}_{\text{dyn}} = \begin{bmatrix} f_{\text{dyn},x} \\ f_{\text{dyn},y} \\ f_{\text{dyn},z} \\ \tau_{\text{dyn},x} \\ \tau_{\text{dyn},y} \\ \tau_{\text{dyn},z} \end{bmatrix} = m_p r_c \dot{\vartheta}_c^2 \begin{bmatrix} -\cos(\vartheta_c) \\ -\sin(\vartheta_c) \\ 0 \\ c_{m_p,z} \sin(\vartheta_c) \\ -c_{m_p,z} \cos(\vartheta_c) \\ c_{m_p,y} \cos(\vartheta_c) - c_{m_p,x} \sin(\vartheta_c) \end{bmatrix}, \quad (4.3)$$

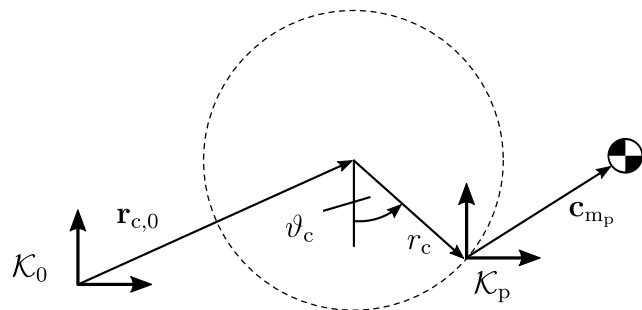


Figure 4.2: Circle trajectory for identifying the actual mass and centre of gravity of the platform

Table 4.1: Comparision of the theoretically derived amplitudes with the experiment

wrench amplitudes	$m_p=25 \text{ kg}$	$m_p=89 \text{ kg}$	$m_p=153 \text{ kg}$			
	theor.	exp.	theor.	exp.	theor.	exp.
$f_{p,x} [\text{N}]$	123.4	180.7	439.2	514.4	755.0	893.5
$f_{p,y} [\text{N}]$	123.4	123.3	439.2	426.9	755.0	751.4
$\tau_{p,x} [\text{Nm}]$	0.6	23.1	117.9	118.7	261.8	272.0
$\tau_{p,y} [\text{Nm}]$	0.6	38.5	117.9	87.4	261.8	242.6

and has a common force amplitude of  $m_p r_c \dot{\vartheta}_c^2$ .

For the experiment, the radius  $r_c$  is set to 0.5 m and an angular velocity  $\dot{\vartheta}_c$  of 0.5  $2\pi$  rad/s is chosen, which yields a centrifugal acceleration  $|\mathbf{a}|$  of 4.93 m/s<sup>2</sup>. The 16 wooden plates used as additional load have a mass of 8 kg each.

According to (4.3), periodic sinusoidal progressions for the inertia force in  $x$ - and  $y$ -axis and the torque in all three axes are expected for a constant velocity. Due to measurement noise of the force sensors and geometrical uncertainties, the result is distorted. Therefore, a discrete Fourier transformation (DFT) is applied on the measured wrench to identify the amplitudes of the first harmonics.

The first harmonics of the forces in  $x$ - and  $y$ -axis for different loads are shown in Fig. 4.3. One can recognize that the amplitudes of the wrench in  $x$ - and  $y$ -axis correlate with the mass of the platform. The first harmonics of the torques around the  $x$ - and  $y$ -axis can be seen in Fig. 4.4. Here, the amplitude rises because the additional weights increase the total mass and the position of the centre of gravity in  $z$ -axis  $c_{m_p,z}$  rises. Both diagrams reveal the expected linear correlation between mass and amplitudes. In Table 4.1, the experimentally gained amplitudes are compared to the theoretical values computed with (4.3) based on the nominal parameters for the weights. Apart from some exceptions, a good correlation between the theoretical and experimental values with an error of roughly 10% can be determined. Next, the mass and centre of gravity are estimated from the amplitudes.

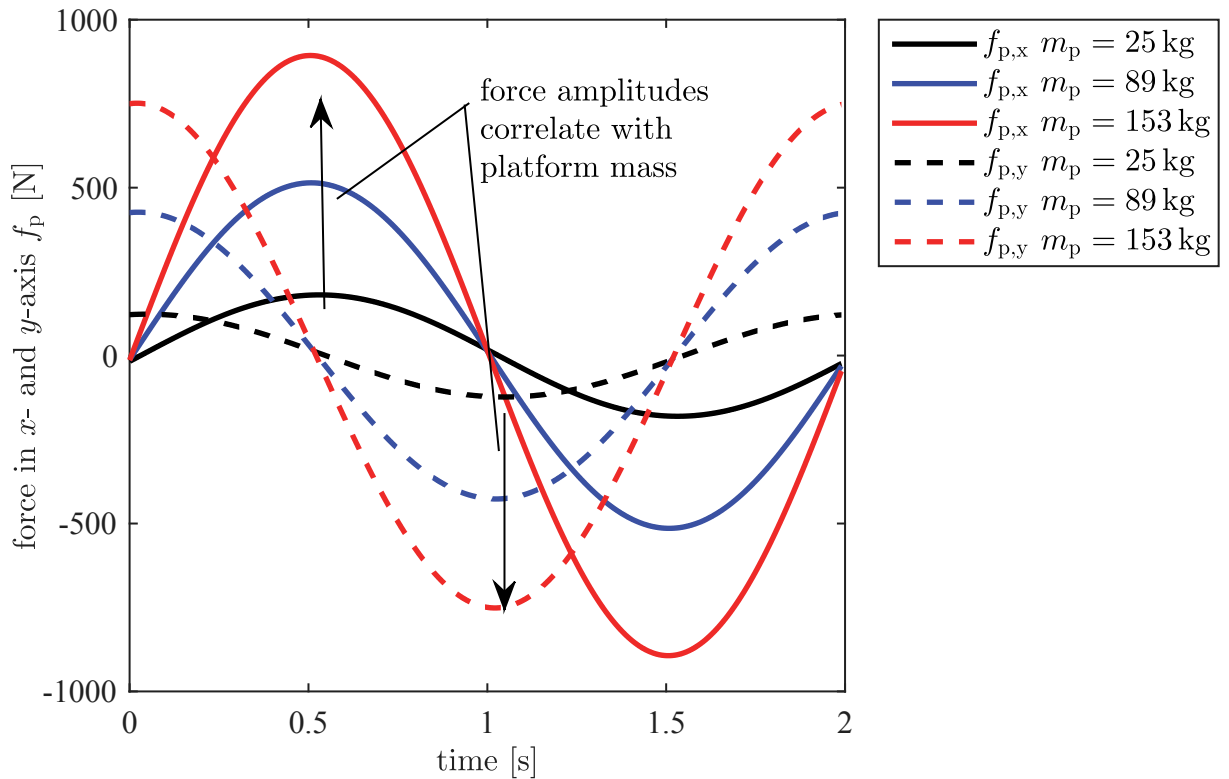


Figure 4.3: First harmonics of the forces in  $x$ - and  $y$ -axis during the circle path identified with DFT from the measurement data

An estimation for the mass can be derived, on the one hand, from the force amplitudes in  $x$ - and  $y$ -axis and the known centrifugal acceleration, and, on the other hand, from the wrench in  $z$ -axis which depends only on gravity during standstill.

The knowledge of the mass from the previous step allows for the estimation of the centre of gravity in  $z$ -axis based on the torque amplitudes around the  $x$ - and  $y$ -axis. As the additional loads are put on the platform, a significant shift of the centre of gravity in positive direction along the  $z$ -axis is expected.

In order to identify the centre of gravity in the  $x$ - and  $y$ -axis according to (4.3), the torque around the  $z$ -axis has to be considered. The identified main oscillation has to be evaluated at discrete points. When angle  $\vartheta_c$  is an integer multiple of  $\pi$ ,  $\sin(\vartheta_c)$  becomes zero and  $c_{m_p,y}$  can be directly derived. In the same manner  $c_{m_p,x}$  can be determined. The alternative way to determine  $c_{m_p,x}$  and  $c_{m_p,y}$  is by analysing the static torque around the  $x$ - and  $y$ -axis which is induced by gravity.

The nominal and estimated values for the load parameters are listed in Table 4.2. Overall, the results reveal a reasonable correlation between measurement and theory with maximum errors in the mass estimation of 20%. The estimation of the centre of gravity in  $z$ -axis is relatively imprecise and the error amounts up to 255 mm. In the following, the approach for the identification of the actual platform mass is proposed and implemented on the robot.

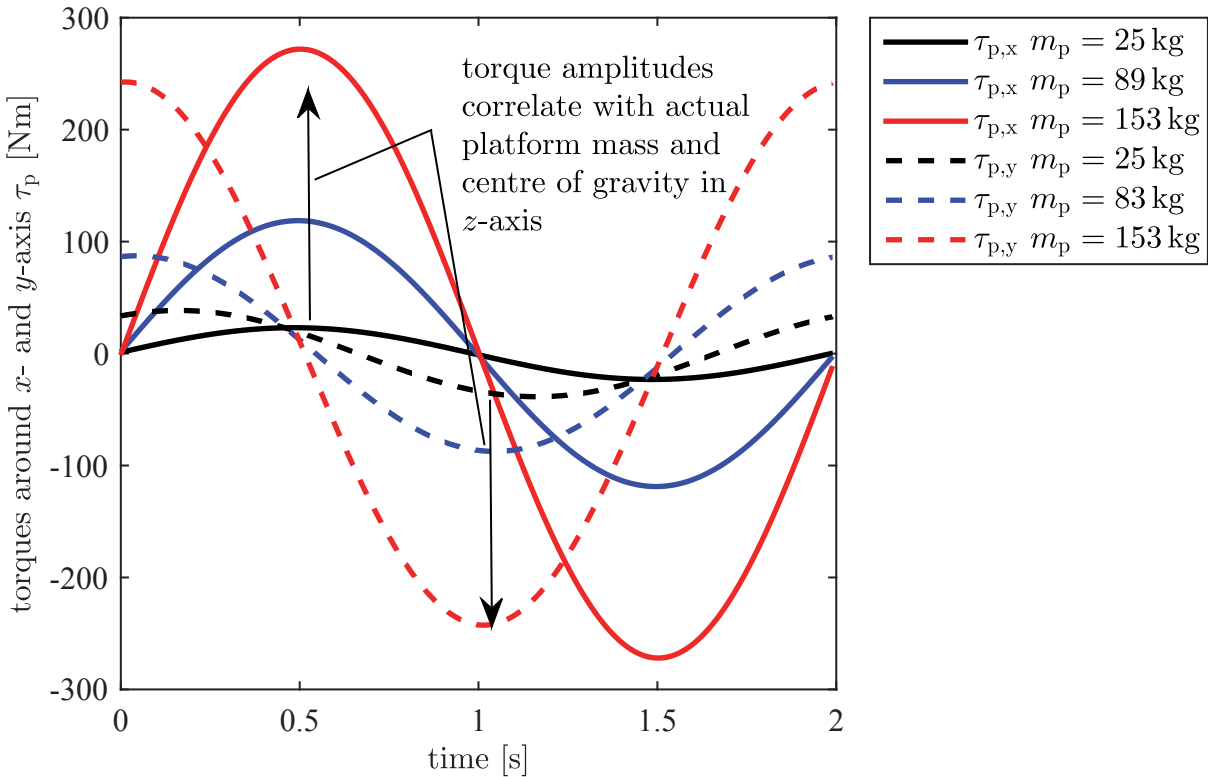


Figure 4.4: First harmonics of the torques around the  $x$ - and  $y$ -axis during the circle path identified with DFT from the measurement data

Table 4.2: Load parameters: comparison of nominal and estimated values derived from the circle path with a diameter of 1.0 m and a frequency of 0.5 Hz

parameter	nominal value from CAD model	estimated value from DFT
$m_{p,0}$ [kg]	25.0	30.8
$m_1$ [kg]	64.0	64.5
$m_2$ [kg]	64.0	71.3
$m_p$ [kg]	153.0	166.7
$\mathbf{c}_{m_{p,0}}$ [mm]	$[0.5 \ 0.5 \ 5]^T$	$[-16.5 \ -9.9 \ 202.7]^T$
$\mathbf{c}_{m_1}$ [mm]	$[-0.4 \ 0.5 \ 371.5]^T$	$[-23.7 \ -12.6 \ 226.7]^T$
$\mathbf{c}_{m_2}$ [mm]	$[-0.4 \ 0.5 \ 455.5]^T$	$[0.1 \ -2.9 \ 438.8]^T$
$\mathbf{c}_{m_p}$ [mm]	$[-0.5 \ 0.5 \ 408.8]^T$	$[-12.2 \ -8.0 \ 312.8]^T$

### 4.1.2 Online Load Identification and Compensation

In the last section, a fixed trajectory was analysed regarding the load parameters. In practical operation of the robot, the trajectory cannot be assumed. Therefore, a more general approach which identifies at least the platform mass on arbitrary trajectories and also works in real-time is necessary. With this approach, the weight of the actual manipulated load is determined and next, the estimated position error due to the gravitational force is compensated.

The load identification is based on the assumption that the position error of the platform is small and, thus, the structure matrix is evaluated for the desired position. Furthermore, it is assumed that also the actual platform acceleration corresponds to the desired value. Thus, the dynamics of the actuator and the platform itself are neglected.

Based on the measured cable forces  $\mathbf{f}$ , the wrench  $\mathbf{w}$  can be directly calculated by the corresponding structure matrix  $\mathbf{A}^T(\mathbf{x})$  using (2.11). For the mass estimation, the gravitational and actual robot acceleration in vertical direction are used. Evaluating the dynamic force equilibrium in  $z$ -axis, which reads

$$\hat{m}_p = -\frac{w_z}{\ddot{x}_{d,z} - g} \quad , \quad (4.4)$$

gives an estimation for the actual mass  $\hat{m}_p$ . In this way, the actual inertia forces are taken into account and a stable estimation of the platform mass under accelerations is received. This allows for short time constants in the filter and for fast adapting to changing loads. Next, the position error due to the elastic cables is estimated for the identified load.

### Load Compensation

For compensating the position error induced by an additional load, the expected displacement of the platform is calculated based on the stiffness model. The operational space stiffness matrix  $\mathbf{K}_x$  is derived according to (2.22). To estimate the position error induced by a given wrench, the stiffness matrix has to be inverted

$$\mathbf{C}_x = \mathbf{K}_x^{-1} \quad (4.5)$$

and one receive the compliance matrix  $\mathbf{C}_x$ . With  $\mathbf{w}_c = [0 \ 0 \ -m_cg \ 0 \ 0 \ 0]^T$ , the desired position offset  $\mathbf{x}_{d,LC}$  is evaluated by

$$\mathbf{x}_{d,LC} = \mathbf{C}_x \mathbf{w}_c \quad . \quad (4.6)$$

The equation above is a linearization for the cable lengths for the actual pose and holds only for small position changes.

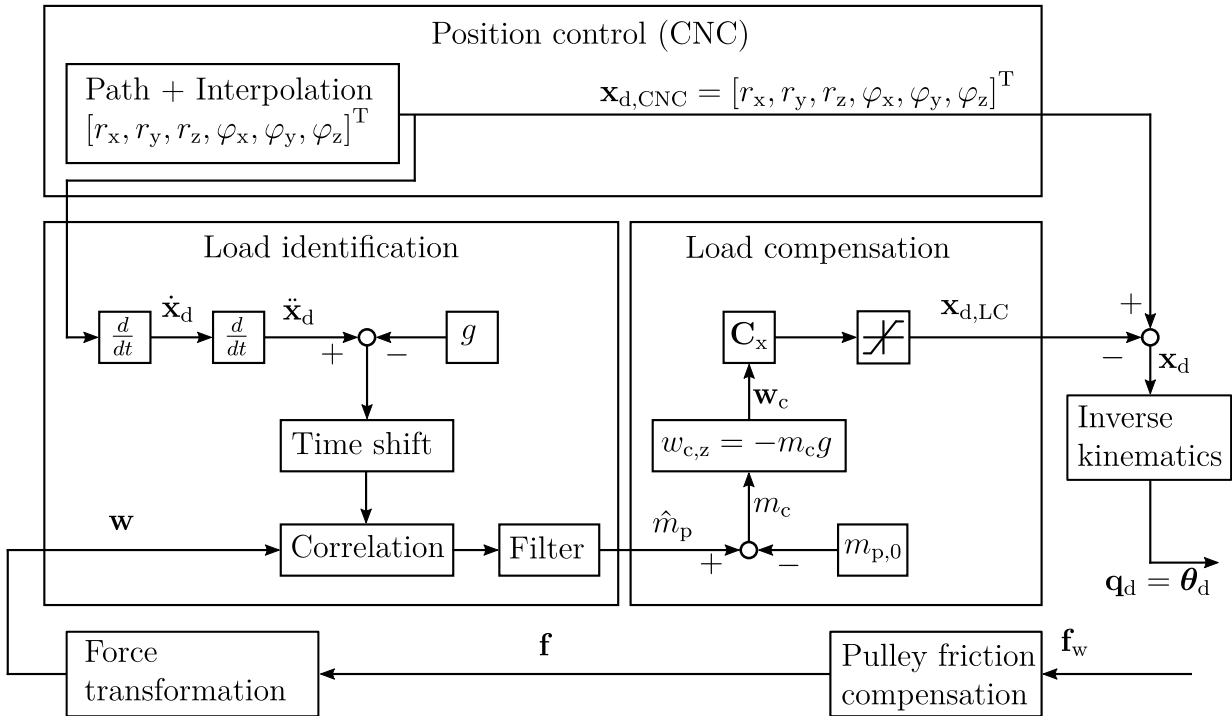


Figure 4.5: Structure of the load identification and compensation

## Controller Design and Implementation

The structure of the implementation of load identification and compensation on the controller is shown in Fig. 4.5. The inverse kinematics is appended by a position offset denoted by  $\mathbf{x}_{d,LC}$ .

In the load identification module, an estimated value for the mass  $\hat{m}_p$  is obtained, based on the desired position, acceleration and the actual cable forces. For this, the actual wrench is determined and correlated with the time-shifted commanded acceleration and the gravity  $g$  according to (4.4). The resulting signal is disturbed by the noise of the force sensor and oscillations of the platform. Therefore, a filter is realized as a moving average for the estimated mass with an experimentally determined time constant of 240 ms.

In the load compensation module, the mass to compensate  $m_c$  is the estimated platform mass reduced by the own weight of the platform. Next, the wrench vector  $\mathbf{w}_c$  is established and based on the compliance matrix  $\mathbf{C}_x$ , the displacement in operational space  $\mathbf{x}_{d,LC}$  is derived.

### 4.1.3 Experimental Evaluation

The load identification and compensation are evaluated on the IPAnema3 robot. The experimental evaluation aims to verify the identification of additional loads and the compensation of the position error induced by the elastic cables. The linear cable model is applied and the specific stiffness constant is experimentally determined to reach the desired

compensation of the position error due to the additional load. The improvement of the position accuracy is measured with the laser tracker.

### Adapting of the Load Compensation on Changing Loads

The impact of the load compensation during adding and removing of 16 weights with each 8 kg on the stationary platform in the position  $\mathbf{r} = [-1.0 \ -1.0 \ 0.5]^T \text{m}$  is depicted in Fig. 4.6. As the weights are put manually on the platform, the measurement signal without load compensation is not synchronized with other signals. Without compensation, the platform sags by about 0.37 mm per 1.0 kg and amounts to 47 mm under the total load of 128 kg. With the load compensation, the position error due to the additional mass is almost completely compensated and reduced to less than 3 mm.

After removing the loads a position error  $\Delta r_z$  of 9.2 mm lasts without load compensation. As the position of the drives  $\theta$  did not change during the experiment, this position error has to be caused by the settlement of the cables. This effect is quite problematic for reaching a high position accuracy, as it can hardly be measured without an external measurement device.

To receive further insight, the internal states of the implementation are considered. The progression of the estimated mass  $m_c$  shows that the additional mass is measured but the final estimation amounts to 120.5 kg, which is 5.9% lower than the nominal mass of 128 kg. As the position error is almost completely compensated, one can conclude that the underestimation of the load is included in the experimentally determined stiffness value. The output of the load compensation  $\mathbf{x}_{d,LC}$  is also given in the diagram and reveals that it amounts under the peak load to 48.9 mm, which is slightly higher than the position error without load compensation.

### Position Accuracy under Changing Loads

The transient response of the platform with payloads of 40 and 80 kg moving to the position  $\mathbf{r} = [2.0 \ 2.0 \ 1.0]^T \text{m}$  is shown in Fig. 4.7. Taking the unloaded position as reference, one can easily see the compliance of the platform and the effect of the load compensation.

The load identification and compensation was applied for the first time on the IPAnema 2 robot (Kraus, Schmidt et al. 2013). In this former investigation, the position accuracy was improved by more than 50% when applying additional loads of 10 and 20 kg. The robot frame had almost the same height as the IPAnema 3, while the footprint amounts only to one fifth.

The evaluation of the load identification and compensation showed that using the cable force sensors the estimation of the actual payload is possible. Simultaneously, the load compensation showed that the estimation of the operational space stiffness matrix fits

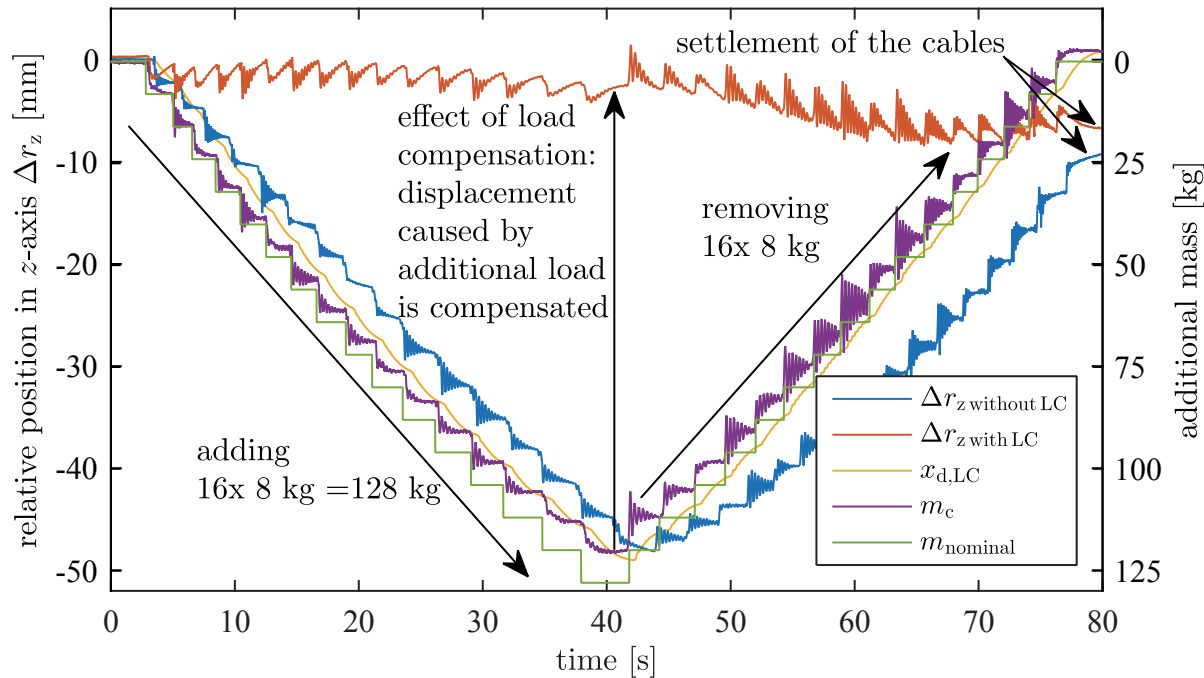


Figure 4.6: Dynamic response of the platform while adding and subsequently removing weights at standstill with and without load compensation (LC)

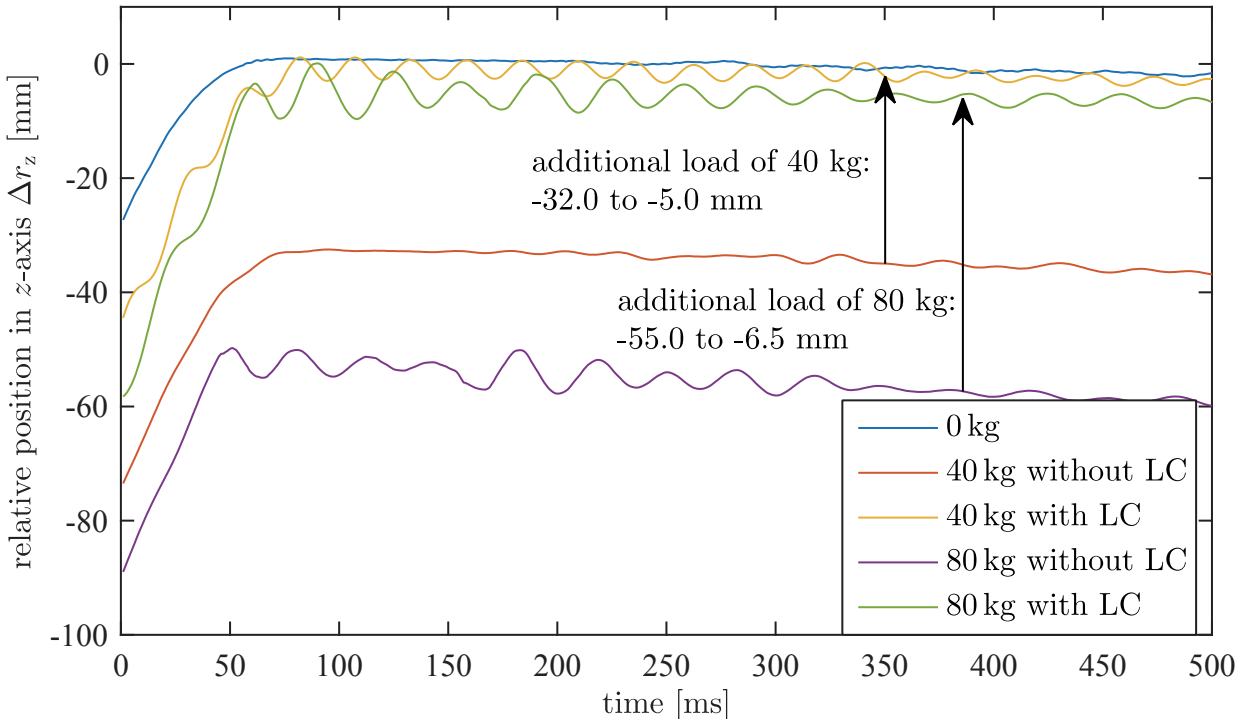


Figure 4.7: Displacement of the platform under different loads and the improvement reached with the load compensation (LC)

with the actual behaviour of the robot. The experimental verification shows a remarkable improvement in position accuracy and a fast response on changing loads.

In the following, a detailed investigation of the position accuracy is presented. The proposed forward kinematics incorporates intrinsically the load identification and compensation by estimating the actual cable elongation. Thus, the load identification and compensation is hereby completed.

## 4.2 Position Accuracy

The following investigations aim to analyse the position accuracy resulting from inverse kinematics and the proposed control scheme. Due to the kinematic structure of the robot and the elasticity of the cables, an influence of the actual payload, tension level and platform position has to be expected. The experiments are conducted in a way to investigate the influence of these effects.

At first, the accuracy of the forward kinematics based on the linear and non-linear cable model is investigated for different tension levels. Next, several points within the workspace are investigated using minimal and medium tension level and with an additional payload. Subsequently, the scope of the investigation is set on the workspace border. This investigation gives insight in the behaviour of the robot at its operation limit. The experiment can be interpreted as a comparison between the workspace derived from the simulation and the real robot behaviour. This is an important issue regarding the reliability of the workspace analysis. After the static investigation, the robot behaviour is investigated under exploitation of the maximum velocity. The investigations are all carried out on the IPAnema 3, only for the dynamic investigation additional results from the IPAnema 3 Mini are reported.

### 4.2.1 Comparison of linear and non-linear Cable Model

The forward kinematics plays a key role in the reachable position accuracy, as it delivers the actual platform position for which the control error  $e_x$  is determined. As stated in section 3.2, the forward kinematics can incorporate the non-linear cable model. In the following, it is investigated if the position accuracy can be increased using the non-linear cable model compared to the linear model. For this reason, the position accuracy is measured in one static pose ( $\mathbf{r} = [-2.0 \ -2.0 \ 0.7]^T \text{m}$ ) for different tension levels. In the ideal case, the platform position should not change while modifying the tension level because only the internal tensions are affected.

For the investigation of the model accuracy, the cable forces are adopted from minimal to maximal tension level using the QP algorithm. The evaluation shows that with both models position and orientation errors occur while changing the tension level. In the diagrams, the

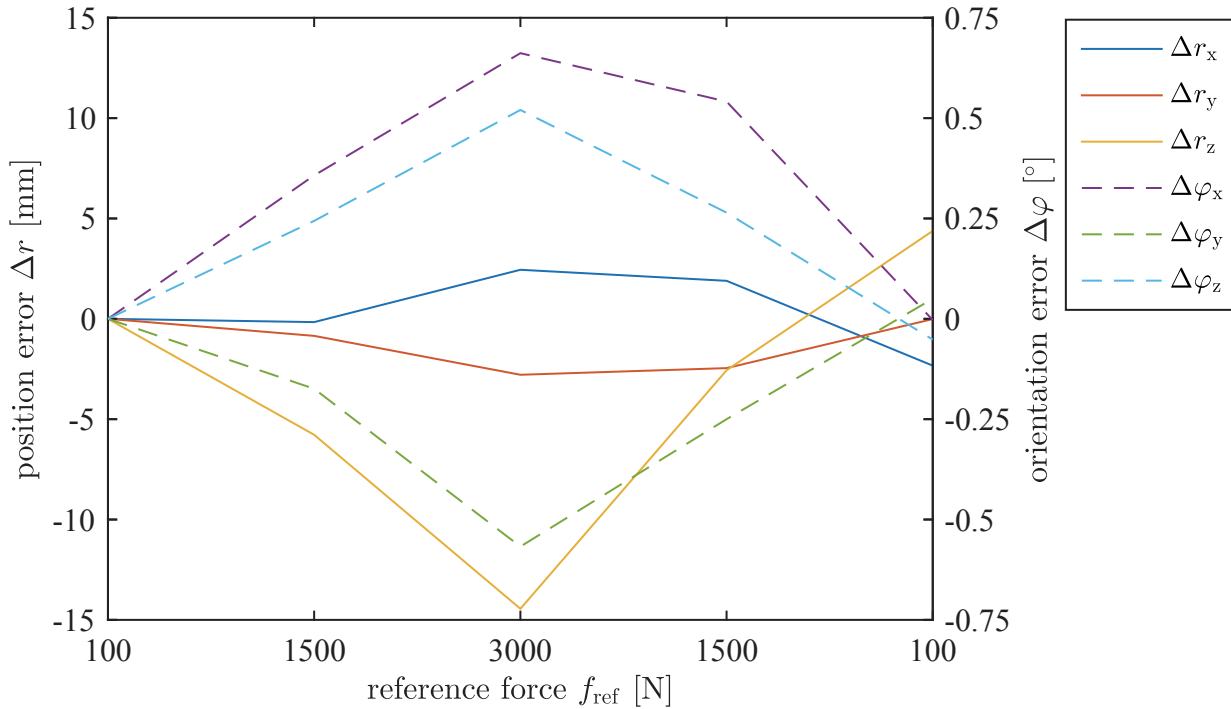


Figure 4.8: Progression of the pose while increasing and decreasing the cable tension using the linear cable model

configuration with  $f_{\text{ref}} = 100$  N is used as reference for the relative position accuracy. Using the linear model for the forward kinematics, the platform moves at the highest tension level 15 mm downwards, as can be seen in Fig. 4.8. The orientation changes by about 0.5° around each axis. With the non-linear cable model, the position error behaves slightly differently under changing tension level as presented in Fig. 4.9. Here, the platform moves 12.5 mm upwards and the translational position errors in  $x$ - and  $y$ -axis are a bit higher compared to the linear model, while the orientation errors are smaller.

One reason for the error lies in the settlement of the cable which is not considered in the model. Exemplary for one cable, the cable force  $f$  and the output of the cable force controller  $\Delta q_{\text{d,CFC}}$  are presented in Fig. 4.10. Especially when reaching the highest cable force of 1200 N, one can see that the output of the cable force controller rises, while the cable force remains constant. The platform can be assumed to stand still and, thus, the additional desired cable elongation is needed to compensate for the settlement of the cable.

The analysis delivered that the tension level influences the platform position. Thus, the following investigation of the position accuracy is conducted for minimum and medium tension level. In the following, the reported results are based on the linear cable model due to the limited availability of the test set-up. The position accuracy under application of the non-linear cable model may be slightly higher.

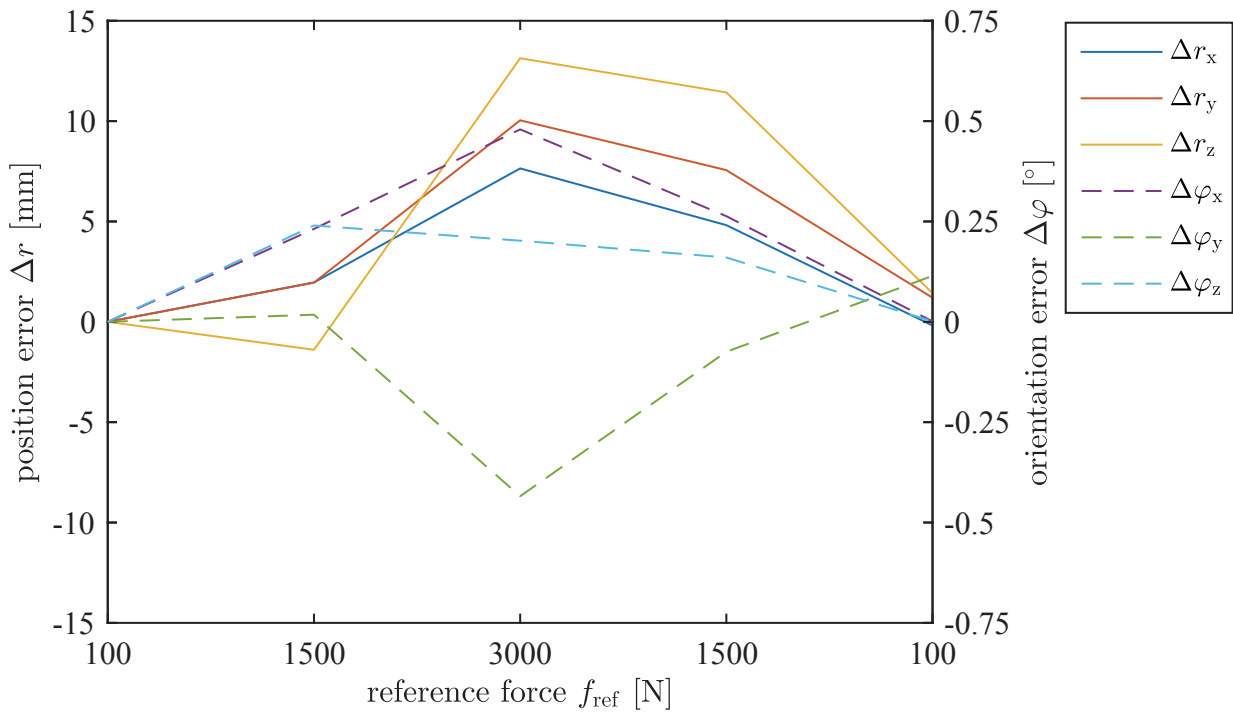


Figure 4.9: Progression of the pose while increasing and decreasing the cable tension using the non-linear cable model

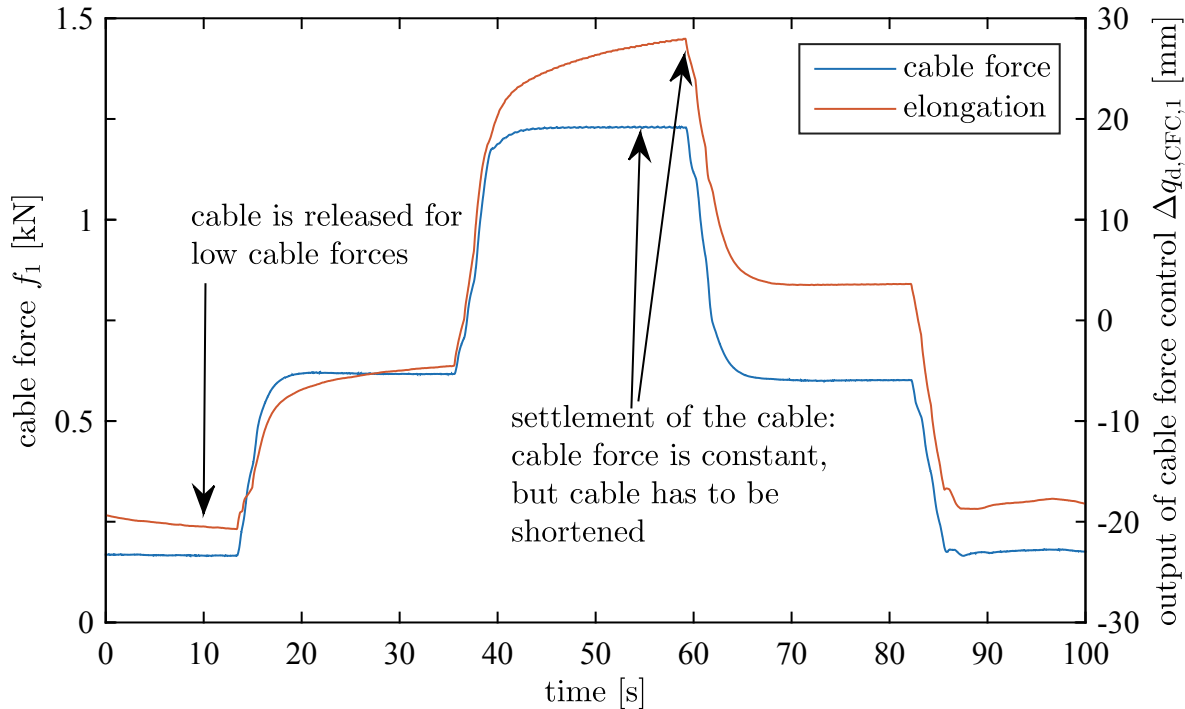


Figure 4.10: Settlement of the cable while reaching a new tension level

Table 4.3: Investigated points within the workspace with  $m_p=25\text{ kg}$  and  $m_p=105\text{ kg}$  (IPAnema 3)

nr		$r_x [\text{m}]$	$r_y [\text{m}]$	$r_z [\text{m}]$
{1, 6, 11}	{-1.0, -3.0, -5.0}	0.0	2.0	
{2, 7, 12}	{-1.0, -3.0, -5.0}	-3.0	1.5	
{3, 8, 13}	{-1.0, -3.0, -5.0}	-4.0	0.0	
{4, 9, 14}	{-1.0, -3.0, -5.0}	-2.0	0.0	
{5, 10, 15}	{-1.0, -3.0, -5.0}	0.0	0.0	

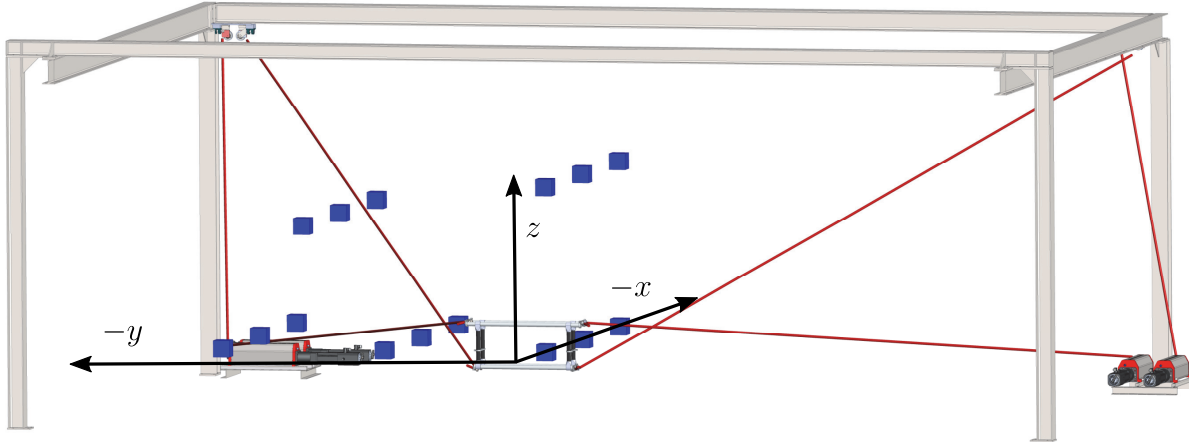


Figure 4.11: Investigated points (blue boxes) within one quarter of the robot's workspace

### 4.2.2 Static Investigation

The investigation of the position accuracy is based on a grid of 15 points, which are visualized in Fig. 4.11 and their numbers are given in Table 4.3. The grid is located in one quarter of the workspace, which can be reached from one fixed position of the laser tracker. As the robot geometry is symmetric, the results received in one quarter can be generalized for the complete robot. The points can be reached both with the unloaded platform and an additional payload of 80kg. Thus, the same grid is used which makes the results easier to compare.

The results for the position accuracy for the grid are presented in Fig. 4.12 for the inverse kinematics, in Fig. 4.13 for the force control with minimal cable forces and in Fig. 4.14 for the force control with medium cable forces.

For all three approaches, the results are in the same order of magnitude: the mean position accuracy amounts to 50 mm and the orientation to 2°. Looking more into detail, one recognizes that the standard deviation is comparatively smaller using IK, whereas the force controlled results have higher deviations. As the IK works in open-loop, it is less influenced by disturbances, whereas the position accuracy achieved with the force controlled

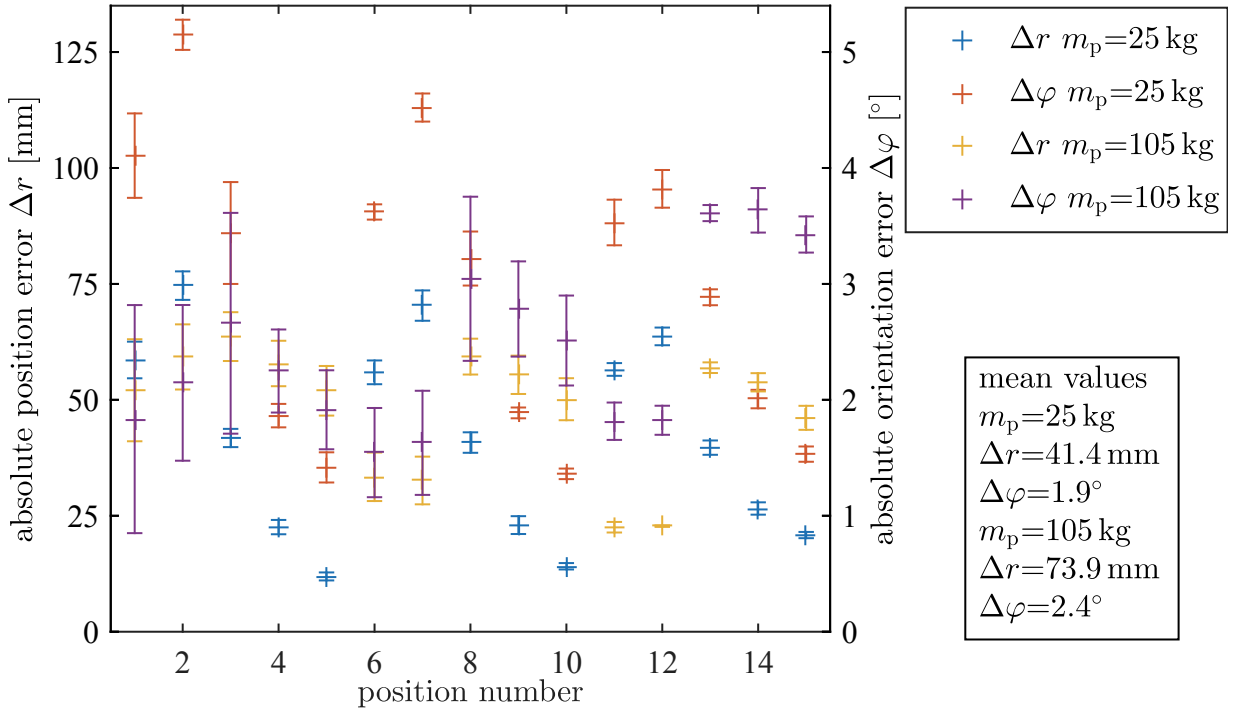


Figure 4.12: Absolute position and orientation accuracy reached with inverse kinematics

approaches is influenced by many parameters. With the medium cable forces derived by the ACF, the accuracy is roughly 20% higher compared to QP and IK.

From the evaluation of the points within the workspace, one can conclude that inverse kinematics and force control lead to comparatively the same position accuracy. In the next step, the focus lies on the investigation of the workspace border.

### 4.2.3 Experimental Workspace Analysis

The workspace of a robot is one of the most important design criteria of a robot. From the definition of the WFW given in section 2.2.1 follows that at the workspace border at least one cable force reaches either the minimum or maximum cable force. At the workspace border, the robot is at its extreme point of operation which raises the question of stability and position accuracy.

To receive deeper insight of the influence of the relative distance to the workspace, discrete points on a straight line starting from the workspace centre toward the border are investigated, as depicted in Fig. 4.15. The straight line parametrized with  $\chi$  for  $0 \leq \chi \leq 1$  by

$$\mathbf{x}_d = \mathbf{x}_{sp} + \chi(\mathbf{x}_{ep} - \mathbf{x}_{sp}) \quad , \quad (4.7)$$

where the starting point is set to  $\mathbf{x}_{sp} = [1 \ 1 \ 1]^T \text{m}$ . For the unloaded case, the endpoint is set to  $\mathbf{x}_{ep} = [-1.0 \ -3.5 \ 2.5]^T \text{m}$ , and with payload to  $[-1.0 \ -2.63 \ 1.88]^T \text{m}$ . For the experiments,

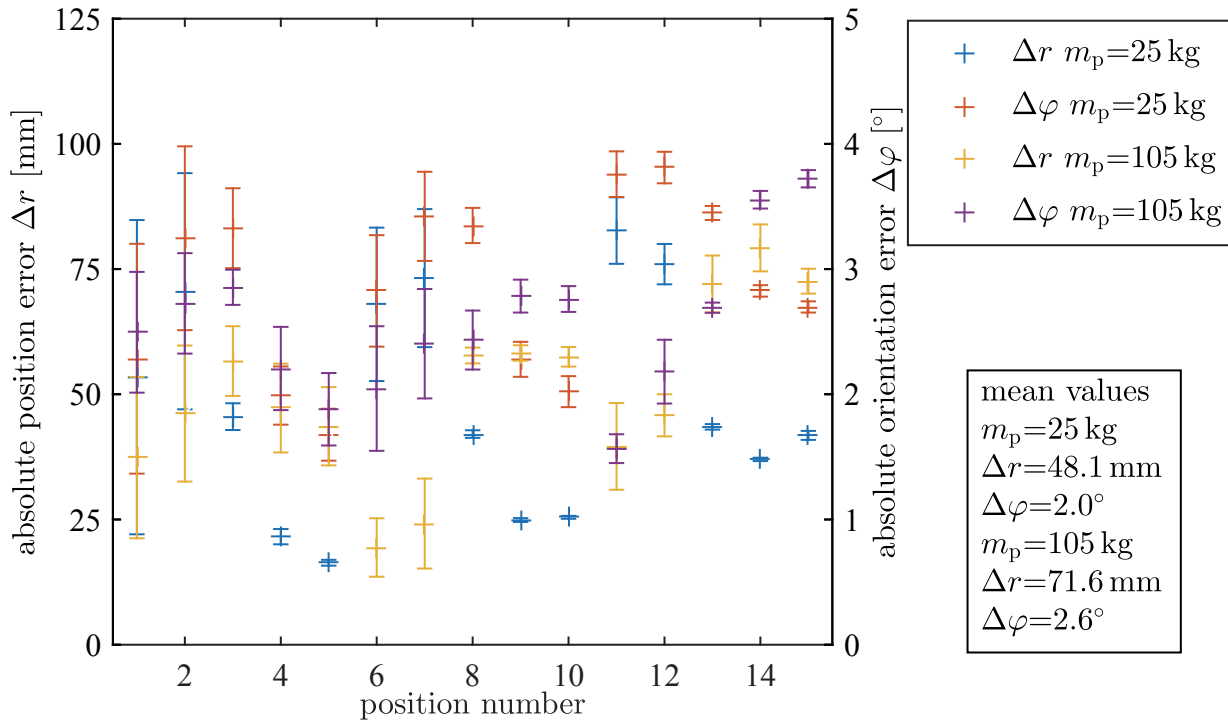


Figure 4.13: Absolute position and orientation accuracy reached with force control and minimal cable forces derived by QP algorithm

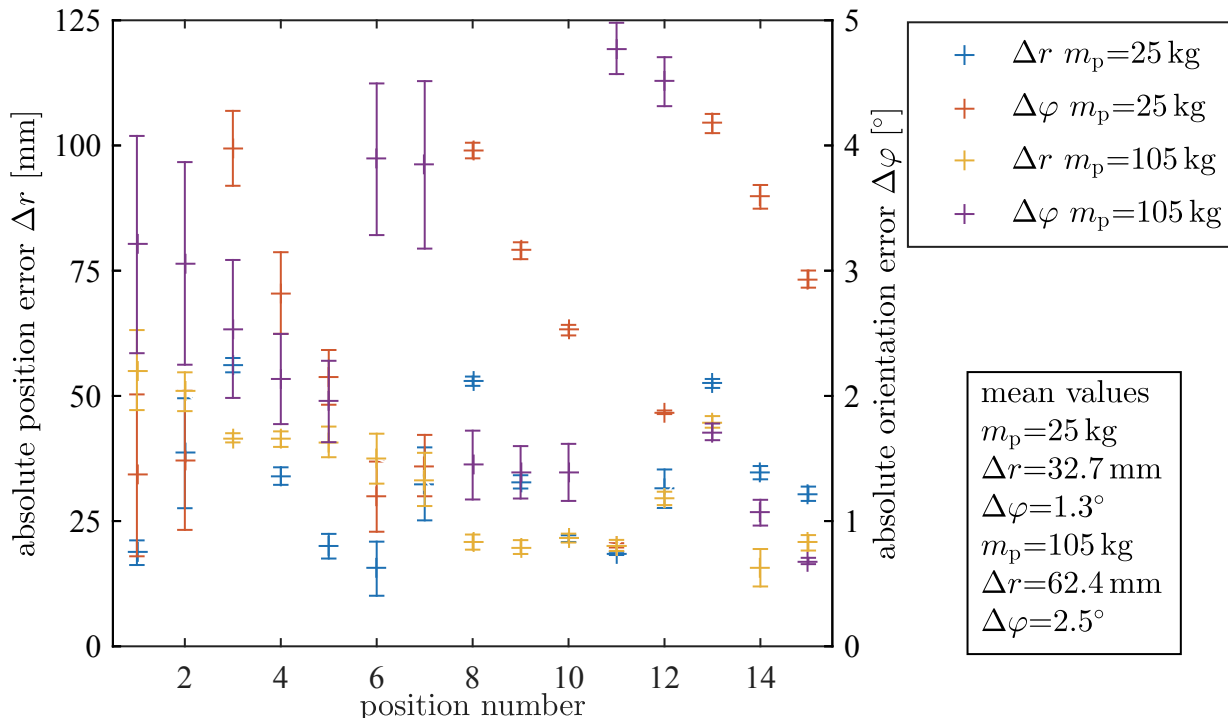


Figure 4.14: Absolute position and orientation accuracy reached with force control and medium cable forces derived by ACF algorithm

Table 4.4: Investigated points at the workspace border with  $m_p=25\text{ kg}$  and  $m_p=105\text{ kg}$  (IPAnema 3)

nr	$r_{x,25\text{ kg}} [\text{m}]$	$r_{x,105\text{ kg}} [\text{m}]$	$r_{y,25\text{ kg}} [\text{m}]$	$r_{y,105\text{ kg}} [\text{m}]$	$r_{z,25\text{ kg}} [\text{m}]$	$r_{z,105\text{ kg}} [\text{m}]$
1	-2.58	-2.39	-4.48	-4.08	0.92	0.73
2	-1.31	-1.23	-4.45	-4.03	0.70	0.52
3	-1.43	-1.23	-4.32	-3.49	1.90	1.31
4	-2.86	-2.33	-3.73	-2.91	2.54	1.73
5	-1.35	-2.04	-2.86	-1.56	2.81	2.20
6	-1.25	-1.97	-1.77	-0.65	3.01	2.40
7	-2.43	-1.86	-1.97	0.25	3.00	2.52
8	-2.28	-1.95	-0.82	1.13	3.12	2.36
9	-2.12	-2.99	0.25	1.26	3.18	2.35
10	-2.28	-2.85	1.32	0.25	3.11	2.50
11	-3.28	-3.03	0.25	-0.78	3.16	2.40

investigated points on a straight line with  $m_p = 25\text{ kg}$  (blue) and  $m_p = 105\text{ kg}$  (red)

investigated points on the workspace border with  $m_p = 25\text{ kg}$  (black) and  $m_p = 105\text{ kg}$  (orange)

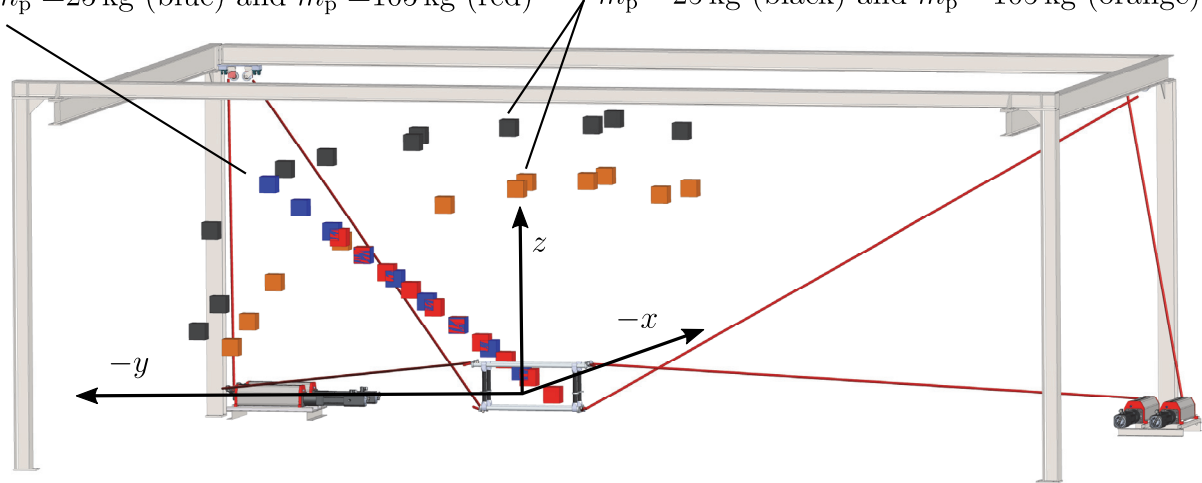


Figure 4.15: Investigated points at the workspace border

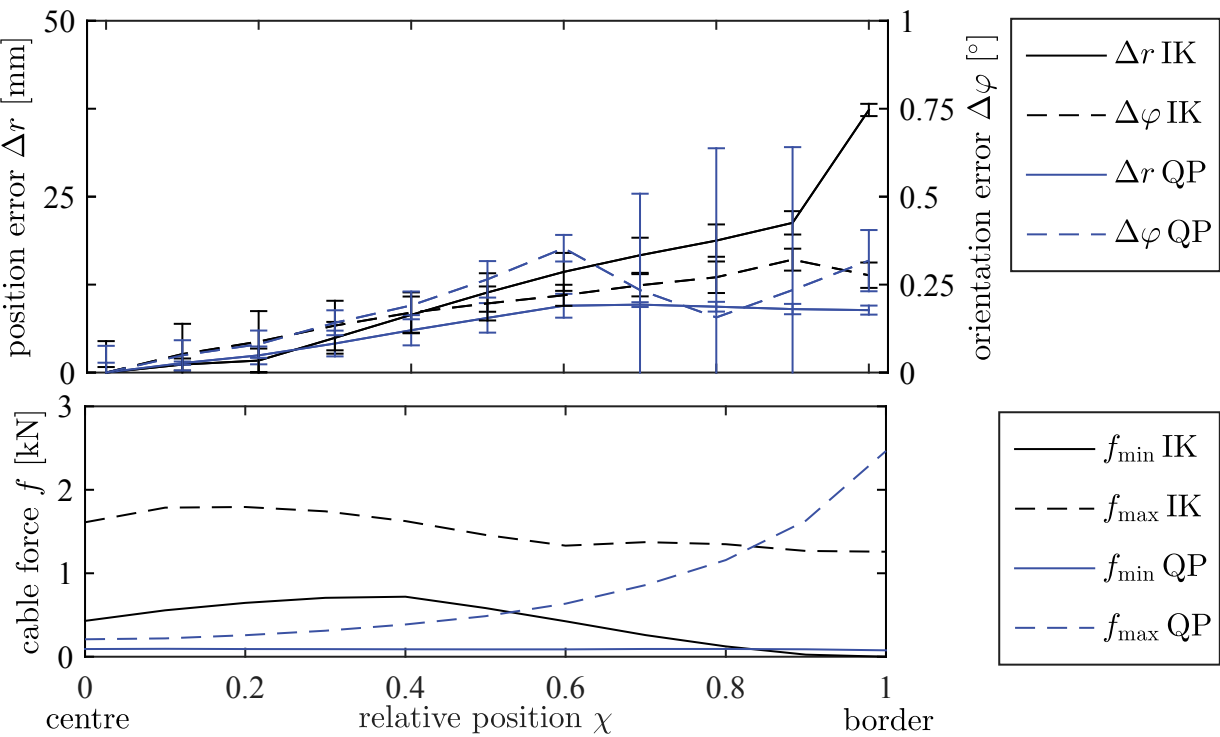


Figure 4.16: Experimental investigation of the position accuracy and cable forces on a straight line from centre to workspace border with  $m_p = 25 \text{ kg}$  (IPAnema 3)

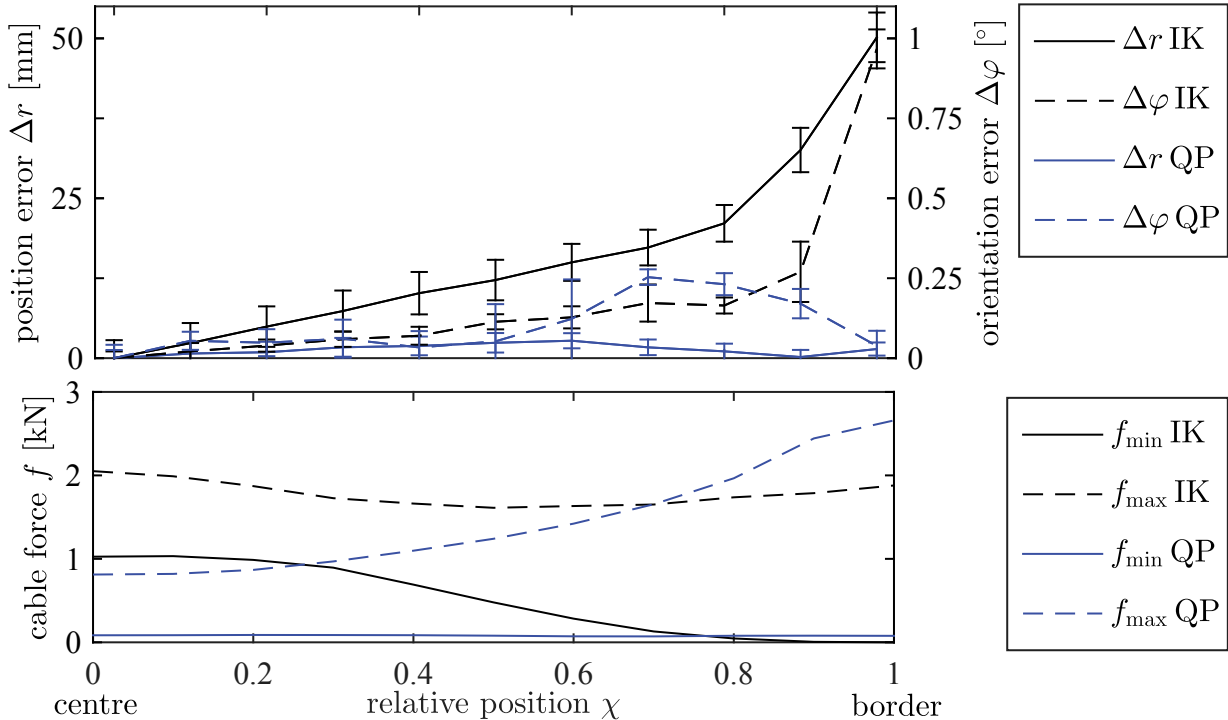


Figure 4.17: Experimental investigation of the position accuracy and cable forces on a straight line from centre to workspace border with  $m_p = 105 \text{ kg}$  (IPAnema 3)

11 evenly distributed points on the straight line are investigated and depicted in form of blue and red boxes.

The experimental results are summarized for the unloaded case in Fig. 4.16 and with payload in Fig. 4.17. The position and orientation errors with their standard deviations are visualized in the upper diagram and the actual minimum and maximum cable forces, which are derived from the cable force sensors, are shown in the lower diagram. The evaluation shows that using the IK the position and orientation errors rise mainly linear but increase very strong in the last segment before the workspace border. The large position error is caused by the sagging of single cables. Without load, this point is reached at 90% and with payload at 80% of the straight line. Before reaching this turning point, the cables are well tensed.

Using cable force control, the cable forces are within the valid limits on the complete trajectory which leads to a significantly better position and orientation accuracy when approaching the workspace border. At the progression of the cable forces, one can also recognize the effect of the cable force minimization: independent from the actual payload and position of the platform, the minimum cable force is always on the same level. Moving the platform towards the workspace, only the maximum cable force rises.

The pre-tension of the cables expressed in cable lengths as  $\Delta\mathbf{q}_0$  in the home position plays an important role when operating the robot with inverse kinematics. The experiment showed that the cables tend to sag when reaching the workspace border. To get a deeper insight into this phenomenon, the experiment is conducted in an inverted way: using cable force control, the robot is moved to the end position of the straight line. There, the actual cable length offset derived from the cable force controller needed to reach feasible cable forces is used as constant offset and, thus,  $\Delta\mathbf{q}$  is added to  $\Delta\mathbf{q}_0$ . Driving back with only IK and application of this offset leads to feasible cable forces also at the beginning of the straight line. This shows that with a suitable choice of the pre-tension, the workspace border can be reached without cable force control. As this pre-tension seems hard to find in advance, the straight line experiment suggests that the force control is necessary at the workspace border.

To place the analysis of the robot behaviour at the workspace border on a broader data base, 11 points lying on the workspace border are investigated. The points are derived from the workspace hull for the actual payload of the robot and are visualized in Fig. 4.15 and given as numbers in Table 4.4.

For the border points, a path was programmed which always approaches the point starting from the workspace centre. This allows for observing the cable forces. The recorded cable forces on the trajectory are discretized regarding their position relative to the workspace border. The cable forces are defined as valid, when all cable forces are between 50 and 3,200 N. As the trajectory lies within the wrench feasible workspace, the cable forces should

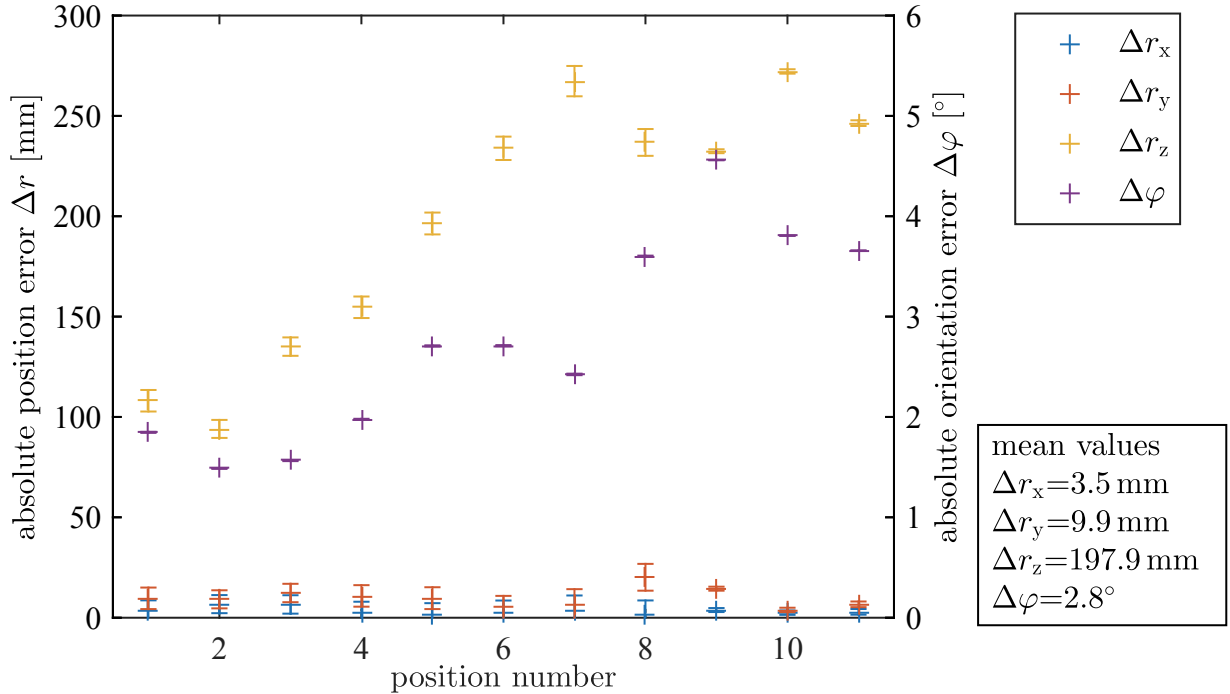


Figure 4.18: Position accuracy at the workspace border using IK with  $m_p = 105\text{ kg}$  (IPAnema 3)

be all valid. The evaluation, presented in Fig. 4.20, confirms the findings that using only inverse kinematics and with additional payload the cables are tensed until roughly the last 20% of the workspace. Using cable force control, the validity of the cable forces is significantly higher. Reasons for non-valid cable force distributions in spite of cable force control can be saturation or model inaccuracies. Also the disturbances and calibration error of the cable force measurement contribute to this result.

Beside the cable forces, the position and orientation when the robot reaches the border points are also measured. The results with inverse kinematics and force control are presented for  $m_p = 105\text{ kg}$  in Fig. 4.18 and Fig. 4.19, respectively. The evaluation shows that the position error arises mainly in the vertical axis and amounts up to 250 mm in position 7 and 10. Using force control, the position accuracy is significantly higher. Especially in vertical direction, large parts of elastic displacement are compensated by the force control and accuracy is improved by more than 50%.

The previous findings are all derived from static investigations: during measurement, the desired position is constant, all control loops are settled and the platform stands still. In the following, the accuracy during movement of the robot is investigated.

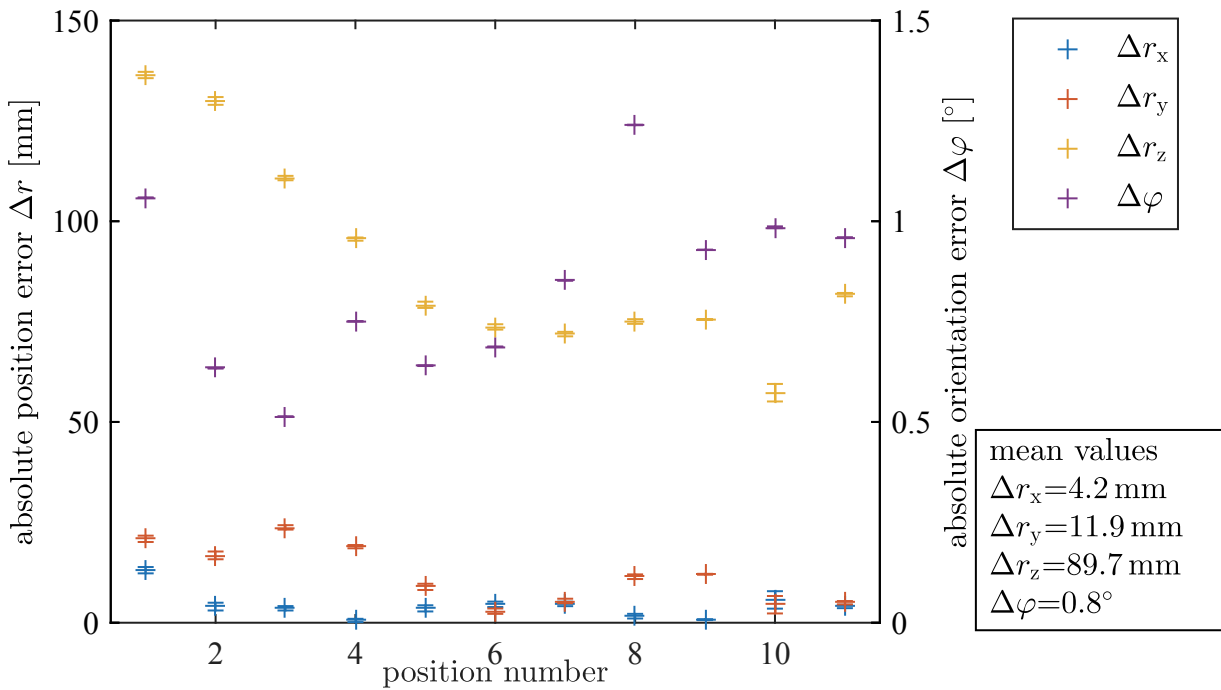


Figure 4.19: Position accuracy at the workspace border using force control with  $m_p = 105 \text{ kg}$  (IPAnema 3)

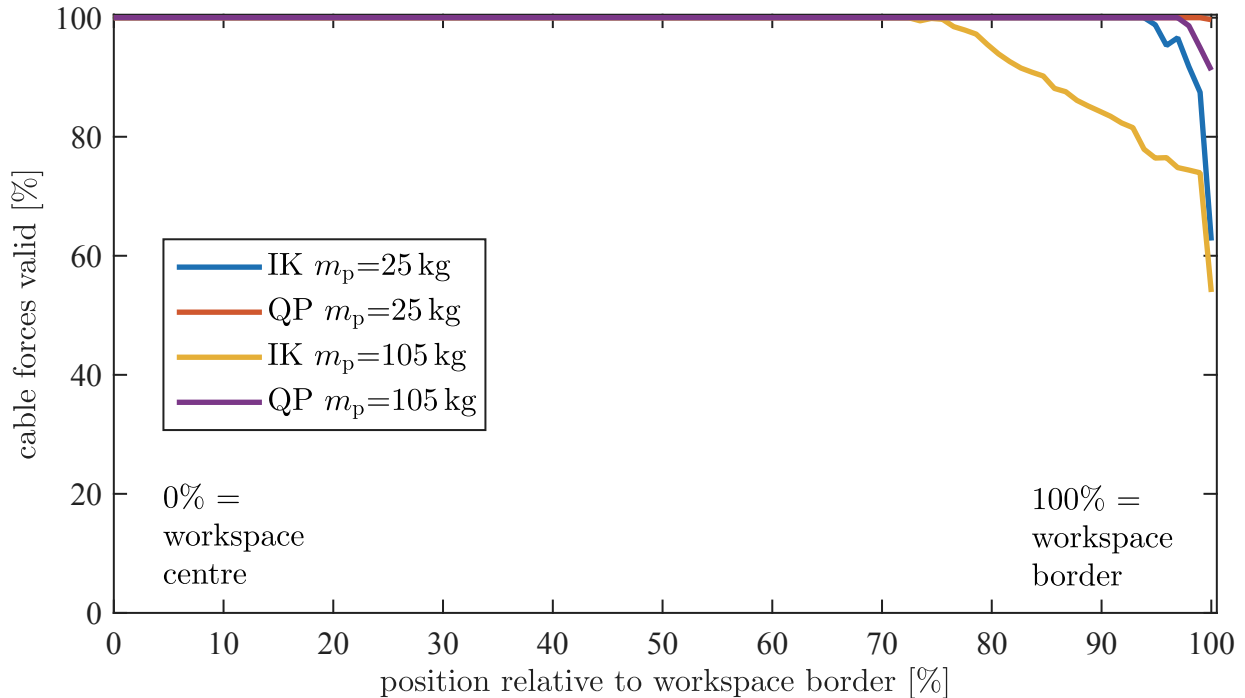


Figure 4.20: Validity of the cable forces at the position relative to the workspace border using inverse kinematics and force control and different payloads (IPAnema 3)

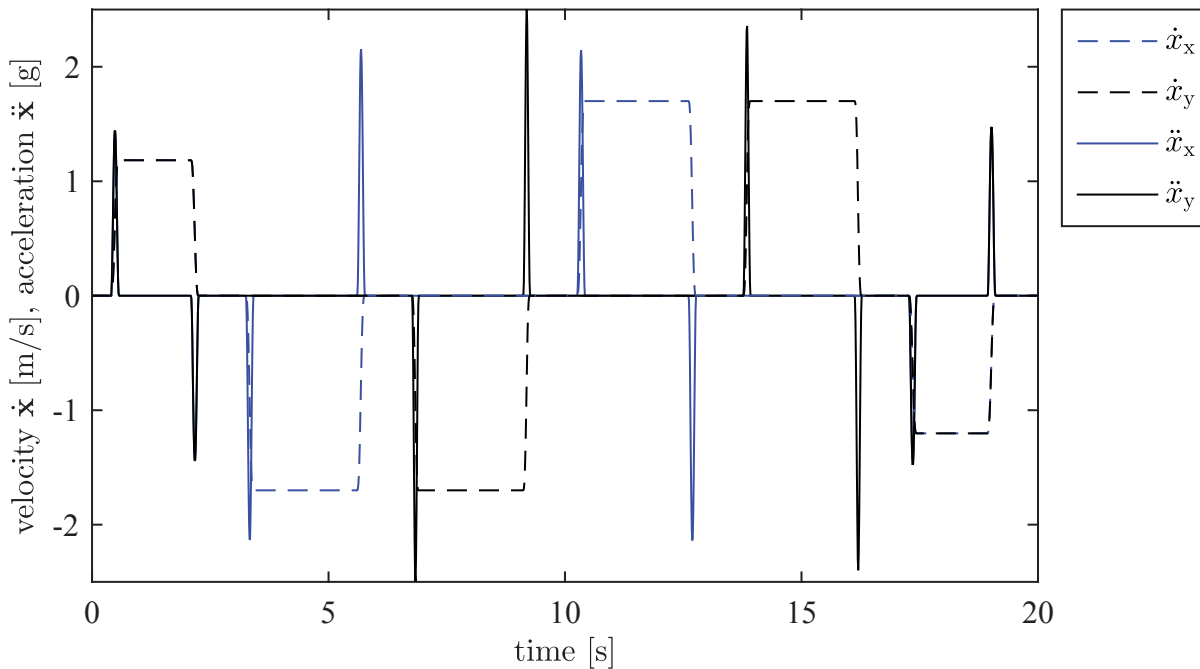


Figure 4.21: Progression of velocity and acceleration along the trajectory with  $\dot{x}_{\max}=1.7 \text{ m/s}$  and  $\ddot{x}_{\max}=25 \text{ m/s}^2$  (IPAnema 3)

#### 4.2.4 Dynamic Investigation

Beside the static position accuracy, also the dynamic behaviour regarding path accuracy, stability and reachable dynamic is of interest. Trajectories on IPAnema 3 and IPAnema 3 Mini are investigated exploiting their maximum dynamic capabilities.

For the IPAnema 3, a rectangle which measures 4 by 4 m is chosen with a maximum velocity of  $\dot{x}_{\max}=1.7 \text{ m/s}$  and acceleration of  $\ddot{x}_{\max}=25 \text{ m/s}^2$ . The progression of velocity and acceleration are presented in Fig. 4.21. Based on the position measurement with the laser tracker, the path accuracy shown in Fig. 4.22 is established. One can see that the overall accuracy is better with force control but the peaks arising from the acceleration and deceleration are lower with inverse kinematics. This result underlines that the open-loop control using the inverse kinematics is more robust in withstanding transient disturbances.

On the IPAnema 3 Mini, a cuboid measuring 0.44 m by 0.4 m by 0.4 m with  $\dot{x}_{\max}=2.0 \text{ m/s}$  and  $\ddot{x}_{\max}=40 \text{ m/s}^2$  is investigated. The nominal and measured acceleration forces in  $x$ -axis are shown in Fig. 4.23. The progression of the cable forces during this dynamic trajectory is depicted in Fig. 4.24. Due to the minimal tension level, the cable forces are on a low level but especially during the acceleration phases, some forces fall temporarily below the minimum force of 5 N.

The findings are summarized at the end of this chapter. Next, the investigation of the robot dynamics by means of the platform's eigenfrequencies is carried out.

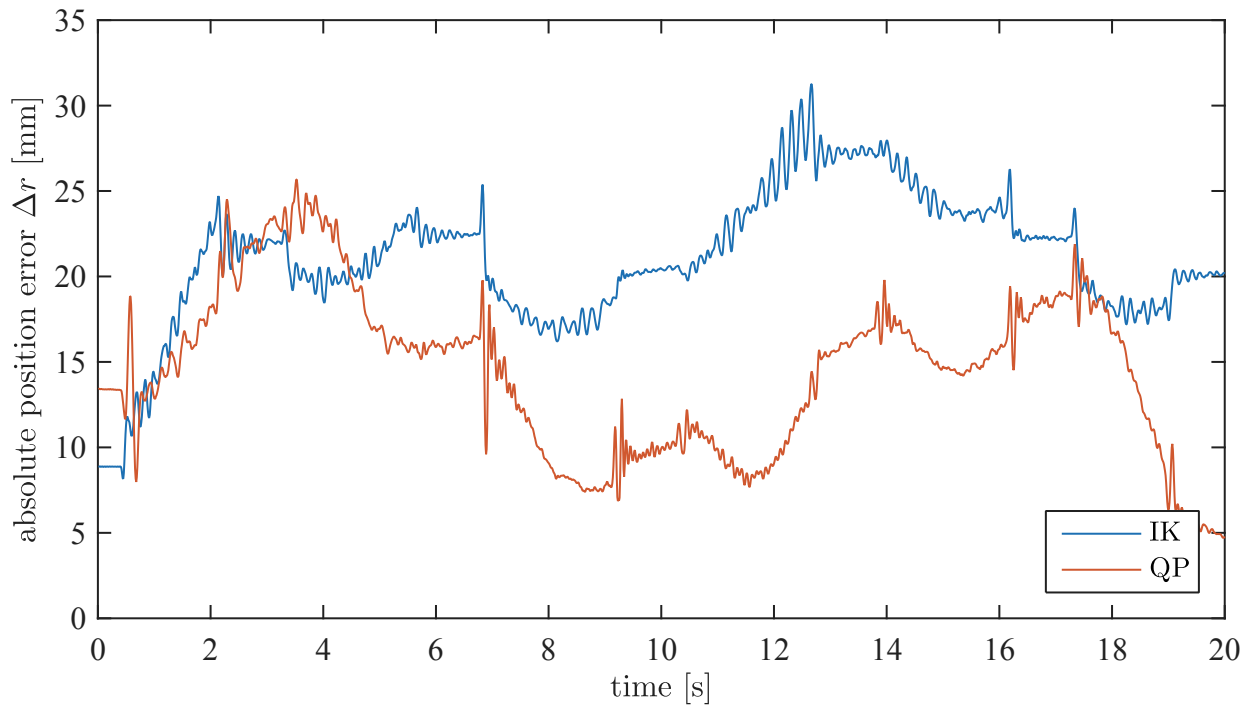


Figure 4.22: Absolute position error on a dynamic trajectory using IK and force control and  $m_p = 25 \text{ kg}$  (IPAnema 3)

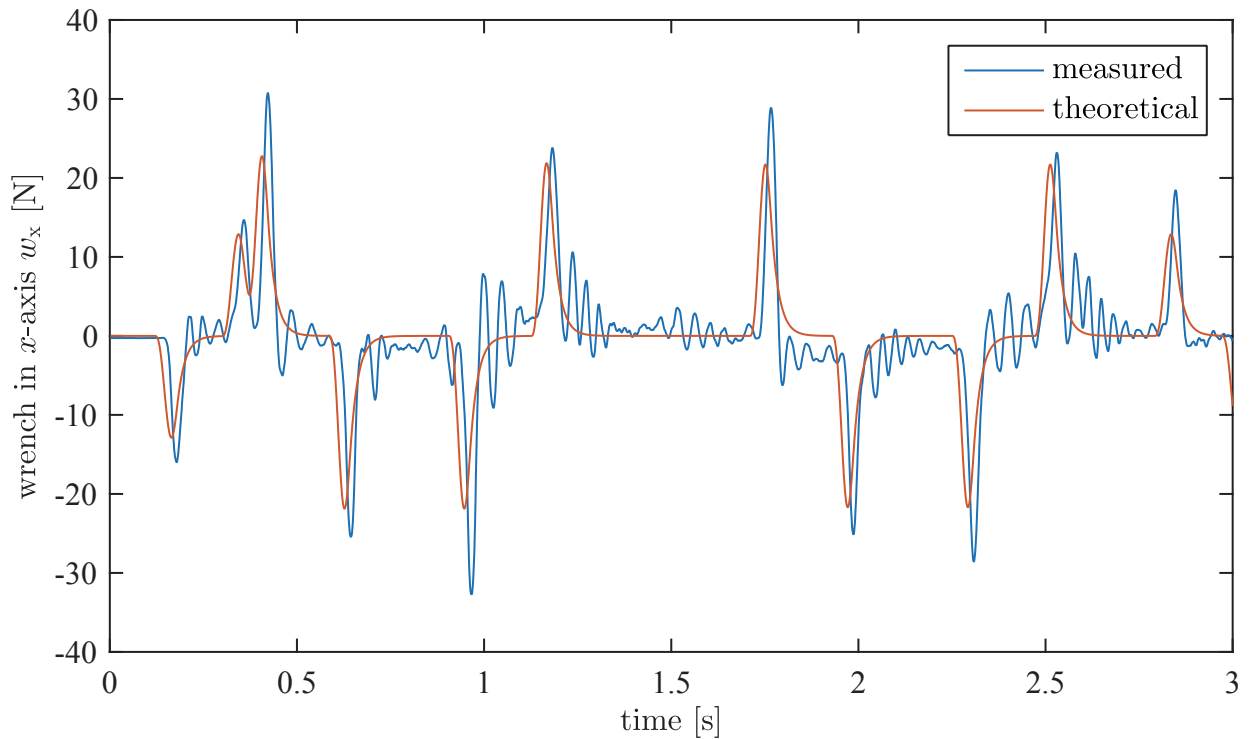


Figure 4.23: Experimental and calculated wrench in  $x$ -axis with a maximum acceleration of  $4.0 \text{ g}$  (IPAnema 3 Mini)

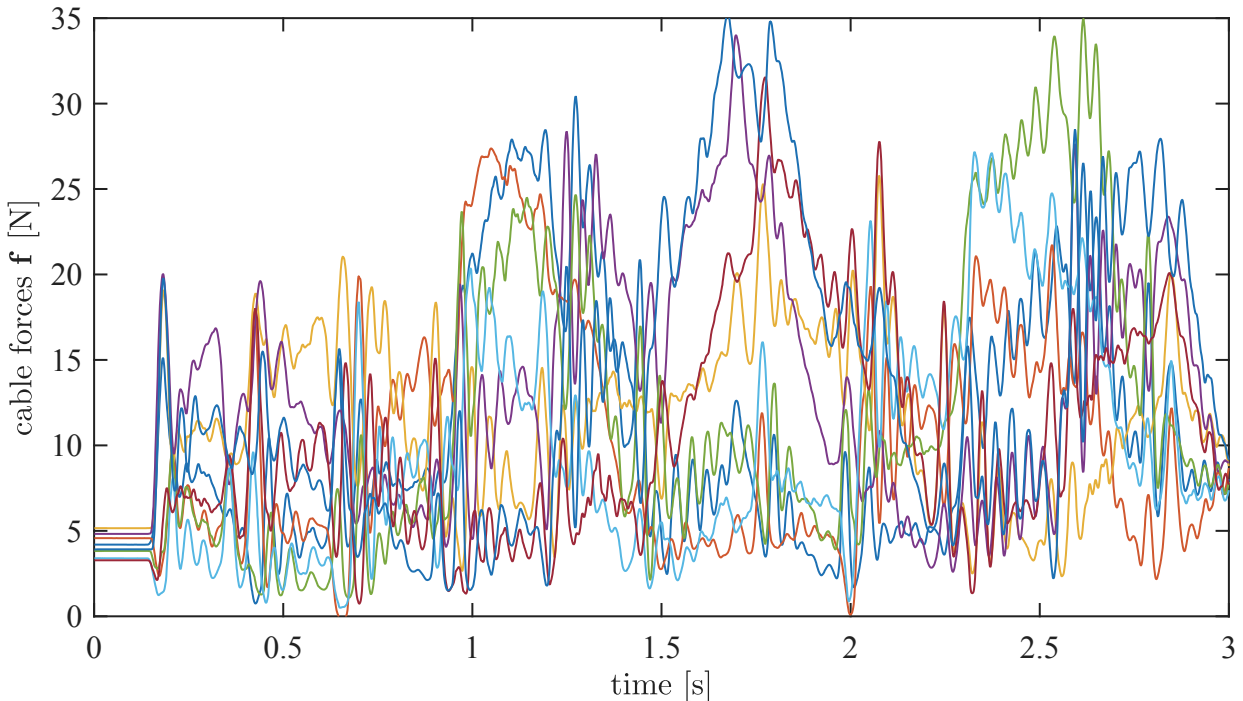


Figure 4.24: Progression of the cable forces along a trajectory with a maximum acceleration of 4.0 g (IPAnema 3 Mini)

### 4.3 Eigenfrequencies of the Platform

The eigenfrequency or also denoted as natural frequency is the frequency in which a system oscillates after an external stimulation. Therefore, the eigenfrequency can be experimentally determined for a dynamic system and is as a characteristic value of the system dynamics. The system identification conducted for the stability analysis of the operational space position controller showed that the platform can be modelled as a spring-mass-damper system. The eigenfrequency  $\omega$  of an undamped mechanical system can be derived by

$$\omega = \frac{1}{2\pi} \sqrt{\frac{c_j}{m_p}} , \quad (4.8)$$

where  $c_j$  is a diagonal element of the operational space stiffness matrix  $\mathbf{K}_x$ . It follows that the eigenfrequencies and, thus, the system dynamics change under different platform masses and stiffness. As the payload can amount multiples of the own weight of the platform, the dynamic of a cable robot may change significantly. Especially, the influence of the platform mass on the robot dynamic behaviour is of practical interest, as, for example, in handling applications the payload of the platform changes during the process. Furthermore, the robot stiffness can be increased with higher cable tensions due to the progressive spring behaviour of the cable and the geometrical stiffness. To investigate the influence of the

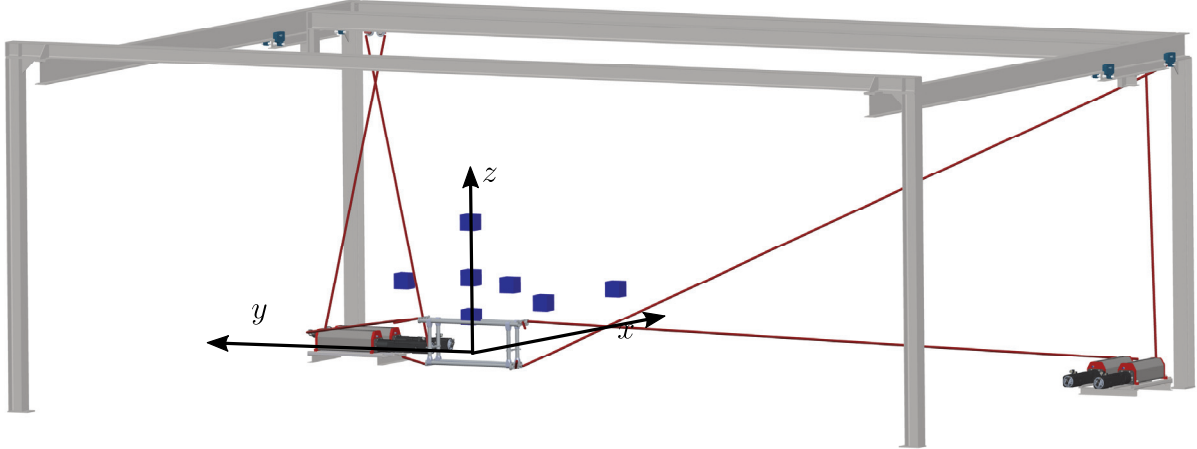


Figure 4.25: Investigated points for the identification of the eigenfrequencies (enlarged view of the IPAnema 3 robot)

Table 4.5: Investigated points for the identification of the eigenfrequencies (IPAnema 3)

nr	1	2	3	4	5	6	7
$r_x$ [m]	0.0	0.0	0.0	2.0	4.0	4.0	4.0
$r_y$ [m]	0.0	0.0	0.0	0.0	0.0	1.5	3.0
$r_z$ [m]	0.5	1.0	1.7	0.5	0.5	0.5	0.5

platform mass and the tension level on the platform dynamic, the eigenfrequency of the platform is experimentally determined.

To study the dynamic behaviour, a sinus oscillation with constant amplitude and rising frequency is applied to the desired position of selected axes in operational space. The resulting platform movement is measured indirectly by the forward kinematics which incorporates the estimated cable elongation based on the cable force measurement. The maximum frequency amounts to 15 Hz. According to the system identification carried out for the drives in section 3.3.1, for the desired frequency band, the transfer function of the drives can be approximated with 1. The dynamic behaviour of other mechanical components like the machine frame and pulleys are insignificant and can be neglected. Thus, the observed dynamic behaviour results only from the platform and the cables. Using the QP algorithm, the cables are tensed on five tension levels with reference forces  $\mathbf{f}_{\text{ref}}$  from 100 to 3,000 N. To exclude the dynamics of the cable force and operational space position controller, the controllers are only used to initially tense the cable but are disabled during the experiment itself.

The experiment is carried out on the IPAnema 3 with the own weight of the platform (25 kg) and an additional load of 80 kg. In total, seven points are investigated which are visualized in Fig. 4.25 and given as numbers in Table 4.5. The evaluation of the eigenfrequencies shows a strong influence of the platform load as can be seen in Fig. 4.26. With

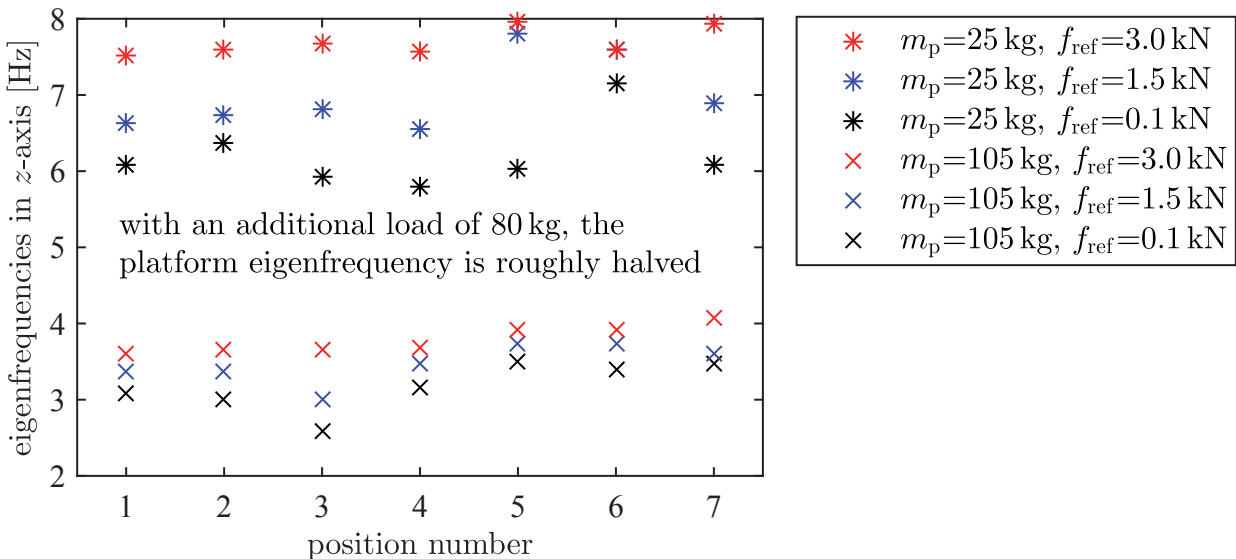


Figure 4.26: Eigenfrequency of the platform in  $z$ -axis for different tension levels (experimentally determined)

the additional payload, the eigenfrequency is approximately halved from 7.0 Hz to 3.5 Hz. The influence of the tension level is lower and the eigenfrequency can be shifted in a range from 15 to 30%.

Obviously, the stiffness of the robot can be influenced with the choice of the cable tension. To get further insight, the eigenvalues  $\lambda$  of the stiffness matrices derived from the stiffness model (2.22) are analysed. The minimal and maximal eigenvalues of the operational space stiffness matrix  $\mathbf{K}_x$  are presented in Fig. 4.27 for three tension levels at seven discrete points in the workspace. The results underline that the stiffness of the platform is position-dependent and correlates in general with the tension level of the cables. This leads to the question, how much the geometrical stiffness contributes compared to the progressive cable stiffness. For this purpose, the eigenvalues of  $\mathbf{K}_g$  and  $\mathbf{K}_l$  are evaluated separately and plotted in Fig. 4.28. The logarithmic scale shows that the cable stiffness is one to two magnitudes higher than the geometrical stiffness. On the relative level, the geometric stiffness rises stronger with higher cable forces. The results give another important insight into the positive definiteness of the geometrical stiffness matrix. Some of the minimal eigenvalues of  $\mathbf{K}_g$  are not depicted because they are negative. In the positions 1, 2 and 4 the minimal eigenvalue is only positive for the higher tension level. From this observation, one can conclude that the positive definiteness of the geometric stiffness matrix depends not only on the robot geometry and pose but also on the force distribution. This is important for the stability of a cable force control which needs a positive definite geometric stiffness matrix, according to section 3.1.3. To ensure stability of a cable force control without additional operational space position control, one has to check the positive definiteness of  $\mathbf{K}_g$  for every pose and cable force distribution.

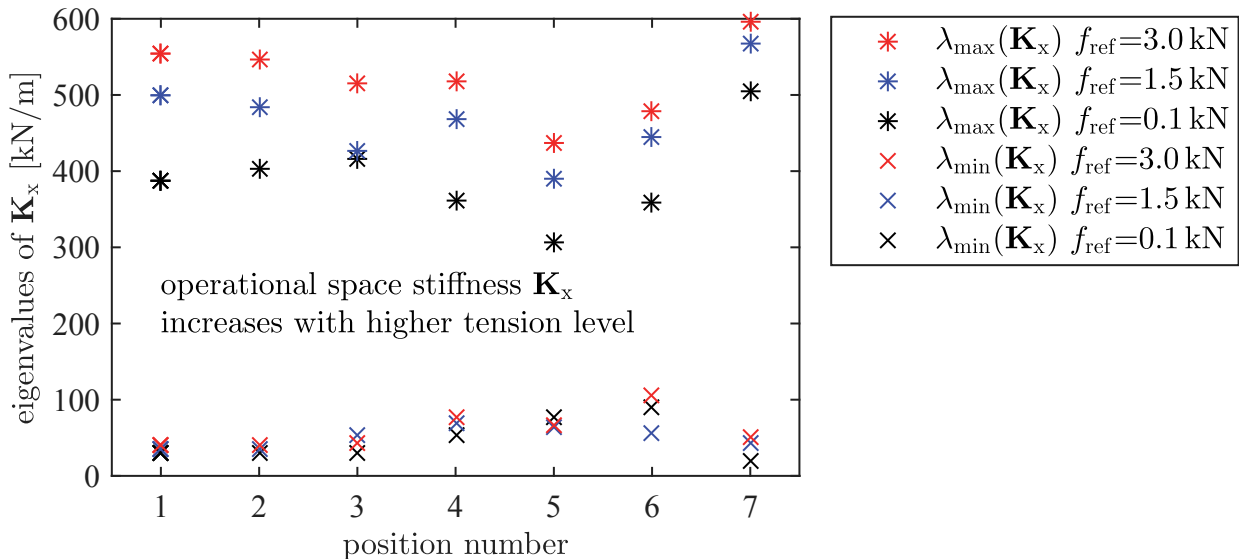


Figure 4.27: Minimal and maximal eigenvalues of the operational space stiffness matrix for different tension levels and  $m_p=105 \text{ kg}$  (model-based)

The investigation of the eigenfrequencies showed that the progressive spring characteristic has a significant influence and the robot's stiffness can be stiffened with higher cable forces. Next, the impact of the tension level on the energy consumption is studied.

## 4.4 Energy Consumption

In the last section, it was shown that high tension levels can increase the eigenfrequency and, thus, the available dynamics of the robot. It is obvious that higher cable forces go with a higher energy consumption of the robot. If there is no need of high stiffness or dynamics, the cable forces can be controlled to the minimal pre-tension using the QP algorithm. As shown in section 4.2.2, the position accuracy remains almost on the same level. To analyse the energy consumption of the robot, a simulation model for the losses of the complete actuator unit is established and verified in the following. Based on this model, the energy efficiency of the cable robot is discussed and compared to a serial industrial robot.

### 4.4.1 Energy Consumption Model of the Actuator Unit

#### Model Structure

The energy consumption model comprises a pulley mechanism for guiding the cable from the winch to the mobile platform, winch, gearbox and drive with servo amplifier, as shown in Fig. 4.29. To derive the total power consumption of the robot, the actual power of all  $m$  legs is summed up under the consideration of recuperation capabilities. Recuperation is possible either between drives within the DC link or with the recovery function of the power

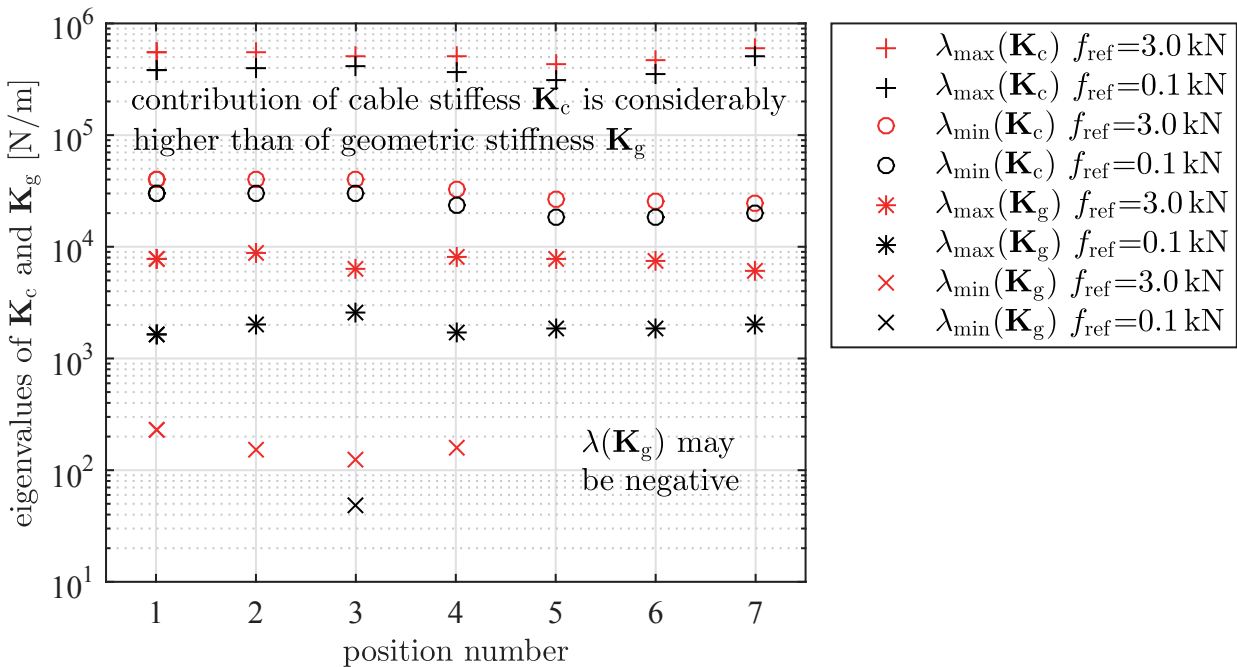


Figure 4.28: Minimal and maximal eigenvalues of the geometric and cable stiffness matrices for minimal and maximal tension level and  $m_p=105 \text{ kg}$

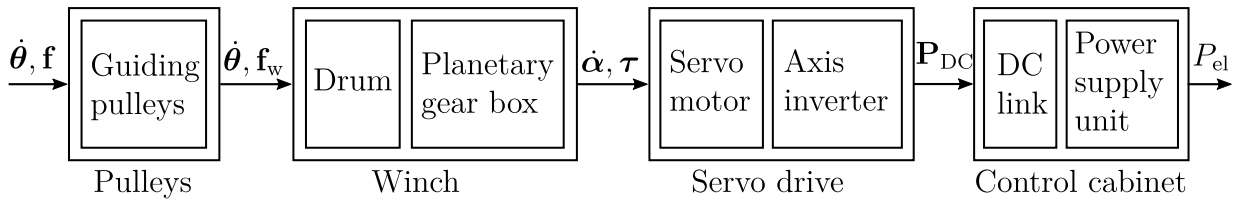


Figure 4.29: Subsystems of the energy consumption model

supply unit back to the electricity grid. In the following, the modelling of the subsystems starting with the pulleys is described in detail.

### Pulley Model

As discussed in detail in section 3.7.2, the transmission between the drum and the platform is realized with a series of pulleys which have friction and contribute for losses. For the simulation of the pulley losses, the model of the pulley friction compensation is taken as base. Contrary to the model applied for cable force measurement, in the energy model, the cable force acting at the platform  $F_{n_p}$  is given, and the force  $f_w$  acting at the drum is searched. Thus, (3.34) has to be solved for the cable force before the pulley  $F_{j-1}$  which gives

$$F_{j-1} = \frac{F_j \left( 2 - \operatorname{sgn}(\dot{\theta}_i) \mu_j \sqrt{2(1 - \cos(\beta_j))} \right) - 2F_{p_v} \dot{\theta}_i}{2 + \operatorname{sgn}(\dot{\theta}_i) \mu_j \sqrt{2(1 - \cos(\beta_j))}} \quad (4.9)$$

and has to be evaluated for each pulley starting from the platform. The index  $i$  refers to the cable number, while the index  $j$  defines the cable segments between the series of pulleys. The total friction force  $F_f$  in the pulley mechanism of one cable is then derived by the difference between the cable forces in the first and last segment according to (3.41). The influence of the microscopic friction on the energy consumption is assumed to be minor and, thus, only the Coulomb and viscose friction model is applied in the following.

### Mechanical Model of the Winch

The subsystem winch describes the mechanical transmission between the cable leaving the drum with velocity  $\dot{\theta}$  and cable force  $f_w$  to the torque  $\tau$  and angular speed  $\dot{\alpha}$  at the motor. The model expands the equation of motion for one joint (2.32) by friction terms. For this purpose, the model includes friction and inertia of the complete winch, planetary gear box and rotor of the drive. The velocity transmission is linear and can be described by

$$\dot{\alpha} = \frac{\dot{\theta}}{r_w} , \quad (4.10)$$

where  $r_w$  is the transmission ratio defined by the drum diameter and gear ratio. The force transmission of the winch is described by  $r_w f_w$ . The rotational inertia of the mechanical parts is summarized in  $J_w$  and the inertia moment is derived by  $J_w \ddot{\alpha}$ . The friction model for the winch and gear box includes Coulomb friction with  $\mu_w$ , viscous friction described by  $F_{wv}$  and Stribeck friction parametrized with velocity  $\dot{\alpha}_s$  and static friction coefficient  $F_s$  (Andersson, Söderberg et al. 2007). The model for the motor torque  $\tau$  is

$$\tau = r_w f_w - J_w \ddot{\alpha} - (r_w f_w \mu_w + (F_s - r_w f_w \mu_w) e^{-\frac{|\dot{\alpha}|}{\dot{\alpha}_s}}) \operatorname{sgn}(\dot{\alpha}) - F_{wv} \dot{\alpha} , \quad (4.11)$$

which corresponds to the equation of motion of one winch including friction. Next, the electrical model of the servo drive is described.

### Electrical Model of the Servo Drive

The servo drive model outputs the direct current (DC) link power of one drive  $P_{DC}$  for the actual torque and angular velocity at the shaft of the motor. The shaft power of the drive  $P_s$  can be derived by  $c_m \dot{\alpha} \tau$ . The scale factor  $c_m$  represents the inverter losses. The servo current control is typically field orientated: the current is divided into the torque generating current  $i_q$  and magnetizing current  $i_d$  and the total current  $I$  is derived by  $I = \sqrt{i_d^2 + i_q^2}$ . For a non-reluctant drive, the relation between torque and current can be established by the torque constant  $\Psi_m$  with  $\tau = \Psi_m i_q$ . The field weakening current becomes relevant at high speed of the drive, when the voltage limit of the inverter is reached. In cable robots, the cable velocity is always smaller than the platform velocity, except the platform is moving

in the direction of one cable, where it is exactly equal. Accordingly, the maximum speed of a drive is reached only in rare situations. Therefore, we neglect the effect of field weakening and assume  $i_d = 0$ .

The losses of a permanent magnetized synchronous motor can be divided into three categories. The copper losses depend on the actual current and resistance  $R$  and can be calculated according to  $3I^2R$ . Using the torque constant, the copper losses can be derived from the torque by  $3\left(\frac{\tau}{\Psi_m}\right)^2 R$ . The re-magnetization losses correlate with the mechanical angular velocity of the motor  $\dot{\alpha}$  and are scaled in the model with  $c_{n1}$ . The eddy current losses rise by the square of the drive velocity and are scaled with  $c_{n2}$ . The electrical model for the servo drive including the amplifier losses can be summed up by

$$P_{DC} = c_m \dot{\alpha} \tau + 3\left(\frac{\tau}{\Psi_m}\right)^2 R + c_{n1} \dot{\alpha} + c_{n2} \dot{\alpha}^2 , \quad (4.12)$$

which is valid for both motor and generator operation.

## Electrical Model of the Control Cabinet

The model for the control cabinet summarizes all electrical components of the robot including the power supply unit for the DC link. The idle power consumption  $P_0$  includes the power consumption of peripheral equipment like fans and logical circuits of the control cabinet. All axis inverters are connected to the same DC link. Thus, there is a DC link recovery  $P_{DC,rec}$  between winches in motor and generator operation which can be described by

$$P_{DC,rec} = \sum_{i=1}^m |P_{DC,i}| - \left| \sum_{i=1}^m P_{DC,i} \right| . \quad (4.13)$$

For the total power consumption of the robot, the DC link power of each drive  $P_{DC,i}$  is summed up. The efficiency of the power supply unit in motor operation is modelled by  $c_{p,m}$ . Due to friction losses, the robot typically consumes energy. During deceleration or lowering of heavy loads, generator operation of the drives can outweigh, which means that the power contribution of all drives to the DC link  $\sum_{i=1}^m P_{DC,i}$  is negative. If the power supply unit has a recovery function, the excessive energy is fed back to electricity grid with an efficiency of recovery  $c_{p,g}$ . Otherwise, brake resistors are used which transforms the excessive energy to heat which corresponds to  $c_{p,g} = 0$ . Another possibility is the use of short term storage, e.g. in form of capacitors. The power consumption model for the control cabinet can be described by

$$P_{el} = \begin{cases} P_0 + \sum_{i=1}^m P_{DC,i} c_{p,m}, & \sum_{i=1}^m P_{DC,i} \geq 0 \\ P_0 + \sum_{i=1}^m P_{DC,i} c_{p,g}, & \sum_{i=1}^m P_{DC,i} < 0 \end{cases} , \quad (4.14)$$

where  $P_{\text{el}}$  corresponds to the actual power consumption of the robot which can be measured at the input of the control cabinet.

#### 4.4.2 Identification and Verification of the Energy Consumption Model

For the identification of the model parameters, several experiments are conducted. As the mechanical components as well as the drives are subject of production tolerances, an individual parameter set is established for each leg of the robot. The identification of the pulley model was already described in section 3.7.2. The winch and servo drive models are parametrized based on a trajectory consisting of standstill, rising velocities up to  $v_{\text{max}}$  and different cable tensions.

The recovery function of the power supply unit needs special consideration. To bring the robot system into a stationary generator operation, one single winch with a load is investigated. Lowering the load, the potential energy is recovered by the servo drive and fed back to the AC grid.

The identified parameters for the cable robot IPAnema 3 are summarized in Table 4.6 and are the basis for the following evaluation.

For the verification of the energy consumption model, a path covering one half of the workspace is investigated for different velocities up to the maximum velocity. The total power consumption derived from the measurement at the input of the control cabinet and simulation model are compared in Fig. 4.30. The mean absolute error in power consumption amounts to 245.2 W. By summing up the errors over the complete trajectory, over and under-estimations are averaged, which leads to a mean model error of 40.7 W. Thus, for this trajectory the prediction error of the power consumption amounts only to 0.89%.

#### 4.4.3 Analysis of Energy Efficiency

The developed energy consumption model allows for analysing the energy efficiency of the cable robot from different points of view. At first, the allocation of the losses to the subsystems is analysed. Next, the efficiency of the winch is determined and the influence of the tension level on the energy consumption is pointed out. In order to be able to classify the energy consumption of the cable robot, a comparison with an industrial robot is carried out.

##### Allocation of the Losses to the Subsystems

For the further analysis, the source of losses according to the modelled subsystems is investigated. Three scenarios for the robot are defined: in the first, the platform is unloaded

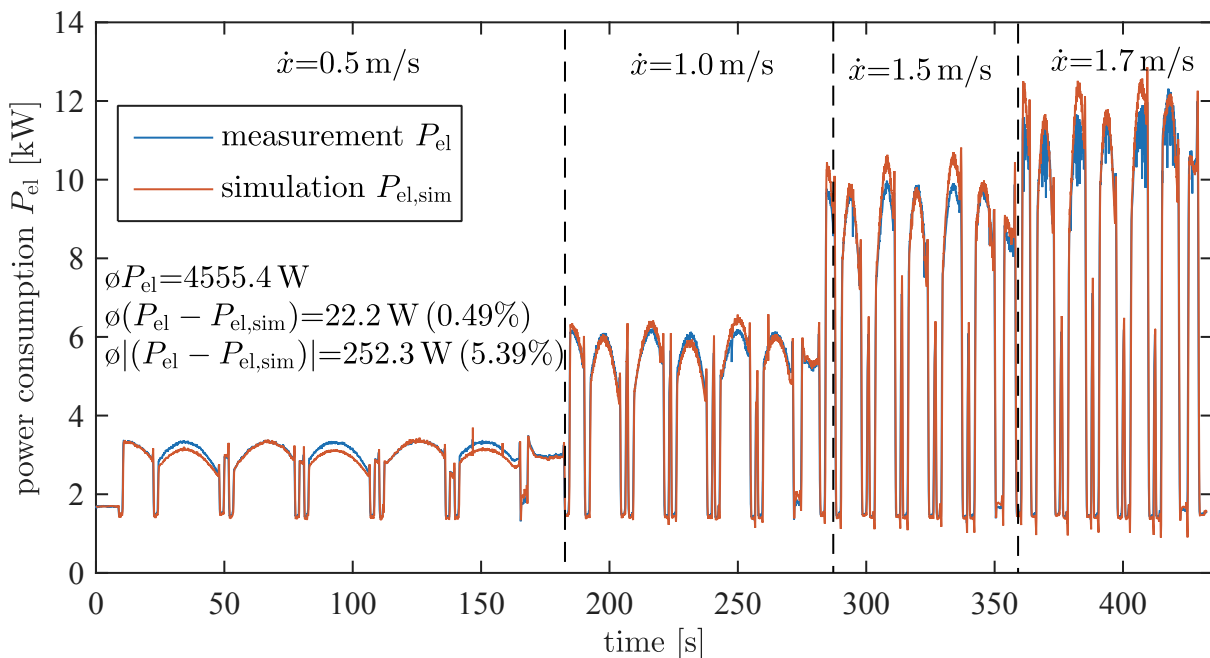


Figure 4.30: Verification of the energy consumption model using the robot and different platform velocities

Table 4.6: Identified parameters for the energy consumption model (parameters are only given for winch 1)

parameter	definition	value	unit
$\mu_p$	Coulomb friction coefficient of pulley	0.010	-
$F_{pv}$	velocity-dependent friction coefficient of pulley	41.71	N/m
$r_w$	drum radius including gear ratio	0.004338	m
$J_w$	rotational inertia of gear box and winch with respect to the drive	0.004562	kgm <sup>2</sup>
$\mu_w$	Coulomb friction coefficient of winch	0.3434	-
$F_{wv}$	viscous friction	0.0061	Nms
$F_s$	static friction	1.374	Nm
$\dot{\alpha}_s$	Stribeck velocity	608.6	rad/s
$c_m$	efficiency of the servo amplifier	0.939	-
$R$	Ohm's resistance	1.532	$\Omega$
$\Psi_m$	torque constant (from motor data sheet)	2.05	Nm/A
$c_{n1}$	re-magnetization losses	0.0489	Ws
$c_{n2}$	eddy current losses	0.000274	Ws <sup>2</sup>
$P_0$	constant losses of the control cabinet	1289	W
$c_{p,m}$	efficiency of the power supply unit in motor operation	0.975	-
$c_{p,g}$	efficiency of the power supply unit in generator operation	0.939	-

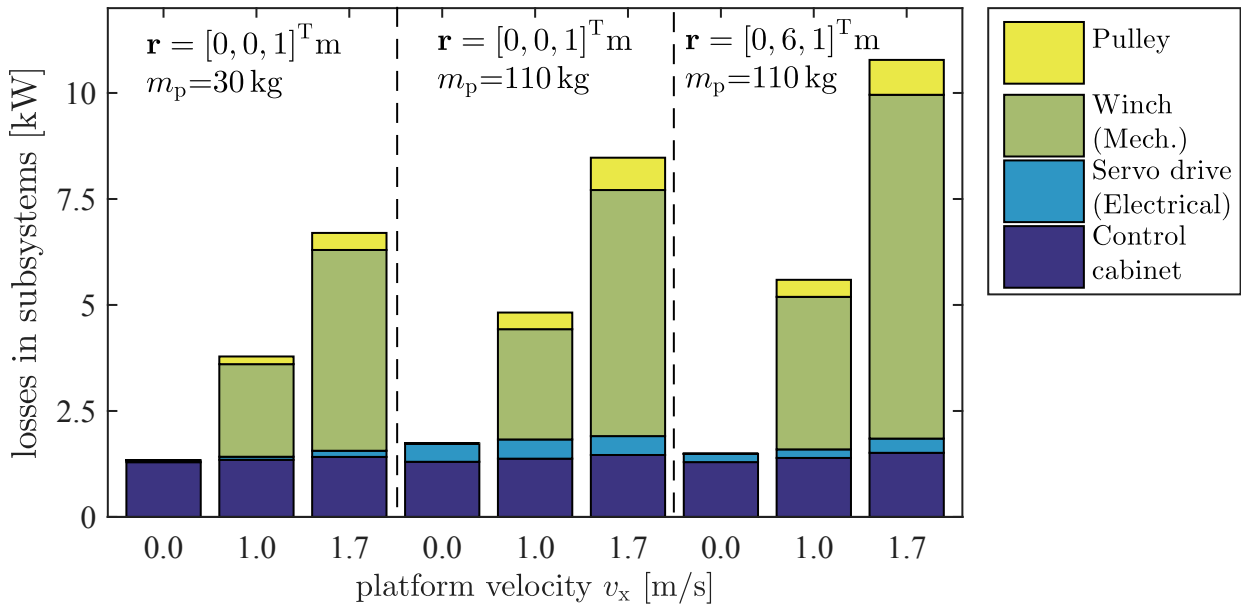


Figure 4.31: Distribution of the losses on the subsystems for different velocities, payloads and positions. Cable forces are derived by QP algorithm and  $\mathbf{f}_{\text{ref}} = \mathbf{f}_{\text{min}}$

and located in the middle of the workspace, in the second, the platform has an additional payload of 80 kg. In the third scenario, the platform is at the workspace border. The losses are evaluated for standstill, a velocity of 1.0 m/s and the maximum velocity of 1.7 m/s. The diagram presented in Fig. 4.31 shows that the losses in the control cabinet are almost independent from the point of operation as the idle losses  $P_0$  are dominant. In standstill, no losses arise in the mechanical parts of the robot, as the servo drives statically balance the load and the cables can be assumed to standstill. It is worth to note that the losses involved in creating a static torque are small, compared to the points when the robot moves. One can conclude that closing the motor brakes during standstill of the robot will only marginally improve the energy consumption. Under movement, the mechanical losses in the pulleys and the winches amount up to two-thirds of the total losses. Next, the mechanical losses are analysed in more detail.

### Winch Efficiency

The efficiency of a system depends often on the point of operation. For the winch, the point of operation is described by the actual cable velocity and force. The efficiency  $\eta_w$  describes the relation between the input and output power of the winch  $P_w = f_w \dot{\theta}$  and  $P_s = \tau \dot{\alpha}$ , respectively, which is calculated by

$$\eta_w = \frac{P_{\text{out}}}{P_{\text{in}}} = \left( \frac{P_s}{P_w} \right)^{\text{sgn}(P_w)}, \quad (4.15)$$

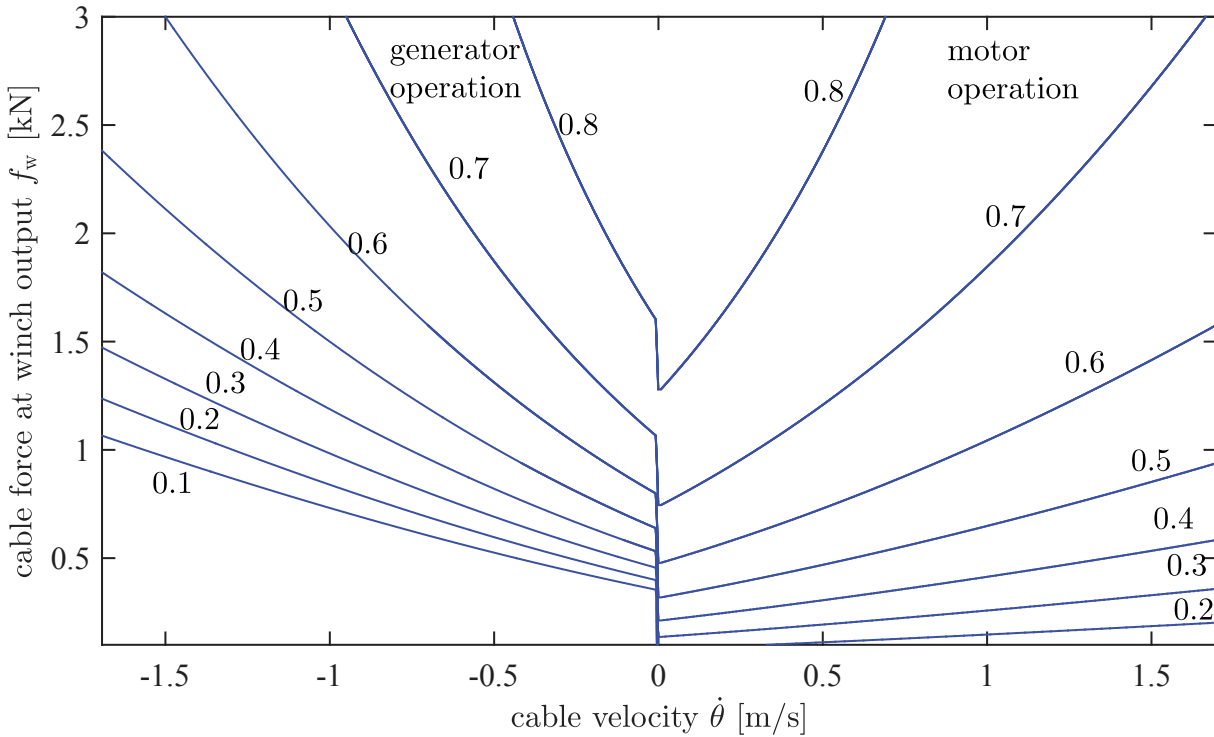


Figure 4.32: Efficiency map of the IPAnema 3 winch including planetary gear box

and is defined for both motor and generator operation. The efficiency is visualized as efficiency map in Fig. 4.32 and shows the relative losses of the mechanical model of the winch derived by (4.11) in the permissible operation range. Similar to a typical torque-over-speed diagram of an electrical drive, the right part of the diagram corresponds to the motor generation and the left part to generator operation. For this, the cable velocity is entered in inverted way on the  $x$ -axis. The efficiency map reveals that efficiencies of up to 85% can be reached at high forces. In generator operation and with low cable forces, the cable force is not sufficient to overcome the friction in the winch. Basically, additional power from the motor is needed in this area to unwind the cable and, thus, the coefficient  $\eta_w$  is not defined.

Obviously, the height of the cable forces influences the efficiency of the system. In contrast to a crane winch, the cable force in a cable robot is not only the result of the manipulated load but also of the internal tension. Next it is investigated, to what extent the energy consumption can be influenced by the choice of the tension level.

### Energy Consumption under Different Tension Levels

To get insight into the influence between the tension level and the energy consumption of the robot, the same scenarios are now investigated for minimal ( $\mathbf{f}_{\text{ref}} = \mathbf{f}_{\text{min}}$ ), medium ( $\mathbf{f}_{\text{ref}} = (\mathbf{f}_{\text{min}} + \mathbf{f}_{\text{max}})/2$ ) and maximal ( $\mathbf{f}_{\text{ref}} = \mathbf{f}_{\text{max}}$ ) cable forces. The resulting energy consumptions are presented in Fig. 4.33, and the change of  $P_{\text{el}}$  is given relative to the medium tension

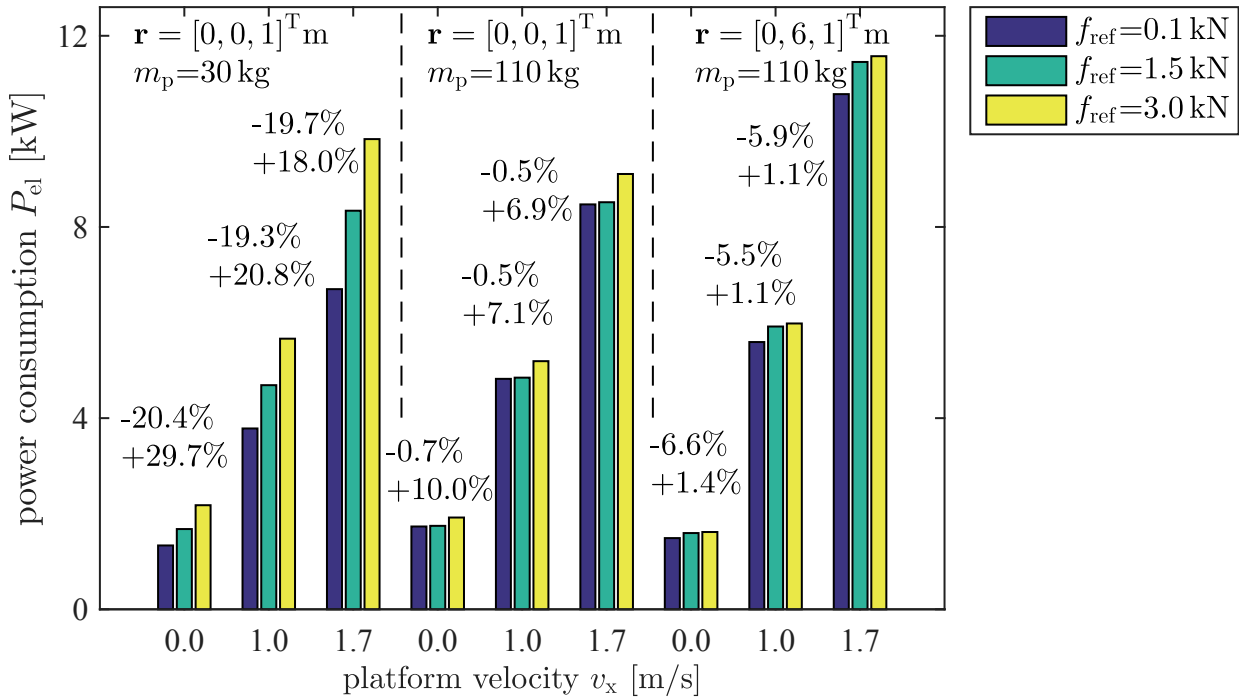


Figure 4.33: Effect of the tension level on the power consumption of the robot

level. Carrying only the own weight of 30 kg, the energy consumption can be influenced strongly in a range from -20 to almost +30% in standstill. Under movement, the relative change decreases, as the absolute power consumption arising from the velocity-dependent friction rises. With the payload of 80 kg, the effect of changing the tension level on the power consumption is lower because the variability of changing cable forces becomes limited under a significant external load.

### Comparison of the Energy Efficiency with an Industrial Robot

In the following, the energy consumption of the cable robot IPAnema 3 is compared with an industrial robot. The industrial robot is a standard six-axis jointed-arm robot of Comau (Smart NJ 130-2.6) with a payload of 130 kg. The characteristic and performance data of the robot systems are very different. For the comparison of the energy efficiency, a manipulation task with following trajectory is taken as base. A load of 100 kg is lifted up by 1.0 m, moved 2.4 m horizontally and lowered by 1.0 m. The path velocity  $\dot{x}_{\max}$  amounts to 1.5 m/s with a maximal acceleration  $\ddot{x}_{\max}$  of 5 m/s<sup>2</sup> and a maximum jerk  $\dddot{x}_{\max}$  of 20 m/s<sup>3</sup>. The path is depicted in Fig. 4.34.

The comparison is based on energy consumption models. For the cable robot, the model described in section 4.4.1 in combination with the minimal cable forces derived from the QP algorithm is applied. The model of the industrial robot was developed in an earlier project (Müller, Spiller et al. 2011). The same trajectory using the jerk-limited acceleration ramps is applied to both kinematics.

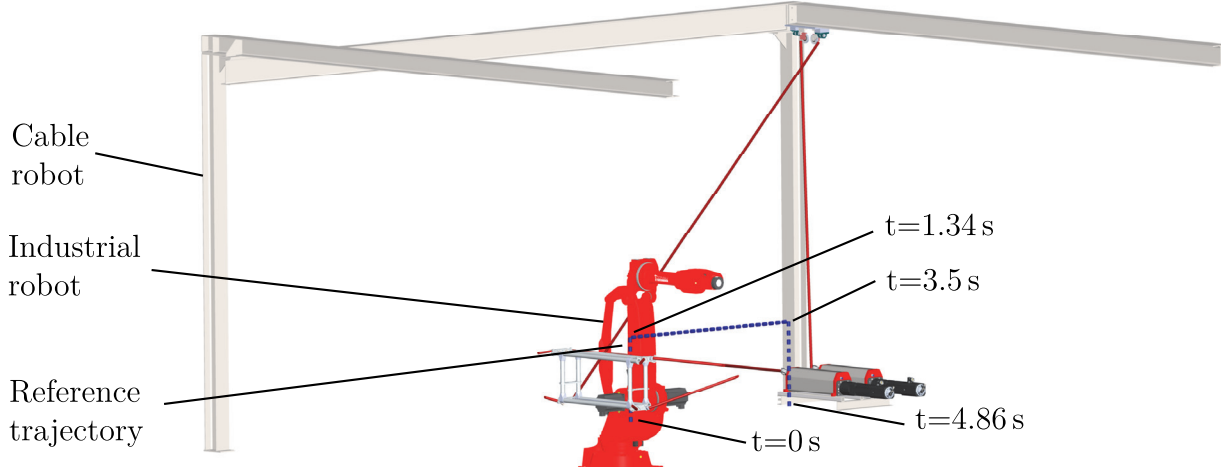


Figure 4.34: Cable robot IPAnema 3 (one quarter is visualized), industrial robot Comau Smart NJ 130-2.6 and reference trajectory

The power consumption over the complete trajectory amounts to 4.76 Wh for the industrial robot and 4.12 Wh for the cable robot, while the curves of the power consumption over the trajectory reveals strong differences as can be seen in Fig. 4.35. The main reason is the different topology of the kinematics: in the serial kinematics, the macroscopic movement is mainly done by the first three joints, while in the parallel kinematics, all drives are involved. Furthermore, the moved mass of the industrial robot is higher than the cable robot's mass. This can be seen comparing the peak powers: the peak power on the trajectory of the industrial robot is 15 kW, whereas the cable robot reaches only 8 kW.

With the analysis of the energy consumption, the evaluation of the robot properties is completed. In the following, the main findings of this chapter are summarized.

## 4.5 Summary of this Chapter

In this chapter, cable robots were investigated from different viewpoints. As an overview the main results are concluded.

With the load identification, an estimation of the actual platform mass with an error of 10% was obtained, while the experiments showed worse results for the estimation of the vector to the centre of gravity. With the subsequent load compensation, the influence of the cable elasticity on the accuracy is reduced. The approach is a reasonable extension of the inverse kinematics to improve the position accuracy.

The comparison between the linear and non-linear cable model unveils uncertainties of the stiffness model and settlement of the cables which leads to significant lasting errors in the forward kinematics. Despite these model errors of the cable elongation, the forward kinematics delivers a reasonable estimation of the platform pose. Probably, this is due to

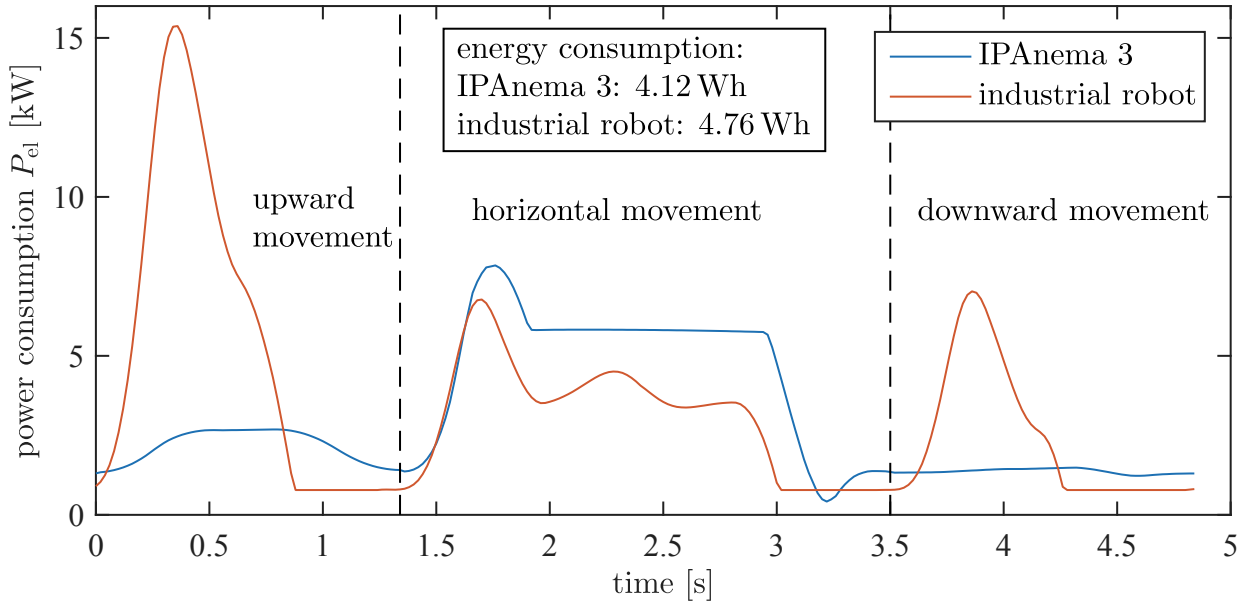


Figure 4.35: Model-based comparison of the power consumption along a trajectory between industrial and cable robot

the balancing of the error with the corresponding cable stiffness, which mainly depends on the free cable length. With the non-linear cable model, a slightly better estimation of the platform pose under changing tension levels could be reached compared to the linear model.

As overview of the measured position accuracies, the mean values in the investigated scenarios are summarized in Table 4.7. The investigation delivers a widespread picture: Within the workspace and during high dynamic movements, both approaches perform almost equally good. Significant differences appear when reaching the workspace border. At the workspace border, the cables tend to sag using the inverse kinematics, which is reflected by a significantly worse position accuracy with errors more than 250 mm. A significant enhancement of the position accuracy is reached at the workspace border using force control. With force control, the position accuracy at the workspace border equals almost the values reached inside the workspace.

The investigation of the eigenfrequencies delivered insight into the dynamic behaviour of cable robots. An important finding for the practical use of cable robots is the strong decrease of the dynamics under additional payloads. Due to the low own weight of the platform, additional payloads have a strong impact on the platform dynamics. In combination with a low stiffness of the platform, this leads to low eigenfrequencies, which limit the available dynamics. This is also of practical interest while programming trajectories of a cable robot, as the acceleration ramps have to be chosen conservatively, when the platform carries an additional load. With the QP approach, the dynamics can be partly regained by choosing high tension levels, whereby the stiffness and subsequently the eigenfrequencies rise.

Table 4.7: Summary of the absolute position accuracies evaluated in different scenarios

scenario	IK [mm/°]		QP [mm/°]	
	$m_p=25\text{ kg}$	$m_p=105\text{ kg}$	$m_p=25\text{ kg}$	$m_p=105\text{ kg}$
discrete grid within the workspace	41.4/1.91	73.9/2.44	48.1/2.02	71.6/2.55
straight line between centre and workspace border	19.3/0.58	29.7/0.58	14.3/0.28	15.3/0.50
workspace border	198.2/1.73	268.4/ 2.76	59.0/0.88	90.6/0.84
dynamic trajectory	21.1/-	-/-	14.5/-	-/-

The low own weight-to-payload ratio considers only the platform of cable robots and suggests that they are in general energy efficient. For a comprehensive consideration, the winches and the electrical components have to be modelled as well. The evaluation delivered that the efficiency of the investigated winches amounts in the optimal point of operation to roughly 85%. The analysis showed that during movement of the cable robot significant losses occur in the mechanical parts of the winches, while the losses of the power electrics are minor. The energy efficiency of cable robots is further reduced due to the parallel structure of the robot, which generally involves all winches in the motion of the platform. For a given task, the energy consumption can be improved with the minimal cable force derived from the QP approach. Especially when the platform is empty, the energy savings can amount almost up to 20% compared to a medium tension level. In the comparison with an industrial robot, both robots consumed almost the same amount of energy, while in the detailed progression of the energy consumption the differences between the kinematics become visible. Due to the high moved mass of the industrial robot, its peak power is higher.

---

# 5 Operational Space Force Controller

Operational space force controllers aim to control the external forces of the robot's platform and allow for interaction between the robot and the environment. The basic control laws are well-known from serial industrial robots and are incorporated in the control architecture of the cable robot. For this purpose, the cable force controller proposed in chapter 3 has to be taken into account to ensure the feasibility of the cable forces.

The hybrid position and force control presented in this chapter allows controlling selected DOF of the platform to either a desired position or a desired external force. With this control scheme, it becomes possible to control the contact force between the platform and a work piece in one direction, while the platform follows a desired path along a work piece in position control. A possible application is the grinding of large work pieces like blades of wind turbines or air planes.

For haptic interaction between the robot and a user, a controller for human-robot-cooperation is investigated in the second part of this chapter. With the proposed admittance controller, the platform behaves according to a programmable virtual system behaviour and simulates the dynamics, e.g. of a compliant spring, a body which is moved through a viscose fluid or a body which is much heavier than the robot platform itself. Within this thesis, a virtual workspace is introduced whose borders are represented as springs. The applications of haptic input devices are manifold and are in the field of e.g. programming paths for a robot, power assistance and tele-operation.

Both force controllers use the cable force sensors to estimate the wrench and, thus, no additional force-torque sensor at the robot's platform is necessary. For verification, both controllers are investigated on the demonstrators.

## 5.1 Hybrid Position and Force Control

In this section, the design and experimental evaluation of the hybrid position and force control for a cable robot is presented. The main challenges are the division of the DOF into either force or position control, the contact establishment and the incorporation of the cable force controller. Existing solutions for contact control are adopted and for cable force control, the approach developed in chapter 3 is extended. At first, the control task is described with help of a task frame.

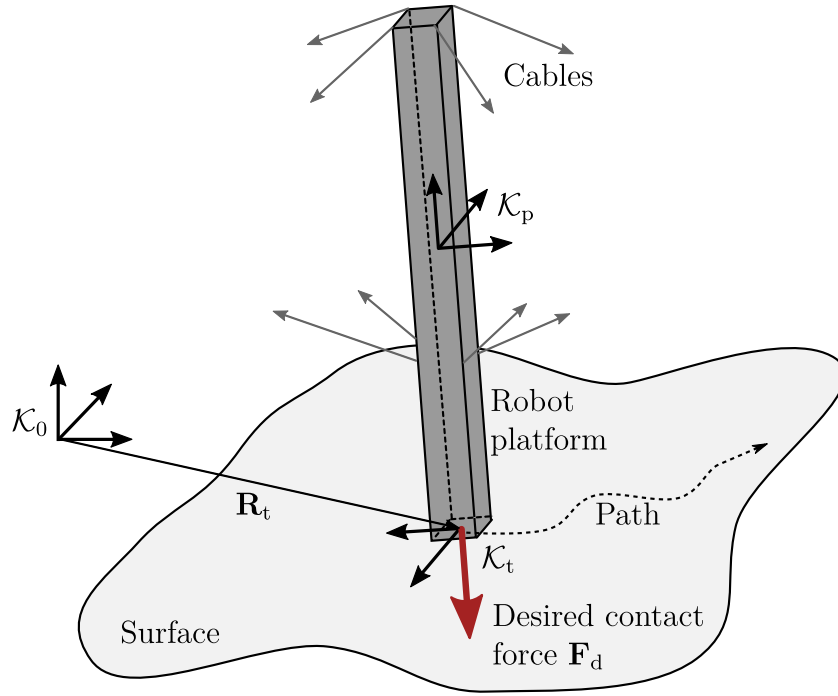


Figure 5.1: Principle set-up at the mobile platform and coordinate systems for hybrid position and force control

### 5.1.1 Approach

The principle setup of the force control at the platform of the cable robot is depicted in Fig. 5.1. The desired force vector  $\mathbf{F}_{d,0}$  is described in the task coordinate frame  $\mathcal{K}_t$ . The origin lies in the contact point and the  $z$ -axis coincides with the desired force direction. The orientation w.r.t. the world frame  $\mathcal{K}_0$  is parametrized with the rotation matrix  $\mathbf{R}_t$ . Beside the desired force, the path  $\mathbf{x}_d$  is parametrized along the surface. To make the force control accessible by standard industrial machine interfaces, new commands based on standardized G-Code are established.

For the synchronous control of the platform to a desired contact force and a motion along the desired path, the typical approach is the hybrid position and force control mentioned in section 1.2 and shown in Fig. 5.2. The control problem is divided into parallel control loops for position and force control with their set-points  $\mathbf{x}_d$  and  $\mathbf{f}_d$ , respectively. With the selection matrix  $\mathbf{S}$ , the DOF are assigned to be either force- or position-controlled. For the cable robot, several adoptions are necessary. The major difference to the classic hybrid control law is the additional cable force control loop to control the internal cable tensions. Another difference is the use of joint space force measurement and transformation into operational space instead of a force-torque sensor at the platform. As the cable force sensors already exist for cable force control, additional costs for sensors can be avoided and no additional sensor has to be added to the platform. Furthermore, closed-loop position control in the joint space is assumed, instead of closed-loop position control in operational

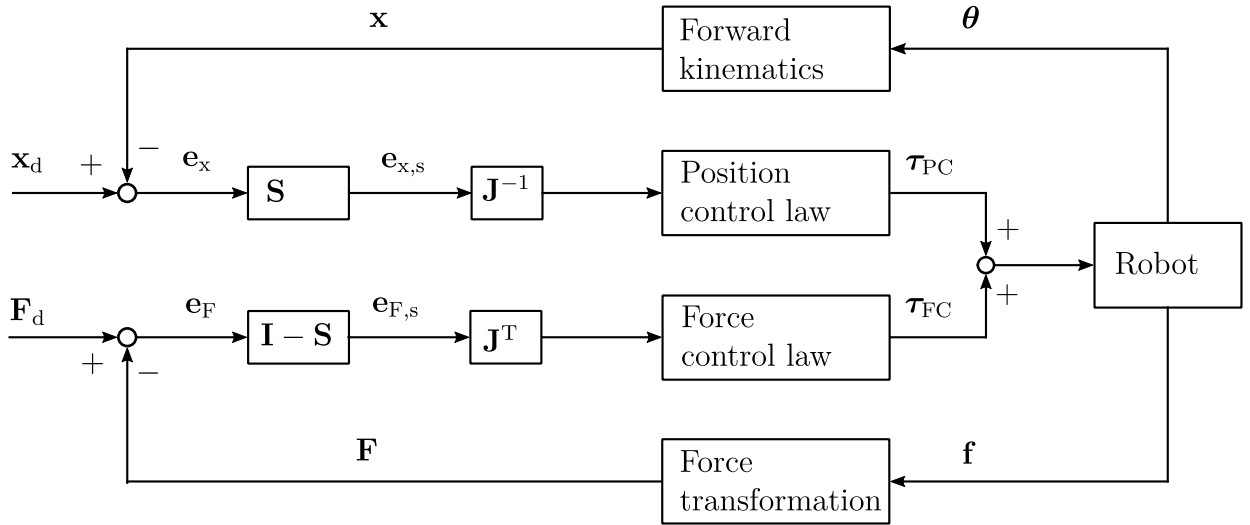


Figure 5.2: Hybrid position and force control proposed by Raibert and Craig (1981)

space. The position control is encapsulated in the motion generator and, therefore, the selection matrix  $\mathbf{S}$  cannot be realized for position control and the decoupling is realized in the force control implementation.

The establishment of the contact between the platform and the environment is challenging, as the system dynamic abruptly changes from a free floating body to a unilateral stiff force transmission. For contact establishment, several methods are described in section 1.2. The state machine-based approach presented in (Assuncao and Schumacher 2003) is applied, which uses a position control to bring the platform into contact. When the robot is in contact, the closed-loop force control is activated.

Using the cable robot for applying an external force on the environment, the feasibility of the cable forces have also be considered. This is especially important for the simultaneous position-controlled movement in the tangential plane, as friction forces have to be overcome. For this reason, the cable force controller presented in section 3.5.2 is incorporated.

Compared to the initial approach presented in Fig. 5.2, an additional control loop for the cable forces has to be added. For a cable robot, the control problem is divided into three parts as depicted in Fig. 5.3:

- The motion control with the CNC delivers  $\mathbf{x}_{d,CNC}$  to move the platform along a path.
- The operational space force control generates a change in the desired operational space position  $\mathbf{x}_{d,HPFC}$  to control the contact force.
- The cable force control keeps the cables under tension. For this purpose, a feasible force distribution is calculated for the measured wrench  $\mathbf{w}$ . The controller output is the modification  $\Delta\mathbf{q}_{d,CFC}$  of the cable length set-point.

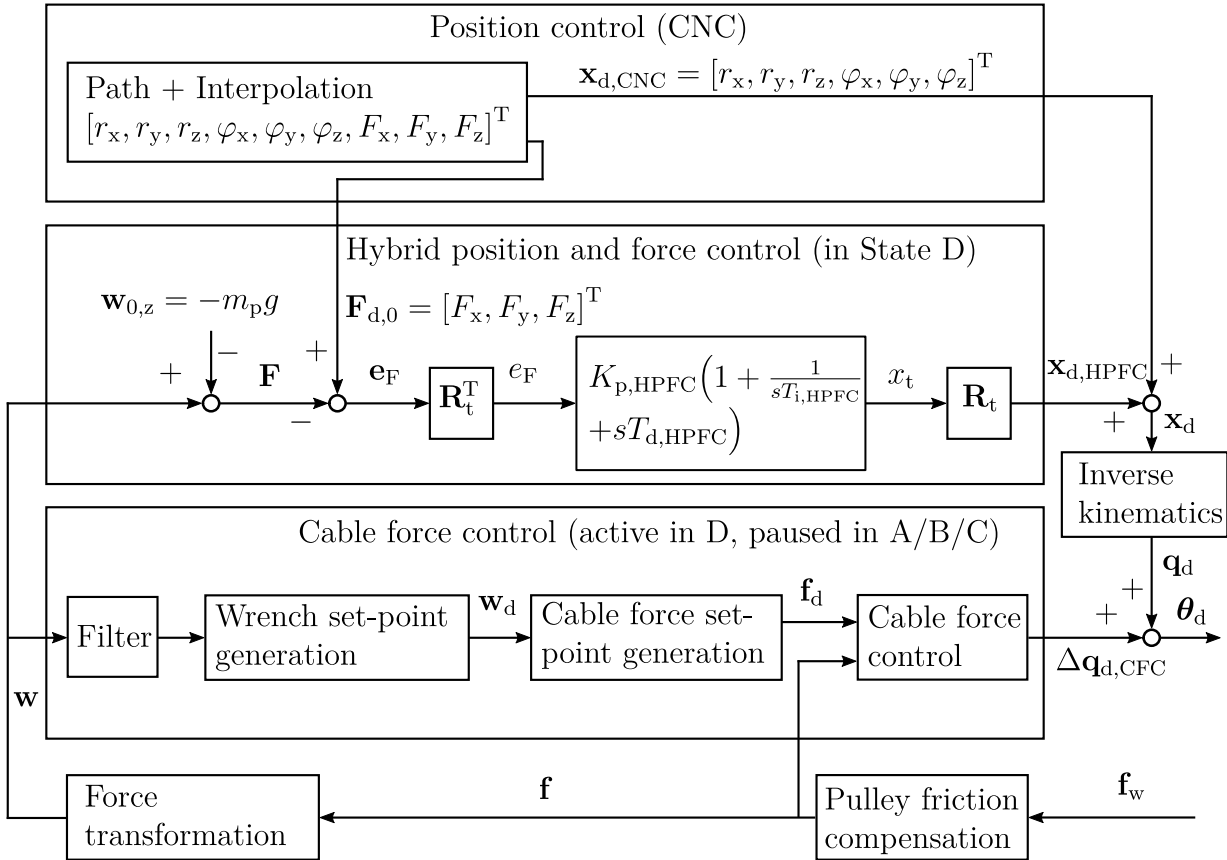


Figure 5.3: Proposed implementation of the hybrid position and force control incorporating cable force control

The outputs of the three controllers are summed up by

$$\boldsymbol{\theta}_d = \text{IK}\{\mathbf{x}_{d,CNC} + \mathbf{x}_{d,HPFC}\} + \Delta \mathbf{q}_{d,CFC} , \quad (5.1)$$

which results in the cable length set-point  $\boldsymbol{\theta}_d$  which is commanded to the servo drives. In the following, the operational space force control and the necessary adjustments of the cable force control are described in detail.

### 5.1.2 Controller Design and Implementation

The proposed implementation of the hybrid position and force control is visualized in Fig. 5.3. Hereby, the CNC executes the position control for a path programmed in G-code and delivers the desired position  $\mathbf{x}_d$ . For the programming of the desired contact force, three additional motion axes are added to the CNC and interpolated in the interpolation cycle. These three axes constitute the desired force vector  $\mathbf{F}_{d,0} = [F_x \ F_y \ F_z]^T$ . In this way, the desired force vector changes smoothly and is consistent with the movement along the surface.

For measuring the contact forces, the wrench  $\mathbf{w}$  is calculated from the measured cable forces  $\mathbf{f}$  which are derived from the pulley friction compensation. For the estimation of the contact force  $\mathbf{F}$ , the own weight of the platform  $-m_p g$  is subtracted from the wrench.

For the implementation of the hybrid position and force control the task coordinate frame  $\mathcal{K}_t$  is applied, which is visualized in Fig. 5.1. The desired force vector  $\mathbf{F}_{d,0}$  is transformed by

$$\mathbf{F}_{d,t} = \mathbf{R}_t^T \mathbf{F}_{d,0} \quad \text{with } \mathbf{F}_{d,t} = [0 \ 0 \ F_d]^T , \quad (5.2)$$

to the task coordinate frame, where the  $z$ -axis points in the direction of the desired force  $F_d$ . With the same transformation, the actual scalar contact force  $F$  is derived from the vectorial representation  $\mathbf{F}$ . With this approach the control problem becomes one-dimensional. Thus, the control error in contact force  $e_F = F_d - F$  and the output of the controller which is formulated in a desired position w.r.t. the task frame  $\mathcal{K}_t$  are one-dimensional variables.

With the coordinate transformation, the process of contact establishment and subsequently the closed-loop force controller are described. The approach presented in (Assuncao and Schumacher 2003) uses a state machine with four states and is adopted for contact establishment as visualized in Fig. 5.4.

Basically, the contact is established in position control (States A-C) and closed-loop force control is performed when the platform is in contact (State D). The inputs of the state machine are the actual contact force  $F$  and the deviation from the desired contact force  $e_F$ . The output is the position offset denoted by  $x_t$  in the direction of the desired force vector.

In state A, the platform moves in the direction of the desired force with a maximal velocity  $v_{\max,HPFC}$ . During the movement, the force  $F$  is observed. The contact between the platform and the surface is detected when the threshold force  $F_{th}$  is exceeded, thus,  $F \geq F_{th}$  is fulfilled. When the contact is detected, the state machine switches to state B where the platform is slowed down. When standstill is reached, the closed-loop force controller is activated in state D. During the force control along a surface, it may occur that the robot loses the contact to the surface. The loss of the contact is detected when the contact force falls below the threshold force. In this case, the state machine switches to state C and a position controller brings the platform again in contact.

The closed-loop force control which is applied in state D is presented in more detail according to Fig. 5.3. With the help of the state machine, it is ensured that the platform is in contact with the environment. The contact is a unilateral force transmission for pressure forces, contrary to the cables which can only transmit pull forces. The static transmission behaviour of the contact can be considered as a serial arrangement of the robot stiffness caused by the elastic cables and the stiffness of the environment in the direction of the desired force. In the proposed controller, fixed control values are applied and, thus, the controller has to deal with changing transfer behaviour of the control plant.

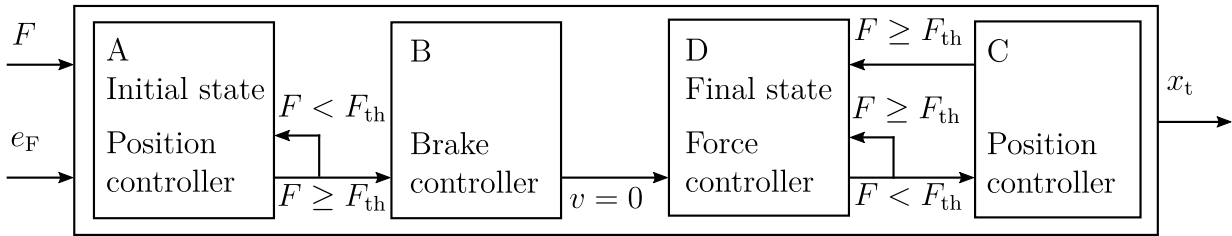


Figure 5.4: State machine with transition conditions for the contact establishment

Table 5.1: Control parameters of hybrid position and force control

parameter	definition	value	unit
$K_{p,HPFC}$	proportional gain (stiffness)	22,000	N/m
$T_{i,HPFC}$	integrator reset time	2.6	s
$T_{d,HPFC}$	derivative time constant	0.03	$s^{-1}$
$T_{MA,HPFC}$	time constant of moving average for wrench filtering	2.0	s
$F_{th}$	threshold force for contact detection with the environment	25	N
$v_{max,HPFC}$	maximum approaching velocity	0.05	m/s

The manipulated variable is a position and, thus, the controller needs an integral part to reach static accuracy in the contact force. For fast reaction on transient disturbances which is necessary to keep the contact, a proportional and derivative action is applied. The transfer function of the PID controller  $G_{c,HPFC}(s)$  reads as

$$G_{c,HPFC}(s) = \frac{\mathcal{L}\{x_t(t)\}}{\mathcal{L}\{e_F(t)\}} = K_{p,HPFC} \left( 1 + \frac{1}{sT_{i,HPFC}} + sT_{d,HPFC} \right) , \quad (5.3)$$

with the gain  $K_{p,HPFC}$ , integrator reset time  $T_{i,HPFC}$  and derivative time constant  $T_{d,HPFC}$ . The gain  $K_{p,HPFC}$  incorporates the effective stiffness of the cable robot and the environment in the direction of the desired force.

The cable force control has to be slightly expanded for the hybrid force control. To avoid instabilities due to the synchronous control of the external wrench and the internal cable forces, a moving average filter is applied on the wrench to slow down the control loop. The contact establishment is obviously accompanied by abruptly changing cable forces, which may destabilize the cable force controller and subsequently also the contact establishment. To avoid these disturbances, the cable force controller is paused during contact establishment which corresponds to the states A to C of the state machine.

The control approach is implemented on the IPAnema3 robot. The control parameters are experimentally determined and listed in Table 3.1. Next, the experimental evaluation is carried out.

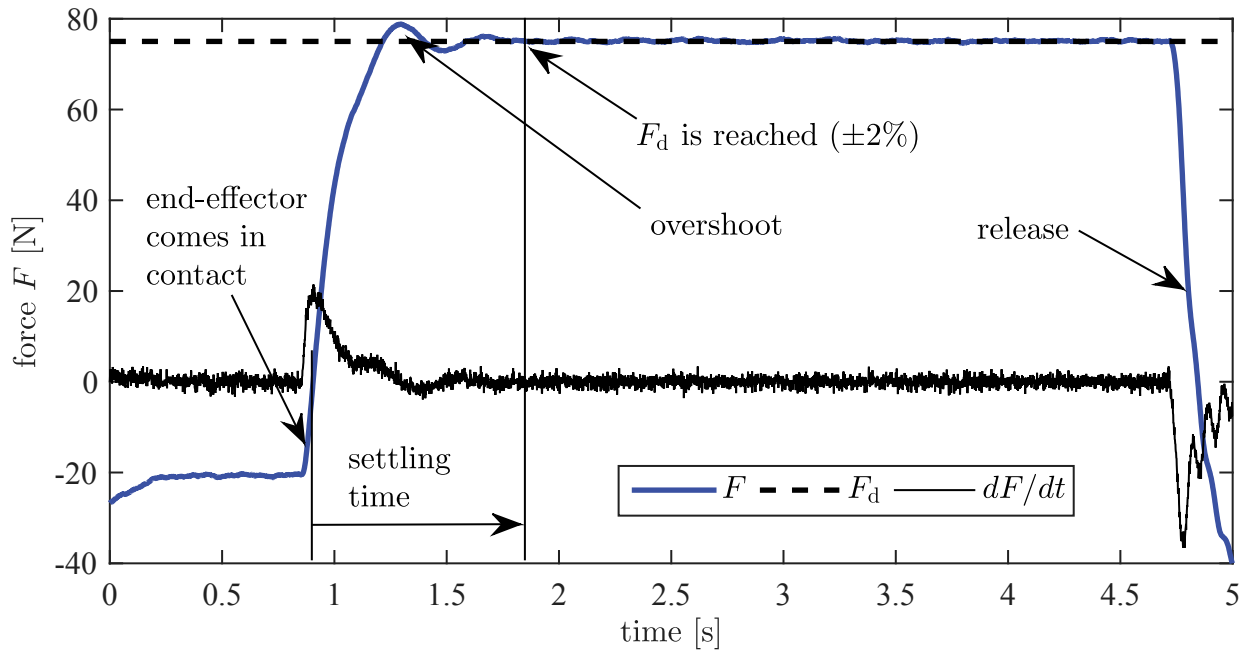


Figure 5.5: Progression of the force during contact establishment, force control with  $F_d = 75$  N and release

### 5.1.3 Experimental Evaluation of Contact Establishment and Following Behaviour

At the beginning of this section, the contact establishment and following behaviour during hybrid position and force control are identified as the main challenges. In the following, the performance of the controller regarding these points is experimentally investigated. The PID controller (5.3) is parametrized with constant values, while the robot stiffness is position-dependent. Thus, the effective stiffness in the contact differs from the position of the robot which can lead to instabilities of the contact control. To take into account this effect in the experimental evaluation, the contact establishment is studied at different positions within the robot's workspace. To investigate the following behaviour of the robot, a cylindrical work piece is chosen, on which a force is applied while the robot moves along its surface. Due to the availability of the robot, the contact establishment is investigated on the IPAnema 3 as described in section 2.3.1, while the following behaviour is studied on a previous set-up of the IPAnema 3. The main differences are the steel frame which measured 7 m x 4 m x 3 m and the use of thinner Dyneema® cables with a diameter of 2.5 mm (Kraus, Miermeister et al. 2015).

The process of the contact establishment is visualized in detail in Fig. 5.5. The diagram shows the sharp rise of the contact force, when the mobile platform comes in contact with the environment. Also this can be seen in the time derivative of the contact force  $dF/dt$  which is noisy but clearly signals when the platform comes in contact. The course of the force shows a transient oscillation where the contact force  $F$  exceeds the desired force  $F_d$

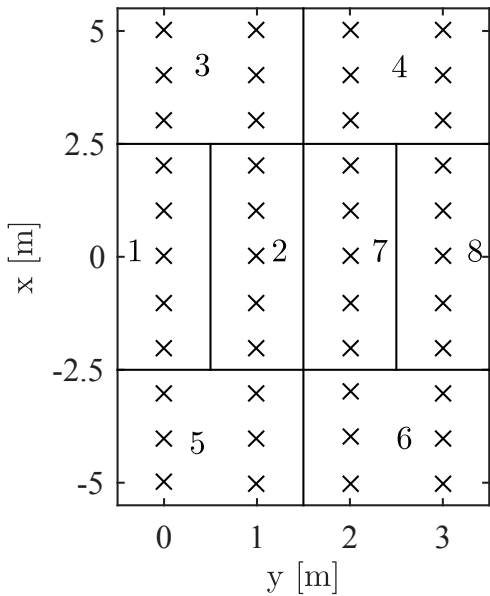


Figure 5.6: Investigated areas for contact establishment

area	overshoot		settling time	
	mean [%]	$\sigma$ [%]	mean [s]	$\sigma$ [s]
1	9.44	0.69	3.07	0.85
2	10.14	0.26	2.51	0.09
3	10.34	2.34	2.68	1.39
4	9.29	1.89	1.86	0.41
5	9.55	1.61	2.05	0.53
6	9.49	3.16	1.75	0.24
7	10.33	0.48	2.33	0.08
8	11.30	0.55	1.74	0.06
mean	9.98	-	2.25	-

Table 5.2: Resulting overshoot and settling time while contact establishment for  $F_d=500$  N

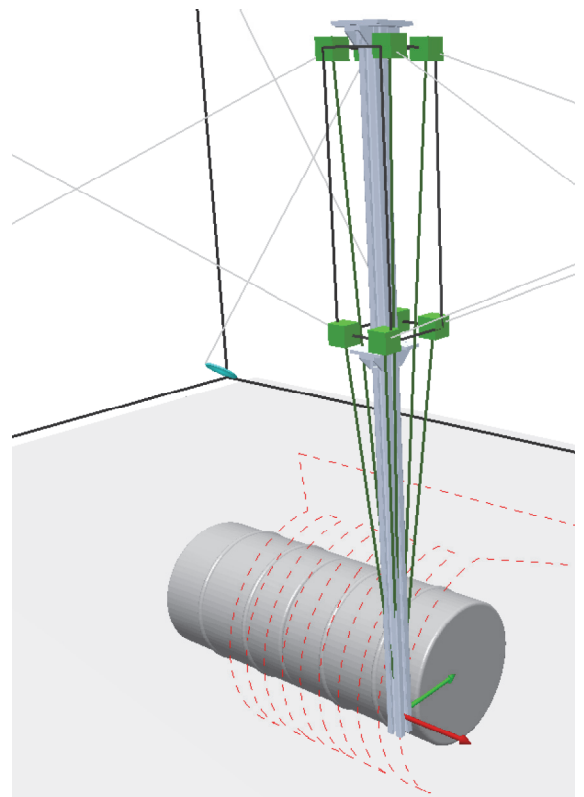
which is defined as overshoot. The contact is assumed to be in steady state, when the control error is smaller than 2% relative to the desired force. The settling time is defined as the time from the first contact to the surface until the control error is in steady state.

The overshoot and the settling time are used as evaluation criteria for the contact establishment. For the following experiment the approaching velocity is 50 mm/s and the desired force amounts to 500 N. The results are a compromise between acceptable overshoot and settling time. By changing the approaching velocity, this compromise can be influenced in favour of one evaluation criteria.

To investigate the contact establishment within the workspace, the HSPC is applied on the floor at 44 different positions in an area of 3 by 10 meters. For better clarity, the positions are clustered into eight areas as visualized in Fig. 5.6. Analogue to Fig. 5.5, in each position, the contact is established and the evaluation criteria are determined. The experimental results are presented in Table 5.2 in form of the mean value and the standard deviation  $\sigma$  from the three repetitions of the experiment. The maximum overshoot amounts to 11.3%, whereas the average lies at 9.98%. The mean settling time is in average 2.25 s. The evaluation presented in Table 5.2 shows a marginally higher overshoot in the centre of the workspace (areas 1, 2, 7, 8) but basically also in the edges of the workspace (area 4 and 6) the contact is established successfully. The contact is thus established almost equally well within the workspace. This is an important result for industrial applications, as the position of the work piece can arbitrarily be chosen within the workspace of the robot and the position does not influence the performance of the contact establishment.



(a) Test set-up with IPAnema 3



(b) Path along the oil barrel

Figure 5.7: Test set-up for the evaluation of the following behaviour

The settling time is now compared to experimental results which can be found in literature. In (Kröger, Finkemeyer et al. 2004), the settling time for a serial industrial manipulator lies between 0.6 and 1.7 s. In another scenario shown in (Lange, Bertleff et al. 2013), a settling time of 0.8 s for an industrial robot was achieved. The set-point forces of these experiments amount only to 60 and 200 N, respectively, whereas for the cable robot 500 N is chosen, what shortens the stroke and subsequently the time needed to reach the desired contact force. With a desired force of 75 N, the settling time of the cable robot amounts only to one second as can be seen in Fig. 5.5. It can be concluded that the proposed control scheme for the cable robot delivers comparable results regarding the contact establishment.

Next, the focus lies on the evaluation of the following behaviour of the force control during a simultaneous motion of the mobile platform.

The test set-up using the IPAnema 3 and an oil barrel is shown in Fig. 5.7a. The test scenario is exemplary for a cylindrical surface which can be found at wings of air planes or blades of wind turbines. The path along the oil barrel is programmed offline and visualized as dotted line in Fig. 5.7b. Additionally, also the desired force vector is programmed which is aligned to the normal vector of the surface.

The quantitative behaviour of the contact force along the surface is shown in Fig. 5.8 and the corresponding cable forces are presented in Fig. 5.9. The desired force  $F_d$  amounts

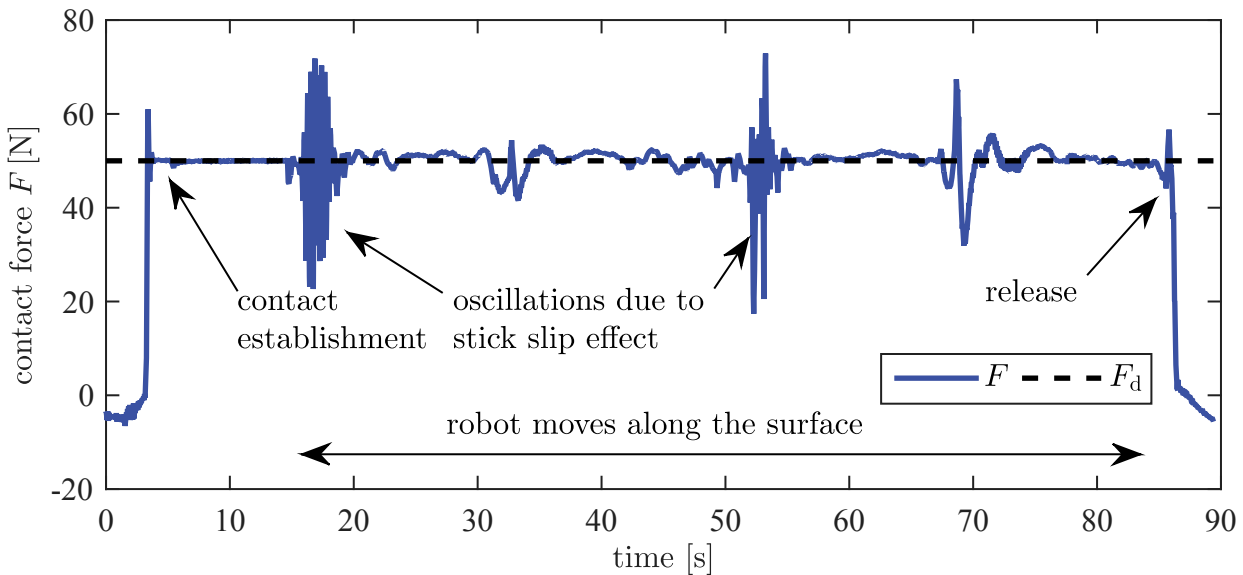


Figure 5.8: Course of the contact force normal to the surface on the oil barrel

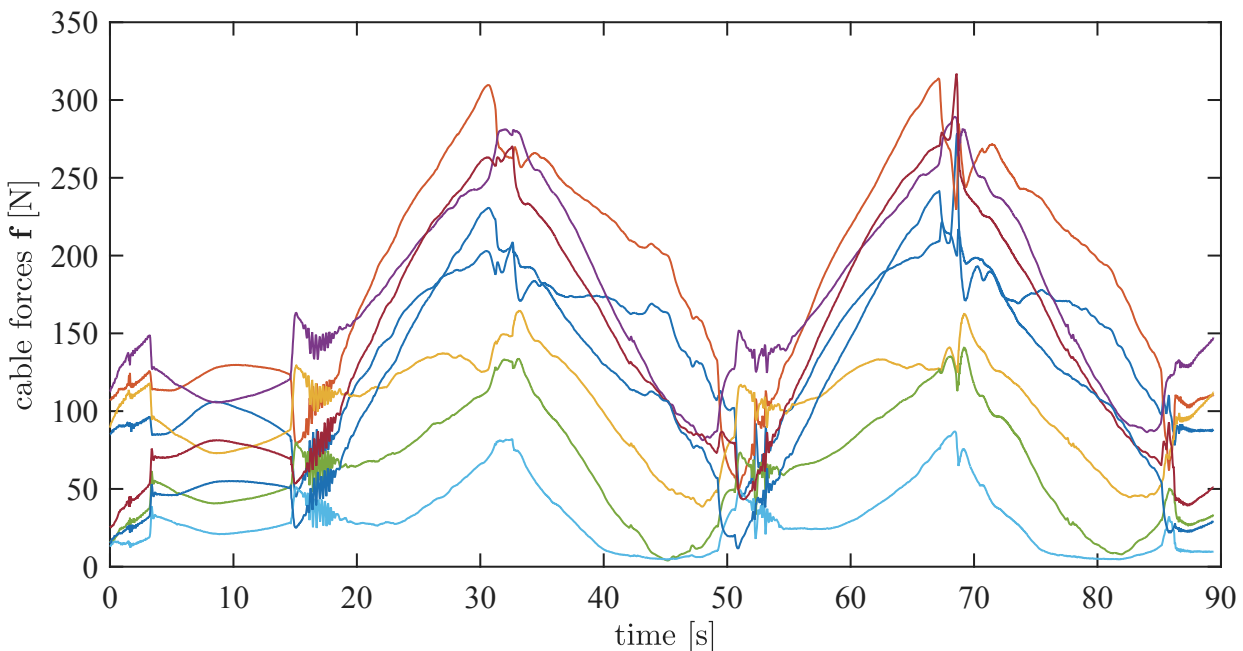


Figure 5.9: Course of the cable forces during the force control along the oil barrel

to 50 N. As the contact point of the platform to the oil barrel is eccentric, the stiffness is low and stick slip effects in the contact generate oscillations. The oscillation is relatively high, when the robot moves position-controlled into a direction where the platform is not very stiff. Since the cables are tensed, these critical positions are overcome.

It can be concluded that the well-known hybrid position and force control approach can be applied on a cable robot. By using the measured wrench as input for the set-point determination of cable forces, it becomes possible to control the internal cable forces during the contact control. The admittance control law presented in the following is also able to control the interaction with the environment but the focus lies on achieving a desired system behaviour. This can be used for haptic interaction between the robot and a user grasping the platform.

## 5.2 Haptic Interaction with Admittance Control

For haptic interaction, the human has physical contact with a machine. The aim of the haptic interaction is to exchange information between the user and the robot by reacting on the user forces in a defined manner. The control of a haptic system can be realized either by impedance or admittance control. Both of them allow controlling the movement of an actuator according to the interaction between the user and the actuator. In the admittance control, for a measured force, the equation of motion, of e.g. a spring-mass-damper system is computed which results in a desired platform position. In case of the impedance control, the input is the actual platform position and the output is a corresponding force. This force is then the input for a force-controlled actuator. The admittance control uses the actual applied force as an input and outputs a position set-point. Here, an admittance control is implemented as it integrates well with the position control loop of the servo drive.

In the following, control algorithms for cable robots which give the user an interactive haptic feedback are investigated. An admittance control to emulate a virtual system behaviour, represented by a spring-mass-damper system, is implemented on the IPAnema 3 Mini robot depicted in Fig. 2.9. To guide the user within the workspace, virtual workspace borders based on switchable stiffness are introduced. The maximum feasible dynamics of the simulated system is evaluated according to the transfer function of the robot. The haptic interface can be used to teach positions or as haptic device for the simulation of virtual systems. The approach was published in an earlier version in (Kraus, Mangold et al. 2014).

### 5.2.1 Virtual System Behaviour for Haptic Interaction

The admittance control transforms an external force to a motion of the platform according to a virtual system behaviour. The dynamic behaviour of a mechanical system can be

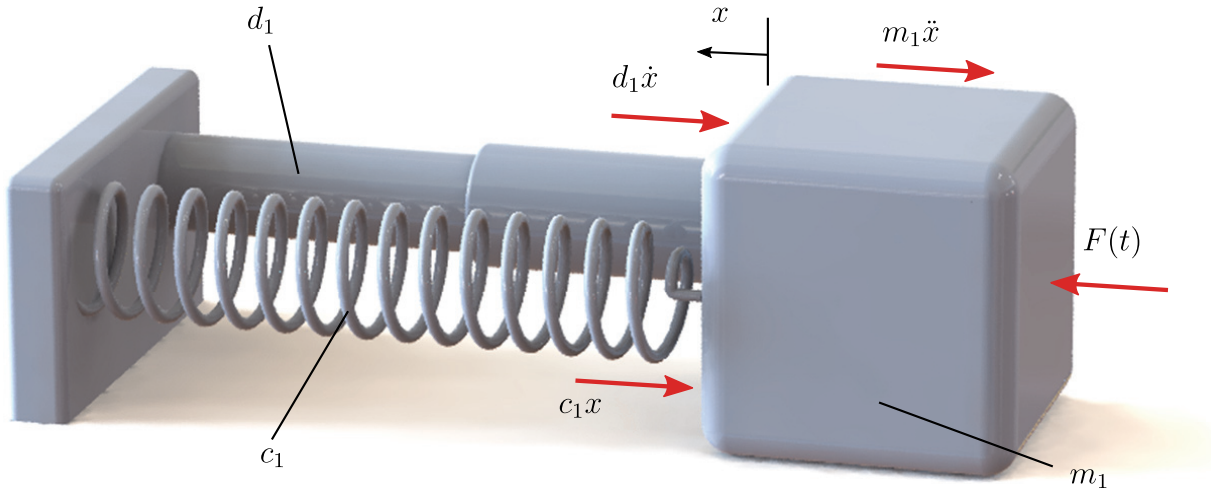


Figure 5.10: Model of a 1D spring-mass-damper system with external force  $F(t)$

described with a model of a spring-mass-damper system. An one-dimensional system, as shown in Fig. 5.10, consists of a stiffness  $c_1$ , a mass  $m_1$  and a damping coefficient  $d_1$  and is described by the following differential equation

$$m_1 \ddot{x} + d_1 \dot{x} + c_1 x = F(t) , \quad (5.4)$$

with the position  $x$  of the body and its time derivatives  $\dot{x}$  and  $\ddot{x}$ . For a given external force, the position, velocity and acceleration of a body can be calculated by time-integration according to (5.4). To describe a system with six decoupled DOF, (5.4) is generalized to

$$\mathbf{M}_d \ddot{\mathbf{x}}_d + \mathbf{D}_d \dot{\mathbf{x}}_d + \mathbf{C}_d \mathbf{x}_d = \mathbf{w}(t) , \quad (5.5)$$

with the desired pose  $\mathbf{x}_d$  and its time derivatives  $\dot{\mathbf{x}}_d$  and  $\ddot{\mathbf{x}}_d$ . The external forces and torques are the elements of the wrench  $\mathbf{w}(t)$ . The matrices are

$$\mathbf{M}_d = \text{diag} \left( [m_x \ m_y \ m_z \ I_{\varphi_x} \ I_{\varphi_y} \ I_{\varphi_z}] \right) , \quad (5.6)$$

$$\mathbf{D}_d = \text{diag} \left( [d_x \ d_y \ d_z \ d_{\varphi_x} \ d_{\varphi_y} \ d_{\varphi_z}] \right) \quad \text{and} \quad (5.7)$$

$$\mathbf{C}_d = \text{diag} \left( [c_x \ c_y \ c_z \ c_{\varphi_x} \ c_{\varphi_y} \ c_{\varphi_z}] \right) . \quad (5.8)$$

The characteristic of the platform can be arbitrarily chosen by setting values for  $\mathbf{M}_d$ ,  $\mathbf{D}_d$  and  $\mathbf{C}_d$ . E.g. by setting high values for the mass, an inert system can be simulated. In the following, a possible set-up with switchable stiffnesses to model a virtual workspace is proposed. If (5.5) is used in the algorithm without any modification, it would be possible for the user to move the platform to a certain pose by applying a wrench. As soon as the wrench is removed, the platform will return to its origin because of the spring force-term in

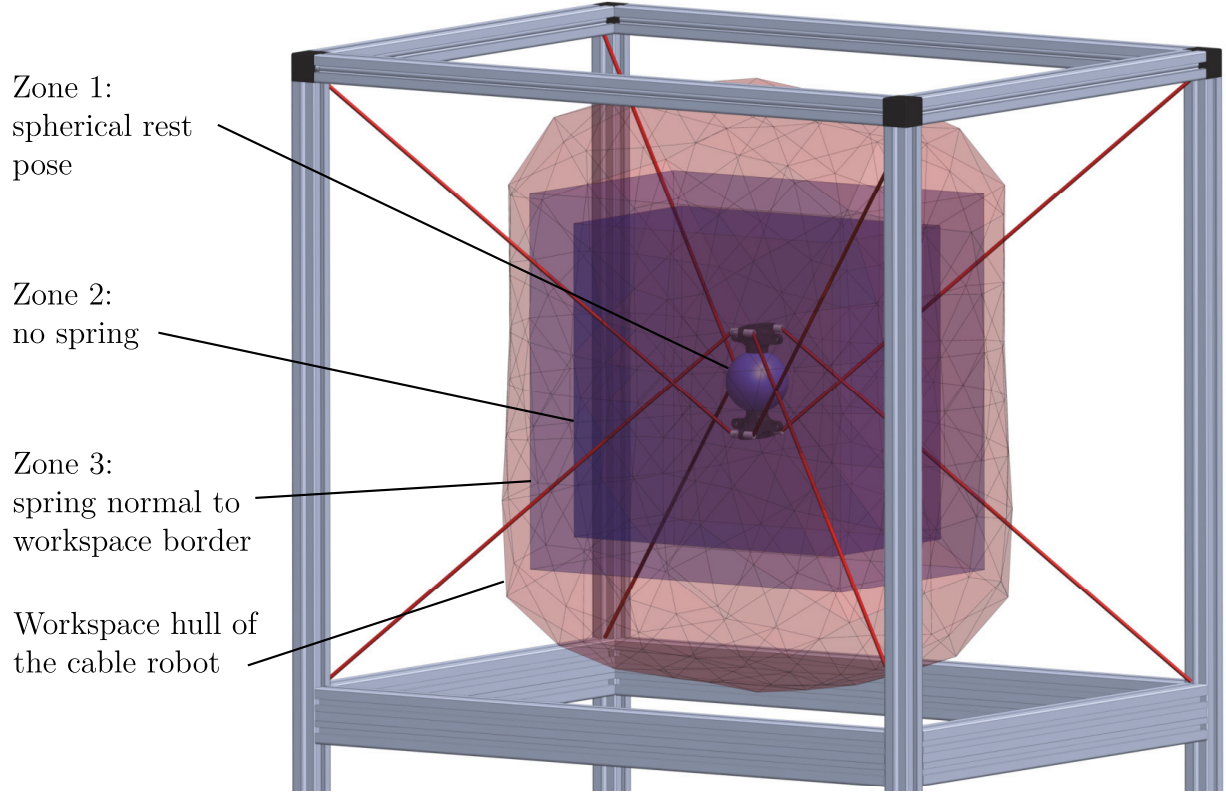


Figure 5.11: Zones of the virtual workspace and workspace hull of the cable robot

(5.5). To allow for positioning the platform, the spring force has to be toggled on and off on demand. For this, a virtual workspace is introduced, in which the elements of the stiffness matrix  $\mathbf{C}_d$  are a function  $\mathbf{C}_d = f(\mathbf{x}_{d,\text{Adm}})$  of the pose. With the introduction of virtual walls in all six DOF, the workspace can be limited to a box. This allows the user to feel the virtual workspace border and additionally guides him back into the allowed workspace. For this purpose, the virtual workspace is divided into three zones which are visualized in Fig. 5.11:

**Zone 1 (spherical rest pose):** This zone is a sphere with the radius  $R1$  and its midpoint corresponds to the origin of the world frame  $\mathcal{K}_0$ . As long as the midpoint of the platform is inside Zone 1, a spring force-vector is pointing to the origin of the sphere. Therefore, a spring force-vector pulls the platform to the origin. This works as a rest pose for the platform.

**Zone 2 (no spring force):** In Zone 2, the spring is disabled and only the damping and inertia of the virtual system are activated. If the external force is removed, the platform is slowed down by the damping and remains in the desired position.

**Zone 3 (spring force-vector normal to the borders of the workspace):** If the platform is in Zone 3, the spring force-vector, which is normal to the borders of the workspace, is toggled on. This force signals the workspace border.

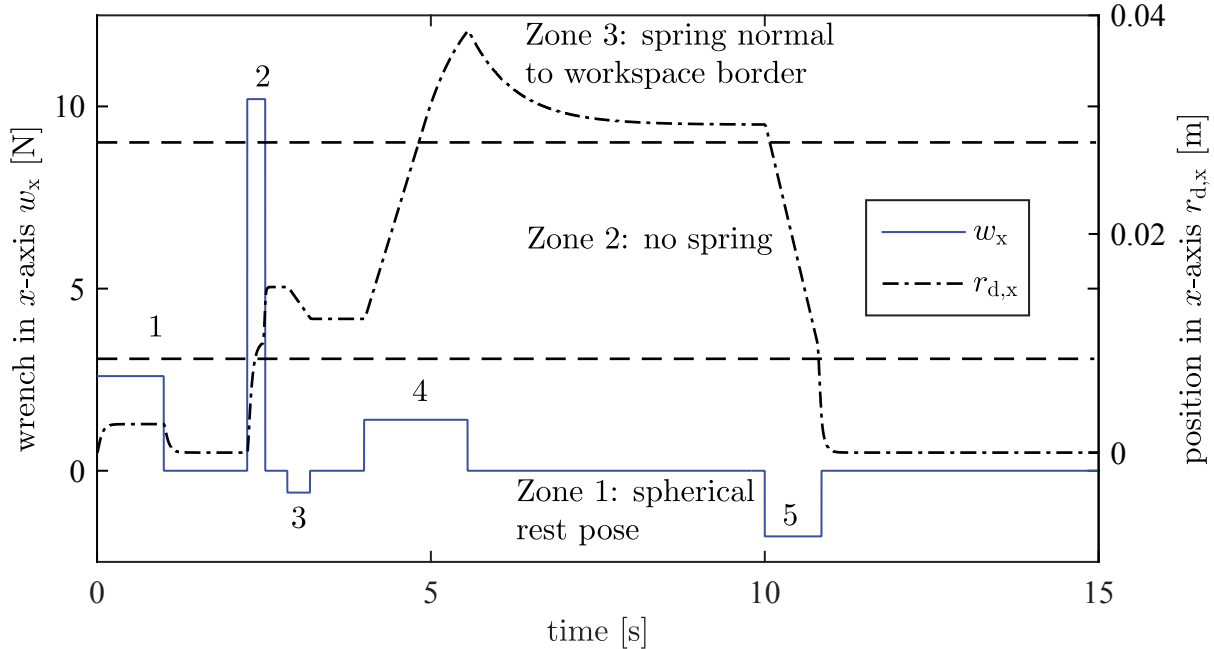


Figure 5.12: Simulation of the virtual workspace with force pulses 1 to 5 and resulting position  $r_{d,x}$

The virtual workspace has to lie within the robot workspace whose hull is also depicted in Fig. 5.11. Apart from that, the dimensions of the virtual workspace can be arbitrarily chosen.

The spring constant  $\mathbf{C}_d$  is calculated according to the description above and applied to the virtual equation of motion (5.5). To exemplary demonstrate the behaviour of the virtual system, an external force in  $x$ -axis is generated and applied to the system. The force is designed to cover all three zones to show the different behaviour of the system. The simulation results are shown in Fig. 5.12 and described in the following:

**Force pulse 1:** In the time range  $0 \text{ s} < t < 1 \text{ s}$ , a constant force with the magnitude of  $w_x = 2.6 \text{ N}$  is applied to the platform. When the platform reaches a distance of  $0.0026 \text{ m}$  to the origin, the force equilibrium with the virtual spring is reached. Thus, the applied force is not strong enough to guide the platform out of the Zone 1. As soon as the force is removed, the platform is moving back to the origin.

**Force pulse 2:** The second force pulse is applied to the platform in a time range of  $2.25 \text{ s} < t < 2.52 \text{ s}$  with a magnitude of  $10.2 \text{ N}$ . This time, the force is strong enough to overcome the counter-wise spring force of Zone 1. As soon as the platform crosses the border to Zone 2, the spring constant is set to zero. After removing the external force, the platform is stopped by the system damping and keeps its position.

**Force pulse 3:** At the time  $2.85 \text{ s} < t < 3.2 \text{ s}$ , the platform is in Zone 2. In this area of the virtual workspace, no spring force is active and the platform moves according to

the applied external force. As soon as the external force becomes zero, the platform is decelerated by the damping.

**Force pulse 4:** In this section ( $4.0 \text{ s} < t < 5.5 \text{ s}$ ), the platform is moving through Zone 2 with constant velocity. At the time of  $4.9 \text{ s}$  the platform reaches the border of the working area ( $0.03 \text{ m}$ ). It is visible that the platform is slowed down by the counter force of Zone 3. After the external force is removed, the platform is guided back into the allowed workspace described by Zone 2 and remains at the borderline.

**Force pulse 5:** The last force pulse starting at  $t = 10 \text{ s}$  brings the platform towards the origin. It is visible that the spring force of Zone 1 is catching the platform as soon as it reaches the area of the sphere, describing the border of Zone 1.

The simulation showed how the behaviour of the platform can be influenced by switching the spring constant. Next, the controller design is presented.

### 5.2.2 Controller Design and Implementation

In the following, the control structure visualized in Fig. 5.13 is described. The admittance control is based on an indirect force measurement through the cable force sensors and uses (2.11) for the transformation from joint to operational space. The wrench includes the gravitational force of the platform and also measurement errors. At start-up of the admittance control, the actual wrench  $\mathbf{w}_{\text{init}}$  is stored. Acceleration of the platform leads also to inertia forces of the real platform which are measured by the force sensor. Therefore, the inertia forces  $m_p \ddot{\mathbf{x}}_d$  derived from the platform mass  $m_p$  and the desired acceleration  $\ddot{\mathbf{x}}_d$  have to be excluded. The mass  $m_p$  corresponds to the real mass of the platform and is estimated by  $m_p = \frac{\mathbf{w}_{\text{init}}}{g}$ .

The input signal of the admittance control  $\mathbf{w}_{\text{Adm}}$  yields

$$\mathbf{w}_{\text{Adm}} = \mathbf{w} - \mathbf{w}_{\text{init}} - m_p \ddot{\mathbf{x}}_d \quad , \quad (5.9)$$

which is smoothed with a PT<sub>1</sub>-Filter with a time constant of  $T_1=3 \text{ ms}$ .

The desired position of the admittance control  $\mathbf{x}_{d,\text{Adm}}$  is transformed from operational to joint space with the inverse kinematics according to (2.9) and delivers the cable length  $\mathbf{q}_d$ . Using a cable robot, the cable forces have to be considered for stable operation as well. Therefore, the cable force control is applied to keep the cables under tension. The output is a change in cable length  $\Delta \mathbf{q}_{d,\text{CFC}}$ . The outputs of the admittance and cable force controller are summed up by

$$\boldsymbol{\theta}_d = \mathbf{q}_d + \Delta \mathbf{q}_{d,\text{CFC}} \quad , \quad (5.10)$$

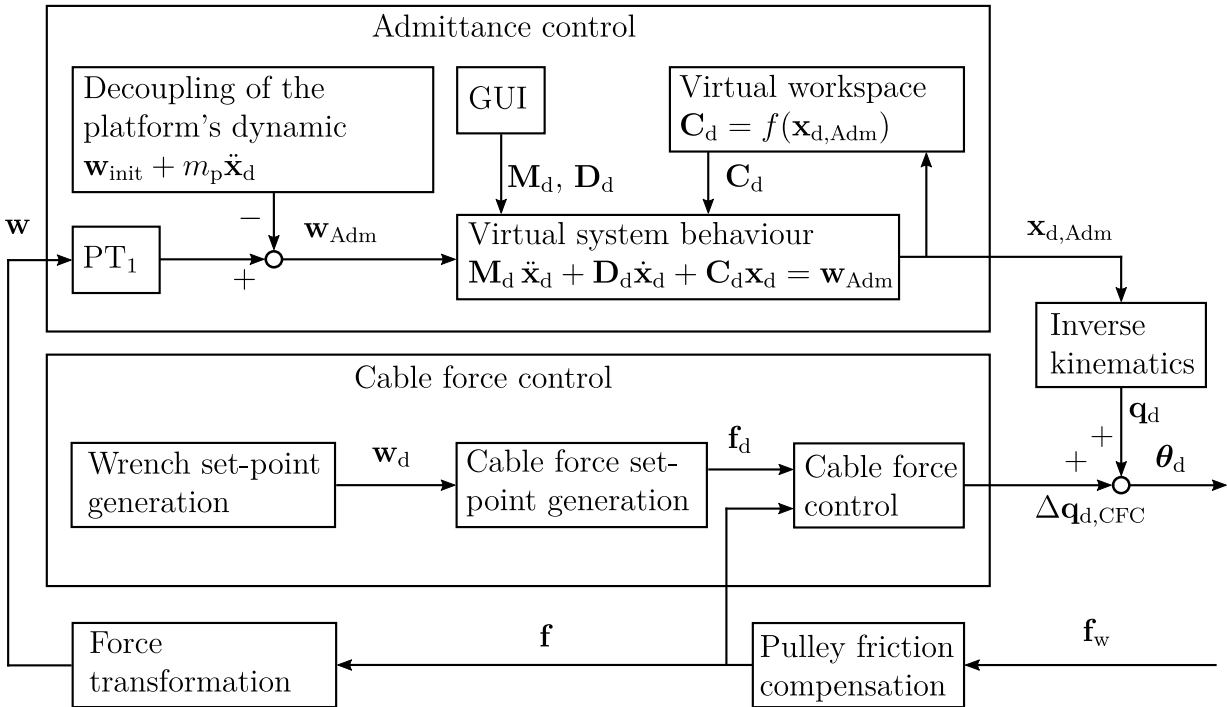


Figure 5.13: Structure of the implementation with admittance and cable force controller

to the desired actuator variable  $\theta_d$  which is commanded to the servo drives. Based on this implementation, the experimental investigation is carried out.

### 5.2.3 Experimental Investigation of the Performance

In the following, the performance and accuracy of the emulation of a desired system behaviour is experimentally investigated. The maximum dynamic which can be emulated by the robot is limited by the robot's dynamic. The drives of the IPAnema3 Mini do not prove the same following behaviour as the IPAnema3 drives. Thus, in the current robot, the robot's dynamic is characterized by the bandwidth of the actuator unit. To get insight into the feasible bandwidth, the transfer function  $G_a(s)$  describing the relation between desired position value  $\theta_{d,1}$  and the encoder feedback value  $\theta_1$  for winch 1 is established.

The servo motor with the winch is a typical spring-mass-damper system. Therefore, a second order system

$$G_a(s) = \frac{1}{1 + 2\zeta_a T_{w,a} s + (T_{w,a} s)^2} \quad (5.11)$$

is assumed for the transmission behaviour. For the parameter identification based on a noise response, the Matlab System Identification Toolbox is used. The resulting parameters are  $T_{w,a} = 0.0139$  and  $\zeta_a = 0.587$ . The identified transfer function matches the measurement with 98.5%. The deviation of 1.5% arises from sensor noise which is not modelled.

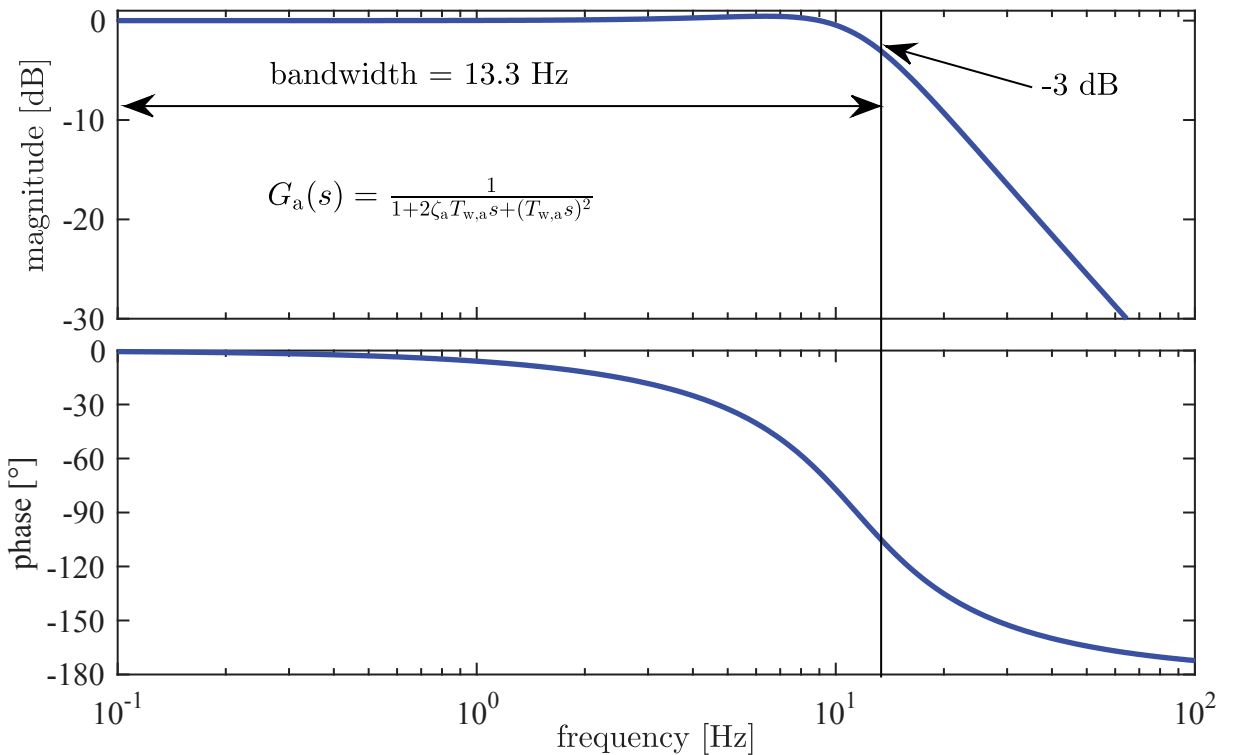


Figure 5.14: Bode diagram of the transfer function of the IPAnema 3 Mini drive  $G_a(s)$ .

Table 5.3: Verification of the dynamic parameters of the simulated system

Measurement	$c_x$ [N/m]	$d_x$ [Ns/m]	$m_x$ [kg]	$\omega_{d,\text{theo}}$ [Hz]	$\omega_{d,\text{exp}}$ [Hz]
1	31.9	5	20	0.2	0.203
2	197.5	5	20	0.5	0.504
3	395.4	5	10	1.0	0.997
4	9870.2	5	10	5.0	5.124

The Bode diagram for  $G_a(s)$  is shown in Fig. 5.14. The transfer function  $G_p(s)$  reaches the -3 dB margin at a frequency of 13.3 Hz, which corresponds to the bandwidth of the haptic interface.

In the following, the natural oscillations for given spring-mass-damper systems are investigated. For this, the parameters  $c_x$ ,  $d_x$  and  $m_x$  are set to certain values. The theoretical eigenfrequency  $\omega_{d,\text{theo}}$  of a damped system is determined by

$$\omega_{d,\text{theo}} = \sqrt{\frac{c_x}{m_x} - \left(\frac{d_x}{2m_x}\right)^2} . \quad (5.12)$$

For this experiment, the user moves the platform manually out of the home position and releases it. Then, the resulting platform oscillations are measured and the eigenfrequency is determined. The input parameters  $c_x$ ,  $d_x$  and  $m_x$ , the theoretical eigenfrequency  $\omega_{d,\text{theo}}$

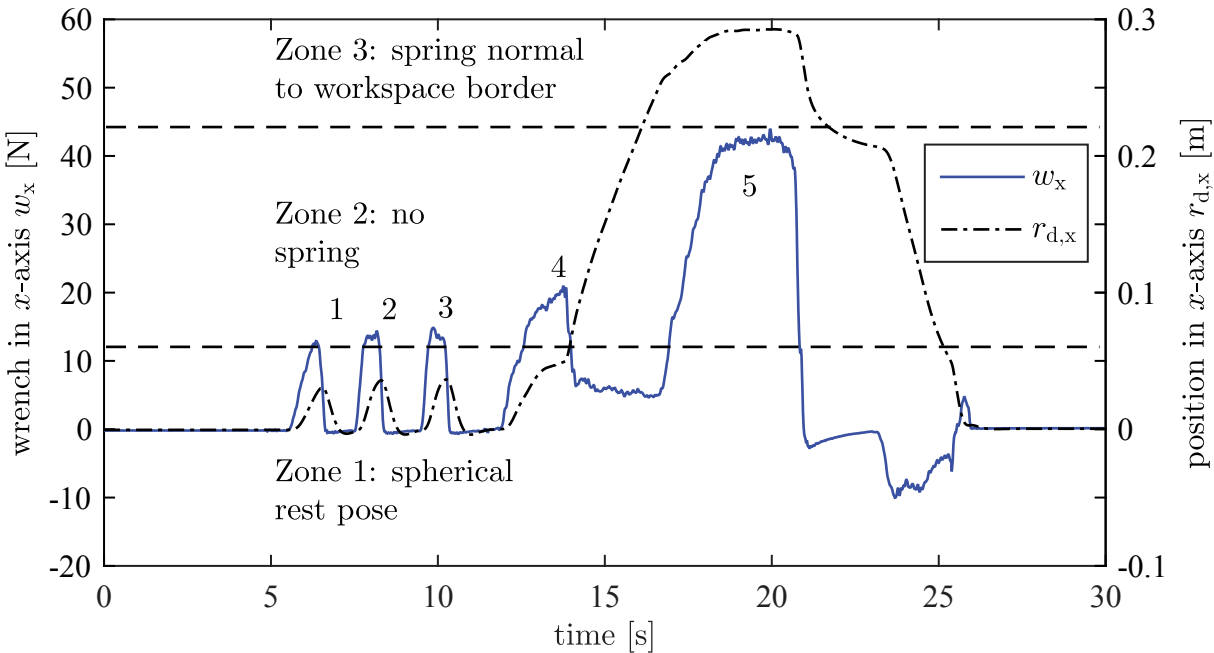


Figure 5.15: Experiment: measured user-applied force  $w_x$  and resulting position  $r_{d,x}$

according to (5.12) and the experimentally determined eigenfrequency  $\omega_{d,\text{exp}}$  are listed in Table 5.3. The evaluation shows a good correlation of the robot behaviour with a maximum error in the eigenfrequency of 2.5%.

For the experimental evaluation of the virtual system behaviour, the applied wrench in  $x$ -axis  $w_x$  and the resulting movement in  $x$ -axis  $r_{d,x}$  are plotted in Fig. 5.15. In this experiment, a user grasps the platform and shifts it to several positions.

The first three force pulses are not strong enough to bring the platform out of Zone 1 and the platform is dragged back to the origin by the spring force. The fourth force pulse brings the platform to Zone 2, where the spring is turned off. The sudden missing of the stiffness increases the slope of the position and leads to a drop of the applied force  $w_x$ . The user's impression at this point is comparable to the feeling of dragging two magnets apart. Then, the applied force stays in a constant range while the slope of the position can be also described as constant in this area. This shows the active damping in Zone 2. After the platform reaches the border of the workspace, the  $w_x$  value rises with a small delay. This delay is caused by the virtual inertia of the system. Due to that, the platform enters Zone 3 without additional user force. After the virtual kinetic energy is transformed into spring energy and energy dissipated in the virtual damper, the user has to increase the force to move the platform further into Zone 3. As it is visible, the user pushes the platform into the Zone 3 by a constant force. The position of the platform is not changing because the spring force of Zone 3 equals the applied user force. After the user releases the force, the platform is moving back to Zone 2. The user feels a guiding force in normal direction to the border plane between Zone 3 and Zone 2. Back in Zone 2 the platform is moved

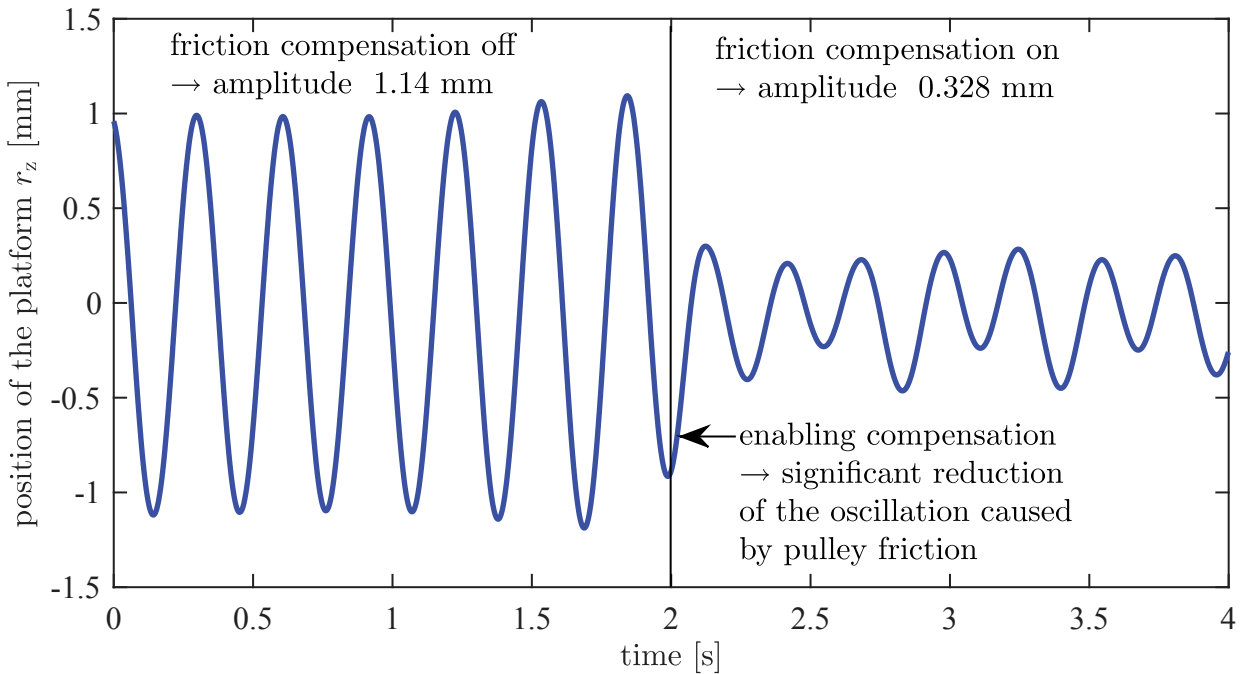


Figure 5.16: Reduction of the oscillation of the admittance control in idle mode using the pulley friction compensation

towards the origin. Finally, the spring force of Zone 1 catches the platform and drags it to the robot's origin.

As it can be seen from Fig. 5.15, the system behaves identical to the idealized one evaluated in Fig. 5.12. The position of the platform is very responsive to the user input and the system behaviour can be controlled very precisely.

#### 5.2.4 Elimination of Oscillations due to Pulley Friction

Since the cable force sensors were moved from the platform to the indirect measurement over the pulley system, the platform tends to oscillate in idle mode of admittance control, as the pulley friction is interpreted as user force. Actually, in idle mode, no user force is applied and the platform should stand still. This phenomenon can be reduced by the friction compensation presented in section 3.7: the amplitude of the oscillation can be damped by two-thirds from 1.14 mm to 0.328 mm as can be seen in Fig. 5.16.

In this section an admittance controller for a cable robot was developed and demonstrated. A switchable stiffness was introduced to guide the user with force feedback within the workspace. The bandwidth of the investigated cable robot was determined to 13.3 Hz, which enables a very responsive system that can simulate a virtual system in a very high range.

---

# 6 Conclusions and Outlook

## 6.1 Conclusions

This PhD thesis studies the force control of redundant cable robots using decentralized position-controlled drives. A control architecture is proposed incorporating cable force control and operational space position and force control. To ensure feasible cable forces, the obvious idea is to add position offsets for each drives derived from a closed-loop cable force control. In this approach, no control loop for the platform position is applied. An important finding of this thesis is that cable force control will decrease the stiffness of the robot. Furthermore, the stability of the cable force control depends on the geometrical stiffness matrix. From this analysis, it can be concluded that it is not sufficient to control only the cable forces. For this reason, the null-space control is introduced, which divides the control problem into the position control of the platform in operational space and the cable force control in the null-space. With this approach, the desired drive positions are determined to control the platform to the desired position and to keep the cable forces within the feasible limits.

In the area of the forward kinematics, existing approaches are further developed. With the pre-calculation of the point where the cable leaves the pulley, the objective function of the iterative forward kinematics algorithm is simplified which saves roughly 30% computational run-time. This simplification may also be implemented in simulation environments for cable robots to accelerate the computing time. With the incorporation of the non-linear cable model in the forward kinematics, a starting point is set for the implementation of more sophisticated cable models.

The force control of redundant cable robots makes the real-time calculation of cable force distributions necessary. For this purpose, the quadratic programming approach is further developed. With the proposed extension in form of a reference force, the tension level can be arbitrarily adjusted. Simultaneously, the application of an automatic code generation for the implementation of the quadratic programming algorithm is applied, which yields a ten time faster computational run-time compared to a state of the art implementation. A further simulation showed that also with higher degree-of-redundancy than two, the iterative algorithm shows an acceptable computational run-time.

In winch-integrated cable force measurement, pulley friction disturbs the force signal by roughly 8% on the IPAnema 3 Mini what is a significant disturbance. For the compensation, a model based on Coulomb and viscose friction and the Dahl model is derived. The verification showed that the wrench hysteresis is almost completely compensated and the oscillations are reduced by two-thirds.

Implementing the control approach on a small and on a large cable robot prototype, the feasibility and scalability is demonstrated.

The evaluation of the position accuracy reached by the forward kinematic for different tension levels delivered that the non-linear cable model is slightly more precise than the linear model. One can conclude that the actual cable model does not sufficiently represent the occurring effects.

The investigation of the position accuracy on the IPAnema 3 showed that the absolute position accuracy within the workspace amounts to 41.4 mm and 1.9° using inverse kinematics and 32.7 mm and 1.3° using the developed approach, what lies in the same range. The experimental investigation revealed a significantly better accuracy for the force controlled robot at the workspace border.

The evaluation of the eigenfrequencies showed that the payload of the platform and the tension level have an important influence. In the experiment, the eigenfrequency was halved by a payload of 80 kg. Using the maximum tension level, the eigenfrequency and thus the available bandwidth of the robot can be increased in a range of 15-30%. The increase of the stiffness is mainly caused by the non-linearity of the cable stiffness, whereas the investigation confirmed that the geometric stiffness has only a minor influence.

With the energy consumption model, the influence of the tension level was investigated from the view point of energy efficiency. Applying the minimal tension level allows for saving of up to 20% of energy compared to the medium tension level. The analysis showed that the mechanical parts of the gear box and the winch have proportionally the largest losses. The comparison with an industrial robot delivered that both robots have roughly the same energy consumption for a reference task.

For the interaction with the environment, external force controller were implemented. The hybrid position and force control law showed promising results on the IPAnema 3. The analysis of the contact establishment delivered, that in spite of position-dependent robot stiffness no dependency between the criteria, overshoot and settling time, and the position within the workspace was recognized.

The admittance control law was successfully adopted to the cable robot. With the introduction of virtual walls under application of virtual springs, a virtual workspace was proposed as scenario for human robot cooperation. The verification delivered a fit of 97.5% for the desired eigenfrequencies. With a system identification of the actuator unit, the bandwidth was determined to the reasonable value of 13.3 Hz.

## 6.2 Outlook

The experimental evaluation of the position accuracy showed that in spite of closed-loop operational space position control, position errors remain. Consequently, the underlying model of the forward kinematics does not sufficiently cover all effects. Further work is necessary in the field of calibration of the geometrical parameters and modelling of the cables to increase the position accuracy of the robot.

The results of this work offer several possibilities to be integrated into simulation models and design tools for cable robots. The identified dynamic models can be incorporated into a robot simulation model. The observed cable effects like non-linear stiffness, settlement and eigenfrequencies can be included in further work. The energy consumption model can be easily applied for dimensioning of the drives including the relevant friction losses. For this, the scenario-based dimensioning presented in (Kraus and Pott 2013) can be expanded. In the planning of new cable robots, this will allow for a reliable selection of the necessary drive performance for a given task. The investigation of the robot behaviour at the workspace border showed that due to uncertainties in the robot geometry and cable force measurement, the real workspace is smaller than expected from the workspace analysis. These uncertainties have to be considered in design tools for cable robots.

For the control strategies, two opposite directions regarding the control frequency can be pursued: from high control frequencies computed torque control benefits and which can result in high dynamic movements in the direction of delta kinematics. Low frequency control becomes important for winches with small bandwidth for dynamic movement. This can be crane winches for the realization of payloads of several tons as well as low cost winches with only an on/off control.

The external force controller can be further developed for specific applications. For the hybrid position and force control, the next step may be attaching a grinder and running the process. The admittance control implementation can be coupled with a virtual reality engine or expanded for teleoperation, e.g. for minimal invasive surgery.

---

# References

- Agrawal, Peine et al. (2010) Agrawal, Varun, Peine, William J., and Yao, Bin, 2010. Modeling of Transmission Characteristics Across a Cable-Conduit System, *IEEE Transactions on Robotics* **vol. 26**(5) pp. 914–924, doi: 10.1109/TRO.2010.2064014
- Albu-Schaeffer, Ott et al. (2003) Albu-Schaeffer, Alin, Ott, Christian, Frese, Udo, and Hirzinger, Gerd, 2003. Cartesian Impedance Control of Redundant Robots: Recent Results with the DLR-Light-Weight-Arms, *IEEE International Conference on Robotics and Automation (ICRA)*, Taipei, Taiwan, September 14-19 2003, ISBN 0-7803-7736-2
- Albus, Bostelman et al. (1992) Albus, James S., Bostelman, Roger V., and Dagalakis, Nicholas G., 1992. The NIST ROBOCRANE, *Journal of Research at the National Institute of Standards and Technology* **vol. 97**(3) pp. 373–385
- Almeida, Lopes et al. (1999) Almeida, Fernando, Lopes, António, and Abreu, Paulo, 1999. Force-Impedance Control: a new control strategy of robotic manipulators, *Recent Advances in Mechatronics*, Istanbul, Turkey, May 1999, pp. 126–137, ISBN 9814021342
- Andersson, Söderberg et al. (2007) Andersson, Sören, Söderberg, Anders, and Björklund, Stefan, 2007. Friction models for sliding dry, boundary and mixed lubricated contacts, *Tribology International* **vol. 40**(4) pp. 580–587, doi:10.1016/j.triboint.2005.11.014
- Assuncao and Schumacher (2003) Assuncao, Ventura and Schumacher, Walter, 2003. Hybrid Force Control for Parallel Manipulators,

*Mediterranean conference on control and automation*, Rhodes, Greece, June 17–20 2003

- Behzadipour and Khajepour (2006) Behzadipour, Saeed and Khajepour, Amir, 2006. Stiffness of cable-based parallel manipulators with application to stability analysis, *Journal of Mechanical Design, Transactions of the ASME* **vol. 128**(1) pp. 303–310, URL <http://www.scopus.com/inward/record.url?eid=2-s2.0-33645776218&partnerID=40&md5=d454bfa2fd3e5e639e51ce9d06573dc2>
- Billette and Gosselin (2009) Billette, Greg and Gosselin, Clément, 2009. Producing rigid contacts in cable-driven haptic interfaces using impact generating reels, *IEEE International Conference on Robotics and Automation (ICRA)*, Kobe, Japan, May 12-17 2009, pp. 307–312, doi:10.1109/ROBOT.2009.5152302, URL <http://ieeexplore.ieee.org/stamp/stamp.jsp?arnumber=5152302>
- Borgstrom, Borgstrom et al. (2008) Borgstrom, Per Henrik, Borgstrom, Nils Peter, Stealey, Michael J., Jordan, Brett L., Sukhatme, Gaurav, Batalin, Maxim A., and Kaiser, William J., 2008. Generation of Energy Efficient Trajectories for NIMS3D, a Three-Dimensional Cabled Robot, *IEEE International Conference on Robotics 2008*, Pasadena, CA, USA, May 19-23 2008, pp. 2222–2227, doi:10.1109/ROBOT.2008.4543544
- Borgstrom, Jordan et al. (2009) Borgstrom, Per Henrik, Jordan, Brett L., Sukhatme, Guarav S., Batalin, Maxim A., and Kaiser, William J., 2009. Rapid Computation of Optimally Safe Tension Distributions for Parallel Cable-Driven Robots, *IEEE Transactions on Robotics* **vol. 25**(6) pp. 1271–1281, doi:10.1109/TRO.2009.2032957, URL <http://ieeexplore.ieee.org/stamp/stamp.jsp?arnumber=5306101>

- Bosch Rexroth AG (2010) Bosch Rexroth AG, 2010. Rexroth IndraDyn S, MSK Synchronous Motors, Project Planning Manual, Lohr am Main, Germany
- Bosscher, Riechel et al. (2006) Bosscher, Paul, Riechel, Andrew T., and Ebert-Uphoff, Imme, 2006. Wrench-Feasible Workspace Generation for Cable-Driven Robots, *IEEE Transactions on Robotics* **vol. 22**(5) pp. 890–902
- Bouchard, Moore et al. (2010) Bouchard, Samuel, Moore, Brian, and Gosselin, Clément, 2010. On the ability of a cable-driven robot to generate a prescribed set of wrenches, *Journal of Mechanisms and Robotics* **vol. 2**(1) pp. 1–10, doi:10.1115/1.4000558, URL <http://www.scopus.com/inward/record.url?eid=2-s2.0-78651563640&partnerID=40&md5=c38295e45251f9867a7ab0ec3793dd42>
- Bruckmann (2010) Bruckmann, Tobias, 2010. *Auslegung und Betrieb redundanter paralleler Seilroboter*, PhD thesis, University of Duisburg-Essen, Duisburg, Germany
- Burkhardt, Seifried et al. (2014) Burkhardt, Markus, Seifried, Robert, and Eberhard, Peter, 2014. Experimental Studies of Control Concepts for a Parallel Manipulator with Flexible Links, *Asian Conference on Multibody Dynamics*, Busan, Korea, June 20-July 3 2014
- Canudas de Wit, Olsson et al. (1995) Canudas de Wit, Carlos, Olsson, H., Aström, Karl Johann, and Lischinsky, Pablo, 1995. A new model for control of systems with friction, *IEEE Transactions on Automatic Control* **vol. 40**(3) pp. 419–425
- Carricato and Merlet (2010) Carricato, Marco and Merlet, Jean-Pierre, 2010. Geometrico-Static Analysis of Under-Constrained Cable-Driven Parallel Robots, *Advances in Robot Kinematics (ARK)*, Piran, Slovenia, June 27-July 1 2010, pp. 309–319, ISBN 9048192617
- Cone (1985) Cone, Lawrence L., 1985. Skycam, an aerial robotic camera system, *Byte Magazine*, vol. 10, pp. 122–132

- Currie and Wilson (2012) Currie, Jonathan and Wilson, David I., 2012. OPTI: Lowering the Barrier Between Open Source Optimizers and the Industrial MATLAB User, Nick Sahinidis and Jose Pinto (eds.), *Foundations of Computer-Aided Process Operations*, Savannah, Georgia, USA
- Dahl (1968) Dahl, P. R., 1968. A solid friction model, *The Aerospace Corporation*, El Segundo, CA, May 1968
- Deng, Lee et al. (2010) Deng, Wenbin, Lee, Hyuk Jin, and Jeh-Won, Lee, 2010. Dynamic Hybrid Position-Force Control for Parallel Robot Manipulators, *Robot Design, Dynamics and Control (ROMANSY)*, Udine, Italy, July 5–8 2010, pp. pp 57–64, ISBN 978-3-7091-0276-3
- Duan and Duan (2014) Duan, Q. J. and Duan, Xuechao, 2014. Workspace Classification and Quantification Calculations of Cable-Driven Parallel Robots, *Advances in Mechanical Engineering* **vol. 2014** p. 9, doi:10.1155/2014/358727, URL <http://dx.doi.org/10.1155/2014/358727>
- Dupont, Hayward et al. (2002) Dupont, Pierre, Hayward, Vincent, Armstrong, Brian, and Altpeter, Friedhelm, 2002. Single state elastoplastic friction models, *IEEE Transactions on Automatic Control* **vol. 47(5)** pp. 787–792
- Fang (2005) Fang, Shiqing, 2005. *Design, Modeling and Motion Control of Tendon-Based Parallel Manipulators*, PhD thesis, University of Duisburg-Essen, Duisburg, Germany
- Fortin-Côté, Cardou et al. (2014) Fortin-Côté, Alexis, Cardou, Philippe, and Gosselin, Clément, 2014. An Admittance Control Scheme for Haptic Interfaces Based on Cable-Driven Parallel Mechanisms, *IEEE International Conference on Robotics and Automation (ICRA)*, Hong Kong, China, May 31-June 7 2014, doi:10.1109/ICRA.2014.6906949

- Gallina and Rosati (2002) Gallina, Paolo and Rosati, Giulio, 2002. Manipulability of a planar wire driven haptic device, *Mechanism and Machine Theory* **vol. 37**(2) pp. 215–228, doi:10.1016/S0094-114X(01)00076-3, URL <http://www.sciencedirect.com/science/article/pii/S0094114X01000763>
- Gallina, Rosati et al. (2001) Gallina, Paolo, Rosati, Giulio, and Rossi, Aldo, 2001. 3-d.o.f. Wire Driven Planar Haptic Interface, *Journal of Intelligent and Robotic Systems* **vol. 32**(1) pp. 23–36, doi:10.1023/A:1012095609866
- Gravagne and Walker (2000) Gravagne, I. A. and Walker, I. D., 2000. On the structure of minimum effort solutions with application to kinematic redundancy resolution, *IEEE Transactions on Robotics and Automation* **vol. 16**(6) pp. 855–863, doi:10.1109/70.897797
- Hassan and Khajepour (2011) Hassan, Mahir and Khajepour, Amir, 2011. Analysis of Bounded Cable Tensions in Cable-Actuated Parallel Manipulators, *IEEE Transactions on Robotics* **vol. 27**(5) pp. 891–900, doi:10.1109/TRO.2011.2158693, URL <http://ieeexplore.ieee.org/stamp/stamp.jsp?arnumber=5959225>
- Izard, Gouttefarde et al. (2012) Izard, Jean-Baptiste, Gouttefarde, Marc, Baradat, Cédric, Culla, David, and Sallé, Damien, 2012. Integration of a Parallel Cable-Driven Robot on an Existing Building Façade, Bruckmann, Tobias and Pott, Andreas (eds.), *Cable-Driven Parallel Robots*, Stuttgart, Germany, September 3–4 2012: Springer, Mechanisms and Machine Science, pp. 149–164, ISBN 978-3-642-31987-7, doi:10.1007/978-3-642-31988-4\_10
- Kawamura and Ito (1993) Kawamura, Sadao and Ito, Ken, 1993. New type of master robot for teleoperation using a radial wire drive system, *IEEE International Conference on Intelligent Robots and Systems (IROS)*, Tokyo, Japan, July 26 - 30 1993, pp. 55–60, doi:10.1109/IROS.1993.583079

- Kawamura, Kino et al. (2000) Kawamura, Sadao, Kino, Hitoshi, and Won, Choe, 2000. High-speed manipulation by using parallel wire-driven robots, *Robotica* **vol. 18**(1) pp. 13–21
- Khosravi and Taghirad (2014) Khosravi, Mohammad A. and Taghirad, Hamid D., 2014. Dynamic Modeling and Control of Parallel Robots With Elastic Cables: Singular Perturbation Approach, *IEEE Transactions on Robotics* **vol. 30**(3) pp. 694–704, doi:10.1109/TRO.2014.2298057, URL <http://ieeexplore.ieee.org/stamp/stamp.jsp?arnumber=6719560>
- Klimchik, Pashkevich et al. (2012) Klimchik, Alexandr, Pashkevich, Anatoly, Chablat, Damien, and Hovland, Geir, 2012. Compensation of compliance errors in parallel manipulators composed of non-perfect kinematic chains, *Advances in Robot Kinematics (ARK)*, Innsbruck, Austria, June 24–28 2012
- Kraus and Pott (2013) Kraus, Werner and Pott, Andreas, 2013. Scenario-Based Dimensioning of the Actuator of Parallel Cable-Driven Robots, Viadero, Fernando and Cecarelli, Marco (eds.), *Mechanisms and Machine Science*, Santander, Spain, September 18-22 2012: Springer Netherlands, pp. 131–139, ISBN 978-94-007-4901-6, doi:10.1007/978-94-007-4902-3\_14
- Kraus, Schmidt et al. (2012) Kraus, Werner, Schmidt, Valentin, Pott, Andreas, and Verl, Alexander, 2012. Investigation on a planar cable-driven parallel robot, *German Conference on Robotics (ROBOTIK)*, Munich, Germany, May 21 - 22 2012: VDE-Verlag, pp. 193–198, ISBN 978-3-8007-3418-4
- Kraus, Schmidt et al. (2013) Kraus, Werner, Schmidt, Valentin, Rajendra, Puneeth, and Pott, Andreas, 2013. Load identification and compensation for a Cable-Driven parallel robot, *IEEE International Conference on Robotics and Automation*, Karlsruhe, Germany, May 6-10 2013, pp. 2485–2490, ISBN 978-1-4673-5641-1, doi: 10.1109/ICRA.2013.6630915

- Kraus, Spiller et al. (2013) Kraus, Werner, Spiller, Alexander, and Pott, Andreas, 2013. Energieeffizienz von parallelen Seilrobotern, *SPS IPC DRIVES*, Nürnberg, Germany, November 26-28 2013
- Kraus, Mangold et al. (2014) Kraus, Werner, Mangold, Alexander, Ho, Wei Yang, and Pott, Andreas, 2014. Haptic Interaction with a Cable-Driven Parallel Robot Using Admittance Control, Pott, Andreas and Bruckmann, Tobias (eds.), *Cable-Driven Parallel Robots*, Duisburg, Germany, August 24-27 2014: Springer International Publishing, Mechanisms and Machine Science, pp. 201–212, ISBN 978-3-319-09488-5, doi:10.1007/978-3-319-09489-2\_14
- Kraus, Schmidt et al. (2014) Kraus, Werner, Schmidt, Valentin, Rajendra, Puneeth, and Pott, Andreas, 2014. System Identification and Cable Force Control for a Cable-Driven Parallel Robot with Industrial Servo Drives, *IEEE International Conference on Robotics and Automation (ICRA)*, Hong Kong, China, May 31-June 7 2014, pp. 5921–5926, doi:10.1109/ICRA.2014.6907731
- Kraus, Kessler et al. (2015) Kraus, Werner, Kessler, Michael, and Pott, Andreas, 2015. Pulley Friction Compensation for Winch-Integrated Cable Force Measurement and Verification on a Cable-Driven Parallel Robot, *International Conference on Robotics and Automation (ICRA)*, Seattle, WA, USA, May 26-30 2015, pp. 1627–1632, doi:10.1109/ICRA.2015.7139406
- Kraus, Miermeister et al. (2015) Kraus, Werner, Miermeister, Philipp, Schmidt, Valentin, and Pott, Andreas, 2015. Hybrid Position/Force Control of a Cable-Driven Parallel Robot with Experimental Evaluation, Flores, Paulo and Viadero, Fernando (eds.), *New Trends in Mechanism and Machine Science*, Guimarães, Portugal, September 16-20 2014: Springer International Publishing, Mechanisms and Machine Science, pp.

- Kröger, Finkemeyer et al. (2004) 553–561, ISBN 978-3-319-09410-6, doi:10.1007/978-3-319-09411-3\_59
- Kröger, Torsten, Finkemeyer, Bernd, Heuck, Markus, and Wahl, Friedrich M., 2004. Adaptive implicit hybrid force/pose control of industrial manipulators: compliant motion experiments, *IEEE International Conference on Intelligent Robots and Systems (IROS)*, Sendai, Japan, September 28 - October 2 2004
- Lalo (2013) Lalo, Wildan, 2013. *Ein Beitrag zur Entwicklung von Assistenzsystemen für serielle und parallele Roboter am Beispiel von Autobetonpumpen und seilbasierten Regalbediengeräten*, PhD thesis, University of Duisburg-Essen, Duisburg, Germany
- Lamaury and Gouttefarde (2013a) Lamaury, Johann and Gouttefarde, Marc, 2013. A Tension Distribution Method with Improved Computational Efficiency, *Cable-Driven Parallel Robots*, Springer, pp. 71–85
- Lamaury and Gouttefarde (2013b) Lamaury, Johann and Gouttefarde, Marc, 2013. Control of a large redundantly actuated cable-suspended parallel robot, *IEEE International Conference on Robotics and Automation*, Karlsruhe, Germany, May 6-10 2013, pp. 4659–4664, ISBN 978-1-4673-5641-1, doi:10.1109/ICRA.2013.6631240, URL <http://ieeexplore.ieee.org/stamp/stamp.jsp?arnumber=6631240>
- Lamaury, Gouttefarde et al. (2013) Lamaury, Johann, Gouttefarde, Marc, Chemori, Ahmed, and Hervé, Pierre-Élie, 2013. Dual-Space Adaptive Control of Redundantly Actuated Cable-Driven Parallel Robots, *IEEE International Conference on Intelligent Robots and Systems (IROS)*, Tokyo, Japan, November 3-8 2013, doi:10.1109/IROS.2013.6697060
- Lange, Bertleff et al. (2013) Lange, Friedrich, Bertleff, Wieland, and Suppa, Michael, 2013. Force and trajectory control of in-

- dustrial robots in stiff contact, *IEEE International Conference on Robotics and Automation*, Karlsruhe, Germany, May 6-10 2013, pp. 2927–2934, ISBN 978-1-4673-5641-1, doi:10.1109/ICRA.2013.6630983
- Laroche, Chellal et al. (2012) Laroche, Edouard, Chellal, Ryad, Cuillon, Loïc, and Gangloff, Jacques, 2012. A Preliminary Study for  $H_\infty$  Control of Parallel Cable-Driven Manipulators, Bruckmann, Tobias and Pott, Andreas (eds.), *Cable-Driven Parallel Robots*, Stuttgart, Germany, September 3–4 2012: Springer, Mechanisms and Machine Science, pp. 353–369, ISBN 978-3-642-31987-7, doi:10.1007/978-3-642-31988-4\_22
- Lee, Jeong et al. (2013) Lee, Giuk, Jeong, JI, Kim, S, Lee, D, and Kim, Jongwon, 2013. Energy saving by using a redundantly actuated parallel mechanism, *Global Conference on Sustainable Manufacturing*, Berlin, Germany, September 23–25 2013, pp. 348–352
- Leica Geosystems AG (2008) Leica Geosystems AG, 2008. User Manual Absolute-Tracker, Unterentfelden, Switzerland
- Li and Bone (2011) Li, Yan and Bone, Gary M., 2011. Are parallel manipulators more energy efficient?, *IEEE International Symposium on Computational Intelligence in Robotics and Automation*, Budapest, Hungary, November 21–22 2011, pp. 41–46, doi:10.1109/CIRA.2001.1013170
- Liu, Xu et al. (2004) Liu, Guanfeng, Xu, Jijie, and Li, Zexiang, 2004. On geometric algorithms for real-time grasping force optimization, *IEEE Transactions on Control Systems Technology* **12**(6) pp. 843–859, doi:10.1109/TCST.2004.833630
- Liu, Zhang et al. (2009) Liu, Pan, Zhang, Lixun X., Wang, Keyi Y., and Zhang, Jinyu, 2009. Dynamic modeling and control of a wire-driven rehabilitation robot, *Journal of Harbin Engineering University* **30**(7) pp. 811–815, URL

- [http://www.scopus.com/inward/record.url?  
eid=2-s2.0-69749091043&partnerID=40&md5=  
0481848c987da80fd6baa0b75c085066](http://www.scopus.com/inward/record.url?eid=2-s2.0-69749091043&partnerID=40&md5=0481848c987da80fd6baa0b75c085066)
- Lunze (2010) Lunze, Jan, 2010. *Regelungstechnik 1*, Berlin, Heidelberg: Springer, 10th edn., ISBN 3642295320
- Madani and Moallem (2011) Madani, M. and Moallem, Mehdi, 2011. Hybrid position/force control of a flexible parallel manipulator, *Journal of the Franklin Institute* pp. 999–1012
- Mahvash and Okamura (2006) Mahvash, Mohsen and Okamura, Allison M., 2006. Friction compensation for a force-feedback tele-robotic system, *IEEE International Conference on Robotics and Automation (ICRA)*, Orlando, Florida, USA, May 15-19 2006, pp. 3268–3273, doi:10.1109/ROBOT.2006.1642200
- Mattingley and Boyd (2012) Mattingley, Jacob and Boyd, Stephen, 2012. CVXGEN: a code generator for embedded convex optimization, *Optimization and Engineering* **vol. 13**(1) pp. 1–27, doi:10.1007/s11081-011-9176-9
- Meike and Ribickis (2011) Meike, Davis and Ribickis, Leonids, 2011. Analysis of the Energy Efficient Usage Methods of Medium and High Payload Industrial Robots in the Automobile Industry, *International Symposium on Topical Problems in the Field of Electrical and Power Engineering*, Pärnu, Estonia, January 10-15 2011, pp. 62–66
- Meunier, Boulet et al. (2009) Meunier, Gabriel, Boulet, Benoit, and Nahon, Meyer, 2009. Control of an Overactuated Cable-Driven Parallel Mechanism for a Radio Telescope Application, *IEEE Transactions on Control Systems Technology* **vol. 17**(5) pp. 1043–1054, doi:10.1109/TCST.2008.2004812, URL <http://ieeexplore.ieee.org/stamp/stamp.jsp?arnumber=4816104>
- Miermeister, Kraus et al. (2012) Miermeister, Philipp, Kraus, Werner, and Pott, Andreas, 2012. Differential Kinematics for Calibration, System Investigation, and Force Based For-

- ward Kinematics of Cable-Driven Parallel Robots, Bruckmann, Tobias and Pott, Andreas (eds.), *Cable-Driven Parallel Robots*, Stuttgart, Germany, September 3–4 2012: Springer, Mechanisms and Machine Science, pp. 319–333, ISBN 978-3-642-31987-7, doi:10.1007/978-3-642-31988-4\_20
- Miermeister, Kraus et al. (2014) Miermeister, Philipp, Kraus, Werner, Lan, Tian, and Pott, Andreas, 2014. An Elastic Cable Model for Cable-Driven Parallel Robots Including Hysteresis Effects, Pott, Andreas and Bruckmann, Tobias (eds.), *Cable-Driven Parallel Robots*, Duisburg, Germany, August 24-27 2014: Springer International Publishing, Mechanisms and Machine Science, ISBN 978-3-319-09488-5, doi:10.1007/978-3-319-09489-2\_2
- Ming and Higuchi (1994) Ming, Aiguo and Higuchi, Toshiro, 1994. Study on Multiple Degree-of-Freedom Positioning Mechanism using Wires (Part 1), *International Journal of the Japan Society for Precision Engineering* vol. 28(2) pp. 131–138
- Müller, Reichert et al. (2014) Müller, Katharina, Reichert, Christopher, and Bruckmann, Tobias, 2014. Analysis of Geometrical Force Calculation Algorithms for Cable-Driven Parallel Robots with a Threefold Redundancy, *Advances in Robot Kinematics (ARK)*, Ljubljana, Slovenia June 29-July 3 2014, pp. 203–211, ISBN 978-3-319-06697-4, doi:10.1007/978-3-319-06698-1\_22
- Müller, Spiller et al. (2011) Müller, Verena, Spiller, Alexander, and Verl, Alexander, 2011. Mehr Energieeffizienz in Roboteranwendungen, *wt Werkstattstechnik online* (105)
- Osypiuk and Kröger (2011) Osypiuk, Rafal and Kröger, Torsten, 2011. Parallel Stiffness Actuators with Six Degrees of Freedom for Efficient Force/Torque Control Applications, *Robotic Systems for Handling and Assembly*, Springer, vol. 67, ISBN 978-3-642-16784-3

- Otis, Mokhtari et al. (2008) Otis, Martin J.-D., Mokhtari, Marielle, Du Tremblay, Charles, Laurendeau, Denis, Rainville, Francois Michelle de, and Gosselin, Clément, 2008. Hybrid Control with Multi-Contact Interactions for 6DOF Haptic Foot Platform on a Cable-Driven Locomotion Interface, *Symposium on haptic interfaces for virtual environment and teleoperator systems (HAPTICS)*, pp. 161–168, ISBN 978-1-4244-2005-6, doi:10.1109/HAPTICS.2008.4479937, URL <http://ieeexplore.ieee.org/stamp/stamp.jsp?arnumber=4479937>
- Otis, Nguyen Dang et al. (2009) Otis, Martin J.-D., Nguyen Dang, Thien-Ly, Laliberté, Thierry, Quellet, Denis, Laurendeau, Denis, and Gosselin, Clément, 2009. Cable Tension Control and Analysis of Reel Transparency for 6-DOF haptic foot platform on a cable-driven locomotion interface, *International Journal of Electrical, Computer, and Systems Engineering* pp. 520–532
- Paccot, Andreff et al. (2009) Paccot, Flavien, Andreff, Nicolas, and Martinet, Philippe, 2009. A Review on the Dynamic Control of Parallel Kinematic Machines: Theory and Experiments, *The International Journal of Robotics Research* **vol. 28(3)** pp. 395–416, doi:10.1177/0278364908096236
- Park (2006) Park, Jaeheung, 2006. *Control strategies for robots in contact*, PhD thesis, Stanford University, Stanford, CA, USA
- Pellicciari, Giovanni et al. (2011) Pellicciari, Marcello, Giovanni, Berselli, Leali, Francesco, and Alberto, Vergnano, 2011. A Minimal Touch Approach for Optimizing Energy Efficiency in Pick-And-Place Manipulators, *International Conference on Advanced Robotics*, Tallinn, Estonia, June 20 - Jun 23 2011, pp. 100–105, doi:10.1109/ICAR.2011.6088620
- Pott (2008) Pott, Andreas, 2008. Forward Kinematics and Workspace Determination of a Wire Robot for In-

- dustrial Applications, *Advances in Robot Kinematics (ARK)*, Batz-sur-Mer, France, June 22 - 26 2008: Springer-Verlag, pp. 451–458
- Pott (2010) Pott, Andreas, 2010. An algorithm for real-time forward kinematics of cable-driven parallel robots, *Advances in Robot Kinematics (ARK)*, Piran Portoroz, Slovenio, June 28-July 1 2010: Springer-Verlag
- Pott (2012) Pott, Andreas, 2012. Influence of Pulley Kinematics on Cable-Driven Parallel Robots, *Advances in Robot Kinematics (ARK)*, Innsbruck, Austria, June 24–28 2012, pp. 197–204, doi:10.1007/978-94-007-4620-6\_25
- Pott (2014a) Pott, Andreas, 2014. An Improved Force Distribution Algorithm for Over-Constrained Cable-Driven Parallel Robots, Thomas, Frederico and Perez Gracia, Alba (eds.), *Computational Kinematics*, Springer, vol. 15, pp. 139–146, ISBN 978-94-007-7213-7, doi:10.1007/978-94-007-7214-4\_16
- Pott (2014b) Pott, Andreas, 2014. On the Limitations on the Lower and Upper Tensions for Cable-Driven Parallel Robots, *Advances in Robot Kinematics (ARK)*, Ljubljana, Slovenia June 29-July 3 2014, pp. 243–251, ISBN 978-3-319-06697-4, doi:10.1007/978-3-319-06698-1\_26
- Pott, Bruckmann et al. (2009) Pott, Andreas, Bruckmann, Tobias, and Mikelsons, Lars, 2009. Closed-form Force Distribution for Parallel Wire Robots, *Computational Kinematics*, Duisburg, Germany, May 6 - 8 2009: Springer, pp. 25–34
- Pott, Meyer et al. (2010) Pott, Andreas, Meyer, Christian, and Verl, Alexander, 2010. Large-scale assembly of solar power plants with parallel cable robots, *International Symposium on Robotics (ISR) and German Conference on Robotics (ROBOTIK)*, Munich, Germany, June 7-9 2010, pp. 1–6, ISBN 978-3-

- 8007-3273-9, URL <http://ieeexplore.ieee.org/stamp/stamp.jsp?arnumber=5756909>
- Pott, Mütherich et al. (2012) Pott, Andreas, Mütherich, Hendrik, Kraus, Werner, Schmidt, Valentin, Miermeister, Philipp, and Verl, Alexander, 2012. IPAnema: A family of Cable-Driven Parallel Robots for Industrial Applications, Bruckmann, Tobias and Pott, Andreas (eds.), *Cable-Driven Parallel Robots*, Stuttgart, Germany, September 3–4 2012: Springer, Mechanisms and Machine Science, pp. 119–134, ISBN 978-3-642-31987-7
- Raibert and Craig (1981) Raibert, Marc H. and Craig, John J., 1981. Hybrid Position/Force Control of Manipulators, *Journal of Dynamic Systems, Measurement, and Control*, vol. 103, pp. 126–133
- Reichert, Müller et al. (2014) Reichert, Christopher, Müller, Katharina, and Bruckmann, Tobias, 2014. Robust Internal Force-Based Impedance Control for Cable-Driven Parallel Robots, Pott, Andreas and Bruckmann, Tobias (eds.), *Cable-Driven Parallel Robots*, Duisburg, Germany, August 24-27 2014: Springer International Publishing, Mechanisms and Machine Science, pp. 131–143, ISBN 978-3-319-09488-5, doi:10.1007/978-3-319-09489-2\_10
- Reichert, Unterberg et al. (2015) Reichert, Christopher, Unterberg, Ulrich, and Bruckmann, Tobias, 2015. Energie-optimale Trajektorien für seilbasierte Manipulatoren unter Verwendung von passiven Elementen, *First IFToMM D-A-CH Conference*, Dortmund, Germany, March 11 2015, doi:10.17185/duepublico/37261
- Sato (2002) Sato, Makoto, 2002. Development of string-based force display: SPIDAR, *International Conference on Virtual Systems and Multi Media*, Gyeongju, Korea, September 25-27 2002, pp. 1034–1039
- Schmidt and Pott (2012) Schmidt, Valentin and Pott, Andreas, 2012. Implementing Extended Kinematics of a Cable-Driven

- Parallel Robot in Real-Time, Bruckmann, Tobias and Pott, Andreas (eds.), *Cable-Driven Parallel Robots*, Stuttgart, Germany, September 3–4 2012: Springer, Mechanisms and Machine Science, pp. 287–298, ISBN 978-3-642-31987-7, doi:10.1007/978-3-642-31988-4\_18
- Schmidt, Kraus et al. (2014) Schmidt, Valentin, Kraus, Werner, and Pott, Andreas, 2014. Presentation of Experimental Results on Stability of a 3 DOF 4-Cable-Driven Parallel Robot Without Constraints, Pott, Andreas and Bruckmann, Tobias (eds.), *Cable-Driven Parallel Robots*, Duisburg, Germany, August 24-27 2014: Springer International Publishing, Mechanisms and Machine Science, pp. 87–99, ISBN 978-3-319-09488-5, doi:10.1007/978-3-319-09489-2\_7, URL [http://dx.doi.org/10.1007/978-3-319-09489-2\\_7](http://dx.doi.org/10.1007/978-3-319-09489-2_7)
- Schmidt, Mall et al. (2015) Schmidt, Valentin, Mall, Alexander, and Pott, Andreas, 2015. Investigating the Effect of Cable Force on Winch Winding Accuracy for Cable-Driven Parallel Robots, Flores, Paulo and Viadero, Fernando (eds.), *New Trends in Mechanism and Machine Science*, Guimarães, Portugal, September 16-20 2014: Springer International Publishing, Mechanisms and Machine Science, vol. 24, pp. 315–323, ISBN 978-3-319-09410-6, doi:10.1007/978-3-319-09411-3\_34, URL [http://dx.doi.org/10.1007/978-3-319-09411-3\\_34](http://dx.doi.org/10.1007/978-3-319-09411-3_34)
- Schulte and Gerland (2004) Schulte, Horst and Gerland, Patrick, 2004. A systematic load identification procedure for parallel robot manipulators, *International Congress of Theoretical and Applied Mechanics (ICTAM)*, Warsaw, Poland, August 15-21 2004, ISBN ISBN 83-89697-01-1
- Shiqing, Franitza et al. (2004) Shiqing, Fang, Franitza, Daniel, Marc, Torlo, Frank, Bekes, and Hiller, Manfred, 2004. Motion control of a tendon-based parallel manipulator using optimal

- tension distribution, *IEEE/ASME Transactions on Mechatronics* **vol. 9**(3) pp. 561–568, doi:10.1109/TMECH.2004.835336, URL <http://ieeexplore.ieee.org/stamp/stamp.jsp?arnumber=1336812>
- Skalecki (2014) Skalecki, Patric, 2014. *Implementierung und Vergleich von computed-torque Regelstrategien für parallele Seilroboter*, Bachelor thesis, University of Stuttgart
- Smith (1959) Smith, Otto J. M., 1959. A Controller to Overcome Dead Time, *ISA Journal* (6) pp. 28–33
- Spong (1987) Spong, Mark W., 1987. Modeling and Control of Elastic Joint Robots, *Journal of Dynamic Systems, Measurement, and Control* **vol. 109**(4) pp. 310–318, doi:10.1115/1.3143860, URL <http://dx.doi.org/10.1115/1.3143860>
- Surdilovic, Jinyu Zhang et al. (2007) Surdilovic, Dragoljub, Jinyu Zhang, and Bernhardt, Rolf, 2007. STRING-MAN: Wire-robot technology for safe, flexible and human-friendly gait rehabilitation, *International Conference on Rehabilitation Robotics (ICORR)*, Noordwijk, Netherlands, June 13-15 2007, pp. 446–453, doi:10.1109/ICORR.2007.4428463
- Taghirad and Bedoustani (2011) Taghirad, Hamid D. and Bedoustani, Yousef Babazadeh, 2011. An Analytic-Iterative Redundancy Resolution Scheme for Cable-Driven Redundant Parallel Manipulators, *IEEE Transactions on Robotics* (99) pp. 1–7, doi:10.1109/TRO.2011.2163433, URL <http://ieeexplore.ieee.org/stamp/stamp.jsp?arnumber=6011703>
- Tang, Yao et al. (2011) Tang, Hai Tao, Yao, Jian Tao, Cheng, Li, and Zhao, Yong Sheng, 2011. Hybrid Force/Position Control Investigation of Parallel Machine Tool with Redundant Actuation, *Applied Mechanics and Materials* **vol. 121-126** pp. 2040–2044, doi:10.4028/www.scientific.net/AMM.121-126.2040

- Verdonck (2004) Verdonck, Walter, 2004. *Experimental robot and payload identification with application to dynamic trajectory compensation*, PhD thesis, Leuven University, Leuven, Belgium
- Verhoeven (2004) Verhoeven, Richard, 2004. *Analysis of the Workspace of Tendon-based Stewart Platforms*, PhD thesis, University of Duisburg-Essen, Duisburg, Germany
- Voss, Wijk et al. (2012) Voss, Kevin H. J., Wijk, Volkert, and Herder, Just L., 2012. Investigation of a Cable-Driven Parallel Mechanism for Interaction with a Variety of Surfaces, Applied to the Cleaning of Free-Form Buildings, Lenarčič, Jadran and Hustý, Manfred L. (eds.), *Advances in Robot Kinematics (ARK)*, Dordrecht: Springer Netherlands, pp. 261–268, ISBN 978-94-007-4619-0, doi:10.1007/978-94-007-4620-6\_33
- Wang, Wu et al. (2009) Wang, Jinsong, Wu, Jun, Wang, Liping, and You, Zheng, 2009. Dynamic feed-forward control of a parallel kinematic machine, *Mechatronics* **vol. 19**(3) pp. 313–324, doi:10.1016/j.mechatronics.2008.11.004
- Williams II (1998) Williams II, Robert L., 1998. Cable suspended haptic interface, *International Journal of Virtual Reality* **vol. 3**(3) pp. pp 13–21
- Yu, Eberhard et al. (2013) Yu, Haidong, Eberhard, Peter, Zhao, Yong, and Wang, Hao, 2013. Sharing behavior of load transmission on gear pair systems actuated by parallel arrangements of multiple pinions, *Mechanism and Machine Theory* **vol. 65** pp. 58–70, doi:10.1016/j.mechmachtheory.2013.02.010, URL <http://www.sciencedirect.com/science/article/pii/S0094114X13000475>
- Yu, Lee et al. (2010) Yu, Kun, Lee, Leng-Feng, Tang, Pei Ching, and Krovi, Venkat N., 2010. Enhanced Trajectory Track-

- ing Control with Active Lower Bounded Stiffness Control for Cable Robot, *IEEE International Conference on Robotics and Automation (ICRA)* doi: 10.1109/ROBOT.2010.5509458
- Zengxi and Hui (2009) Zengxi, Pan and Hui, Zhang, 2009. Improving robotic machining accuracy by real-time compensation, *International Joint Conference ICCAS-SICE*, Fukuoka, Japan, August 18-21 2009, pp. 4289–4294, ISBN 9781424450725

In Seilrobotern werden Seile zur Kraftübertragung eingesetzt. Da Seile nur Zugkräfte übertragen, stellen Seilroboter hohe Anforderung an die Regelung. Die in dieser Arbeit zu Grunde gelegten Seilroboter besitzen mehr Seile als Bewegungsfreiheitsgrade der Plattform und zählen damit zur Klasse der redundanten Roboter. Die Redundanz erlaubt es, die Seile gegeneinander zu verspannen. In dieser Arbeit werden Kraftregler für die Regelung der internen Verspannung der Seile und der externen Kräfte zwischen Roboterplattform und der Umgebung entwickelt und verifiziert.

ISBN 978-3-8396-0979-8



9 783839 609798